Hybrid structures for molecular level sensing

by

Melburne Charles LeMieux

A dissertation submitted to the graduate faculty

in partial fulfillment of the requirements for the degree of

DOCTOR OF PHILOSOPHY

Major: Materials Science and Engineering

Program of Study Committee:
Vladimir V. Tsukruk, Major Professor
Ashraf Bastawros
Zhiqun Lin
Murti Salapaka
Xiaoli Tan

Iowa State University

Ames, Iowa

2006

Graduate College
Iowa State University

This is to certify that the doctoral dissertation of

Melburne Charles LeMieux

has met the dissertation requirements of Iowa State University

Signature was redacted for privacy.

Major Professor

Signature was redacted for privacy.

For the Major Program

TABLE OF CONTENTS

ACKNOWLEDGEMENTS

I would like to thank my POS Committee for taking time out of their busy schedule to make time for me. This includes Prof. Ashraf Bastawros, Prof. Zhiqun Lin, Prof. Murti Salapaka, and Prof. Xiaoli Tan.

This all started for me essentially five months out of high school, when as a freshman in the college of engineering at Western Michigan University, I received a college-wide email from one Dr. Vladimir Tsukruk. I immediately responded to his email that was asking for undergrad students to help out in his research lab, and he immediately responded back telling me, in true Prof. Tsukruk form: come see me ASAP! So, we chatted for a few minutes before he took me to the lab, and within one hour, I was already scanning on the atomic force microscope (AFM). He hadn't even officially hired me, and yet I was working in his lab, and after a few hours, he said "Ok Melbs, so I will see you tomorrow." I left wondering if I officially had the job or not (money was tight, and I was living solely off of my student loans and a crappy job through the loan program at the library). Furthermore, that next day, I had classes straight thru from 8am – 8pm. The next day came, I skipped all of my classes that day, and spent the entire day in the lab, and the rest, as they say, is history.

Obviously, I would not be here today if not for Vladimir Tsukruk, and to him I owe my greatest thanks. Mentors like this, with amazing motivation (and the amazing ability to straddle that *very* fine line between driving students to succeed/driving students to insanity) that pay sincere attention to your work, put students in great positions to achieve ultimate success. Therefore, Professor, thank you.

I need to thank my labmates, and by labmates, I mean best friends. Especially close to me throughout this work have been John Hazel, Duangrut Julthongpiput, Kirsten Larson-Genson, Dr. Igor Luzinov, Dr. Valeriy Gorbunov, Sergiy Peleshanko, Michael McConney, and Srikanth Singamaneni.

This work has been done through many collaborations with other labs, and I would like to thank the following people for their support and mutual respect: Dr. Alex Noy (LLNL), Prof. Sergiy Minko (Clarkson University), Prof. Ned Thomas (MIT), Dr. Denys Usov (Dresden), Dr. Dan Sordelet (Ames Lab), Dr. Jean-Marie Dubois (Ecole des Mines de Nancy, France) and Dr. Mike Dugger (SNL).

Finally, I would like to thank my parents, Mick and Barb, and all of my family. You are my sole inspiration and my heroes. Thank you for all of your support, patience, and love throughout this chapter of my life.

ABSTRACT

With substantial molecular mobility and segment dynamics relative to metals and ceramics, all polymeric materials, to some extent, are stimuli-responsive by exhibiting pronounced chemical and physical changes in the backbone, side chains, segments, or end groups induced by changes in the local environment. Thus, the push to incorporate polymeric materials as sensing/responsive nanoscale layers into next-generation miniaturized sensor applications is a natural progression. The significance and impact of this research is wide-ranging because it offers design considerations and presents results in perhaps two of the most critical broad areas of nanotechnology: ultrathin multifunctional polymer coatings and miniaturized sensors. In this work, direct evidence is given showing that polymer coatings comprised of deliberately selected molecular segments with very different chemistry can have switchable properties, and that the surface composition can be precisely controlled, and thus properties can be tuned: all in films on the order of *20 nm and less*. Furthermore, active sensing layers in the form of plasma-polymerized polymers are successfully incorporated into actual silicon based microsensors resulting in a novel hybrid organic/inorganic materials platform for microfabricated MEMS sensors with record performance far beyond contemporary sensors in terms of detection sensitivity to various environments. The results produced in this research show thermal sensors with more than two orders of magnitude better sensitivity than what is attainable currently. In addition, a humidity response on the order of parts per trillion, which is four orders of magnitude more sensitive than current designs is achieved. Molecular interactions and forces for organic molecules are characterized at the picoscale to optimize polymeric nanoscale layer design that in turn optimize and lead to microscale hybrid sensors with unprecedented sensitivities.

Chapter 1

Sensors and the Dynamic Nature of Polymers

1.1 Polymers in Sensors

Sensors, a field of global research in which, over the last decade, there has been an exponential increase in development and an astronomical augmentation in ideas that promises to incite the work of, and affect scientists from all disciplines. Seemingly, every major breakthrough in nanoscale science is directly funded by a proposal with the word "sensor" somewhere in the title, or can be indirectly applied to a possible "sensor application".[1] Sensors, sensing, sensor design, sensing materials; so much work being done in so many directions, but how does one make sense of all this sensor work? Especially at the nanoscale, sensor development is very intricate in that specific designs and materials are implemented to detect even single molecules in chemical and biological sensors. Because of this, not only a deep knowledge of the "database" of specific interactions is required, but there also is a need for a deep, full understanding of the fundamentals of molecular scale interactions that will lead to future sensor development and enhance this "database". The subject of this work is designing polymer based assemblies made of polymeric, or more generally, organic nanocomposite materials as active sensing nanolayers and engineering them into hybrid organic-inorganic, next generation sensors. To do this requires a few major components: 1) Designing nanolayers for a specific intended sensing purpose, *or* desired response. This involves asking the questions of what physical information do we want to obtain from our environment (physical, chemical, biological), why we want this information or response (who really cares!), and how we get this information (what are the *fundamental interactions* that allow this). 2) Implementing highly controllable polymer surfaces into microelectromechanical systems (MEMS and now NEMS), thereby facilitating these sensing/response layers into real sensors that can be feasibly batch-processed through established microfabrication. 3) Characterization. Proof of principal in terms of their response because after all, it has to work.

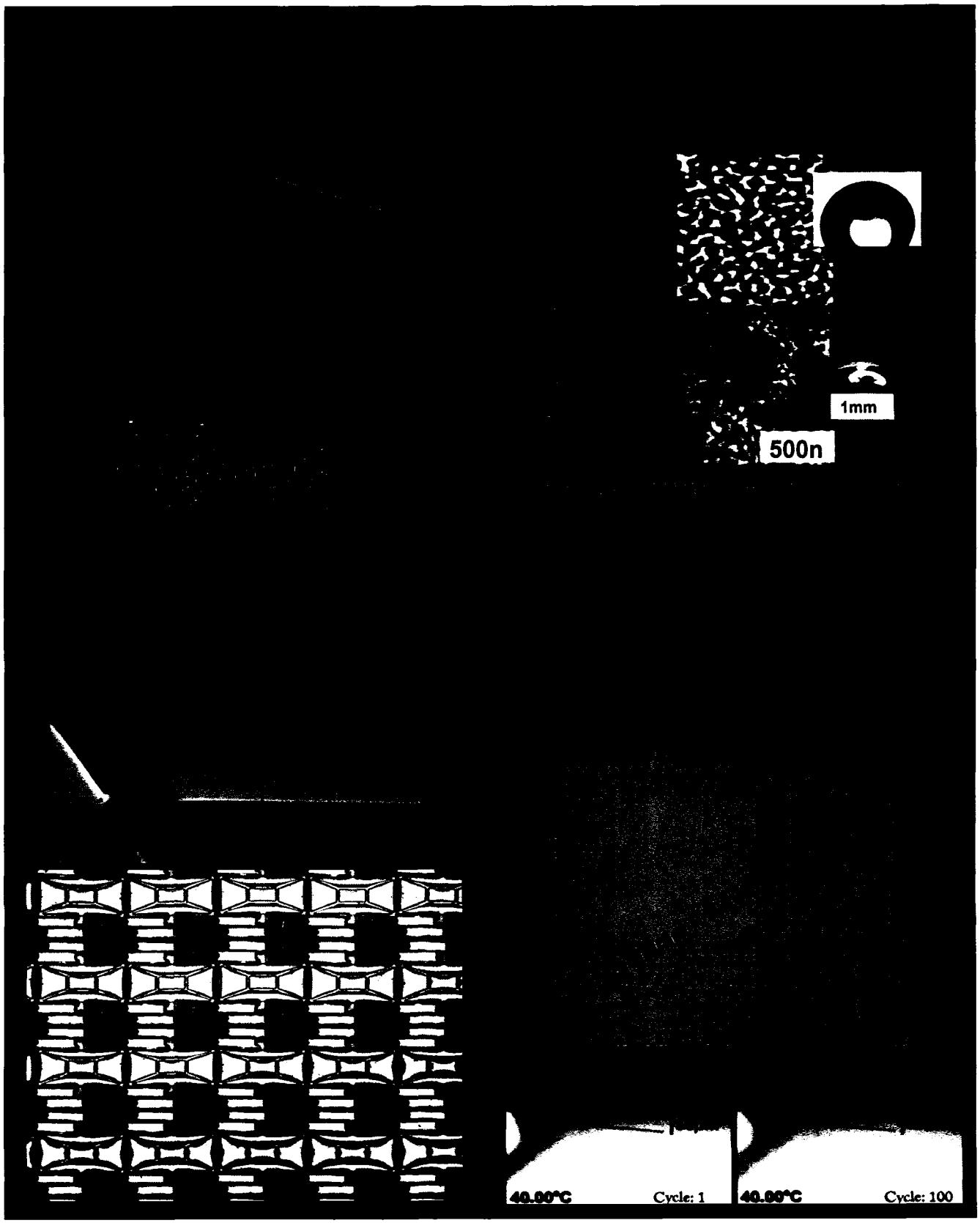

Figure 1-1. Process overview of sensor research.

In carrying out this research project, it was of primary importance to recognize what potential new insights can ultimately be achieved to make this work significant. To do this, several considerations must be made which will be outlined and described in this chapter. The first step is to understand the current state of sensor research, and what improvements can be made in terms of sensor materials, sensor size/feasible integration into microdevices, and of course sensitivity. As stated above, the overall theme of this research is to understand and successfully design organic and polymeric active sensing layers and develop working hybrid sensors incorporating these new materials. Thus, one aspect of the design is set in concrete: the use of these materials to develop ultrasensitive hybrid sensors.

Why Hybrids? Because we want to crossbreed the best of both worlds: inorganic ceramics (such as silicon) are well established in microdevices and microfabrication, and this foundation is not likely to change anytime soon. On the other hand, polymers are the best *active sensing* materials but do not always supply the best miniaturized platform. Thus, by definition, hybrid sensors will consist of two very diverse components to advance sensor science. Semiconductors and semiconducting metal oxides have been the traditional *active sensing materials* in sensing applications. However, especially in the last five years, polymers have gained a tremendous footing in the field of artificial sensors based on the principal of mimicking natural sensing structures in organisms.[2] These traditional materials are not dynamic enough for suitable response selectivity. For example sensors are required to analyze specific proteins in vitro or ultratrace levels of environmental pollutants, and traditional materials cannot do this because of intrinsic limitations in sensitivity.[3] Moreover, multifunctional sensors are required today that require surfaces with very different chemistry in a *single* material, and traditional materials are limited in this regard as well. Additionally, polymeric based sensors bring a desirable diversity in signal transduction principals that traditional materials cannot offer.[4]

For advanced sensing, polymeric materials are the clear-cut best choice for these applications not only because of ease and versatility of synthesis, fabrication, and processability, but because to some extent, flexible polymer chains will always respond to the local environment or an applied stimuli by exhibiting pronounced structural changes in

the backbone, side chains, segments, or end groups relative to each other.[5] This is because polymers have segmental dynamics and substantial molecular mobility compared to ceramics or metals, and all materials have a fundamental tendency to always try to reorganize their surface to minimize the interfacial free energy with the local environment. In fact, the term "polymer materials" may be suitably described as "Stimuli responsive materials", or SRMs.[67] SRMs are defined as polymers that undergo relatively large *and abrupt* physical, chemical, or structural changes in response to small external changes in the local environmental conditions.[8] The push to incorporate polymeric materials into next-generation sensor applications is, literally, a natural progression.[9]

On one hand, response to stimuli is a natural process of living, and many synthetic polymers are currently being designed to mimic important biomaterials that perform vital sensing functions in living organisms (in fact, as you will see later, the design approach for the sensors in this thesis is a bioinspired design). Put simply, nature has selected (bio)polymers as building blocks for cells and tissues, and these cells and tissues are champions in terms of complex sensing capabilities. On the other hand, synthetic polymers are like a child's (or curious adult) Lego blocks; through endless interchangeable building, they offer a wealth of opportunities (by changing chemical groups) to design responsive materials triggered by external stimuli. Additionally, polymeric materials, because they can be designed with a virtually endless combination of length and branching, can possess unique topologies[10] (overall architecture) leading to never before seen physical properties[11], or be rendered biodegradable[12] for biomedical and drug-delivery mechanisms.[13]

This nature of polymers is translated into many commonplace items in our lives. Thin organic or polymeric coatings are often applied to the surfaces of these objects to better control their interaction with the environment, or in a more intuitive way, allow better "sense and respond" mechanisms. Such thinking has been empirically acknowledged by civilizations for thousands of years, and the coating industry of today is a healthy multi-billion dollar business.[14] But what if the band-aide could "sense" when we wanted to remove it, and it instantly switched from a sticky surface to a repellant surface to prevent the infamous ripping of body hair? Similarly, it would be very convenient if the outside surface

of the windows in our homes could "sense" the temperature and amount of sunlight, and "respond" by adjusting the tint accordingly. The concept of fabricating *sensing* or *responsive* surfaces has stimulated intense research in polymer interface science towards the design of such materials.[15,16,17] The need for increased selectivity, faster response speed, and enhanced sensitivity in sensors is now, more than ever, of great interest. Most assuredly, novel polymer based sensing layers especially when hybridized into inorganic MEMS structures, will provide dramatic benefits for nanoscience, and in particular, the growing sensor field.[14]

1.2 Polymers in various sensors

There are numerous examples of thermal, gas, chemical, and biosensors based on exploiting specific interactions with organic materials, with selected cases given in Tables 1-1 – 1.4.[17] For example, polyacetylene, which is actually known to be the first organic conducting polymer (OCP), experiences a change in conductivity of eleven orders of magnitude when exposed to iodine vapor.[18] Other heterocyclic polymers, which retain the π-system of polyacetylene, were later developed. Such heterocyclic OCPs include polyfuran, polythiophene, and polypyrrole.[19,20] The intrinsic mechanism in these polymers allowing this is the π-conjugated macromolecules show strong changes in electrical and optical properties when they are exposed to a flux (negative or positive) of some chemical analyte. These property changes can be observed at room temperature when they are exposed to very low concentrations (a few parts per million (ppm)), which make them ideal candidates for materials in gas sensors.[21]

In terms of pH sensing in aqueous media, sensors employing thin films of polyaniline have been very effective.[22] These films possess excellent stability (can be stored in air for months) and show rapid reversible color change upon pH change due to varying degrees of protonation of the imine nitrogen atoms in the polymer.[23,24] Advanced applications also include potential sensors in micro – fluidic systems such as pH sensitive gates, oxidoreduction sensitive gates, and photocontrolled chemical gates to regulate flow through membranes.[25,26,27,28] Humidity sensors (Table 1-4) based on polymer materials have been developed that work on the principal that ion conducting polymer systems undergo variation of the electrical conductivity with water vapor.[29]

Table 1-1: Polymer based biological sensors (from Ref. 17)

Sensor type	Polymer used	Fields of applications	Special features
Biosensor	Cellulose membrane of bacterial origin	Glucose sensor	Improvement in the long-term stability of the amperometric sensor
Biosensor	PVC	Analysis of creatinine in urine	Polymer membrane with natural electrically neutral lipids as plasticizer
Biosensor	Polyaniline	Estimation of glucose, urea, triglycerides	Polymer deposition and enzyme immobilization done electrochemically
Biosensor	Poly (o-aminophenol)	Glucose biosensors	Immobilization on platinized GCE
Biosensor	Polypyrrole	Estimation of glucose	Electrode immobilization of an enzyme by electropolymerisation of pyrrole
Biosensor	Polytyramine	Estimation of L-amino acids	Enzyme immobilization by electropolymerisation
Biosensor	Poly (o-aminophenol)	Detection of uric acid	Polymer modified bienzyme carbon paste electrode used for detection
Biosensor	Nafion	Estimation of glucose	Sensor based on polymer modified electrodes optimized by chemometrics method
Biosensor	Cross-linkable redox polymer	Enzyme biosensors	Cross-linkable polymers used in construction of enzyme biosensors
Biosensor	Polysiloxane	Blood glucose determination	Composite membrane was formed by condensation polymerisation of dimethyldichlorosilane at the surface of a host porous alumina membrane
Biosensor	Polypyrrole, Poly (2-hydroxy ethyl methacrylate)	Estimation of glucose	Polypyrrole and enzyme is entrapped in poly(2-hydroxy ethylmethacrylate)
Biosensor	Poly [3-(1-pyrrolyl) propionic acid, Poly (o-phenylene diamine)PPD, Nafion	Estimation of glucose	PPD and Nafion forms inner films Carbodiimide forms covalent linkage between GOD and polypyrrole derivatives
Biosensor	Polypyrrole derivative containing phosphatidyl choline, Nafion or poly (o-phenylenediamine)	Estimation of glucose	Hemocompatible glucose sensor
Biosensor	Poly (1,2-diaminobenzene) Polyaniline	Sensing glucose	Insulating poly (1,2-diaminobenzene) was grown on polyaniline film to vary sensitivity
Biosensor	Polyaniline	Sensing glucose	Sensor was constructed in bread/butter/jam configuration
Biosensor	PVC-NH2 membrane	Glucose and urea detection	Enzyme immobilized on solid-state contact PVC-NH2 membrane
Biosensor	Polypyrrole	Can sense fructose	Enzyme entrapped in membrane shows sharp increase in catalytic activity
Biosensor	Polypyrrole	Can sense H2O2	Pyrrole oligomers can act as mediator
Biosensor	Ferrocene modified pyrrole polymer	Estimation of glucose.	Ferrocene – pyrrole conjugate efficient oxidant of reduced GOD
Biosensor	Polymerized phenols and its derivatives	Estimation of glucose	Electrochemical immobilization of enzymes
Biosensor	Polypyrrole	Estimation of glucose	GOD was covalently attached to polypyrrole at N-(2-carboxyethyl) group
Biosensor	Redox polymer	Detection of glucose, lactate, pyruvate	Glucose, lactate, pyruvate biosensor array based on enzyme – polymer nanocomposite film

Table 1-2: Polymer based chemical sensors (from Ref. 17).

Chemical sensor	Poly (vinyl chloride)	Estimation of pethidine hydrochloride in injections and tablets	Pethidine – phosphate tungstate ion association as electroactive material
Chemical sensor	Divinyl styrene polymer and isoprene polymer	Environmental control of trace organic contaminants	Piezoelectric
Chemical sensor	Methyl and butyl acrylate copolymer	Measurement of Cu ion concentrations	Polymer paste used to produce ion-sensitive membranes
Chemical sensor	Hydrophobic polymers	To detect organic pollutants in drinking water	Polymer and macrocyclic calixarene forms the sensitive layer
Chemical sensor	Nafion	Detection of dissolved O2 in water	Gold-solid polymer-electrolyte sensor
Chemical sensor	PVC	Determine phentermine	PVC with tris(2-ethylhexyl)phosphate as solvent mediator and NaHFPB as ion-exchanger
Chemical sensor	Polyaniline (emeraldine base)	Can sense humidity, NH3, NO2. Can be used to fabricate other molecular devices	Nanocomposite ultra-thin films of polyaniline and isopolymolybdic acid
Chemical sensor	Polyester	Determination of H2O2	Glassy carbon and graphite/polyester composite electrode modified by vanadium-doped -zirconia
Chemical sensor	Polyaniline and its derivatives	Sensing aliphatic alcohols	Extent of change governed by chain length of alcohol and its chemical
Chemical sensor	Cross-linked PVA	Sensing chemicals	Polymer used for immobilizing indicators
Chemical sensor	Epoxy resin	Lithium ion detection	L-MnO2-based graphite-epoxy electrode
Chemical sensor	PVC	Used for detection of phosphate ions	Plasticised PVC membrane containing uranyl salophene derivative
Chemical sensor	Carbon black poly(ethylene-co-vinyl acetate) and poly (caprolactone) composite	Vapor detector	Composite gives reversible change in resistance on sorption of vapor
Chemical sensor	Poly (dimethyl siloxane)	Sensing chemicals	Support membrane is coated with polymer
Chemical sensor	Polyaniline	Measure pH of body fluids and low ionic strength water	Polymer thin film electrodeposited onto ion-beam etched carbon fiber
Chemical sensor	Polyaniline	pH sensing	Optical method

Table 1-3: Polymer based gas sensors (from Ref. 17).

Gas sensor	Copolymers of poly (EDMA-co-MAA)	Detection of terpene in atmosphere	Piezoelectric sensor coated with molecular imprinted polymer
Gas sensor	Polyethylmethacrylate, chlorinated polyisoprene, polypropylene (isotactic, chlorinated), styrene/butadiene, aba block copolymer, styrene/ethylene/butylene aba block copolymer, polyepichlorohydrin	Identify gases and gas mixtures	Polymer -carbon black composite films used
Gas sensor	Nafion	Detection of ethanol gas concentration	Fuel cell with polymer electrolyte membrane were used
Gas sensor	Polyaniline (PANI), polyaniline and acetic acid mixed film PANI-polystyrenesulfonic acid composite film	NO2 was detected	Layers of polymer films formed by Langmuir-Blodgett and self-assembly techniques
Gas sensor	Poly [3-(butylthio)thiophene]	Gas Sensor	Films of polymer prepared via LB deposition and casting
Gas sensor	PVC	Detection of gaseous NO2 in air	A solid polymer electrode of 10% PVC is present in the sensor
Gas sensor	Polypyrrole nanocomposite	Sensing CO2,N2,CH4 gases at varying pressures	Nanocomposite of iron oxide polypyrrole were prepared by simultaneous gelation and polymerisation process
Gas sensor	Propylene – butyl copolymer	Detection of toluene, xylene gas	Polymer film coated quartz resonator balance

Table 1-4: Polymer based humidity sensors (from Ref. 17).

Humidity sensor	PVA	Optical humidity sensing	Crystal violet and Methylene blue are incorporated in PVA/H3PO4
Humidity sensor	Poly (o-phenylene diamine), poly (o-amino phenol), poly (m-phenylene diamine) or poly (o-toluidine) and PVA	Sensing change in humidity	In this sensor various polymer composites used
Humidity sensor	Poly (ethylene oxide)	Humidity sensing	Alkali salt doped poly (ethylene oxide) hybrid films used
Humidity sensor	Perfluorosulfonate ionomer (PFSI)	Humidity sensing	Incorporation of H3PO4 improves sensitivity

While most of these sensors have performance, in terms of sensitivity, that surpass that of sensors made of traditional inorganic materials, they still have several drawbacks, and are not optimal for advanced sensing applications. The primary negative aspect of most of these sensors is the thickness of the sensing layer, which is usually several microns thick. For implementation into microsensors with nanoscale dimensions, this is simply not feasible, and the main purpose of the research in this project is to design and develop *nanoscale* responsive/sensing coatings for microsensors. Even the labeled "ultrathin" sensors in the above tables incorporate 100 nm thick films in the best (thinnest) cases.[30,31] However, these nanoscale coatings are commonly applied to electrodes[31] by a photopatterning process involving complicated photolithography and elaborate substrate design or even porous substrates.[32] Unfortunately, all of this implies many extra fabrication steps.

To this end, for most of these listed sensors, the active sensing layer is deposited by Langmuir-Blodgett (LB) techniques[33], layer-by-layer growth[30], or casting[34]. Not only are these coating methods impossible to integrate in microfabrication techniques, but they also provide for very poor adhesion to any substrate. In fact, when reading through the individual articles cited in the above tables, most of the lifetimes of the sensors were within a few months.[17] Another aspect of these coating techniques to consider is the conformation of the flexible polymer chains in the film. While it is true that dynamic, flexible polymer chains will always react to their environment, as will be shown below, the most optimal conformation of a polymer chain in terms of response/sensing is in the non-equilibrium "brush" conformation in which only one end is covalently grafted to the surface (see section 1.4). Thus, there is a strong need to improve upon these sensors and design sensing layers that are covalently grafted to the surface or adhered very strongly.

Besides the size, construction, and quality issues, the sensors listed in the above tables are engineered to sense one specific analyte or mode (either pH, or humidity), and it is unclear whether they can be made to diversify. Mainly, these are "niche" sensors and are only useful if one specific response must be determined. However, in real-life applications, this is not practical. For example, weapons or threat sensing applications require a sensor to

sense several different gases or chemicals. It is useless if a sensor reads "all clear" to VX nerve gas because it does not sense the necessary thiolate group, but the user drops dead to mustard gas because the sulfonium salt that attacks the skin could not be detected. Clearly, sensors must be as dynamic as possible, capable of responding to many environments. One way to do this is by incorporating several different chemistries in a single sensor that can be exposed at the surface simultaneously, or at least change the surface properties of the sensor through a large, dynamic range. Another possible way is to have novel design considerations that incorporate a tuned amount of residual stresses (mechanical strain) or charged ions and radicals trapped within the sensing layer. Such considerations have yet to be incorporated into real sensors, and as will be seen, these approaches will be used in this work.

Another major drawback of the sensors listed here is their complexity in detection. Due to the design, the signal transduction is typically represented by a change in resistance, capacitance, or conductivity, which requires additional electronics integrated into the sensor. As will be seen with the work in this thesis, a much simpler method is monitoring a signal requiring no additional interconnects.

Finally, one last comment should be made about sensor types. As can be seen from these tables, overall, the literature is lacking in thermal/IR sensors designed from polymeric materials. A major undertaking in this project was to design this type of sensor. It was immediately clear that this type of sensor incorporating polymeric or organic materials has yet to be realized, and thus the work in this thesis is truly novel as the development of hybrid organic/inorganic thermal sensors has yet to be achieved.

1.3 Thermal IR sensors

While a portion of this project aims to develop SRMs for potential sensor applications, there was an additional project undertaking with a private company (Agiltron, INC) to immediately develop and incorporate SRM into actual working sensors. Thus, to focus on an actual application of practical significance incorporating these materials, I will design and

implement an optimal polymer or nanocomposite polymer coating to enhance the detection sensitivity of a MEMS (microelectromechanical systems) based infrared (IR) sensor. Such an application will require polymer layers that sense temperature and/or IR radiation changes. Infrared sensors and imagers are critical for many civilian security applications such as gas detection and environmental surveys, and human or weapons sensing/tracking for defense related purposes can be potentially improved with more sensitive IR technology. To be practical for these applications, the IR device needs to possess high sensitivity, along with being small, compact, and batch processed for cost reduction.

IR detectors can be sorted into two general classifications based on their detection type: photon detection and thermal detection (Table 1-5). Typical IR sensors employing cooled photon detectors (usually cryogenic cooling to around 80 K) to reduce thermal noise have typical sensitivities (measured as the noise-equivalent temperature difference, or NETD, and this will be defined later) of 5 – 20 mK.[35,36]

Table 1-5: Classification of the IR detector technology (From Ref. 38)

Detector type			Advantages	Disadvantages
Thermal (thermopile, bolometer, pyroelectric)			Light, rugged, reliable, and low cost Room temperature operation	Low detectivity at high frequency Slow response (ms order)
Photon	Intrinsic	IV-VI (PbS, PbSe, PbSnTe)	Easier to prepare More stable materials	Very high thermal expansion coefficient Large permittivity
		II-VI (HgCdTe)	Easy bandgap tailoring Well developed theory & exp. Multicolour detection	Non-uniformity over large area High cost in growth and processing Surface instability
		III-V (InGaAs, InAs, InSb, InAsSb)	Good material & dopants Advanced technology Possible monolithic integration	Noncoplanar with large indium mismatch Long wavelength cutoff limited to 7 μm (at 77 K)
	Extrinsic (Si:Ga, Si:As, Ge:Cu, Ge:Hg)		Very long wavelength operation Relatively simple technology	High thermal generation Extremely low temperature operation
	Free carrier (PtSi, Pt_2Si, IrSi)		Low-cost, high yield Large & close packed 2-D arrays	Low quantum efficiency Low temperature operation
	Quantum wells	Type I (GaAs/AlGaAs, InGaAs/AlGaAs)	Matured material growth Good uniformity over large area Multicolour detection	High thermal generation Complicated design and growth
		Type II (InAs/InGaSb, InAs/InAsSb)	Low Auger recombination rate Easy wavelength control	Complicated design and growth Sensitive to the interface
	Quantum dots	InAs/GaAs, InGaAs/InGaP, Ge/Si	Normal incidence of light Low thermal generation	Complicated design and growth

However, the bulky cooling unit drives up the cost of IR devices and severely limits portability but is necessary since thermal noise increases exponentially with temperature in photonic IR detectors. On the other hand, for IR sensors with thermal detectors, the noise varies as $\sqrt{(k_bT)}$ so cooling does not significantly enhance performance.[35] Thus, great effort is being devoted to the development of *uncooled* IR sensors over the past two decades.[37] In fact, the development of uncooled IR technology that is based on optical MEMS structures for imaging and detection at room temperature is seen as a relatively recent revolution in this field, with initial reports emerging around 1995.[38] According to the literature, optimal NETD values of uncooled IR sensors today ranges from 100 – 200 mK.[36,38,39]

A general theory is that the low sensitivity of thermal detectors as compared to cooled photon detectors can be compensated by having a large number of sensing elements arranged in a focal plane array (FPA). In this platform, each sensor represents a "pixel", and thus the push for incorporating many pixels into MEMS devices has become the norm in IR technology. In a few instances, lower values have been reported for MEMS based uncooled IR sensor FPAs. For example, 320 x 240 pixel FPAs have demonstrated NETD values of 35, 23, and 5 mK under various circumstances.[38,40,41,42] Theoretical studies based on current technological limitations predict that the sensitivities of uncooled thermal based detection can approach that of cooled photonic detection.[43,44] Furthermore, the average cost of cooled IR detectors is around $50,000 (plus operating costs of the cryogenic cooling system), while uncooled units can have prices less than $5,000, making them an even more attractive alternative.[38]

Future uncooled IR sensors and imagers consistently need to have NETD values of 10 – 20 mK to be competitive, and research directions need to be focused on reducing the size of the pixels in FPAs, increasing the packing density in FPAs, and enhancing the design of the pixels in the FPA, which consists of optimal shapes and choice of optimal materials. This is the key to increased sensitivity in uncooled IR sensor and imaging technology.

As stated previously, a new class of IR detector based on optical MEMS has recently been developed resulting in unprecedented opportunities for IR imaging technology.[45] The most promising design choice is microbeams or microcantilevers (MCs) similar to those used in atomic force microscopy (AFM) arranged in the FPA. This is because they are easily batch-processed using the well-developed semiconductor micromachining process which also provides great flexibility in design shape and materials that are compatible with the CMOS process, while substantially driving down costs. Micromachining processes are routinely used to produce MEMS devices including actuators, gears, and sensors, in a wide range of sizes with critical dimension capabilities in the tens of nanometers when combined with lithography steps.[46,47]

The main principal behind the operation of these uncooled IR detectors is that the incident radiation is absorbed to change the material temperature, and the resultant change in some physical property is outputted and detected. Uncooled arrays are based on several different types of thermal detection. Currently, changes in electrical conductivity/resistance (bolometer), by gas expansion (Golay cell), or pyroelectricity (pyroelectric detectors) are used (Figure 1.2) in various versions of IR detectors.[38] An alternative approach based upon optical-mechanical IR detection (Figure 1.2) adopting the well – known principle behind AFM: mechanical deformations of a cantilever beam can be detected optically down to tenths of angstroms of deflection. Compared to other detection methods, the optical route is optimal combining low noise with the lowest fabrication costs. This relatively simple type of detection has the main advantage over the others because it eliminates the complicated installation of microelectronics and circuits, reducing fabrication costs.[39,48] Furthermore, the electronic based detection schemes, such as those listed above, all suffer from Johnson noise and non-uniformity in electrical resistance over the pixels.[43] On the other hand, the NETD associated with the optical lever scheme is only limited by noise inherent in the optics, which can be controlled externally, as well as thermal noise of the cantilever beam, which can be controlled by varying the shape and stiffness of the beam. With the simple, compact, and extremely low cost optical – detection approach, it is anticipated that uncooled IR sensors can reach NETD values below 3 mK,[35,45] and potentially revolutionize this technology.

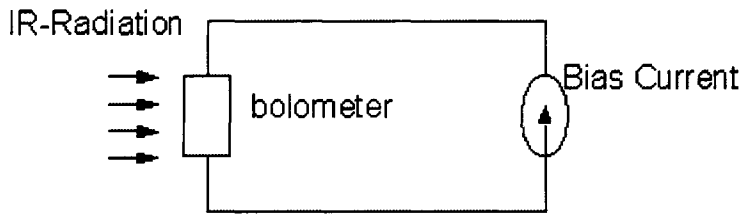

A Bolometer consists of the absorber element made of a material that upon temperature change due to IR flux, undergoes a strong change in resistivity. The material is part of a circuit under bias, and the temperature change is measured as a voltage change, which produces the electric signal.

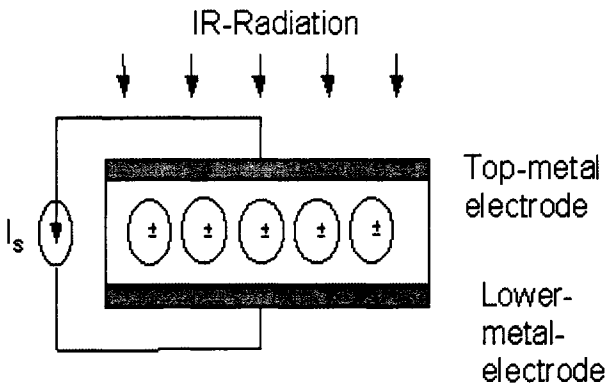

The pyroelectric detector consists of a material that exhibits a spontaneous electric polarization. Opposite faces of certain crystallographic orientations exhibit opposite electrical charges in response to temperature changes. Thus, a change in temperature produces a transient change in the surface charge causing a displacement current (I_s) to flow in an external circuit connected to the pyroelectric material.

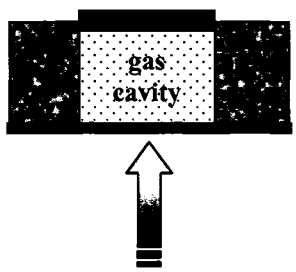

The Golay cell absorbs IR radiation through an IR transparent window causing the gas to heat/cool and expand/contract. The membrane on the other side (typically a silicon derivative in current designs) deflects, and this deflection is monitored by capacitive or optical means.

Bimaterial cantilever is deformed due to IR flux, and the deflection is easily monitored by optical means.

Figure 1.2. Schematic of common uncooled IR detectors platforms.

Another critical issue is the choice of materials for the FPA so that the thermal-mechanical response of each pixel (cantilever beam) in the FPA is maximized. The design that we will propose is based on the recently exploited bimaterial or bimorph approach (Figure 1-2, 1-3).[49,50] This widely used method allows for the bending of a cantilever upon incident IR radiation due to a mismatch in thermal expansion coefficients (α) of the materials.[51,52] This approach was pioneered by Barnes and Gimzewski when they coated microfabricated cantilevers with a metal to form the bimorph.[51] Later, Datskos et al. made the point that 2D arrays of these heat sensitive cantilevers can serve as thermal imaging devices.[53,54] The bimaterial requirements include: large mismatch of α and thermal conductivity (λ) between the two materials, one of the materials needs to have extremely low λ, there must be low residual stresses to eliminate non-thermal bending, and one of the materials may have to absorb in the infrared depending upon the design.

This is an intense area of development with large research efforts in both industry and academia racing to commercialize this type of IR detector. Quate et al. used silicon cantilevers exotically shaped in a flat spiral with an aluminum coating to complete the bimorph.[55] Datskos et al. developed a microcantilever bimorph with silicon as substrate and a 150 nm gold layer coating as the high α component that exhibited temperature sensitivity of 0.4 K.[56] Majumdar et al. applied bimaterial cantilevers of silicon nitride and gold into a complicated comb-like MEMS structure, which resulted in sensitivity of 3 – 5 K.[35] Sarcon Microsystems in combination with Oak Ridge National Laboratory (ORNL) have developed bimaterial cantilevers with sensitivity approaching 5 mK, which is the lowest value reported for uncooled IR detectors based on bimaterial cantilevers.[45] In their design, SiC was the low α component, again being combined with gold as the high α layer.

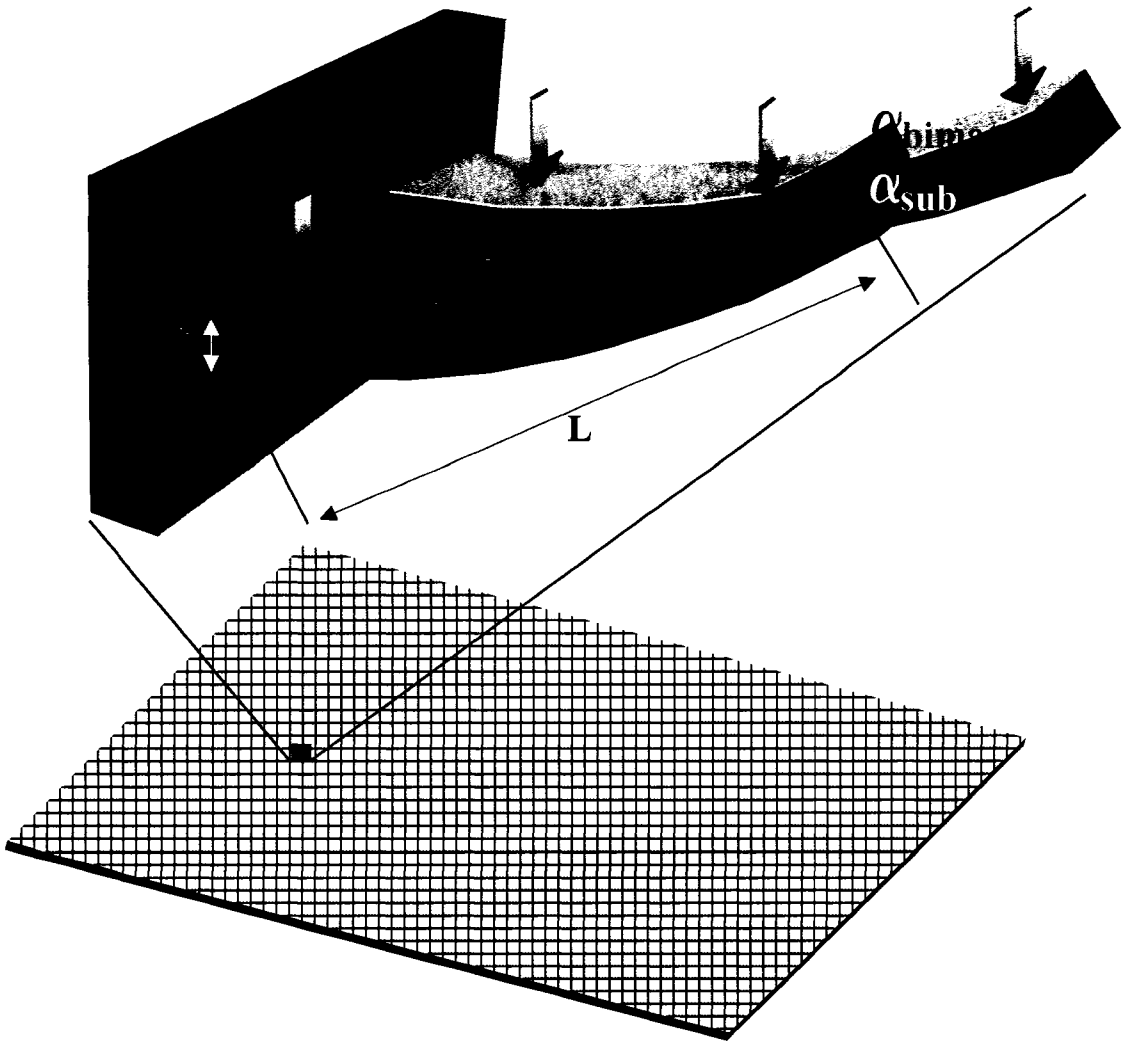

Figure 1-3. Schematic of a FPA (bottom), and one element (pixel) magnified to show that each array has a bimaterial MC. At top, the cantilever with the polymer coating (red) is shown to bend more then the other cantilever with just a gold coating upon incident IR radiation (see equations below).

To date, nobody has incorporated highly sensitive polymer molecules as the high conductivity (α) component in these bimorphs, perhaps due to processing limitations. However, organic or polymeric layers have the potential to increase the sensitivity of IR detection because the thermal expansion coefficient is more than two orders of magnitude higher than the current high α components in these bimaterial cantilevers (Table 1-6). This is

Table 1-6: Parameters for materials commonly used in bimaterial cantilevers for IR detection, compared to polymeric materials.

Material	Poisson's ratio	Elastic Modulus (GPa)	Thermal Expansion coefficient (10^{-6} K^{-1})	Theoretical max S_T (μm/K)
Poly Si	0.2	160	2.6	*NA*
Si_3N_4	0.25	385	0.8	*NA*
$Si0_2$	0.25	100	0.4	*NA*
Au	0.3	80	14.2	*0.068*
Al	0.3	69	23.6	*0.105*

clearly detailed in Table 1-6 where the overall thermomechanical sensitivity (S_T) is more than an order of magnitude better than common materials used in current designs. The equation for deflection of a bimaterial cantilever beam as a function of temperature change (sensitivity) is given by[51] (also see Fig 1-3):

$$S_T = \frac{\delta}{\Delta T} = 3(\alpha_{bimat} - \alpha_{sub})(\frac{n+1}{K})(\frac{L_{cant}^2}{d_{sub}})$$

where K is a structure parameter: $K = 4 + 6n + 4n^2 + \phi n^3 + \frac{1}{\phi n}$

and: $n = \frac{d_{bimat}}{d_{sub}}$ $\phi = \frac{E_{bimat}}{E_{sub}}$

Inspection of this equation indicates that a huge α mismatch will maximize the sensitivity. However, elastic modulus is a factor too, with a higher modulus value being more capable of bending the cantilever. A tradeoff also is present with the cantilever design. For example, cantilever displacement increases with length, but a longer beam will decrease the spring constant making it more flexible causing an increase the thermal noise and lowering the

overall NETD. It should be noted that Table 1-6 does not list the NETD value. The reason is because for a given geometry, the S_T value is the most standard *comparison* parameter since the NETD value also takes into account the noise in the detection system, whether it be optical, electrical, or any other means.

This is a perfect example to emphasize why polymers are seen as the ultimate material in sensing applications because of the fact that the best sensors in nature are essentially biopolymers. In this case, along with the equation above that governs bimaterial performance, additional motivation for this new direction of using polymeric materials stems from the fact that nature, which is the best optimizer, gives us a few exceptional examples of animals that use soft organic materials in their IR "eyes" that have sensitivity of 3 mK[57], nearly the theoretical limit.[38] This design approach consisting of FPAs of soft bimaterial cantilevers mimics what is observed in nature. Physiological studies suggest that pit organs located on the upper and/or lower jaws of certain snakes can function as sensitive infrared receptors, capable of detecting minute temperature variations and providing an additional imaging channel independent of ocular vision.[58] Photophysical studies have confirmed the very high sensitivity of snake IR receptors. Here we summarize lessons learned from recent studies of biological IR receptors and their mechano-sensing mechanism, in conjunction with their nano-structural organization as follows[59]:

- The multi-layered microstructure of beetle IR receptors, composed of alternating compliant and hard nanolayers, provides IR sensing via the thermomechanical expansion and contraction of micro-spherical structures.
- A combination of low surface thermal conductivity and high compliance, along with the presence of a regular array of nanosized surface nanostructures (i.e., nanopits), seems to correlate closely to the IR sensing capacity of biological receptors.

With this in mind, we fabricate hybrid thermal IR sensors capable of being batch processed into microfabricated FPA of cantilevers composed of an inorganic layer coated with an organic, polymeric, polymer nanocomposite, or a polymer/inorganic nanocomposite layer, as will be discussed later.

1.4 Surface Responsive Materials Through Grafted Layers

Now that the current state of sensors has been overviewed, it is necessary to detail the types of polymers that will go into them, namely the surface responsive materials (SRMs). These nanolayers, which are lacking from contemporary sensors and is the reason the work in this thesis is so significant, will be designed, developed, and characterized. Developing surface grafted polymer layers that have multi-sensing capabilities by responding to changes in pH, temperature, or solvent conditions will be pursued. Advances in MEMS and NEMS technology now require that their surfaces be protected from wear, as well as being able to sense and respond to the local environment. In fact, microcantilever-based thermal sensors comprise just one example of an emerging, next generation class of sensors that include chemomechanical and biomechanical sensors[60], capable of working in fluctuating "wet" environments that require adaptive surfaces constructed with "smart" properties that can not only sense or respond to environmental stimuli, but also be robust and possess tailored, on-demand physical properties.[61]

Flexible polymer chains have long been known to respond and conform to subtle local changes in pH, temperature, and solvent quality. Therefore, polymer surface modification, which inherently provides the ability to control and change surface composition allowing on – demand properties, is becoming increasingly significant for practical applications in fields like nanoscale lubrication, sensing and biocompatibility[62,63,64,65,66,67,68,69], or the exciting advancement of functional carbon nanotube devices.[70,71,72,73] *Polymer brush* layers are considered ideal choices in such applications for several reasons. They are chemically tethered to the surface at one end, virtually any chemistry can be designed into the layer depending on intended surface interactions, and the high grafting density combined with uniformity in composition and structure allows the *entire* surface to *quickly* respond to local environmental stimuli. These unique qualities have led to intense theoretical and experimental development of polymer brush systems.[15,16,74,75,76,77,78]

The polymer brush structure can be defined as follows: Under typical equilibrium conditions, a polymer chain takes on the random coil conformation with a radius R_c, also commonly referred to as the radius of gyration (R_g) (Figure 1-4). When polymer chains are strongly adsorbed, or tethered at *one end* to a surface, or interface, with a sufficiently high enough grafting density, the chains act to alleviate overlapping by stretching away from the surface and forming a brush-like structure.[16, 79] Irreversible (chemical) or reversible (physical) grafting of polymer chains to a flat solid interface can generally result in one of three possible conformations depending upon grafting density of the chains.[80,81] At low surface concentrations, the chains lie on the surface and form the "pancake" structure. In the case when there is a relatively medium grafting density, or $d/R_m \approx 1$, the free end of the chain tends to form a mushroom like structure[82] with radius R_m (Fig. 1-4). However, when the tethering density becomes high and crosses a certain threshold in which d/R_m becomes very small, neighboring chains crowd one another. As a result, densely grafted chains will be more apt to stretch away from the grafting site, and strong deformations of the average dimensions will occur.[83]

The resulting layer architecture is known as a *polymer brush*. This situation in which the polymer chains stretch along the surface normal is quite different from typical flexible polymer chain behavior in solution, where the well known, random-walk (Gaussian coil) configuration is found. In other words, the equilibrium conformation is a highly stretched conformation. Sometimes, this stretching is much farther than the typical un-stretched size of a chain, often more than five times, especially in the presence of a good (selective) solvent.[84] These stretched configurations (deformations) are found under equilibrium conditions without the assistance of some external field or under the confinements of surface geometry.[75] The brush structure of the polymer chains is responsible for novel behavior and physical properties, including strong responsive behavior, as will be shown in this thesis.

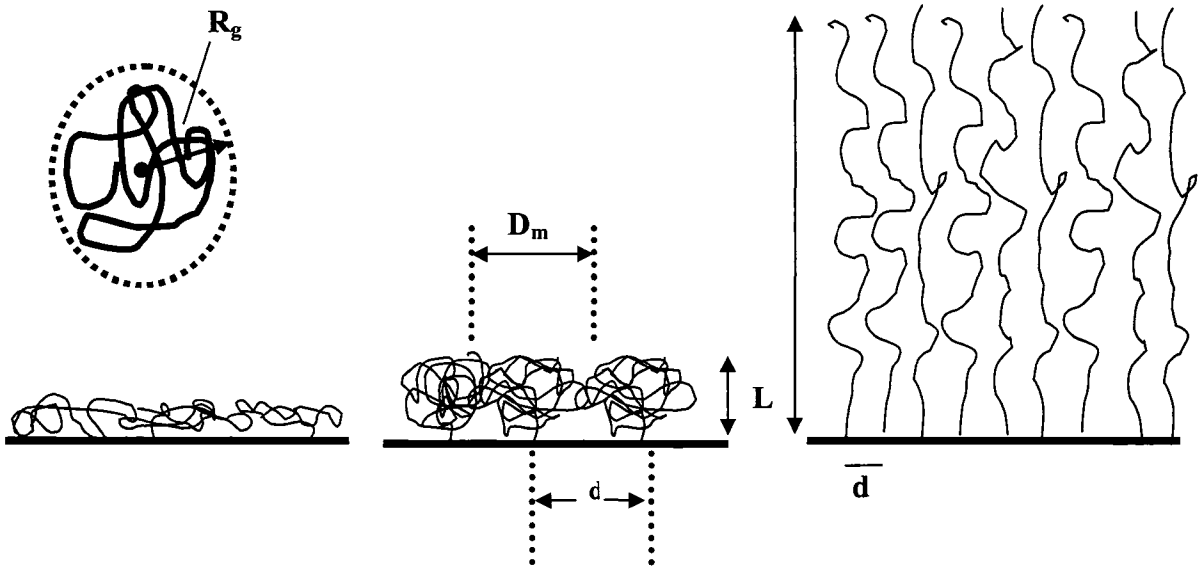

Figure 1-4. Model comparing the conformation of a free polymer chain (top left) and grafted chains as a function of the grafting density (d) on a solid surface. The chain conformation goes from the pancake, to the mushroom, and finally to the brush conformation (far right) at the highest grafting density. The model for the mushroom structure is over-simplified in that there is not this high amount of free volume within the layer underneath the chains.

In the past four years, there has been intense research directed towards surface grafted binary brush layers because these systems allow for supreme interfacial control.[6] An ideal binary system is composed of two separate incompatible polymers with very different chemical, structural, and mechanical properties, grafted onto an interface with the possibility of varying grafting densities for each polymer. Each polymer also has the ability to swell or collapse based on external conditions such as pH, temperature, and solvent quality (Figure 1-5). In the case of binary brushes, the variety of surface morphologies possible greatly increases depending upon the chemical composition. Surface composition and hence properties such as surface energy, adhesion, friction, and wettability have the possibility of being "tuned" to the necessary state.[85,86] Current theory predicts that in ideal situations,

either complete lateral or complete vertical (layered) segregation of the two components within the binary assembly.[87,88,89,90]

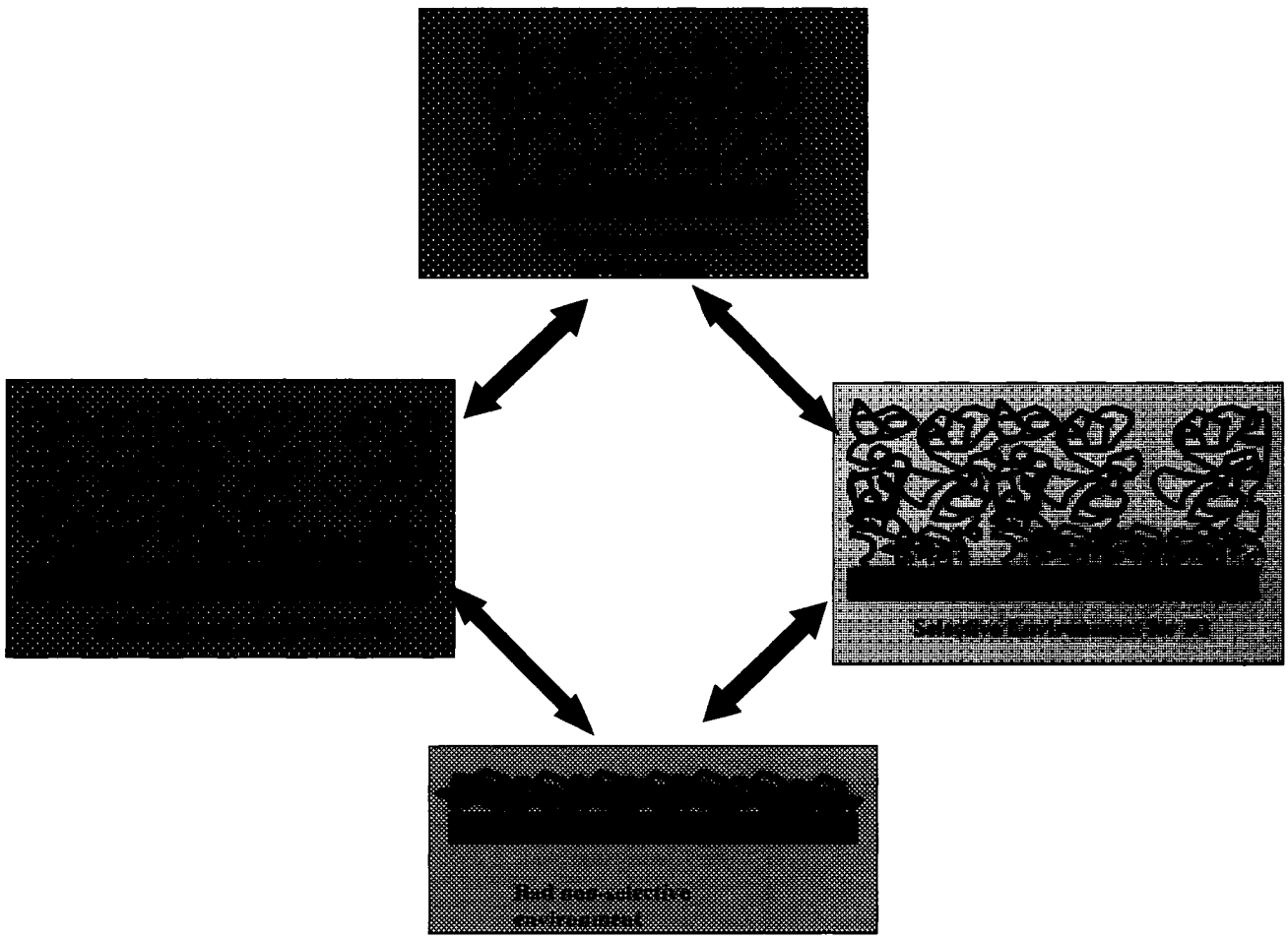

Figure 1-5. Interplay in binary brushes leading to various top surface compositions

To sense or to respond? While in principle all sensors do both, sometimes the question is what is the more primary goal? The literature is saturated with studies describing sensors designed to sense a *particular* analyte, or *one specific* biological species. However, sometimes we do not care how it senses, we just want a certain response. For example, the previous section dealt with applying SRMs on microcantilever sensors to induce actuation. Thus, the polymer is applied to enhance this bending upon sensing thermal flux, although we

are not necessarily concerned with the final structural and mechanical properties inside the polymer layer, so long as the sensor has large lifespan and low hysteresis.

Oftentimes, SRMs show a pronounced change to many stimuli, and the goal is to not quantify the specific stimuli, but to end up with a desired surface that will have advantageous physical properties. This is especially important in next generation sensors that integrate mechanical, optical, fluidic, chemical gating, and biological devices into versatile microsystems to perform complex sensing functions where repeated actuations can cause mechanical damage. Such systems require "smart surfaces", but also need to possess superior nanomechanical and nanotribological properties that exhibit superior wear resistance with controllable friction and adhesion along with mechanical, structural, and thermal stability surpassing that of conventional SAMs and polymers. They must have capabilities of exhibiting both reversible elasticity to large local deformations as well as compression resistance, and be designed with built – in mechanisms for mechanical energy dissipation. All of these traits must be packed into a layer that is sufficiently thin (2 – 100 nm) to assure feasibility into intricate microsensor devices with nanoscale dimensions.

The macroscopic responses of "smart" coatings result from the reorganization of the internal or surface structure with different components reversibly segregating to the surface depending on the environment.[91] In previous work (LeMieux's MS thesis), we designed and developed a polymer surface with emphasis placed on response. In this case, the goal was to have single polymer SRM layer that in one state would be rubbery, and in another state be glassy; a "schizophrenic surface", i.e. a single SRM with completely opposite 'faces' (properties) exposed.[15] An important concept demonstrated by this work is the reversible transformation between hard and soft surface properties. The underlying mechanism of concurrent chemical, topological, *and* mechanical transformations was demonstrated by the work with a binary polymer brush surface (Fig. 1-6).[92] Two incompatible polymers, poly(methyl acrylate) (PMA) and poly(styrene-co-2,3,4,5,6-pentafluorostyrene) (PSF), were chemically grafted sequentially onto silicon via the "grafting from" method, producing thick (20 – 150 nm) dense mixed brush layers (Figure 1-7).

The resulting layers possessed a heterogeneous surface exhibiting vertical and lateral microphase segregation with a characteristic lateral dimension of 100 nm (Figure 1-8). The lateral and vertical reordering of the binary brush layer was observed to be fast (<1min), and reversible for at least 1000 "switches" between good and bad solvent states. Surface composition can be controlled allowing surface energy, adhesion, friction, and stiffness to be "tuned" by controlling a level of vertical and lateral segregation providing a means for tunable tribological properties.[93,94]

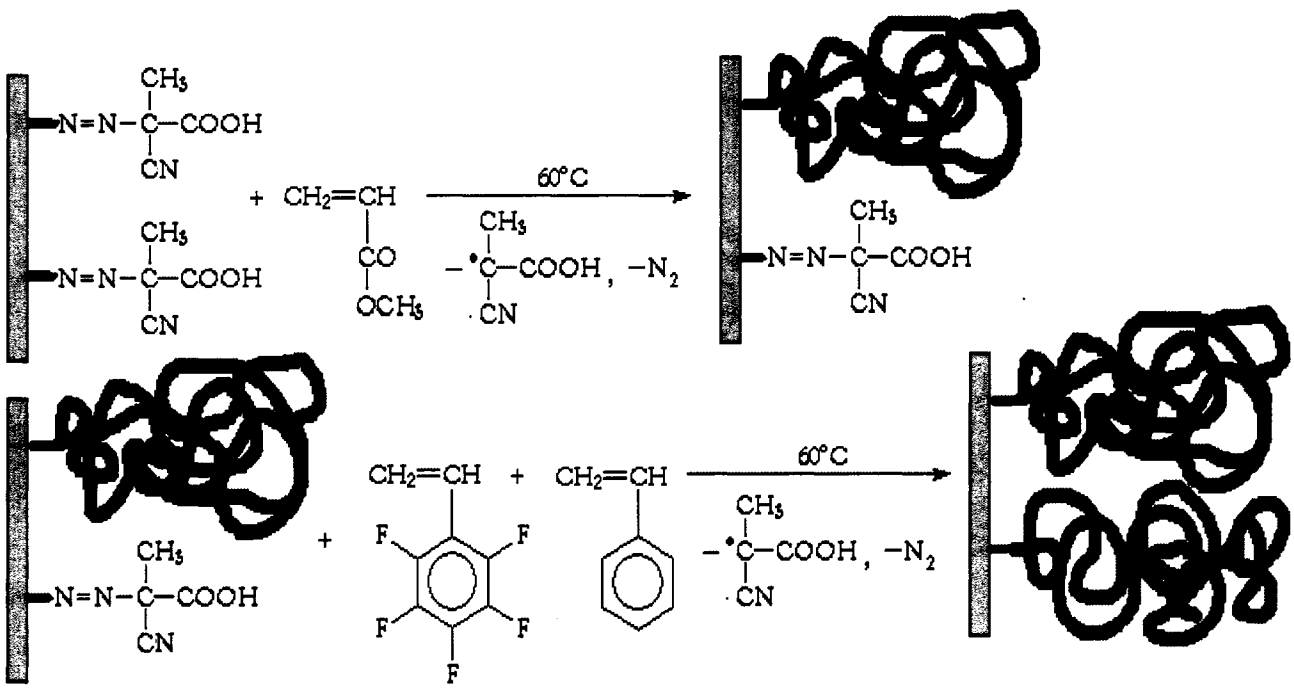

Figure 1-6. Scheme of the two-step synthesis of PMA (black chains) and PSF (grey chains) from the silicon substrate using the azo-initiator.

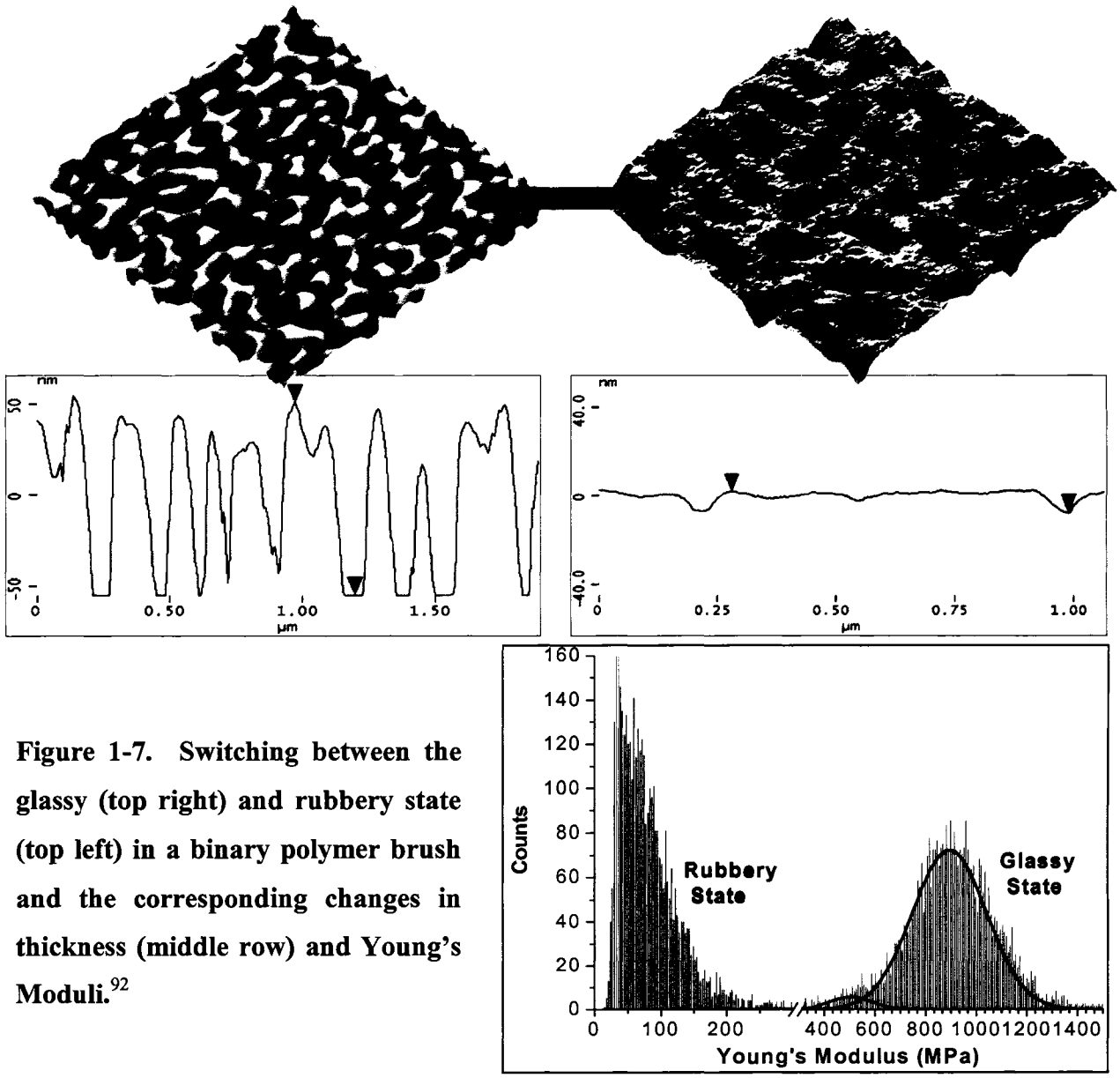

Figure 1-7. Switching between the glassy (top right) and rubbery state (top left) in a binary polymer brush and the corresponding changes in thickness (middle row) and Young's Moduli.[92]

Combining hard and soft components in such coatings can provide a strong matrix or load-bearing skeleton for structural integrity, while the soft component is responsible for mobility, adhesion control, and lubrication. An active component could be in many forms, such as a solid lubrication phase that melts under external load to lubricate the contact area, porous microspheres that rupture spilling internal reactive fluid for self-healing, or weakly bound low-molar mass molecules that diffuse to the contact areas under external pressure to

reduce adhesion.[95,96] Here, the goal of this binary brush surface was to design a single polymer nano layer that can be both sticky and slippery, hard and soft, and amphiphilic depending upon desired use. These features are extremely critical for controlling tribological behavior and surface properties in silicon based microactuators. For example, wear and friction protection must be combined with sensing capabilities in next generation MEMS and NEMS devices. Indeed, AFM force spectroscopy of corresponding surface properties indicate that PSF and PMA are highly mechanically dissimilar (glassy/fluorine enriched and rubbery/polar groups, respectively) as shown in Fig. 1-7 for elastic response.

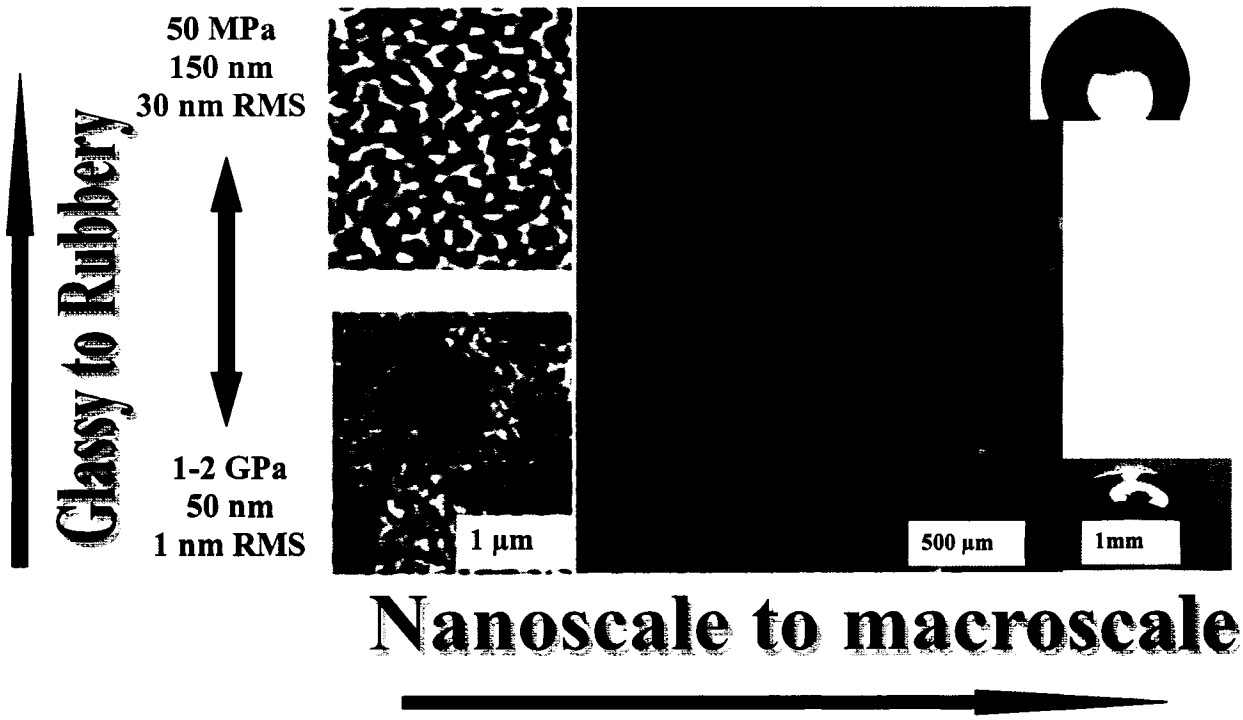

Figure 1-8. The switching of morphology at the nanoscale has dramatic effects on the optical properties at the microscale, as well as the macroscale surface properties, which can be measured by contact angle. In this case, the graded substrate has varying elastic modulus from 2 GPa to 50 MPa. For different environment conditions, it is possible to create more gradual changes in the surface properties of the polymer layer. It is also important to note that the contact angle changes from about 95° in the glassy state to over 120° in the rubbery state due to excessive roughness even with PMA on the surface. This last value is close to the ultra–hydrophobic surface regime which has long been a goal to create in polymer surface science[92], but typically not with a *rubbery* material.

For this SRM, a model of structure reorganization combining both lateral and vertical microphase separations was proposed.[92] The findings were compared with recent structural predictions of a binary brush from theoretical calculations and were found to be in agreement. Additionally, from the optical imaging and contact angle measurements, we show a polymer surface in which the switching of morphology at the nanoscale also switches properties at the micro and macro scale (Figure 1-8). With such a surface, the foundation has been set to fabricate graded surfaces in which the properties can be gradually changed based upon the environment. Furthermore, this is a classic example of the ability to switch a surface between two specific desirable responses based on exposure to general stimulus of a good/bad solvent.

Moving beyond binary polymer brushes. With the research focus on engineering nanoscale responsive surfaces, a necessary step beyond these initial developments is multi-functional grafted polymer layers. By having more exotic architectures than typical polymer brush surfaces, they can exhibit a dual (or more) stepwise (or simultaneous) controlled response to various environmental triggers such as pH, temperature, or radiation that have never before been designed into a polymer layer. While the conventional responsive surfaces consist of either grafted homopolymer, mixed homopolymer (binary), and di- or triblock copolymers in a semi-flexible, linear architecture[16], a substantial modification of this approach is a highly branched, or semi-comb type, graft copolymer brush (Figure 1-9; recently theorized[97]). The advantages are two fold: 1) It increases the number of triggers that can influence the switch in properties of a single polymer layer as well as having a layer with a vertically graded response (i.e. the always confined interlayer is strongly thermosensitive, while the branched segments at the top respond to pH changes; Figure 1-9). 2) The interplay of intramolecular interactions and confinements between the branched segments at the top layer can lead to a broad range of nanomechanical properties based on various grafting conditions and environmental stimuli.

Rather than grafting two homopolymer brushes to create a mixed binary brush, an alternative route to responsive surfaces is grafting block copolymers (BCP) of two

chemically different blocks. These systems are attractive due to the very rich and interesting surface morphologies that are possible depending on block length ratios and interactions between the two blocks relative to each other, and with the local environment.[98,99] The main difference between BCP brushes and binary brushes is that the phase domain structure is usually well ordered and periodic allowing them to be useful in applications of nano-patterning and templates.[100,101]

One type of BCP that is receiving intense interest consists of an architecture in which one block serves as a backbone filled with initiators from which other polymer chains can be attached. These are known in the literature as graft copolymers, or comb copolymers. The vast majority of research dealing with these molecules has been in solution where they adopt a worm like, cylindrical configuration, so they are labeled as bottle-brushes, or cylindrical brushes. We intend to build on this approach by fabricating novel polymer architectures in which one block is an environmentally responsive polymer (strong response to thermal or pH fluctuations) that is capped with a macroinitiator (macromonomer) to which other polymer chains can be grown from or attached (Figure 1-9). However, we intend to have a very asymmetrical backbone in terms of length of the surface block (very long), and the macroinitiator block (very short), which will result in a "palm-tree" like polymer (Figure 1-9).

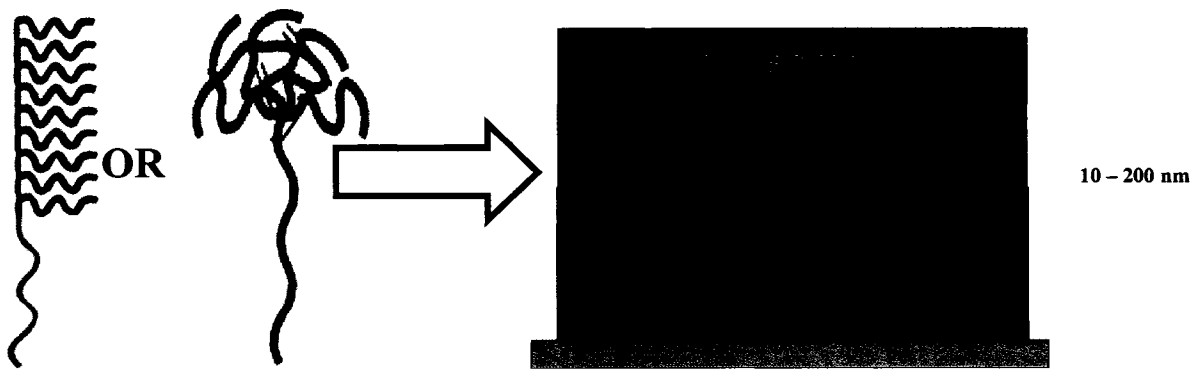

Figure 1-9. Schematic of a "palm-tree" like polymer. At far left is a comb-copolymer, which can take up the palm-tree architecture (middle). The resulting multilayer surface (right) can lead to novel mechanical response.

The majority of research involving graft or comb-type copolymers has either been in solution, or through physisorbed layers, with efforts focused on synthesis and structural characterization. Luzinov et al. have grafted binary brushes to a PGMA layer that serves as a "carpet" of functional epoxy grafting sites (Figure 1-10).[102] However, this is an extremely thin layer (monolayer, 1.5 nm thick) with a lack of physical properties and response mechanisms. Sheiko et al. and Matyjaszewski et al. have established methods to graft side chains to a macroinitiator backbone with a gradient in spacing intervals along the backbone.[103] In a series of recent papers the authors have demonstrated that they are not concerned with fabricating layers of these molecules as they just deposit individual molecules on the surface and observe their structure.[104,105] A critical result illustrated how two different conformations could coexist within an individual comb or graft molecule.[104] Upon external forces, the portion of the molecule with a higher density of branched segments formed globular regions while the rest of the molecule remained in a rod-like conformation. Such a molecule, when confined to the surface by a single graft point, could form a layer with highly asymmetric density profile and nanomechanical response in the vertical direction.

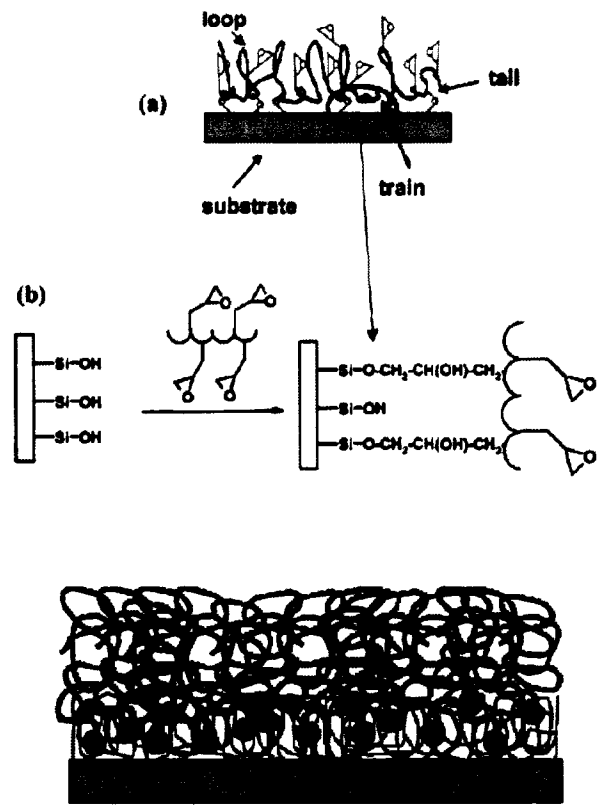

Figure 1-10. Schematic showing PGMA on the surface with the many available epoxy groups (a), and the chemistry of the covalent attachment to the surface (b). At bottom shows the thicker, denser polymer layer (SRM) that forms due to the grafting at different levels that the PGMA macroinitiator allows. From Ref. 105.

One study that touched on the nanomechanical properties of covalently attached graft copolymers has recently been published.[106] Although the grafted molecules did not form uniform layers (Figure 1-11), AFM was used to probe the elastic properties of the widely dispersed poly(HEMA-g-PEG) molecules as a function of the number of side chains (mol. weight), providing a rudimentary insight into the structure-properties relationship. The responsive properties were not tested, but the force to compress the molecules varied slightly with molecular weight requiring 80 pN at 120,000 g/mol, and about 30 pN at 16,000 g/mol. Clearly, the increased level of branched segments made the molecule more resistant upon compression due to enhanced intramolecular interactions.

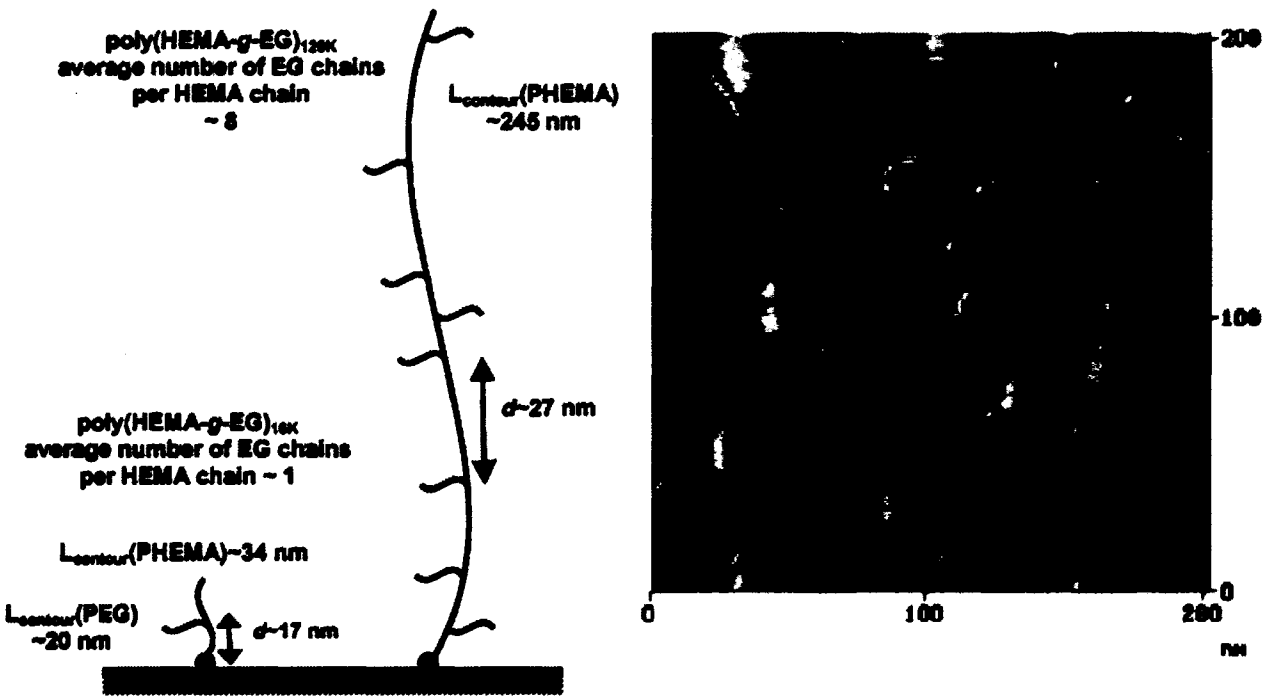

Figure 1-11. At left is a schematic showing the poly(HEMA-g-PEG) molecule construction. Here, poly(ethylene glycol) (PEG) side chains are attached to the poly(2-hydroxyethyl methacrylate) (PHEMA) backbone. As depicted, the PEG chains are grafted along the entire length, offering no capability for density gradients. At left is the AFM topography image of the 'brush' grafted on a rough gold substrate. However, this is far from a brush, as individual clusters of the graft co-polymer are highlighted.

This poses several questions: 1) How much would the elasticity increase if there was not only intramolecular interactions, but interactions and confinements posed by neighboring molecules that would be more tightly packed with a higher grafting density found in the brush regime? 2) What segments will best optimize this effect in terms of incorporating stiffer branches with higher T_g, or charged branches such as Polyelectrolytes? 3) In this study, the molecules were branched completely down the main backbone (comb copolymer). What effect on structure, properties, and responsive switchable properties will a semi-comb (Figure 1-9) brush layer induce where a graded density profile is prevalent? Understanding these questions will force the introduction of a new class of phase diagrams of multi-component polymeric systems, and novel nanoprobing techniques and models to determine the non-uniform nanomechanical properties of such layers with AFM based methods. Not only do these questions remain unanswered, but grafted brush layers of this architecture have yet to be exploited as the next step of focusing on multi-functional responsive polymer layers.

This so called macromonomer approach is an efficient strategy for complex architectures, high functionality, multi-sensing capabilities (responding to dual and multi-stimuli), and unique properties in polymer layers. They are less complicated and more easily synthesized than their dendritic or hyperbranched relatives. In fact, nearly all studies for these types of copolymers have been in solution, or in solution then adsorbed onto surfaces via casting or LB deposition, providing only weak physical adsorption. On the other hand, surface grown polymer layers, much less brushes, of such molecules have been largely unexplored. Furthermore, as in the structure of the "palm-tree" configuration, it is anticipated that due to the relatively high density at the top of the layer compared to the bottom, a multi-layer type structure can result with varying degrees of density (vertical gradient) in a polymer layer. Also, due to the hairy, highly dense structure at the top, a high degree of various non-covalent intramolecular interactions can arise (depending on chemistry, flexibility of the polymers) resulting in superior, never before seen nanomechanical properties in a polymer layer.

Not until recently (within the last two years) have such complex brushes been grown from the surface of silicon substrates due to advancements in polymerization methods such as ATRP and the breakthrough RAFT polymerization technique.[107,108] Furthermore, dense, uniform layers consisting of these molecules have yet to be reported in the literature. We intend to not only make pioneering efforts to fabricate such layers with these polymer nano-assemblies, but to also characterize their nanoscale properties such as adhesion and elastic modulus. A key polymer that will be explored here is poly-n-isopropylacrylamide (pNIPAAM) because it exhibits a lower critical solution temperature (LCST).[109] Only about 5% of all polymers have LCST behavior, and pNIPAAM undergoes this transition at the physiological important temperature of 32°C. Below LCST, pNIPAAM is in a swollen conformation in the presence of water, while above LCST, the chains completely collapse, becoming hydrophobic. In terms of using pNIPAAM as the surface anchored block, there has not even been a systematic study on the copolymerization of NIPAAM with a macroinitiator. Then, by adding various functional, sensing polymer chains to this pNIPAAM copolymer, we anticipate to prepare novel sensing polymer assemblies with reversible, tunable modulus and nanomechanical gradients that have never before been designed into a SRM.

1.5 Surface Responsive Materials Through Vapor Phase Deposition

Because a large part of this thesis will be to implement coatings into real sensors (in this work, microcantilevers (MCs) for enhanced IR and thermal sensors that must be batch processed, applicable coatings had to be pursued. To enhance the IR detection of the MCs within the framework of the bimaterial approach, we intend to coat the MCs with various organic and polymeric materials. Typically, these coatings are applied via a "wet" deposition process as described in the previous section regarding grafted layers. However, due to repeated wetting and drying, induced mechanical stresses can result in the MCs rendering them defective. The overall cost of device production will be decreased if surface modification of the MCs is compatible with the microfabrication process. Chemical vapor deposition (CVD) is a "dry" (solvent less) process compatible with semiconductor fabrication.[110] Among various

CVD methods, plasma enhanced chemical vapor deposition (PECVD) is a very efficient, inexpensive, rapid, and relatively simple method to produce homogeneous organic and polymeric films covalently attached on various sized substrates.[111] PECVD provides excellent control over polymer film parameters such as density, thickness (10 nm – several micron thick films have been produced), and composition.[112,113,114]

This work involves the use of a PECVD chamber in close collaboration with Dr. T. Bunning at the Air Force Research Lab (AFRL). In general, PECVD is suitable to deposit a wide variety of monomers and polymers by breaking down gaseous precursors into radicals, which deposit onto the substrate from which they were polymerized. Plasma polymers are different from typical "wet" grafted polymer chains because they tend to form a three-dimensional cross-linked network.[115] Therefore, the resulting films have different chemical and physical properties than conventional polymer films. A main advantage of these films over conventional films is that they can strongly adhere to several substrates (silicon, glasses, metals, even polymers), and contamination is virtually eliminated.[116]

PECVD has been used to prepare highly conductive polyaniline films with thickness ranging from 30 – 315 nm.[112] Zou et al. fabricated very sticky glycidyl methacrylate layers on silicon with PECVD, and they showed the films were covalently grafted to silicon.[110] One class of polymers that has been widely polymerized on surfaces with PECVD is fluoropolymers. Linear, cyclic, and aromatic fluoropolymers have been deposited on silicon substrates to produce ultra-smooth surfaces, as the AFM measured microroughness was around 0.4nm.[117] The films showed strong IR absorption at atmospheric wavelengths, and exhibited thermal stability of up to 350°C. A main advantage of PECVD, especially considering polymeric systems, is that the deposition can be done close to room temperature. Additionally, since it is a volatile method compared to usual polymer film growth techniques, often times amazing properties will result in films such as a high degree of cross-linking leading to higher modulus values, as well as non-uniform composition leading to super-hydrophobic surfaces.[118]

1.6 Surface Responsive Materials Through Top-Down Lithographic Assembly

An entirely alternative approach to surface responsive materials is the establishment of a completely new design paradigm for multifunctional polymer coatings with a well-ordered and open architecture via a *top-down* fabrication approach.[119] While SRM are generally 2D structures made by self-assembly or *bottom-up* approaches (above examples), recent advances in multifunctional coatings designed, for example, for both photonics and sensing applications are driving the development for novel true 3D micron scale structures with submicron periodicity to act as coatings. It is an advantage to produce 3D microstructures rapidly and economically (with existing microfabrication techniques). In this thesis, an aim was to produce 2D and 3D structures in the form of *microtrusses*. Trusses are highly organized 2D and 3D structural systems composed of beams and nodes (joints) with excellent specific mechanical properties, and are very familiar to the civil engineering (see Figure 1-12) or home-builder.[120]

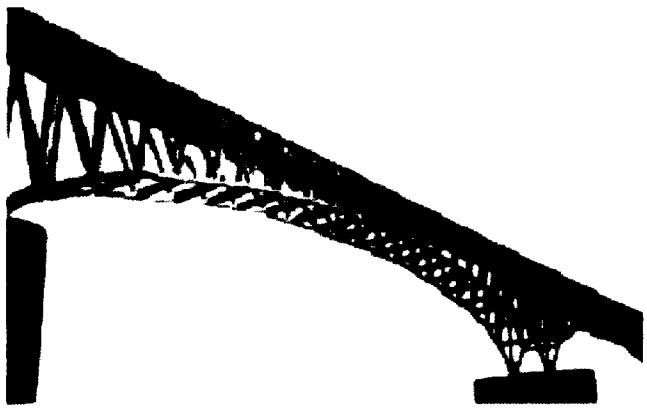

Figure 1-12. Bridge with the lightweight truss configuration that is commonly used in 'macroscale' applications such as bridges and house frames that are high load-bearing structures. From Ref. 123.

Although they possess complex 2D and 3D structures, the microtruss coatings are easily fabricated in a 'one-shot' single exposure of light lasting on the order of only a few nanoseconds to seconds. This is done by exploiting interference lithography (IL) as a microfabrication tool for the design of *microtruss coatings* with periodic topology shaped by the interference light pattern within the polymer material. Holographic IL is a technique that allows fabrication of 1D, 2D, and 3D patterns and open architectures using coherent beams

of light and involves the formation of spatial variation of intensity created by the interference of two or more beams of light (Figure 1-13).[121]

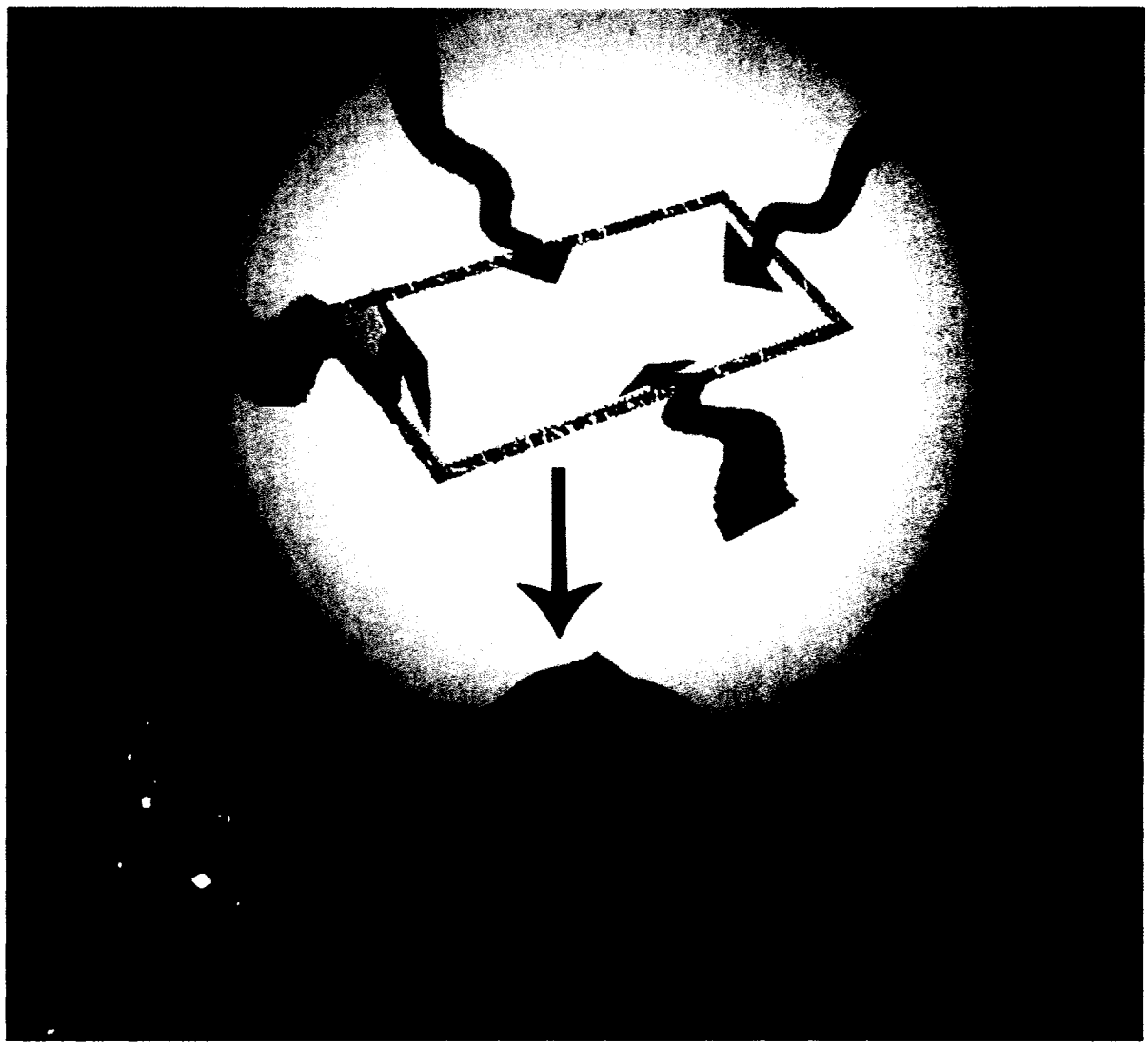

Figure 1-13. Cartoon depicting the IL fabrication in which the polymer layer (typically 1 – 10 μm thick) is subjected (exposed) to the laser interference pattern (top). The polymer layer can then be developed through solvent-less techniques to give the final structure (bottom). The inset is an actual digital image of the apparatus with the substrate being the bright spot in the middle.

As will be shown, the material used in this work is SU-8, which is chosen for several reasons. The original idea to use this material arose from the fact that this is a common photoresist material used in microfabrication procedures and can be readily polymerized.[122] Obviously, in this fabrication regime, the material must be a photoresist material (in this case, a negative-tone resist). Secondly, SU-8 is a tough Novolak resin[123] with an average of eight epoxy groups and a high elastic modulus in the cured state approaching 3 GPa[124], making it an ideal material for a tough truss structure. The third reason is because of the aforementioned epoxy groups, which always has some percentage remaining exposed at the surface of the microframe even after development. Modification of the porous microtruss structure is possible without complete filling of the original skeleton, but with chemical modification of inner pores (Figure 1-14). Modifying the 3D structure of SU-8 may be accomplished via a grafting approach in which functionalized molecules can *covalently* attach to un-reacted (non-crosslinked) epoxy groups. These will still be abundant in SU8 after curing. In this manner, high molecular weight polymers with swollen layer thicknesses ranging from 10 – 1000 nm can be applied to the skeleton.

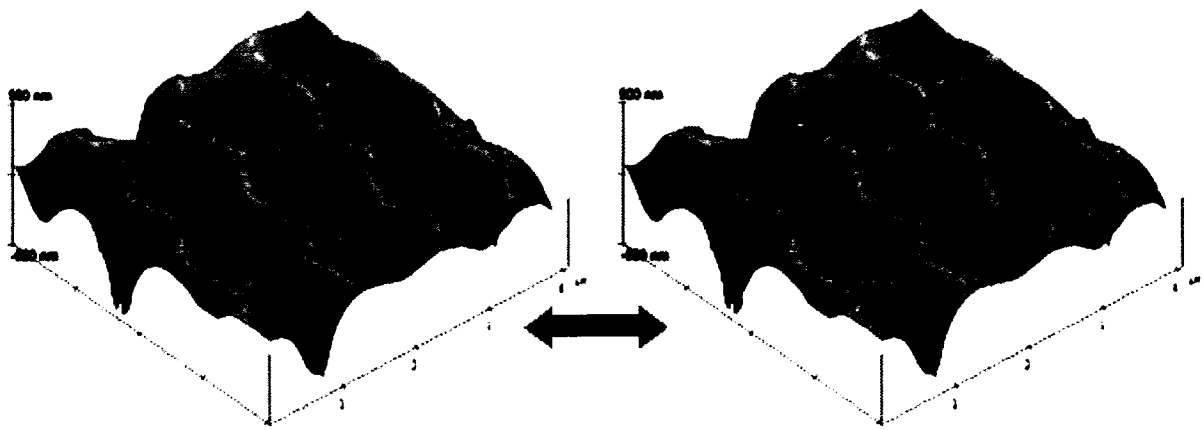

Figure 1-14. Chemical modification with responsive polymers can lead to controllable pore opening: closed (left) and open (right), leading to a 3D surface responsive structure.

The work conducted in this thesis was to prove the principal that these 2D and 3D structures could be produced intact, allowing for a suitably strong frame or platform to build complex SRMs and next generation multifunctional coatings.

To summarize, there is a significant push to incorporate *truly nanoscale* polymeric SRMs into micro and macroscale sensing applications. This is because advanced sensing applications require the dynamic nature of polymeric/organic materials to enhance sensitivity several orders of magnitude better than offered by current designs and materials platforms with faster response times. In addition, SRMs should be made to be versatile, to respond to or sense different stimuli, and able to possess multifunctional surfaces with dual or more properties in a *single* nanoscale layer, and this can be engineered into the design by incorporating carefully selected functional groups and chemistry. Furthermore, the SRM should be strongly adhered and be robust over a relatively long lifetime. To accomplish this will be a significant step in the development of complex nanoscale sensors if such SRM materials can be implemented into working sensors. And finally, actual hybrid microsensors were designed, implemented and characterized.

In this research ultrathin binary polymer brushes are synthesized covalently onto silicon substrates, and the reversible properties are characterized upon sensing of various chemical environments. Then, to move beyond binary polymer brushes as SRM, hybrid polymer brushes composed of molecules with a branched architecture that has never been designed into a polymer brush layer are synthesized. The novel mechanical response upon response to different fluidic and thermal environments was characterized.

As an alternative to the bottom up synthesis methods of the previous techniques, polymer coatings with 2D and 3D truss-like structure are fabricated via a top-down lithographic approach, and their structural and mechanical properties are characterized. These microscale coatings are viewed as 'microframes' that can be modified with active sensing polymer layers for ultimate 3D multifunctional SRMs.

The last phase of the research is to implement actual active sensing coatings onto real MEMS microsensors to fabricate hybrid inorganic/organic sensors with unprecedented sensitivity to thermal fluctuations. This is done through traditional grafting techniques of polymer brushes and polymer nanocomposite surfaces, as well as the largely unexplored PECVD dry (solvent less) deposition for microfabrication compatibility considerations. Furthermore, response of these hybrid sensors to other stimuli such as chemical vapors and humidity are explored and characterized.

1.7 Goal

The *ultimate goal* of this work is to understand and develop multi-functional sensing or responsive surfaces as a result from polymer based structures carefully designed for specific molecular interactions upon various external stimuli. The implementation of innovative molecular architectures into surface grafted polymer brush layers will lead to multi-sensing surfaces, and the goal is to understand the nanomechanical behavior upon response to different environmental stimuli. Additionally, the establishment of a completely new design paradigm for multifunctional polymer coatings with a well-ordered and open architecture to act as microframes for a surface-responsive structure will be developed. Finally, for the application of enhancing IR sensing MEMS devices, polymer coatings will be designed to strongly absorb and respond to thermal flux to allow for hybrid sensors with unmatched sensitivity. To accomplish this goal, surfaces will be fabricated pursuing "wet" and vapor phase methods as well as being integrated into microsensors, along with lithographic approaches to fabricate potential surface responsive 3D structures. An additional aim is to take advantage of the peculiar physical properties of plasma polymers by developing multifunctional hybrid sensors, along with a secondary of understanding the properties of these plasma nanolayers. Plasma vaporized coatings and nanocomposite (with incorporated inorganic nanoparticles) polymer assemblies made compliant with a MEMS fabrication will be implemented into real IR sensor devices and tested. The sensitivities of the bimaterial hybrid sensors will be characterized by measuring their bending deflections by simple optical detection routes.

1.8 Approach and Thesis Organization

To achieve these goals and design, fabricate, and implement SRMs into hybrid organic-inorganic sensors, several steps must be taken. These can be organized into three distinct phases that were outlined earlier in Figure 1-1: Design, integrate, and characterize. The first phase is the Design phase, which is the most important and most complicated step. This phase can be broken down into several major components as a "Design Approach Pyramid" shown in Figure 1-15.

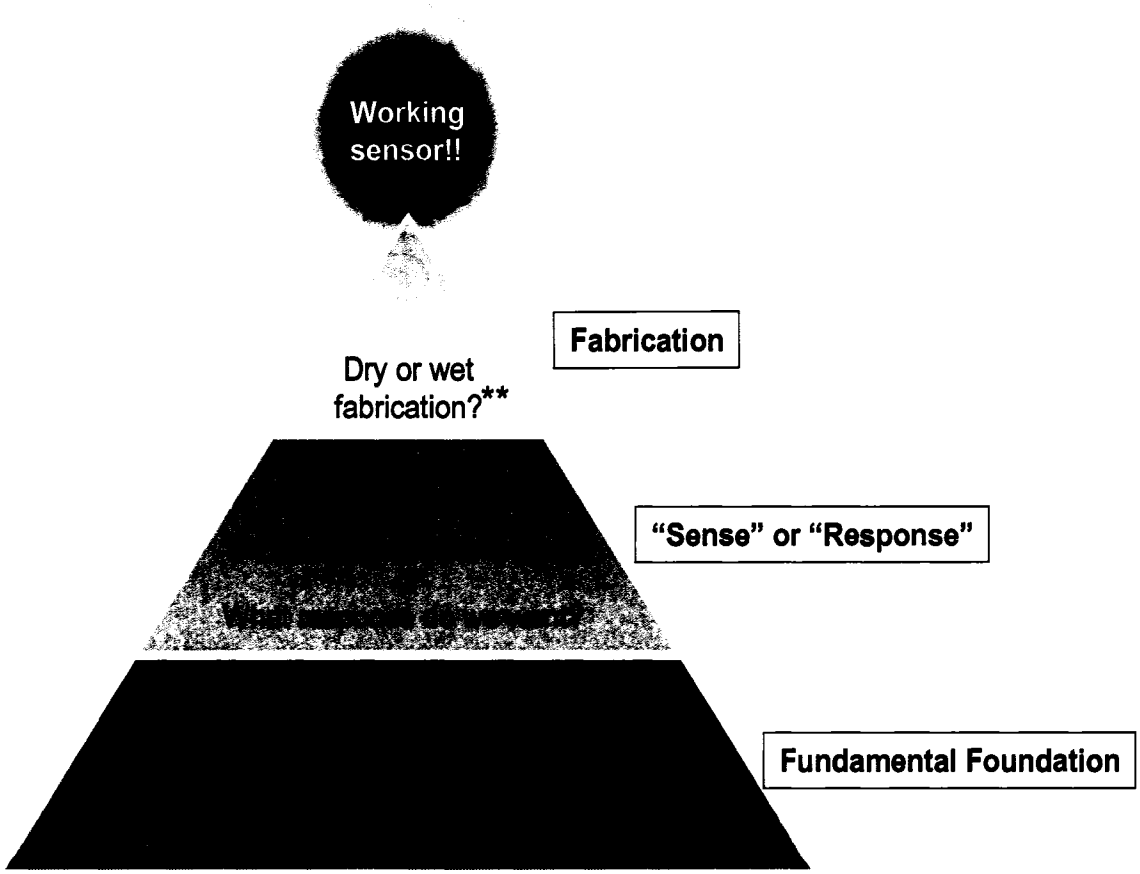

Figure 1-15: Diagram showing the "Approach Pyramid" that depicts the considerations involved in producing a working sensing element.

**** Here, dry or wet means through bottom – up assembly, but top down lithographic approach is an alternative fabrication approach explored in this work.**

As depicted, the strong foundation is the understanding of complex molecular scale interactions in organic materials, and as discussed in Section 1.2, many sensors are designed to interact with a specific analyte or biological species. Knowing exactly what functional groups are necessary to optimize the desired sensing application is key, and the study of individual molecular units and the corresponding macroscopic response has been the driving force in developing SRMs and polymeric sensors.[7]

This thesis is organized in a manner in which each chapter (Chapters 3 – 10) is a results chapter that is in fact an individual paper that is either published, accepted, or submitted to a refereed scientific journal. Chapter 2 gives general considerations and procedures of the experimental methods, while Chapter 11 is a short chapter giving general conclusions.

Chapter 3. This chapter is a paper submitted to *Nature Materials* devoted to understanding the nature of molecular interactions at the smallest possible scale. Many of these molecular interactions have been empirically know for decades; however a major challenge in sensor research is a push for a broad "roadmap" for proper selection of materials for instant identification and improved recognition. Moreover, new sensors are becoming increasingly smaller to be compatible with MEMS and even scaled down to NEMS (such as nanoscale field-effect transistors) in which truly single molecule interactions must be fully characterized. There is no better example of this perhaps then carbon nanotube (CNT) based sensors.[125] To directly characterize the interaction of single molecules with a single CNT is an extremely difficult experiment because of the small size. The only method in which forces can be measured simultaneously with an assurance of being on the nanotube by observing the in-situ nanoscale topography is with AFM. [126] For the polymer surface engineer, the AFM is the most important tool and its invention opened new perspectives for the characterization and manipulation of soft materials and single molecules, which has led to these materials being implemented into advanced applications such as nanoscale sensing.[127,128] AFM can probe interaction forces with sub pico-Newton resolution with resolution of 0.1nm in the vertical direction, while having positioning accuracy of 1nm in the

X-Y plane of a surface to do force measurements at a very precise, prescribed location. The conclusions from such a study would have important implications for the development of chemical functionalization strategies for CNTs, and researchers would also need to consider the fundamental mechanism governing these interactions when designing nanotube based chemical and biological sensors. However, an encompassing ramification of such a result is that by studying the interactions on the smallest of scales possible in materials science, these results can be scaled up and applied into knowledge of building all sensors.

Chapter 4. The next level up on the pyramid is the concept discussed earlier, which is the sense/respond paradox. In Chapter 4, binary polymer brushes are grafted to a silicon surface to make up a reversible SRM with overall thickness of *only 3nm*, and this is a paper that has been published in *Langmuir (2004, 20, 10046-10054)*. In this paper, the focus is on characterizing the *response* of the surface to various environments. In addition to proving a working sensing surface at this extreme nanoscale thickness, the nanotribological properties were also characterized in this ultrathin SRM.

Chapter 5. The idea of this chapter is moving beyond binary polymer brushes and incorporating molecules of novel architecture into a hybrid polymer brush layer SRM. This is a paper submitted to *Langmuir* that shows, with AFM, the change in nanomechanical response of the SRM upon exposure to fluidic environments and temperature change. Never before have molecules incorporated with elaborate architectures been incorporated in a *dense*, end-grafted true brush layer.

****Chapter 6 and Chapter 7.** These two chapters are very similar (same materials, same theme), with the only difference being that Chapter 6 deals with 2D interference lithography (IL) structures while Chapter 7 is work on 3D IL structures. In Chapter 6, 2D microtrusses are produced, and their nanomechanical properties are fully characterized, and this is a paper in *Advanced Functional Materials (2006, 16, 1324-1330)*. Proof that 3D microtruss structures can be easily fabricated as microframes for potential 3D SRM is given in Chapter 7 that is a paper accepted in *Advanced Materials*. The mechanical properties are

also explored, including unique, ordered fracture for crack propagation design, as well as ultimate strain well beyond that for typical glassy polymers. Additionally, this represents an alternative fabrication to the wet or dry approach as highlighted at the top of the pyramid with the double asterisk (Fig. 1-15), by using a lithographic approach which is still compatible for microfabrication processes.

Chapter 8. This chapter is a paper published in *Advanced Materials (2006, 18, 1157-1161)*. The work here is significant for the reason that engineered SRMs, in the form of wet grafted brushes and nanocomposite organic/inorganic layers, are deposited and thereby integrated into actual microsensors. The thermal sensitivity is characterized for various coatings to find the optimal SRM. The focus is on the sensing capabilities of the SRM and the overall hybrid microsensors. One additional significant aspect of this work is this is proof of principal that under careful fabrication conditions, wet fabrication techniques can be used to build complex, nanocomposite SRMs on microsensors. While this approach cannot be integrated into microfabrication array techniques (for example, imaging applications) at this time, these results are very valuable for small scale sensor integration in applications such as microfluidic chambers and complex sensing in nanoscale dimensions.

Chapter 9. This chapter is a paper submitted to *Nature Nanotechnology*. At the top of the design approach pyramid (Fig. 1-15), the final consideration to be made is regarding fabrication. For reasons discussed above, for practical integration of SRMs into real sensors that *must* be batch processed for large-scale microfabrication MEMS structures, the coating procedure must be compatible. Thus, alternate deposition techniques for nanoscale organic layers were explored in this work, and the technique of PECVD was chosen due to its room temperature operating conditions, ease of fabrication, and the fact that nearly all monomers can be deposited with this equipment. The organic SRMs were deposited onto microsensors and integrated into real array sensors, and the resulting thermal sensitivity of the hybrid structures was characterized. Thermal sensitivity was found to be on the order of 2mK, which is manifold times better than current sensor materials platforms. Furthermore, the

microsensors had unprecedented response to humidity, and this will be explained in this chapter.

Chapter 10. This chapter explains the unusual negative thermal expansion phenomenon observed in some of the plasma polymers. This is a paper submitted to *Chemistry Materials*. Negative thermal expansion is a unique phenomenon in polymeric materials. While this has been observed in ultrathin films in which the thickness is on the order of the size of individual polymers, and attributed to entropic effects, never before has this been observed in "thick" nanoscale films (larger than the radius of gyration). Furthermore, this is unexpected for highly cross-linked polymers, and a model is proposed taking into account the intrinsic stresses within plasma polymers related to the nature of deposition.

1.9 Conclusions

Throughout the course of this work, several important innovations and significant contributions were made for the understanding and development of surface responsive materials applied to inorganic surfaces, which can be divided into three categories: fabrication of nanoscale layers, understanding of nanoscale/molecular properties and, most importantly, design for integration into working hybrid sensors.

In terms of fabrication, the design and synthesis of nanoscale SRMs discussed here represents several significant breakthroughs. With binary brush layers, the absolute goal of the design was to provide the capability to switch between a surface with very different mechanical properties and very different surface energies (amphiphilic). This is critical for NEMS devices with actuating parts that can have a nanomechanical switch of actuation, especially considering the total layer is *only* 3nm thick, which represents a major breakthrough in switchable SRMs. Such a surface can be very critical to biomedical applications in which protein/cell adhesion can be turned on/off specifically based on surface energy switching.

In this thesis, a step beyond conventional binary brushes was taken with the development of nanoscale brush layers with complex architecture. This work is groundbreaking in the sense that true brush layers of complex architecture have yet to be achieved, let alone their nanomechanical response characterized. This work is significant for several reasons: 1) Complex, multi-level SRM can be synthesized in a step-by-step fashion by one easy method of polymerization (UV-polymerization). 2) The reversible nanomechanical response is characterized in fluid going through a phase transition near the physiological important temperature (32°C). This information is absolutely imperative for bioengineers to access because these brushes of complex architecture mimic real biological structures with similar hierarchy in structure.

To pursue a 'dry' SRM fabrication approach in order to bridge the gap between complex sensing polymeric nanolayers and microsensors that can potentially lead to a new revolution in sensor research, PECVD was carried out in this research as a novel approach to apply SRMs into microcantilever sensors. Plasma polymer films are, at the present time, stimulating great interest in advanced technologies within the nanotechnology realm. These materials are on the verge of widespread use because it is becoming established that plasma polymerization represents an unusually convenient and versatile coatings technology. There is strong appeal for a one-step, solvent-less process, which provides uniform, conformable coatings of controllable thickness and properties with a vast range of monomers. Plasma polymer layers were fabricated that could respond to temperature and humidity with unprecedented sensitivities, and when integrated into thermal and humidity sensors, they surpassed the performance of contemporary sensors (even similar microcantilever based methods) by orders of magnitude. Another major finding is the huge negative thermal expansion observed, which has never before been achieved in organic layers 50 – 200 nm thick. It is the sincere belief here that the research into plasma polymers in this thesis will have a major impact in sensor applications and surface responsive materials because of the straightforward synthesis effort to produce essentially a new class of materials, which in turn can be incorporated into a new class of sensors with the hybrid materials platform design.

A completely different coating type developed in this work is 2D and 3D microtruss structures instituted in polymer layers via interference lithography. The fact that the classic 'truss' structure can be implemented into novel load-bearing microscale coatings with nanoscale gradients in elastic modulus all by "one-zap" laser lithography approach is truly remarkable. Photopatterned polymer coatings with novel load-bearing mechanisms will impact everything from ballistic protection to stronger automobile parts due to its large scale capability.

In terms of understanding nanomechanical properties, it is the belief here that no other technique offers this ability with nanoscale spatial resolution in complex environments quite like AFM. Therefore, significant achievements were made here that polymer scientists can add to their repertoire to bolster their fundamental understanding of organic materials. Here, AFM was used for the first time ever to measure the interaction forces of a single molecule interacting with another single molecule using chemical force microscopy. Simultaneous modeling simulations verified the fact that indeed the AFM measured only a single electron pair of a single functional molecule interacting with the sidewall of a SWCNT. In addition, this allowed for the fundamental interaction principals of organic molecules with SWCNT was understood, and this is a major breakthrough because CNT are at the center of nanotechnology, and one of the prime aspects impeding their further proliferation is the lack of understanding in integrating them with organic materials.

Finally, in this work, proof of principal of active organic sensing layers crossed with silicon based microsensors to make actual working hybrid sensors is given. The results are invaluable in terms of advanced sensor applications because sensitivities to temperature and humidity that were achieved here are orders of magnitude beyond the detection capabilities for sensors of today. A brief summary of significant achievements include: controlled deposition of coatings onto delicate microsensors, the combination of plasma polymers into microsensors (an ideal that has surprisingly not been exploited) for robust, strongly adhered active sensing layers, and working sensors with high reproducibility to universal stimuli for ultimate multifunctionality.

1.10 References

1 According to NSF 2007 budget proposal, the engineering division is expected to grow by 8.2 %, or roughly 45 million dollars, with 20 million of this going *directly "to support sensor research that is relevant to the detection of explosive devices and related threats."* In addition, the ongoing *Sensors and Sensor Networks Program* at NSF began in 2004 with a first year budget of 47 million dollars

2 Potyrailo, R.A. *Angew. Chem. Int. Ed.* **2006**, 45, 702.

3 Harsanyi, G. *Polymer Films in Sensor Applications*. Technomic: Lancaster, **1995**.

4 Middelhoek, S.; Noorlag, J.W. *Sens. Actuators* **1981/82**, 2, 29.

5 Russel, T.P. *Science* **2002,** 297, 964.

6 Minko, S. *Responsive Polymer Materials*; Blackwell Publishing: Ames, **2006**.

7 Yerushalmi, R.; Scherz, A.; van der Boom, M.E.; Kraatz, H.-B. *J. Mater. Chem.* **2005**, 15, 4480.

8 Gil, E.S.; Hudson, S.M. *Prog. Polym. Sci.* **2004**, 29, 1173.

9 Jeong, B.; Gutowska, A. *Trends Biotechnol.* **2002**, 20, 305.

10 Tezuka, Y.; Oike, H. *Prog. Polym. Sci.* **2002**, 27, 1069.

11 Sheiko, S.S.; Moller, M. *Chem. Rev.* **2001,** 101, 4099.

12 Lu, Y.; Chen, S.C. *Adv. Drug. Delivery Rev.* **2004**, 56, 1621.

13 Langer, R.; Peppas, N. *AIChE J.* **2003**, 49, 2990.

14 Advincula, R.; Brittain, W.J.; Caster, K.C.; Ruhe, J. Eds. *Polymer Brushes*; Wiley-VCH: Weinheim, **2004**.

15 Luzinov, I.; Minko, S.; Tsukruk, V.V. *Prog. Poly. Sci.* **2004,** 29, 635.

16 Zhao, B.; Brittain,W.J. *Prog. Polym. Sci.* **2000**, 25, 677.

17 Adhikari, B.; Majumdar, S. *Prog. Poly. Sci*, **2004**, 29, 699.

18 Chian, C.K.; Park, Y.W.; Heeger, A.J.; Shirakawa, H.; Louis, E.J.; MacDiarmid, A.G. *J. Chem. Phys.* **1978**, 69, 5098.

19 Diaz, A.F.; Kanazawa, K.K.; Gardini, G.P. *J. Chem. Soc. Chem. Comms.* **1979**, 635.

20 Roncali, J. *Chem. Rev.* **1992**, 92, 711.

21 Nicho, M.E.; Trejo, M.; Garcia-Valenzuela, A.; Saniger, J.M.; Palacios, J.; Hu, H. *Sens. Act. B.* **2001**, 77, 657.

22 McQuade, D.T.; Pullen, A.E.; Swager, T.M. *Chem. Rev.* **2000**, 100, 2537.

23 Jin, Z.; Su, Y.; Duan, Y. *Sens. Act. B.* **2000**, 71, 118.

24 Chiang, J.-C.; MacDiarmind, A.G. *Synth. Met.* **1986**, 13, 193.

25 Ito, Y.; Ochiai, Y.; Park, Y.S.; Imanishi, Y. *J. Am. Chem. Soc.* **1997**, 119, 1619.

26 Iwata, H.; Hirata, I.; Ikada, Y. *Macromolecules* **1998**, 31, 3671.

27 Ito, Y.; Nishi, S.; Park, Y.S.; Imanishi, Y. *Macromolecules* **1997**, 30, 5856.

28 Park, Y.S.; Ito, Y.; Imanishi, Y. *Macromolecules* **1998**, 31, 2606.

29 Sadaoka, Y.; Sakai, Y.; Akiyama, H. *J. Mater. Sci.* **1986**, 21, 235.

30 Li, D.; Jiang, Y.; Wu, Z.; Chen, X.; Li, Y. *Sens. Act. B.* **2000**, 66, 125.

31 Revzin, A.F.; Sirkir, K.; Simonian, A.; Pishoko, M.V. *Sens. Act.* **2002**, 81, 359.

32 Myler, S.; Collyer, S.D.; Bridge, K.A.; Higson, S.P.J. *Biosens. Bioelectron.* **2002**, 17, 35.

33 Xie, D.; Jiang, Y.; Pan, W.; Li, D.; Wu, Z.; Li, Y. *Sens. Act. B.* **2002**, 81, 158.

34 Otagawa, T.; Madou, M.; Wing, S.; Rich-Alexander, J.; Kusanagi, S.; Fujioka, T.; Yasuda, A. *Sens. Act. B.* **1990**, 1, 319.

35 Zhao, Y.; Mao, M.; Horowitz, R.; Majumdar, A.; Varesi, J.; Norton, P.; Kitching, J. *J. MEMS* **2002**, 2, 136.

36 Wood, R.A. *Uncooled Infrared Imaging Arrays and Systems, Semiconductors and Semimetals, Vol. 47,* Kruse, P.W.; Skatrud, D.D., Eds. Academic: San Diego, **1997**.

37 Khrebtov, A.; Malyarov, V.G. *J. Opt. Technol.,* **1997**, 64, 511.

38 Rogalski, A. *Prog. Quantum Elec.* **2003**, 59-210.

39 Datskos, P.G.; Lavrik, N.V.; Rajic, S. *Rev. Sci. Instrum.* **2004**, 75, 1134.

40 Murphy, D. F. *Proc. SPIE* **2000**, 4721, 99.

41 Howard, P.E.; Clarke, J.E.; Bradley, M.G.; Ionescu, A.C.; Li, C. *Infrared technology and applications XXVI, Proc. SPIE* **2000**, 4130, 168.

42 Amantea, R.; Knoedler, C.M.; Pantuso, F.P.; Patel, V.K.; Sauer, D.J.; Tower, J.R. *Proc SPIE* **1997**, 3061, 210.

43 Malyarov, V.G. *J. Opt. Technol.* **2002**, 69, 750.

44 Kruse, P.W. *Inf. Phys. Technol.* **1995**, 36, 869.

45 Hunter, R.S. *Proc. SPIE* **2003**, 5074, 469.

46 Sze, S.M. *Semiconductor Devices: Physics and Technology, 2nd Ed.*; Wiley: New York, **2002**.

47 Madou, M. *Fundamentals of Microfabrication*; CRC: Boca Raton, FL, **1997**.

48 Sarid, D. *Scanning Force Microscopy;* Oxford University press: New York, **1991**.

49 Shaver, P.J. *Rev. Sci. Instrum.*, **1969**, 40, 901.

50 Gimzewski, J.K.; Gerber, C.; Meyer, E.; Schlittler, R.R. *Chem. Phys. Lett.* **1994**, 217, 589.

51 Barnes, J.R.; Stephenson, R.J.; Welland, M.E.; Gerber, C.; Gimzewski, J.K. *Nature* **1994**, 372, 79.

52 Varesi, J.; Lai, J.; Perazzo, T.; Shi, Z.; Majumdar, A. *Appl. Phys. Lett.* **1997,** 71, 306.

53 Datskos, P.G.; Oden, P.I.; Thundat, T.; Wachter, E.A.; Warmack, R.J.; Hunter, S.R. *Appl. Phys. Lett.* **1996**, 69, 2986.

54 Oden, P.I.; Datskos, P.G.; Thundat, T.; Warmack, E.A. *Appl. Phys. Lett.* **1996**, 69, 3277.

55 Manalis, S.R.; Minne, S.C.; Quate, C.F.; Yaralioglu, G.G.; Atalar, A. *Appl. Phys. Lett.* **1997**, 70, 3311.

56 Corbeil, J.L.; Lavrik, N.V., Rajic, S., Datskos, P.G. *Appl. Phys. Lett.* **2002**, 81, 1306.

57 Gorbunov, V.; Fuchigami, N.; Stone, M.; Grace, M.; Tsukruk, V.V. *Biomacromolecules* **2002,** 3, 106.

58 Terashima S.; Goris R.C. Eds. *Infrared Receptors and the Trigeminal Sensory System*; Harwood Acadademic Publishers: Amsterdam, **1998**.

59 Tsukruk, V.V.; Ornatska, M.; Sidorenko, A. *Progr. Organic Coatings* **2003**, 47, 288.

60 Hilt, J.Z.; Gupta, A.; Bashir, R.; Peppas, N. *Biomed. Microdev.* **2003**, 5, 177.

61 Muller, R.S. in *Micro/Nanotribology and Its Applications*, Bhushan, B., Ed.; Kluwer Academic Press: Dordecht, **1997**: p 579. *Tribology Issues and Opportunities in*

MEMS, Bhushan, B., Ed.; Kluwer Academic Publishers: Dordrecht, **1997**. Tsukruk, V.V. in: *Nanotribology*, Hsu, S.M.; Ying, C. Z.; Eds.; Kluwer Academic Press: Boston, **2002**, p 347.

62 Ionov, L.; Minko, S.; Stamm, M.; Gohy, J.-F.; Jérôme, R.; Scholl, A. *J. Am. Chem. Soc.* **2003**, 125, 8302.

63 Bliznyuk, V.N.; Everson, M.P.; Tsukruk, V.V. *J. Tribology* **1998**, 120, 489. Tsukruk, V.V.; Bliznyuk, V.N. *Langmuir* **1998**, 14, 446. Sidorenko, A.; Houphouet-Boigny, C.; Villavicencio, O.; McGrath, D.V.; Tsukruk, V.V. *Thin Solid Films,* **2002**, 410, 147. Peleshanko, S.; Sidorenko, A.; Larson, K., Villavicencio, O.; Ornatska, M.; McGrath, D.V.; Tsukruk, V.V. *Thin Solid Films,* **2002**, 406, 233. Ahn, H.; Julthongpiput, D.; Kim, D.I.; Tsukruk, V.V. *Wear* **2003,** 255, 801. Tsukruk, V.V.; Sidorenko, A.; Yang, H. *Polymer* **2002**, 43, 1695. Sidorenko, A.; Julthongpiput, D.; Luzinov, I.; Tsukruk, V.V. *Tribol. Lett.* **2002**, 12, 101.

64 Ito, Y.; Ochiai, Y.; Park, Y. S.; Imanishi, Y. *J. Am. Chem. Soc.* **1997**, 119, 1619.

65 Galaev, I.; Mattiasson, B. *Trends Biotechnol.* **1999**, 17, 335.

66 Jones, D.M.; Smith, R.R.; Huck, W.T.S.; Alexander, C. *Adv. Mater.* **2002**, 14, 1130.

67 Aksay, I. A.; Trau, M.; Manne, S.; Honma, I.; Yao, N.; Zhou, L.; Fenter, P.; Eisenberger, P. M.; Gruner, S. M. *Science* **1996**, 273, 892.

68 Dean, D.; Seog, J.; Ortiz, C.; Grdzinsky, A. J. *Langmuir* **2003**, 19, 5526.

69 Rixman, M. A.; Dean, D.; Ortiz, C. *Langmuir* **2003**, 19, 9357.

70 Qin, S. H.; Oin, D. Q.; Ford, W. T.; Resasco, D. E.; Herrera, J. E. *J. Am. Chem. Soc.* **2004**, 126, 170.

71 Gomez, F. J.; Chen, R. J.; Wang, D. W.; Waymouth, R. M.; Dai, H. J. *Chem. Commun.* **2003**, 190.

72 Viswanathan, G.; Chakrapani, N.; Yang, H. C.; Wei, B. Q.; Chung, H. S.; Cho, K. W.; Ryu, C. Y.; Ajayan, P. M. *J. Am. Chem. Soc.* **2003**, 125, 9258.

73 Artyukhin, A. B.; Bakajin, O.; Stroeve, P.; Noy, A. *Langmuir* **2004**, 20, 1442.

74 Alexander, S.J. *J. Phys.* **1977**, 38, 977.

75 de Gennes, P.G. *Macromolecules* **1980**, 13, 1069.

76 Karim, A.; Tsukruk, V. V.; Douglas, J. F.; Satija, S. K.; Fetters, L. J.; Reneker, D. H.; Foster, M. D. *J. Phys. II* **1995**, 5, 1441. Tsukruk, V. V. *Prog. Polym. Sci.* **1997**, 22, 247. Tsukruk, V. V. *Adv. Mater.* **1998**, 10, 253.

77 Zhao, B.; Brittain, W. J. *J. Am. Chem. Soc.* **1999**, 121, 3557. Zhao, B.; Brittain, W. J.; Zhou, W. S.; Cheng, S. Z. D. *J. Am. Chem. Soc.* **2000**, 122, 2407. Sedjo, R.; Mirous, B. K; Brittain, W. J. *Macromolecules* **2000**, 33, 1492.

78 Wittmer, J.; Johner, A.; Joanny, J. F. *Colloids Surf. A* **1994**, 86, 85.

79 Milner, S.T. *Science* **1991**, 251, 905.

80 Klein, J. *Annual Rev. of Mat. Sci.* **1996**, 26, 581.

81 Granick, S. In *Physics of Polymer Surfaces and Interfaces.* Sanchez, I., Ed. Manning: New York, **1993**.

82 Sperling, L.H. *Introduction to Physical Polymer Science.* Wiley: New York, **2001**.

83 Halperin, A.; Tirrel, M.; Lodge, T.P. *Advances in Polymer Science.* Springer: New York vol. 100, 31, **1992**.

84 Wittmer, J.; Johner, A.; Joanny, J.F. *Coll. Surf. A: Phsiochem. And Eng. Aspects* **1994**, 86, 85.

85 Minko, S.; Patil, S.; Datsyuk, V.; Simon, F.; Eichhorn, K. J.; Motornov, M.; Usov, D.; Tokarev, I.; Stamm, M. *Langmuir* **2002**, 18, 289.

86 Minko, S.; Usov, D.; Goreshnik, E.; Stamm, M. *Macromol. Rapid. Comm.* **2001**, 22, 206.

87 Soga, K. G.; Zuckermann, M. J.; Guo, H. *Macromolecules* **1996**, 29, 1998.

88 Marko, J. F.; Witten, T. A. *Phys. Rev. Lett.* **1991**, 66, 1541.

89 Müller, M. *Phys. Rev. E* **2002**, 65, 30802.

90 Minko, S.; Muller, M.; Usov, D.; Scholl, A.; Froeck, C.; Stamm, M. *Phys. Rev. Lett.* **2002**, 88, 5502.

91 Minko, S.; Muller, M.; Motornov, M.; Nitschke, M.; Grundke, K.; Stamm, M. *J. Am. Chem. Soc.* **2003**, 125, 3896.

92 LeMieux, M.C.; Usov, D.; Minko, S.; Stamm, M.; Shulha, H.; Tsukruk, V.V. *Macromolecules* **2003,** 36, 7244.

93 Blossey, R. *Nat. Mater.* **2003**, 2, 301.

94 LeMieux, M.C.; Julthongpiput, D.; Duc Cuong, P.; Ahn, H.-S.; Lin, Y.; Tsukruk, V.V. *Langmuir* **2004**, 20, 10046.

95 Tsukruk, V.V. *Tribol. Lett.* **2001**, 10, 127.

96 White, S.R.; Sottos, N.R.; Geubelle, P.H.; Moore, J.S.; Kessler, M.R.; Sriram, S.R.; Brown, E.N.; Viswanathan, S. *Nature* **2001**, 409, 794.

97 Hadjichristidis, N.; Pitsikalis, M.; Iatrou, H.; Pispas, S. *Macromol. Rapid Commun.* **2003**, 24, 979.

98 Krausch, G.; Magerle, R.G. *Adv. Mater.* **2002**, 14, 1579.

99 Zhulina, E.B.; Birshtein, T.M.; Priamitsyn, V.A.; Klushin, L.I. *Macromolecules* **1995**, 28, 8612.

100 Park, M.; Christopher H.; Chaikin, P.M.; Register, R.A.; Adamson, D.H. *Science* **1997**, 276, 1401.

101 Sidorenko, A.; Tokarev, I.; Minko, S.; Stamm, M. *J. Am. Chem. Soc.* **2003**, 125, 12211.

102 Iyer, K.S.; Zdyrko, B.; Malz, H.; Pionteck, J.; Luzinov, I. *Macromolecules* **2003**, 36, 6519.

103 Borner, H.G.; Duran, D.; Matyjaszewski, K.; da Silva, M.; Sheiko, S.S. *Macromolecules* **2002**, 35, 3387.

104 Lord, S.J.; Sheiko, S.S.; LaRue, I.; Lee, H.; Matyjaszewski, K. *Macromolecules* **2004**, 37, 4235.

105 Borner, H.G.; Beers, K.; Matyjaszewski, K.; Sheiko, S.; Moller, M. *Macromolecules* **2001**, 34, 4375.

106 Zhang, D.; Ortiz, C. *Macromolecules* **2004**, 37, 4271.

107 McCormick, C.L.; Lowe, A.B. *Acc. Chem. Res.* **2004**, 37, 312.

108 Edmonson, S.; Osborne, V.; Huck, W.T.S. *Chem. Soc. Rev.* **2004**, 33, 14.

109 Nath, N.; Chilkoti, A. *Adv. Mater.* **2002**, 14, 1243.

110 Zou, X. P.; Kang, E. T.; Neoh, K. G.; Zhang, Y.; Tan, K. L.; Cui, C. Q.; Lim, T. B. *Poly. Adv. Technol.* **2001**, 12, 583.

111 Kim, M.C.; Cho, S.H.; Lee, S.B.; Kim, Y.; Boo, J.H. *Thin Solid Films* **2004**, 447-448, 592.

112 Tamirisa, P.; Liddell, K.C.; Pedrow, P.D.; Osman, M.A. *J. Appl. Poly. Sci.* **2004**, 93, 1317.

113 Shi, F. *Surf. Coat. Technol.* **1996**, 82, 1.

114 Biederman, H.; Slavinska, D. *Surf. Coat. Technol.* **2000**, 125, 371.

115 Hiratuka, A.; Karube, I. *Electroanalysis* **2000**, 12, 695.

116 Cruz, G.J.; Morales, J.; Olayo, R. *Thin solid films* **1999**, 342, 119.

117 Yang, G.H.; Oh, S.W.; Kang, E.T.; Neoh, K.G. *J. Vac. Sci. Technol. A* **2002**, 20, 1955.

118 Cicala, G.; Milella, A.; Palumbo, F.; Rossini, P.; Favia, P.; d'Agostino, R. *Macromolecules* **2002**, 35, 8920.

119 Moon, J.H.; Yang, S. *J. Macromol. Sci. C.* **2005**, 45, 351.

120 Smith, J.; Hodgins, J.; Oppenheim, I.; Witkin, A. *ACM Trans. Graph.* **2002**, 21, 295.

121 Berger, V.; Gauthier-Lafaye, O.; Costard, E. *J. Appl. Phys.* **1997**, 82, 60.

122 Hong, G.; Holmes, A.S.; Heaton,M.E. *Microsyst. Technol.* **2004**, 10, 357.

123 Lee, K.Y.; LaBianca, N.; Zolgharnain, S.; Rishton, S.A.; Gelorme, J.D.; Shaw, J.M.; Chang, T.H. *J. Vac. Sci. Technol.* **1995**, B13, 3012.

124 Feng, R.; Farris, R.J. *J. Mater. Sci.* **2002**, 37, 4793.

125 Dekker, C. *Phys. Today* **1999**, 52, 22.

126 Binnig, G.; Quate, C.F.; Gerber, C. *Phys. Rev. Lett.* **1986**, 56, 930.

127 Tsukruk, V.V.; Reneker, D.H. *Polymer* **1995**, 36, 1791.

128 Sheiko, S. *Adv. Poly. Sci.* **2000**, 151, 61.

CHAPTER 2

Experimental Procedures

2.1 General Considerations

This chapter is intended to give a general overview of the experimental *technique, procedures,* and *equipment* that were utilized throughout the research in this thesis. Exact *specific details* are given in each of the Results Chapters to better support the data in each. Overviews will be given of sample preparation and this will be divided into two major classifications categorized by nanolayer fabrication (deposition) approach (wet or dry), not substrate (silicon wafer or microcantilever). In other words, this work consisted of doing wet and dry depositions on both wafers and cantilevers. After explaining general sample preparation procedures, overviews will be given of the characterization equipment and procedures.

2.2 Fabrication: "Wet Approach" Overview

Wet fabrication involves fabrication and deposition of organic monolayers or SRMs onto silicon wafers and microcantilevers using a wet chemistry approach. For synthesizing these layers in the nanoscale regime, the utmost and extensive care in procedure must be taken to assure the elimination of all contaminants. All glassware was first cleaned by glassware soap detergent and rinsed with water. Chromic sulfuric acid solution was prepared by a mixing ratio of 1:10 of potassium dichromate with highly concentrated sulfuric acid. The glassware was submerged in Chromic sulfuric acid solution for roughly 1 hour, rinsed with water, and additionally rinsed with high purity water (18 MΩcm, Nanopure). Then, the clean glassware was dried at 100° C in an oven for at least 12 hours.

Prior to any deposition, the wafers or microcantilevers were appropriately cleaned. The substrates were first placed in nanopure water and cleaned in an ultrasonic bath for 10 minutes, and placed in a hot piranha solution. Piranha solution was prepared by the mixing of 30% H_2O_2 (30% concentrated solution in water) added slowly with 70% concentrated sulfuric acid (97%). The substrates were placed in the 90° C heated piranha solution for roughly 1 hour. Then, the substrates were removed from the solution and rinsed six times with Nanopure water. After that, the substrates were quickly dried under a stream of dry nitrogen, placed into 15 ml vials, filled with nitrogen, firmly closed with Teflon caps, and then immediately taken into the nitrogen-filled glove box with controlled humidity.

On the other hand, microcantilevers cannot withstand the vigorous piranha treatment due to their small size, causing detrimental capillary forces. Furthermore, because wet deposition involves multiple steps, and repeated handling is not feasible with the delicate microcantilevers, they were reversibly glued onto Teflon supports for handling, and piranha solution would have easily etched the epoxy glue, destroying the support (Figure 2-1). In

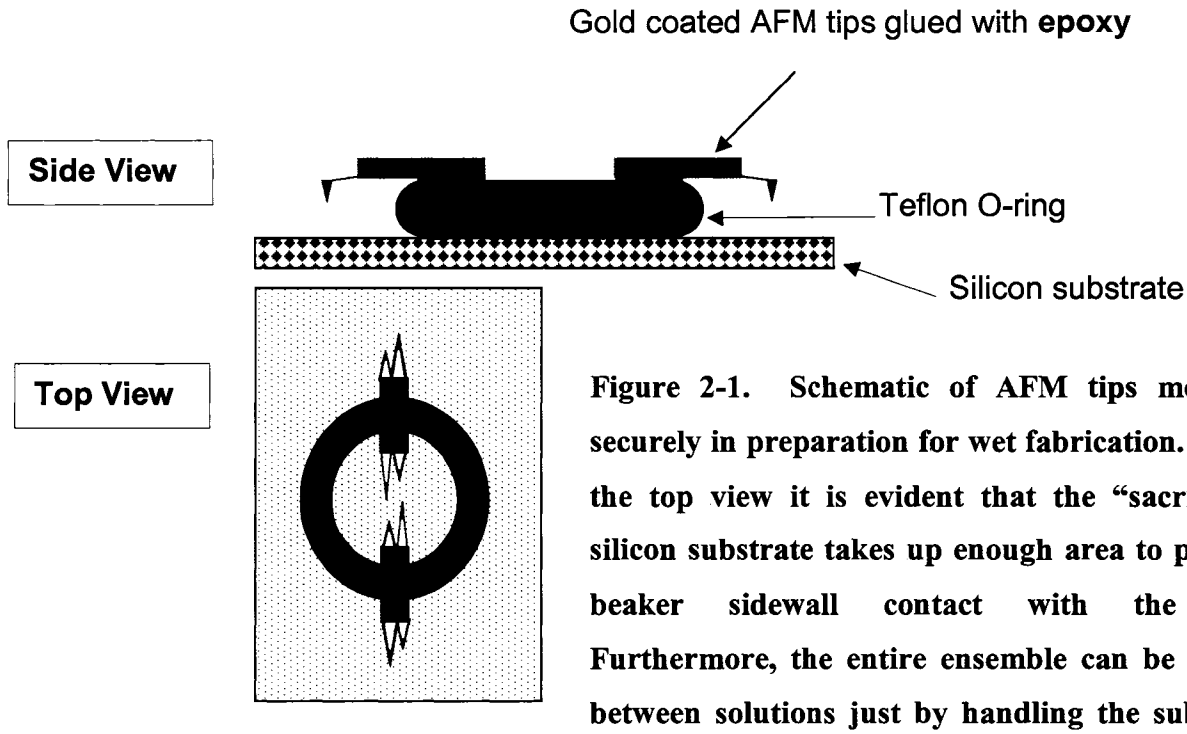

Figure 2-1. Schematic of AFM tips mounted securely in preparation for wet fabrication. From the top view it is evident that the "sacrificial" silicon substrate takes up enough area to prevent beaker sidewall contact with the tips. Furthermore, the entire ensemble can be moved between solutions just by handling the substrate rather than individual intricate AFM tips.

this case, the Teflon O-ring, which is completely inert to all organic solvents, was glued onto the cleaned silicon wafer with a strong epoxy that was again completely inert to organic solvents. Then, the AFM tips were mounted onto the O-ring with the same epoxy. In this way, the AFM tips could be easily transported and handled between different solutions without the worry of breaking.

Thus, the cantilevers were typically washed in chloroform for 30 minutes, and then rinsed with the same solvent that the ensuing deposition would be carried out in (typically toluene or ethanol). This was typically done in glass beakers in which the entire setup could fit (Figure 2-2).

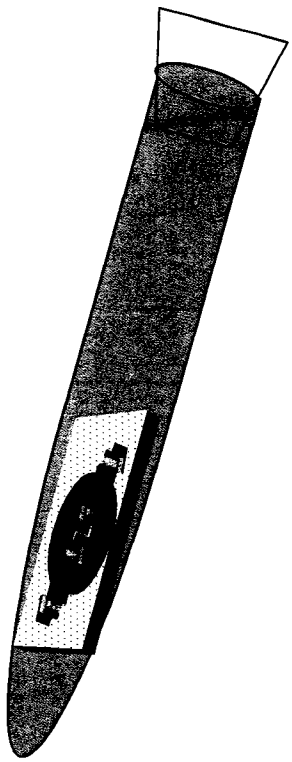

Figure 2-2. Schematic showing the large glass tubes in which cleaning and surface functionalization had to take place in to accommodate the 'sacrificial' silicon substrate the microcantilever sensors are mounted on.

The surfaces modified with SRMs in this work were either silicon (silicon oxide) or gold, as these are the two most relevant materials in microfabrication processes.[1] In order to facilitate the strong chemical attachment of the sensing nanolayers, the substrate is modified with a reactive precursor acting as a coupling agent (a SAM) which has one end covalently reacting with the metallic or semi-conducting surface, and the other end covalently reacts with the end – functionalized polymer (typically it is an epoxy group or a carboxyl group).[2,3,4,5] Chemical grafting has several advantages over physical processes including the ability for a high density of polymer chains attached at the exact desirable locations.

Additionally, covalent attachment of polymer surfaces reduces the possibility of delamination, and aides in long-term chemical stability of the chains. Thus, the first step in the design is the anchoring SAM layer to gold or silicon (Figure 2-3).

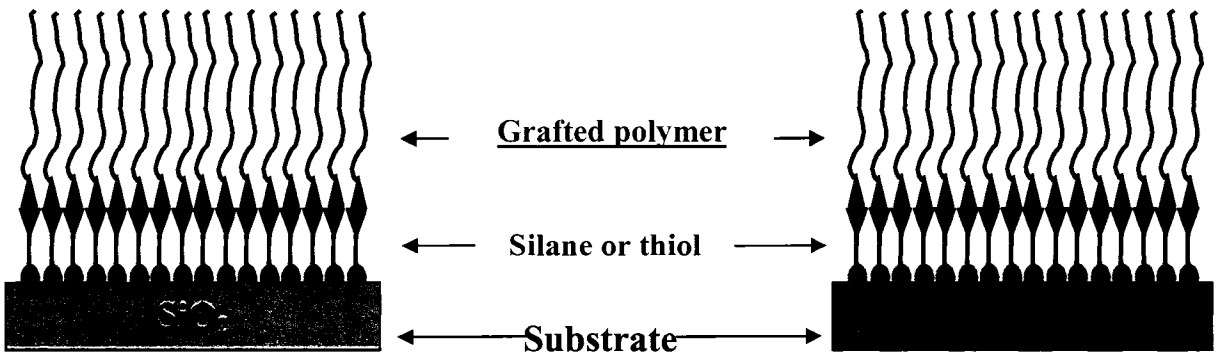

Figure 2-3. Wet fabrication outline for two different substrates used in this work (silicon and gold). Silane anchoring linkers are used for silicon, while thiol anchoring linkers are used for gold surfaces. A subsequent polymer layer is attached to the functional linker, resulting in covalently grafted polymer layers in both cases.

For the grafting onto silicon, this is facilitated with a SAM known as a silane, which is a silicon containing molecule that reacts directly with silicon surfaces (SiO_2, or Si_3N_4), and has built in functionality at the other terminus to react and bond to incoming polymer (Figure 2-4).[6,7,8] The general process of SAM formation is, as the name states, by self-assembly. Specifics for each chapter will be given, but the general principal is shown here with an example of using an epoxysilane SAM, which is the most utilized in the "grafting to" scheme. After the solution preparation, the clean substrates were immersed in the silane solution for different periods of deposition time (typically from 1 minute to 24 hours) as illustrated in Figure 2-5. After the deposition was completed, the modified substrates were removed from the solution, and rinsed four times with a suitable solvent. Additionally, the substrates were placed in the same solvent in the ultrasonic bath for 10 minutes. The SAMs formed were dried under a stream of dry nitrogen inside a cleanroom 100 facility. After

preparation, samples were stored in desiccators to prevent moisture of air which can lead to contamination and undesirable surface reactions.

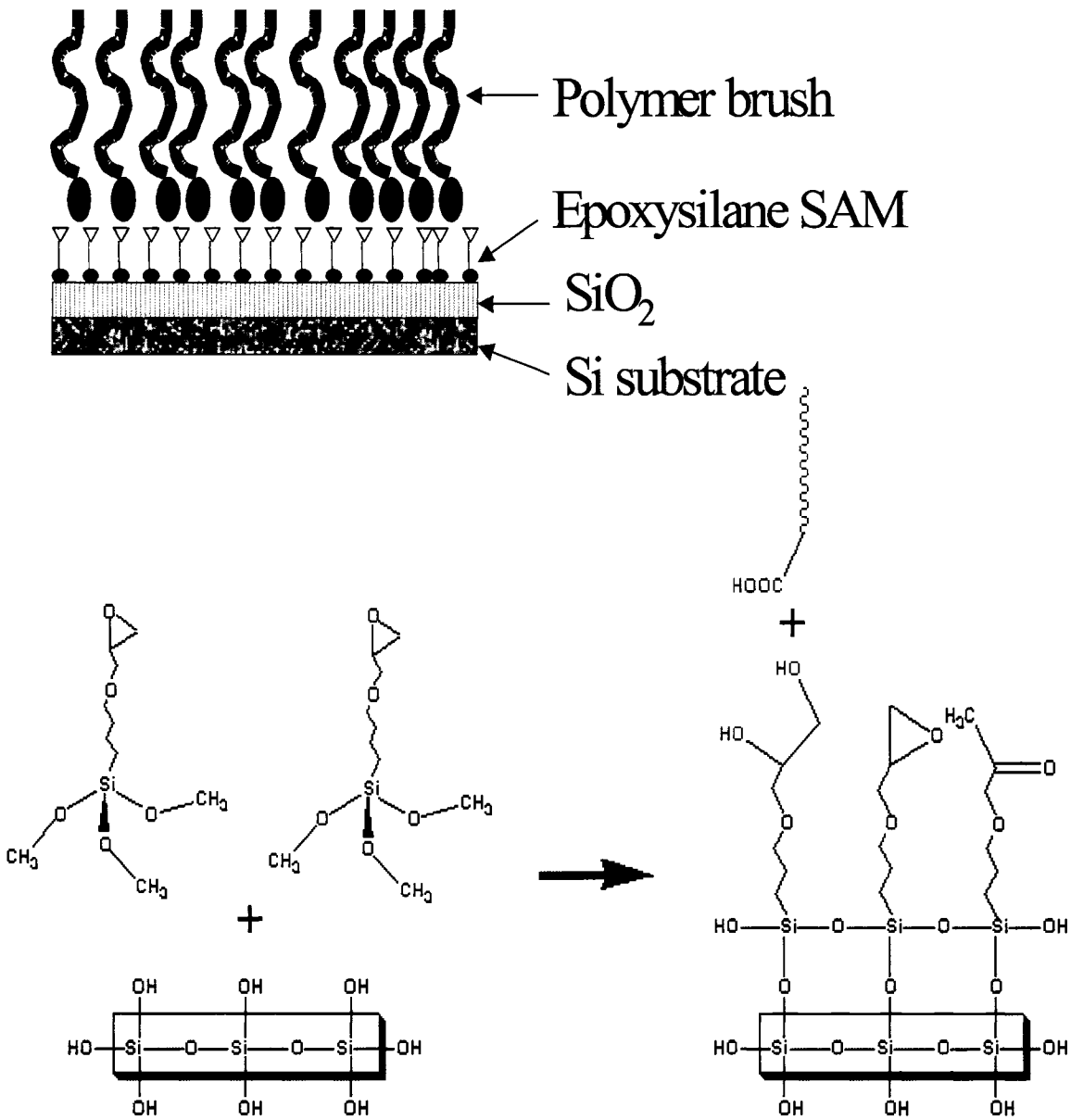

Figure 2-4. Top: structural diagram of the resulting SRM (in the form of a polymer brush) specifically showing grafting to the epoxy – terminated SAM on a silicon wafer. Bottom: Actual silanazation chemistry of the process.[6]

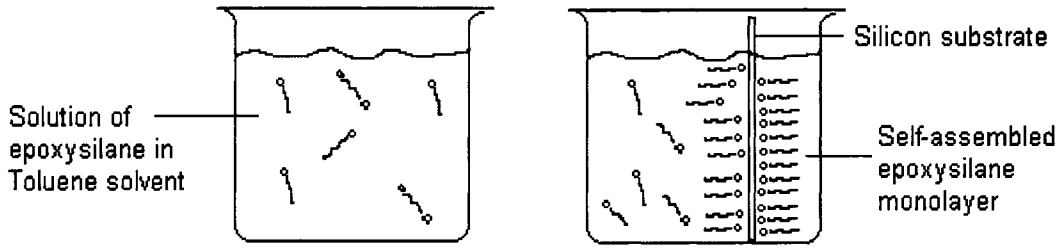

Figure 2-5. Self – assembly mechanism onto the silicon wafer.

For attachment to gold surfaces, there are a couple of different options explored in this work. The most widely used approach is using thiol containing SAMs, and the thiol-gold chemistry has been known since the 80s.[9] We utilized three schemes outlined in Figure

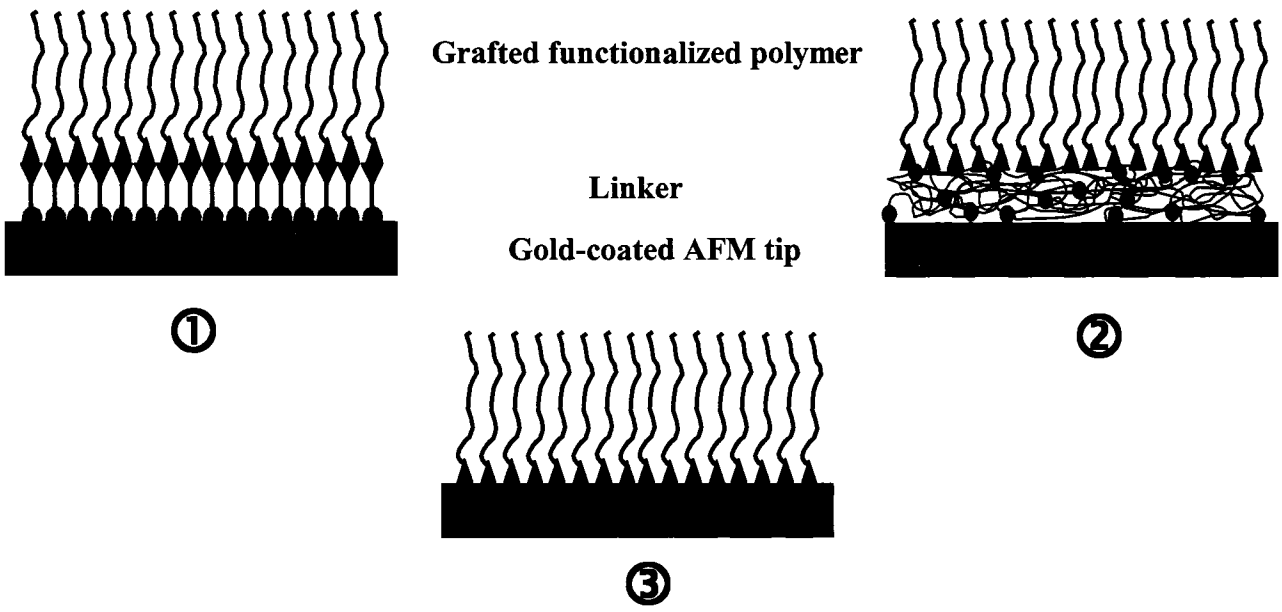

Figure 2-6. Various grafting schemes for fabricating SRMs on gold surfaces. In scheme 1 (top left), polymers are covalently grafted via the functional thiol linker. In scheme 2 (top right), polymers are covalently grafted through a PEI "carpet" linker. PEI has a high density of amino groups with can bond to both gold, with residual groups available for polymer grafting ('grafting through'). Scheme 3 (bottom) simply involves pre-formed thiol-functionalized polymers grafting directly to gold.

2-6: The first is similar to the silane approach in which thiols are used as a coupling agent. The second approach involves using a "carpet" linker. In this case, high molecular polyethylene imine (PEI) (M_n = 25,000 g/mol) is deposited on the surface. PEI offers abundant primary and secondary amino groups that bond strongly to gold, and covalently attach to functionalized polymers. The third approach is the most direct in which thiol-functionalized polymers are directly grafted to gold. While this approach is the simplest, not many polymers can be modified with a thiol group, thus the method is far from universal.

Since a general background of the wet approach was given, how this is applied to each specific chapter in this thesis will now be given. Although detailed experimental information is supplied in each chapter, these are still abridged, and the following sections can be viewed as "supplemental information" to give a full idea of conditions unique to each specific sample. On the other hand, some chapters require no further explanation than what is already detailed in that particular chapter, and this will be noted.

2.3 Fabrication: "Wet Approach" In Chapter 3

A separate, special case involves grafting precise SAM layers directly onto cantilever tips (Figure 2-6) for using modified AFM tips directly in AFM operation, and this procedure

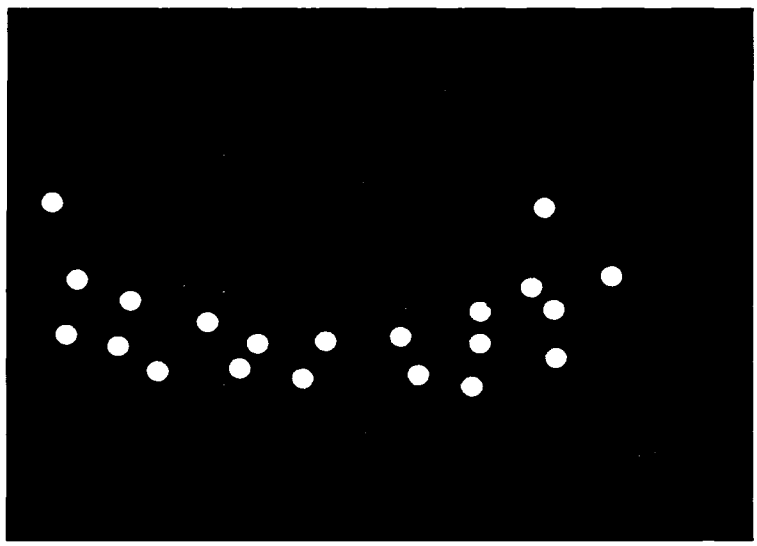

Figure 2-6. Schematic of a silane monolayer on AN AFM tip interacting with CNT in solvent.

was relevant only for Chapter 3. Chemical modification of the AFM tips with specific functional groups, known as chemical force microscopy (CFM), provides a general route for measuring specific interactions with sub-nanonewton force resolution and sub-angstrom distance resolution.[10,11] This approach is valuable, since it allows systematic investigations of the very basic chemical interactions that contribute to the complex interactions involving organic interfaces. Such a tool is invaluable for the development of fundamental nanoscale interactions with organic materials for sensor research (see Chapter 3). In this particular case, the following silanes in Table 2-1 were grafted to the AFM tip. Grafting times are shown for 1% (in anhydrous toluene). These self-assembly times were optimized based on doing the fabrication simultaneously, and measuring properties with AFM, ellipsometry, and contact angle.

Table 2-1: Silanes used in chemical force microscopy with name, grafting conditions, and structure.

Name	Grafting	Structure
1 (3-glycidoxypropyl) trimethoxysilane --epoxysilane--	2 hours (1% solution)	
2 (3-aminopropyl) trimethoxysilane --aminosilane--	30 minutes (1% solution)	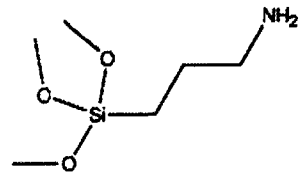
3 Octadecyltrichlorosilane --OTS--	3 hours (1% solution)	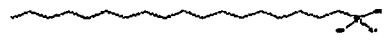
4 (3-cyanopropyl) trimethoxysilane --cyanosilane--	2 hours (1 % solution)	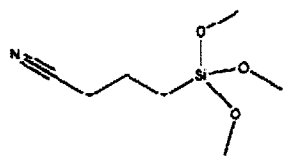

Because the coating procedure involves multiple steps and several rinsings, the tips are immobilized by wedging them into pipette tips with one end cut off with a razor blade (Figure 2-7).

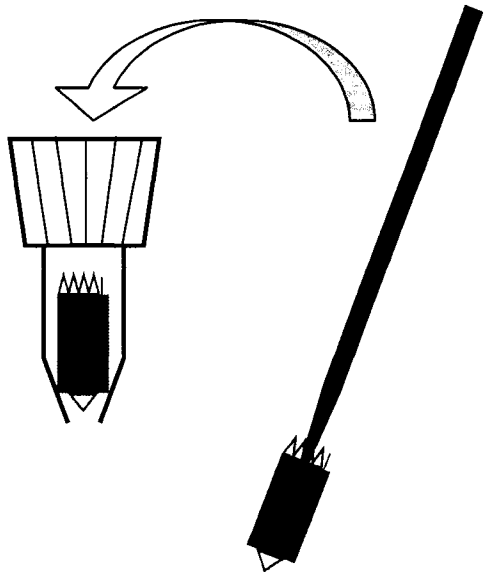

Figure 2-7. Placing the AFM tip into a plastic pipette tip that can be safely transferred into multiple solutions. Notice the end of the pipette tip is cutoff to enable better fluid flow of the solutions.

The tips are cleaned and rinsed in chloroform and, and the entire ensemble is placed into the coating solution, which is contained within small glass vials that are cleaned as described above. All of this is carried out inside a nitrogen glovebox with less than 1% humidity. All solutions are 1% in anhydrous toluene. Once modified, the tips are stored in toluene until the experiment.

Nanotube growth was carried out on freshly cleaned silicon wafers by CVD of pyrolyzed ethylene as a carbon source (Figure 2-8).[12] The catalyst was wet deposited by immersing the clean, dry silicon wafers in a solution of iron(III) nitrate (5 % in 2-propanol) for 30 seconds while in a sonication bath, then rinsing in 2-proponal, followed by a rinsing in hexane, followed by drying with a N_2 gun. The modified wafers were placed in the CVD oven (Fig. 2-8), and baked at 850°C for 10 minutes under only an Argon and Hydrogen gas flow. After this 10 minutes, the precursor gas (ethylene) was turned on for 2-10 minutes (depending on what desired length of nanotube was to be), and then the system was allowed to cool to room temperature, and the samples were removed.

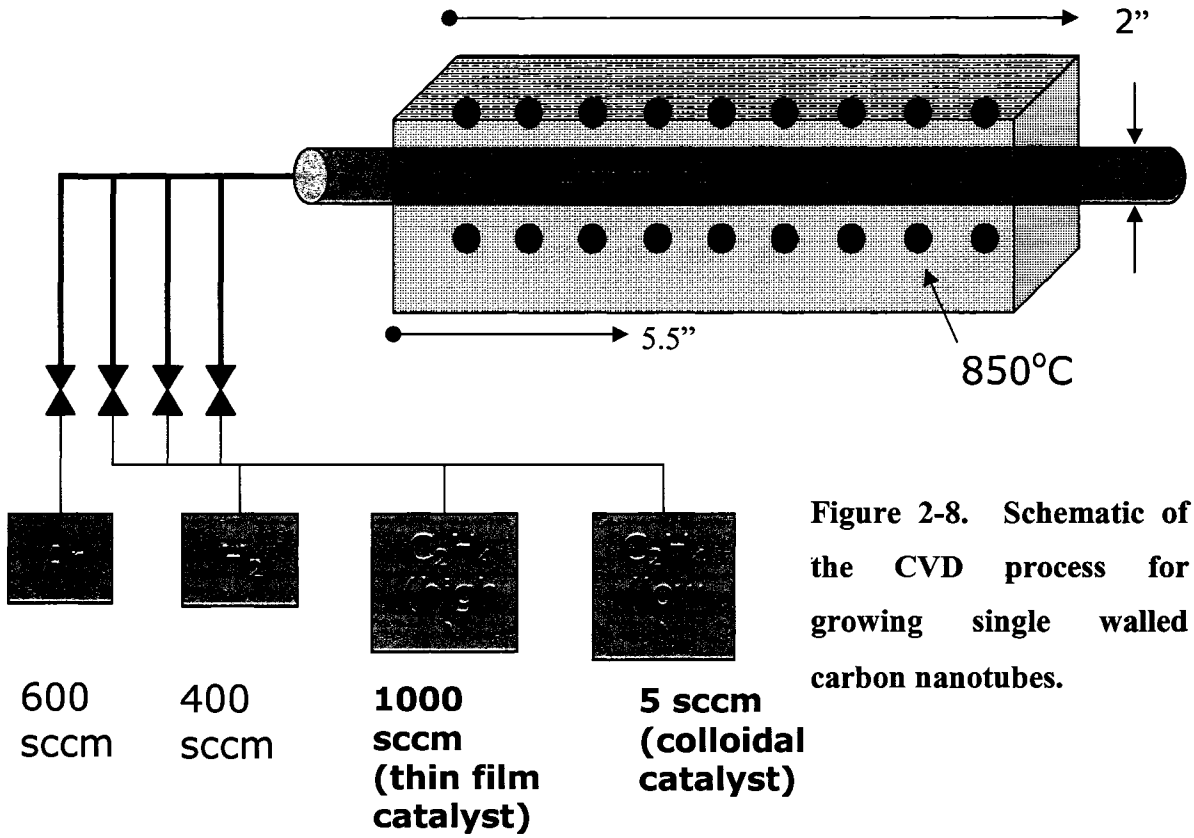

Figure 2-8. Schematic of the CVD process for growing single walled carbon nanotubes.

2.4 Fabrication: "Wet Approach" with Grafting To

This involves the 'grafting to' approach of fabricating binary polymer brush layers as SRMs on silicon wafers. Full detailed sample preparation along with chemical formulas and structures are given in Chapter 4.

2.5 Fabrication: "Wet Approach" with Grafting From

Chapter 4 involves the 'grafting to' and 'grafting from' approach of branched polymer brush layers as SRMs. These samples were fabricated via UV-initiated polymerization, and full detailed sample preparation along with chemical formulas and structures are given in Chapter 5. However, the actual setup of the UV chamber is shown in

Figure 2-9. As shown, the wafer is placed inside the rectangular quartz test tube sealed with the rubber septum. Once the monomer solution is injected via syringe, the wafer is exposed to the UV lamp, and the SRM is fabricated on the silicon wafer.

Figure 2-9. At top is a digital image of the overall setup for UV-polymerization. The light source and sample were placed inside a sealed chamber dark chamber with a cooling fan (to keep sample at constant temperature). The sample was coupled to a stand that could be moved along a marked slider for precise distance positioning of the sample from source (bottom left). At bottom right is a close up digital image of the sample (silicon wafer) in-situ during UV-initiated polymerization.

2.6 Fabrication: "Wet Approach" with Grafting To Nanocomposites

The work in *Chapter 7* involves the wet fabrication of active sensing composite nanolayers on metallic (gold) coated cantilevers. For this, the cantilevers were mounted on supports as shown in Fig. 2.1. The grafting scheme employed in this chapter mimics Scheme 1 in Fig. 2-6 in which the composite SRM was covalently grafted via a linker thiol-SAM. In this case, the SAM was Cysteamine because this particular molecule is thiol (-SH) terminated at one end for attachment to gold, and amino ($-NH_2$) terminated at the other end to facilitate grafting of polymer. The formula for Cysteamine is $SH-CH_2-CH_2-NH_2$. The composite layers where then fabricated as depicted in Figure 2-10. Di-thiol functionalized polystyrene (PS) was attached to the linker via the NH_2 – SH reaction. Then, the other end of the di-thiol PS was covalently attached to NH_2 terminated nanoparticles, or –COOH terminated carbon nanotubes. Finally, in some cases, a topmost polymer layer of Poly(acrylonitrile) (PAN) is added. PAN had terminal COOH groups that could react and bond with residual nanoparticles/nanotubes or di-thiol PS (Fig. 2-10). All other specific molecular weights and structures are given in Chapter 6.

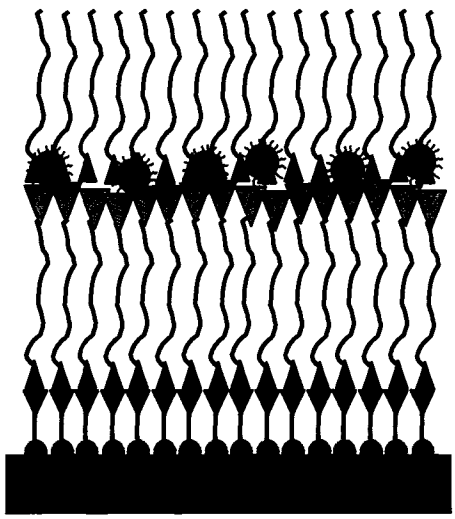

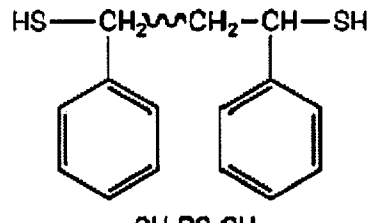

SH-PS-SH

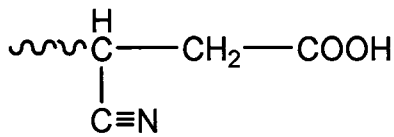

PAN-COOH

Figure 2-10. Schematic of nanocomposite SRMs fabricated on microcantilever sensors (see Chapter 6). The nanocomposites are functionalized polymer and nanoparticles (shown) or nanotubes. The functionalized polymers used (right) are di-thiol-PS and COOH terminated PAN.

2.7 Fabrication: Interference Lithography

This fabrication including all materials and the laser interference setup, took place at MIT's Institute for Soldier Nanotechnology (ISN) Center. All procedures, schematics, chemical structures, and formulas are given in Chapter 6 (for 2D structures) and Chapter 7 (for 3D structures).

2.8 Fabrication: "Dry Approach" with PECVD

In order to be compatible with microfabrication processes, a "dry approach" (solvent less) was used to deposit the SRM as active sensing nanolayers. For this work, plasma enhanced chemical vapor deposition (PECVD) was used to deposit gas phase organic monomers on suitable substrates and cantilevers sensors. The PECVD chamber was built and housed at Wright Patterson Air Force Base in Dayton, Ohio. All procedures, schematics, chemical structures, and formulas are given in Chapter 8.

2.9 Characterization Methods

2.9.1 Contact Angle Measurement

One of the most sensitive methods that provides information on the outermost polymer surface (top molecular layer) is the contact angle technique (Figure 2-11). The measurement supplies the properties characteristic of polymer surfaces such as wettability, roughness, heterogeneity, composition, relative surface energy, and surface mobility.[13] It is a relatively simple, inexpensive, and popular technique for characterizing surfaces. There are two types of the contact angle; static and dynamic. A static angle, which is determined by the equilibrium of interfacial tension, is formed at a stationary liquid front. A dynamic contact angle, which is determined by the balance of the interfacial driving force and the viscous retarding force, is formed at a moving liquid front. Hence dynamic contact angles are rate-dependent. Static contact angle was used in this project and can be analyzed in the

terms of "apparent" surface coverage or the fraction of silicon surface screened by a film, β. The Cassie equation assumes a simple "two-phase" model of surface structure and provides the relationship.[14]

$$\cos(\theta_m) = \beta \cos(\theta_L) + (1-\beta)\cos(\theta_{si})$$

Where θ_m is measured contact angle, θ_L is contact angle for a complete layer, and θ_{si} is contact angle of bare silicon.

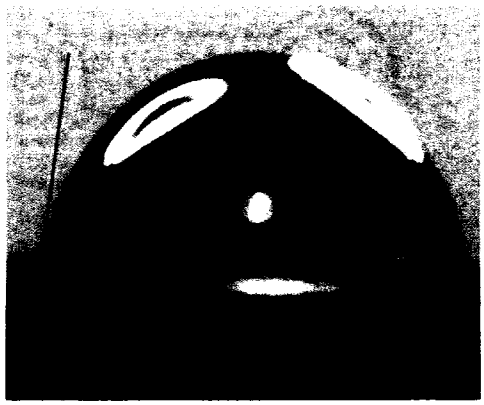

Figure 2-11. Picture depicting how the contact angle is captured and measured on a polymer modified silicon surface.

In this work, film surfaces are examined by static contact angle (sessile droplet) measurements using a custom-designed optical microscopic system. Droplets (4 - 10 μl) of Nanopure water droplets are placed randomly over the surface. Contact angles were determined within one minute after droplet deposition. All reported values were an average of at least six measurements. The shape of the drop is observed with a microscope equipped with a digital camera (Figure 2-12), and the contact angle was measured using image analysis software.

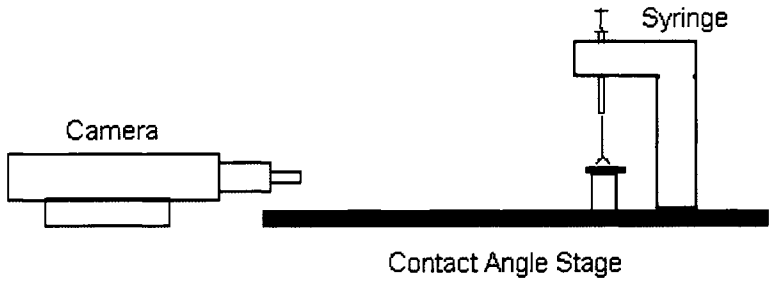

Figure 2-12. The contact angle setup.

2.9.2 Ellipsometry

Ellipsometry (COMPEL Automatic Ellipsometer from InOm Tech, Inc.) was used to measure the dry thickness of polymer brush layers. Ellipsometry is a non-destructive optical technique, which deals with the measurement and interpretation of changes of the polarization state of polarized light undergoing oblique reflection from a sample surface. The quantities measured by an ellipsometer are ellipsometric angles Ψ and Δ which are related to the complex ratio of the Fresnel reflection coefficients R_p and R_s for light polarized parallel (p) and perpendicular (s) to the plane of incidence such as

$$\rho = R_p / R_s = \tan \Psi \exp(i \Delta) \quad \textbf{(10)}$$

The complex reflectance ratio ρ is completely determined by an amplitude ($\tan \Psi$) and a phase Δ and characterizes the differential changes in amplitude and phase. These changes are related to a transformation of a shape and orientation of the ellipse of polarization, respectively.

Figure 2-13 illustrates the schematic diagram of ellipsometry and sample structure model. In order to deduce unknown parameters of a sample under investigation, a model for the sample structure is first constructed with initial estimates of the parameters. These parameters (e.g. thickness and refractive index) are then varied to generate a set of calculated Ψ^{exp} and Δ^{exp}. The initial parameters of the model parameters are transformed finally into true parameters of the sample, such as thickness and optical constants.

In this project, the film thickness was determined by ellipsometry with an angle of incidence of 70°. The silicon oxide thickness was measured for each silicon wafer after the piranha solution treatment and before film deposition. The thickness of the silicon oxide layer was determined to be within 0.8 - 1.2 nm for different wafers. The index of refraction of the silicon oxide was considered to be equal to the "bulk" value of 1.429.[15] Refractive index for all other materials used in this work are given in individual Results chapters (3-8). All

reported thickness values were averaged over six measurements from different areas of the substrate.

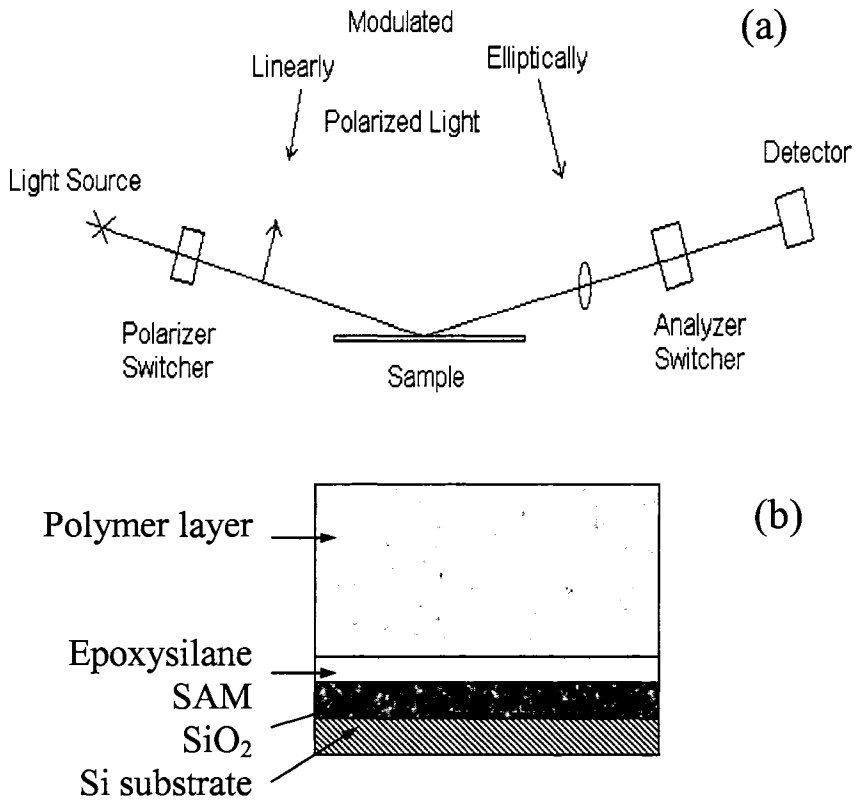

Figure 2-13. Schematic of the ellipsometry set up (a) and an example model of a typical surface measured that is specific to the work in this thesis (b).

2.9.2.2 Thermal Expansion with Ellipsometry

Because of the supreme accuracy of ellipsometry to measure thin film thickness (within ±0.1 nm from the same location), this technique can be used to measure the linear thermal expansion coefficient of organic SRMs. In this case, the sample is mounted on a heating stage that is placed on the Ellipsometer stage (Fig. 2-13). The sample is heated, allowed to equilibrate for 10-20 minutes, and the thickness is measured, and this is repeated at each temperature interval. The expansion coefficient (α) is then obtained with the usual formula: $\alpha = L_0\Delta T/\Delta T$. Each value of α obtained by this method was obtained from

averaging three cycles together, only after the sample was annealed for 24 hours at 50° - 100°C in a vacuum oven.

2.9.3 Atomic Force Microscopy

Determining the morphology, nanotribological, and nanomechanical properties of the polymer brush surfaces with nanometer resolution will be done using both the Dimension 3000 and the Multimode microscopes (Veeco Inc., Santa Barbara) (Figure 2-14). The heart of the AFM is a cantilever with a micro-fabricated tip that deflects a focused laser when interacting with the sample surface. This deflection is detected by optical methods onto a photodiode position sensor that can translate both normal and lateral deflection signal.

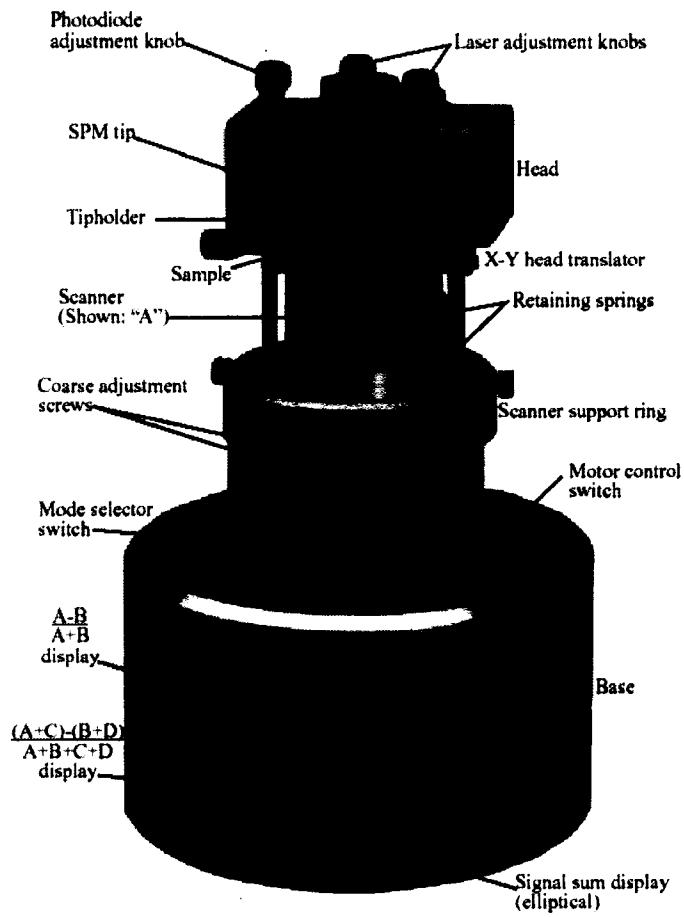

Figure 2-14. The Dimension 3000 AFM (center, left picture) with controller and other hardware. At right is a labeled drawing of the complete multimode AFM (including head and scanner), which is about 12 inches tall (www.veeco.com)

A feedback loop is maintained by a controller that regulates, collects, and processes the data (signal), and drives (or adjusts) the scanner according to pre-set conditions (Figure 2-15). The feedback loop maintains a constant force on the sample by adjusting the height of the cantilever to compensate for topographical features. The result is a three-dimensional map of the sample surface with nanometer resolution allowing for quantitative analysis of the surface roughness.[16] There are two basic modes of operation with the AFM: contact mode and tapping mode.

In contact mode AFM, the tip is dragged across the surface with constant velocity and normal load, always remaining in intimate contact. As the tip is scanned across the features, it encounters hills and valleys that will vertically deflect the cantilever up and down.

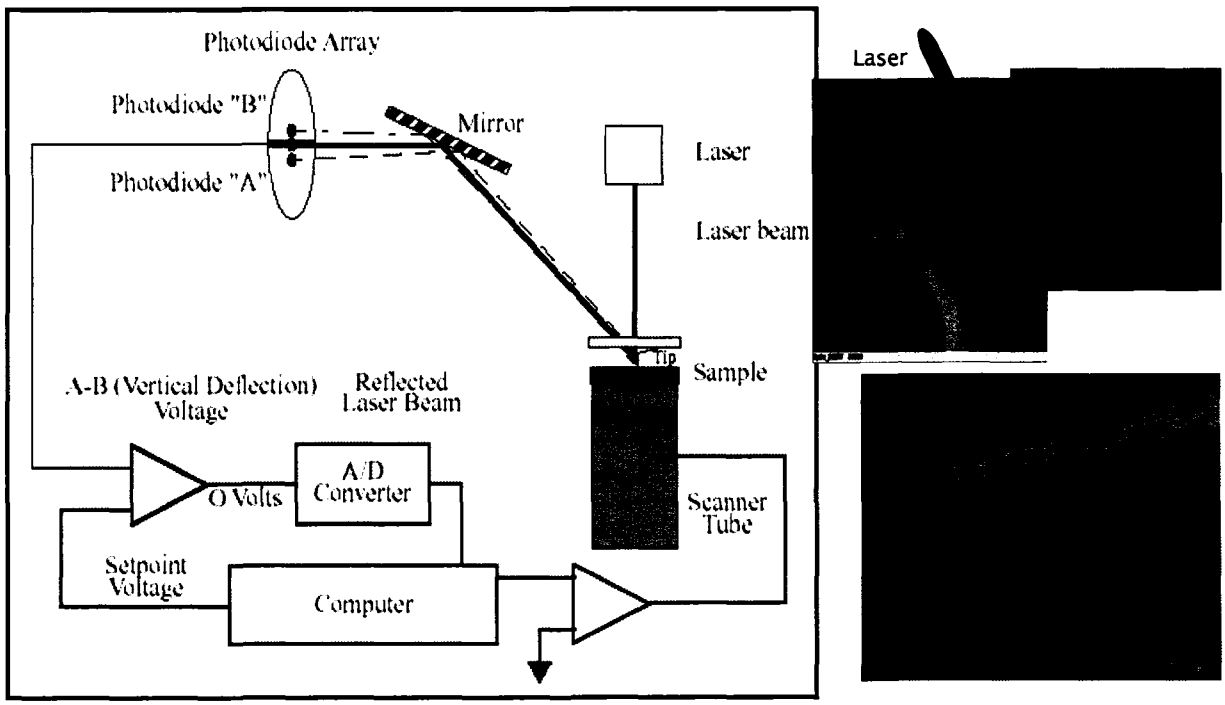

Figure 2-15. Left: The feedback loop of the AFM with the optical detection scheme. Inset is an SEM image of an AFM cantilever (backside and tip) and a schematic demonstrating how the laser is deflected off the backside of the cantilever onto the photodiode detector.

The feedback system attempts to maintain a constant level of cantilever deflection, and this difference gives rise to features in the image (Figure 2-16). The horizontal deflection in contact mode is used to monitor the friction signal in lateral force microscopy (LFM).

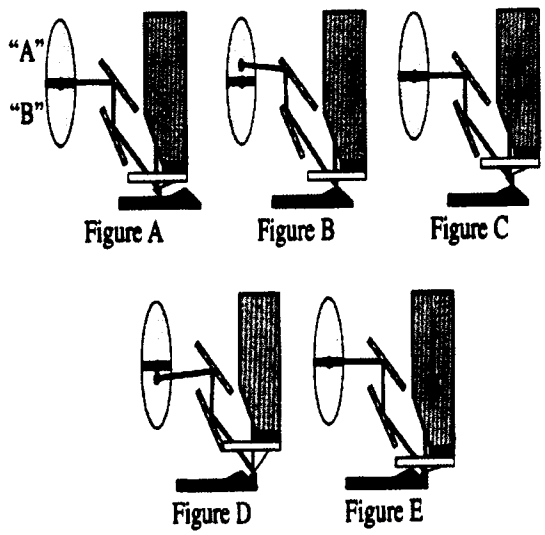

Figure 2-16. Contact AFM Concept. (a) The tip scans a flat position, maintaining the laser beam at the center of the photodiode array. (b) As the tip encounters a raised feature, the cantilever is pushed up, deflecting the laser beam upward. (c) The Z piezo retracts, the cantilever re-centers the laser beam onto the photodiode array. (d) Tip encounters a decline in the sample topology, the cantilever is pushed down, deflecting the laser beam downward. (e) The tip is pushed down until the laser beam re-centers on the photodiode array (A=B).

Contact mode allows for mapping of the surface features with high precision, and atomic scale resolution can be easily achieved. However, since the tip is dragged across the surface, even at very light loads, damage is inflicted upon soft polymer surfaces and the tip also becomes contaminated. Thus, contact mode is rarely used for imaging of polymer surfaces, unless in fluid conditions where forces are minimized.

Tapping mode AFM allows for the high resolution imaging of soft polymeric and biological samples without damage to tip or sample since contact with the surface is minimized. This is achieved by using specially designed probes that oscillate above the

surface at their resonant frequencies of 100 – 500 kHz. The oscillating tip is then moved toward the surface until it begins to lightly touch, or "tap" the surface. During scanning, the vertically oscillating tip alternately contacts the surface and lifts off, generally at a frequency of 100,000 to 500,000 cycles per second. As the oscillating cantilever begins to intermittently contact the surface, the cantilever oscillation is necessarily reduced (Figure 2-17) due to energy loss caused by the tip contacting the surface. The reduction in oscillation amplitude is used to identify and measure surface features. During tapping mode operation, the feedback loop attempts to keep the cantilever oscillation amplitude constant by adjusting the tip height to achieve the pre-set amplitude. This amplitude setpoint is adjusted before the scan by the user.

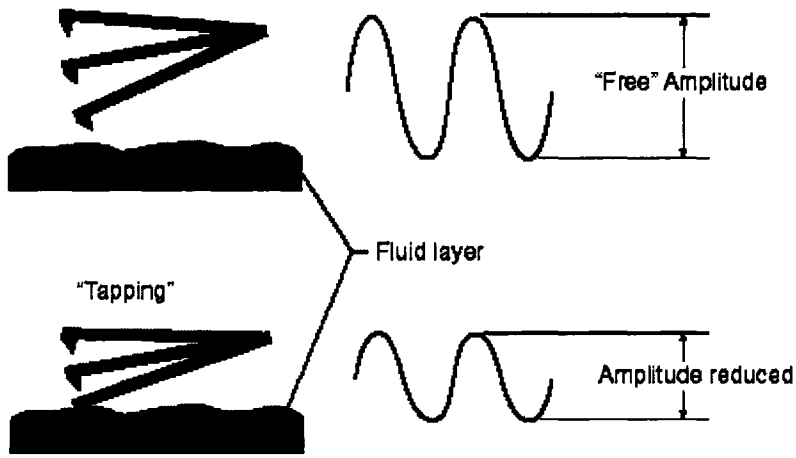

Figure 2-17. Tapping mode cantilever oscillation in free air (top) and near the surface (bottom).

Another imaging mode is possible with tapping mode AFM due to the fact that the phase angle with respect to the cantilever amplitude can change based on interactions with the sample. Although tip-sample interaction is very brief in tapping mode, energy is still dissipated into the sample. Since different materials will dissipate energy differently, phase imaging is used to map out different phases in a sample surface.[17] Major factors contributing to the phase contrast are adhesion, stiffness, and viscoelasticity. The

interpretation of phase images depends upon the amplitude setpoint, and is quite complicated.[18] Briefly, constituents in the surface with varying compliance, adhesion, and viscoelasticity will produce phase contrast. Phase imaging also is able to identify sub-surface domains.[19] For practical scanning, the setpoint ratio (rsp), defined as the ratio of operating setpoint (amplitude) to the free oscillating amplitude of the cantilever, must be taken into account for correct interpretation of phase images as was proposed by Magonov et al. in the terms of two regimes.[56] The attractive regime, or light tapping, is characterized by an rsp of 0.9 – 1, while the repulsive regime, or hard tapping, has rsp of 0.4 – 0.7. In light tapping, the tip sample interaction is strongly influenced by adhesion and the phase shift is greater on the surface with areas of higher attractive forces whereas in the hard tapping regime the elastic response becomes predominant.[20]

A major advantage of AFM is that scanning can be conducted in the ambient, under vacuum, and in a fluid environment. In this work, scanning was done both in ambient and fluid conditions (for scanning in fluid, contact and tapping mode AFM was used). Scanning in fluid gives the advantage of imaging polymer brush layers in their native state while exposed to organic solvents of different quality. Scanning in fluid minimizes forces exerted on the sample by the tip, as well as eliminating capillary and adhesion forces at the tip/sample joint. However, this is not an easy scanning method, and several steps must be followed for quality images to be obtained. In this work, fluid scanning was only done with the Dimension 3000 AFM.

- The tip is inserted into the clean fluid holder and the sample is securely mounted. Double scotch tape can be used to hold the sample if it is assured that no solvent will come in contact with it. In some cases, since small samples were used, the sample had to be clamped down due to solvent spilling over the sides of the sample and underneath it, thus dissolving the scotch tape. All surfaces should be clean since even small contamination will dramatically affect results. The fluid holder should be cleaned with detergent as organic solvents will destroy it. The AFM tip should be immersed beforehand into the pure solvent that scanning will be conducted in.

- After the laser is focused on the cantilever, the surface should be brought into focus. The position of the AFM head should be noted at this point because upon adding the fluid, the surface cannot be seen anymore.
- The tip is carefully lowered to a height of about 1 mm above the surface, and at this point, the fluid is added my using a micro pipette. Usually, about 20 – 40 μL of fluid should be adequate. When adding the fluid, care should be taken not to hit the sample or the tip holder with the end of the pipette. The fluid is held in place between the tip and the sample due to the capillary forces creating a meniscus between the two (Figure 2-18.)
- The photodiode will need to be readjusted after adding the fluid as the organic solvent changes the reflected path of the laser. After this, return the AFM head to the position noted in which the sample was in focus, and engage.

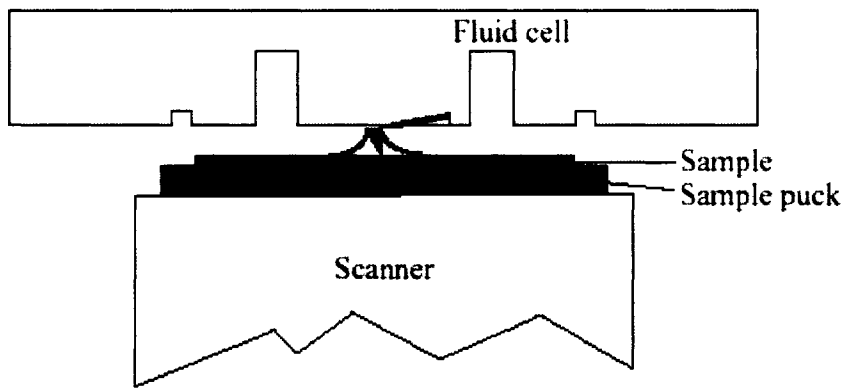

Figure 2-18. The liquid meniscus between tip and sample in contact mode AFM in fluid. From Veeco Tech Support note "Fluid Imaging".

- Additionally, as is the case in Chapter 5, scanning can be done both in fluid while simultaneously at temperatures other than ambient if the sample is placed on a Peltier Stage (Figure 2-19). Special precautions must be taken at higher temperatures as it should be understood that scanning time will be shorter due to faster evaporation of the fluid.

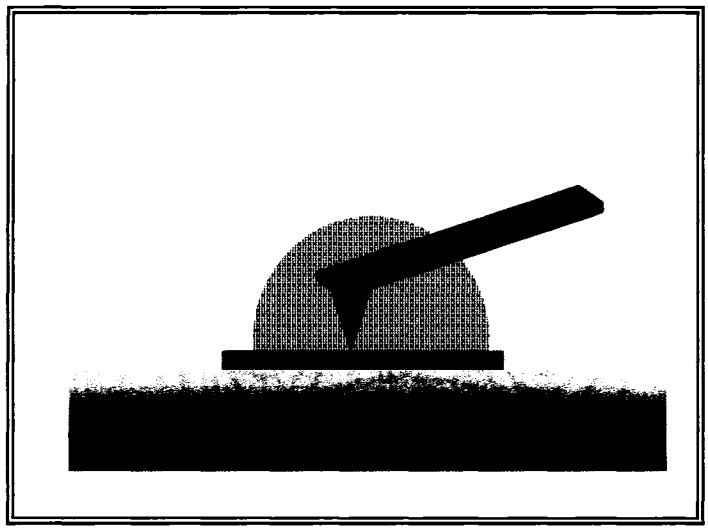

Figure 2-19. Diagram of the setup for doing AFM in fluid while being able to vary the temperature as well.

Previously, it was stated that thickness measurement of polymer layers can me executed with ellipsometry or AFM. The ellipsometry approach was described above. For thickness evaluation from AFM data, a "scratch" test is used. Scratches were produced with a sharp steel needle at different loads or by scanning multiple times with a stiff tip at high normal loads (several μN) in the contact mode. A 1 x 1 μm area of the surface is scanned in contact mode to remove the polymer layer, then a zoomed out tapping mode is executed and section analysis is done on this image to extract the thickness of the layer (Figure 2-20). This approach is used frequently for AFM scanning of organic and polymeric layers, and produces reasonable results comparable with ellipsometry.[21]

Force Volume is another capability of AFM and will be used significantly in this research to map the nanomechanical properties of the sample. A subdivision of contact mode AFM commonly denoted as Scanning Force Microscopy (SFM), it has been shown to be a valuable tool for quantifying adhesion and elastic properties of heterogeneous surfaces of polymer layers on the nanoscale.[22, 23] This mode utilizes the force distance curve (FDC) (Figure 2-21) of the SFM.[24] A single FDC records the forces felt by the tip as it approaches to and retracts from a point on the sample surface. SFM allows a 16 x 16, a 32 x 32, or a 64

x 64 array of FDCs at unique XY coordinates over a pre-set sample area (Figure 2-22).[25] Thus, it essentially is a series of nano-indentations into the polymer layer. This allows for mapping of the mechanical properties (adhesion, elastic modulus) of polymer surfaces with

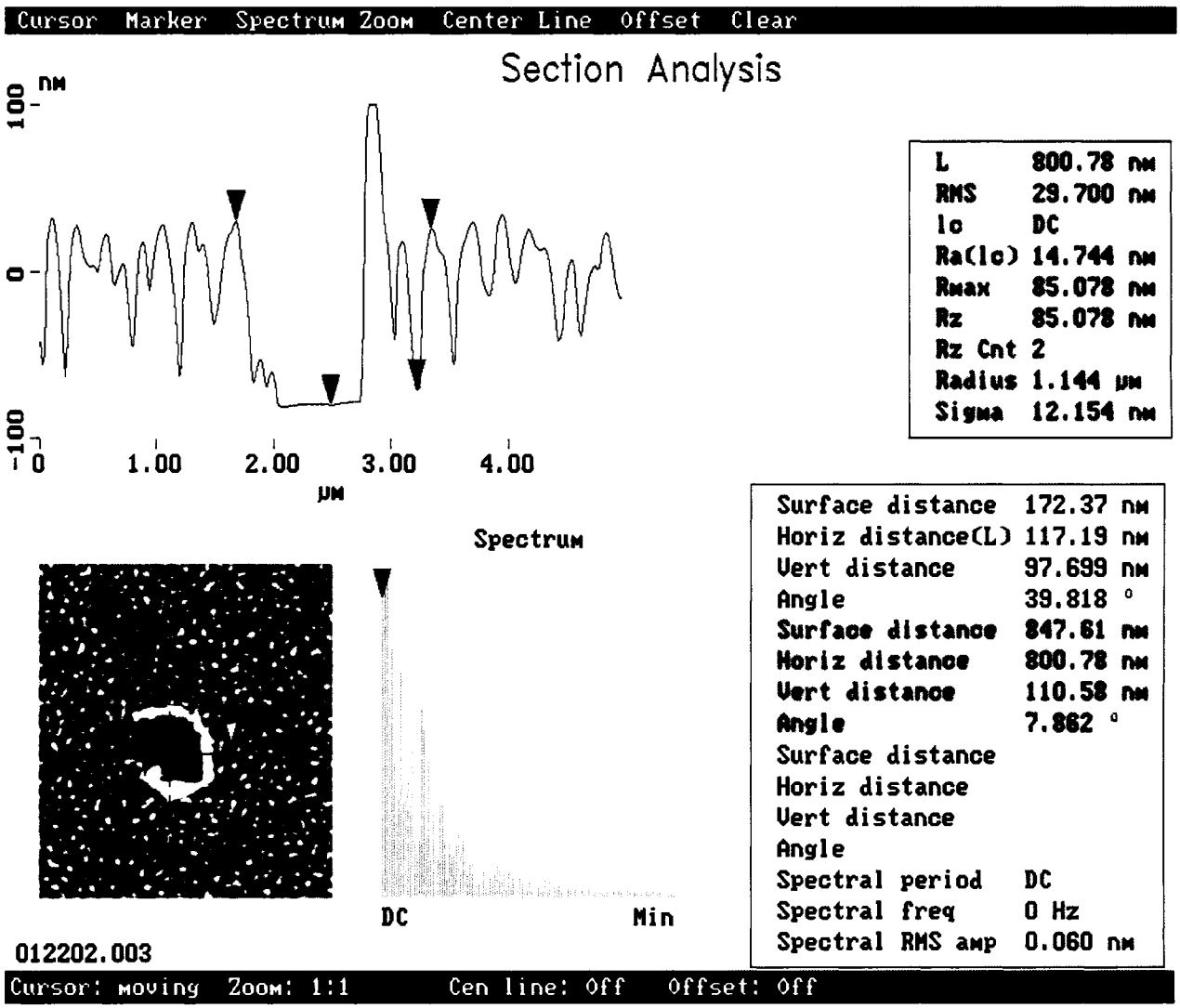

Figure 2-20. Actual raw data showing how the thickness of a SRM can be measured independently with AFM, as long as a portion of the substrate can be scanned as well in the same image as the reference depth.

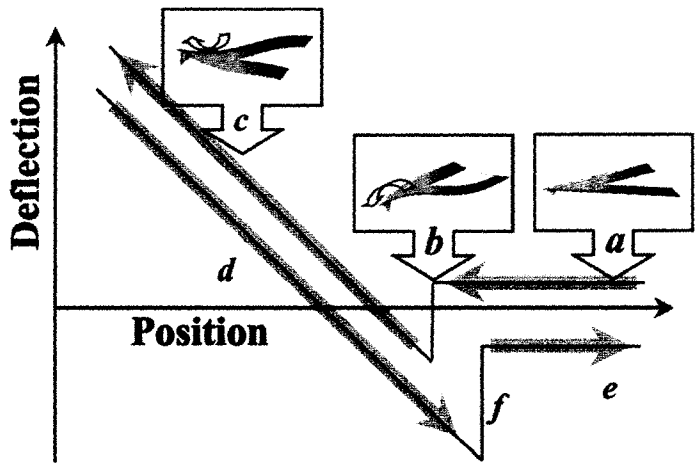

Figure 2-21. Components of an FDC (from Ref. 25). During segment (a), the tip approaches the surface; segment (b) is the jump to contact on the surface; during segment (c), the upward deflection of the tip is occurring from pressing on the surface; withdrawal of the tip takes place during (d). If both (c) and (d) are not straight, plastic and elastic deformation behavior can be arrived at. Finally, at segment (f), the tip snaps out of contact with the surface when the restoring forces of the cantilever exceed the adhesion between tip and sample. Note: in AFM the red curve is commonly referred to as the approaching cycle, while the blue curve is the retracting cycle.

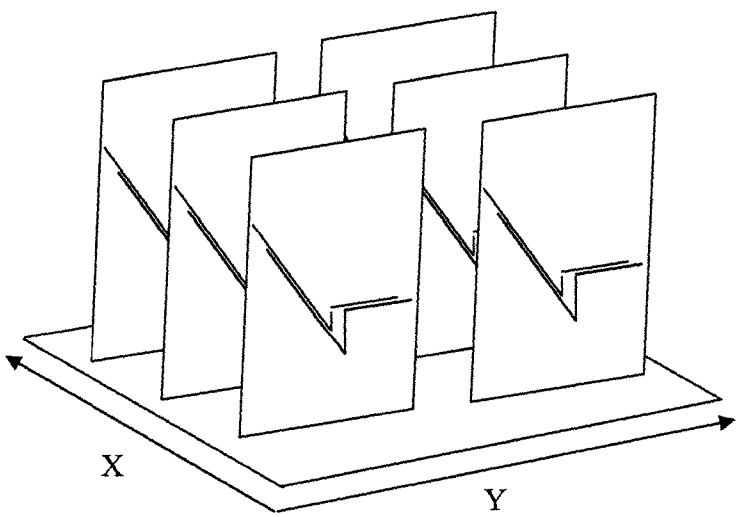

Figure 2-22. Force volume imaging can be regarded as simply obtaining a distribution of force distance curves (from Ref. 25).

nanometer scale resolution, while obtaining topographical information simultaneously. The applied normal load and speed of the nano – indentations are critical parameters to control in force volume. SFM will be done at ambient and elevated temperature using a Digital Instruments thermal stage or thermal controller. The elevated temperature range was up to 120°C, which is limited as the safe working temperature for the AFM piezo. A problem that was encountered with force volume at high temperatures was sample stability. Originally, the brush layer was secured with double scotch tape, which lost resistance at the higher temperature resulting in sample movement and erroneous force volume data. Thus, the sample was tied down with Teflon tape over the heating element of the thermal stage. This practice alleviated the sample movement problem. Force volume also took place in fluid of which will be either a good or a bad solvent for the brush sample of interest.

Data collected were processed using a micromechanical analysis (MMA) software package developed in our lab which provides means for calculation of localized elastic modulus, depth profiling of the elastic modulus, reduced adhesive forces, and surface histograms of elastic moduli and adhesive forces from experimental images as described elsewhere.[26] The MMA utilized Hertzian, JKR, and Sneddon models of solid contacting bodies to derive this data. For absolute quantitative results of the adhesion and elastic modulus from force volume data, the normal spring constant of the tip as well as the radius had to be known with high precision, which is an extremely cumbersome task. Spring constants of cantilevers were determined from the resonant frequencies and the tip-on-tip method according to the procedures described earlier.[27, 28] Tip radii were evaluated with scanning of reference gold nanoparticle specimens in combination with a deconvolution procedure.[29, 30]

It should be noted that tips used in AFM are made of either silicon or silicon nitride. For contact mode and imaging in fluid, tips should be very soft with spring constant less than 0.5 N/m. Fluid imaging tips are usually gold coated for high reflectivity to assure the signal of the laser of the photodiode is large enough. Force volume tip selection is a very critical and the stiffness of the tip used depends upon the expected mechanical response of the surface. It has been determined that only a small range of cantilevers, in terms of spring

constant and, hence, local pressure, are applicable to probe the surface nanomechanical properties of a given polymer (Figure 2-23).[31] In general tips for MMA had radius of 15 – 60 nm, and spring constants ranging from 0.5 to 10 N/m. Tapping mode AFM tips had spring constants ranging from 20 – 50 N/m. Typical tapping mode scans are 1 x 1 μm to 50 x 50 μm with scan rates of 0.8 – 3 Hz and data are. The image is put together with either 256 x 256 or 512 x 512 pixel points. For high resolution tapping mode image, 900 x 900 nm to 100 x 100 nm scans were taken at 512 x 512 pixel resolution, with scan rates of 0.5 – 1.0 Hz.

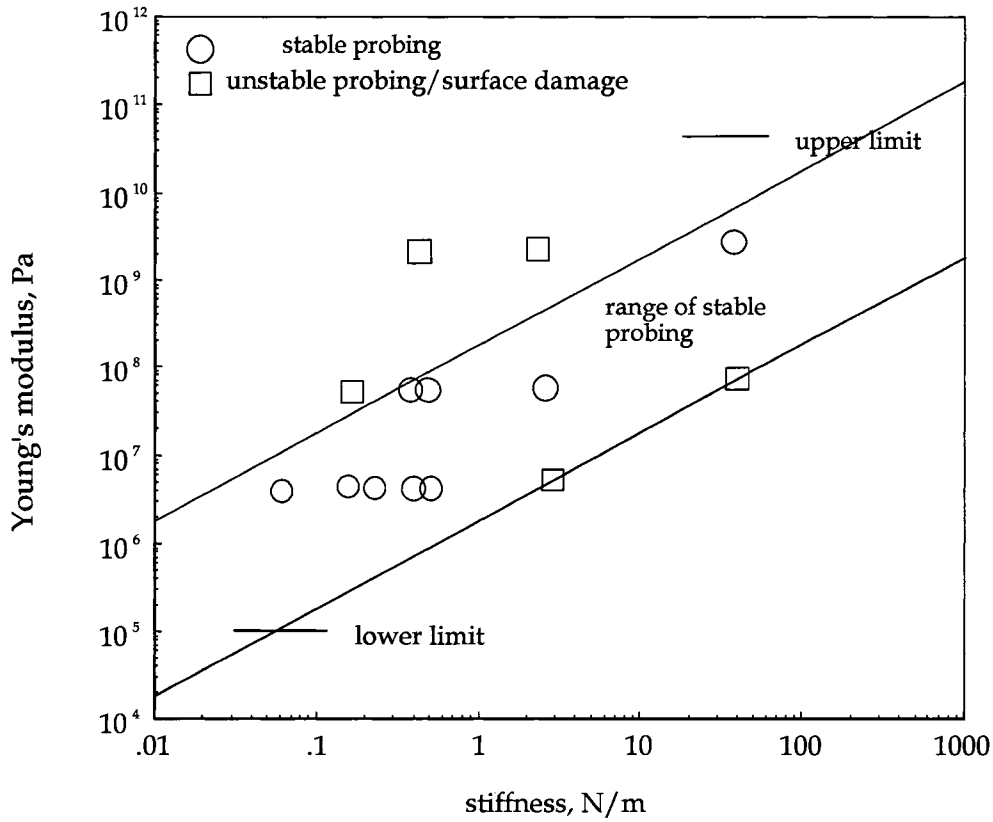

Figure 2-23. The plot shows the relationship of sample stiffness versus tip stiffness for micromechanical mapping. Such a plot is used for tip selection in force volume probing.

Before any quantitative force measurements can be considered respectable and accepted, there is a rigorous process of calibrating all tip parameters including tip geometry and normal spring constant of the cantilever. Unfortunately, many researchers 'accept' the manufacturer's specifications of the tip including tip radius and normal spring constant. However, in reality, these values are not only different, but sometimes can be more than 100% inaccurate, yet many results using this bad practice are published.

The first to do is calibrate the entire system (tip, scanner, photodiode) in terms of nanometers of deflection per voltage applied to the feedback loop. This is done by calibrating the sensitivity of the tip. To do this, a force-distance curve is acquired from bare silicon in air (if you are doing your measurements in fluid, then calibrate sensitivity with bare silicon while in the respective fluid). The forces should be kept minimal, thus the lowest relative trigger possible to get a legitimate force distance curve should be used (usually 3-5 nm for tips with k_n <1, and usually 1nm for tips with k_n >1). A typical force curve on silicon appears in Figure 2-24, and to calculate the sensitivity, as it says in the figure, click and drag a line overlapping, or parallel to the curve.

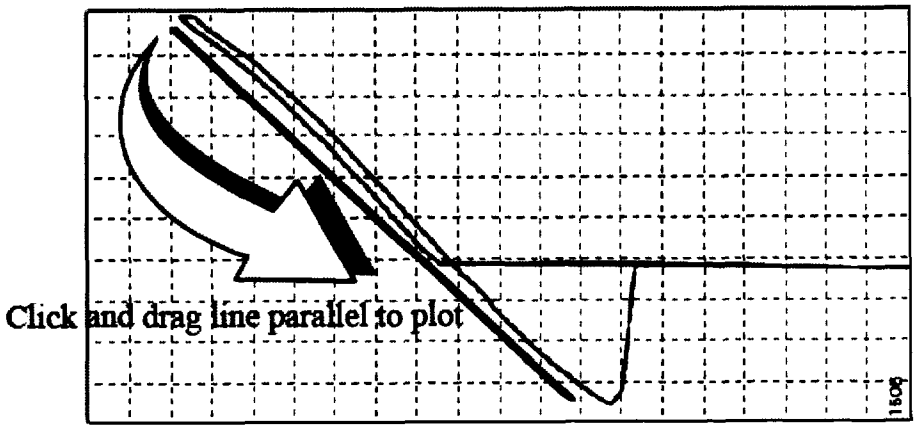

Figure 2-24. Sensitivity calibration procedure, which will give a value in nm/volts, or the inverse depending on the software version. Taken from Veeco manual.

The next step is to calculate the tip radius. While this should be done for all scanning, it is especially important in force mode for correct application of contact mechanics models. The tip radius and geometry is calculated by scanning a reference gold nanoparticle sample (at $1x1\mu m^2$) as described above, and deconvolution of the results in the MMA software program (Figure 2-25).[29,30]

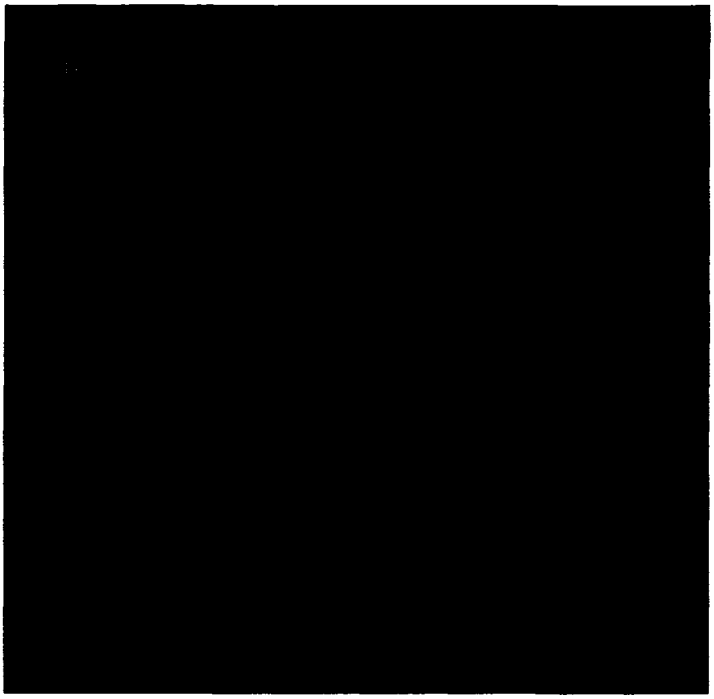

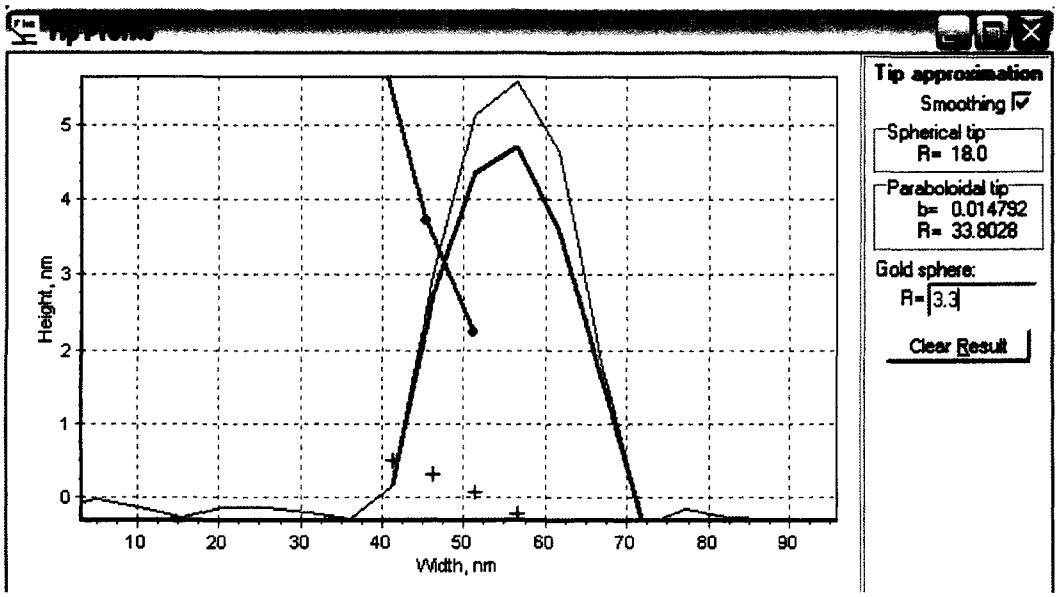

Figure 2-25. At left is an AFM image of the gold nanoparticle surface opened in the MMA program. A line is drawn (in red here) to get the line profile section analysis, and the results are given (below).

It is common for the tip to become completely destroyed or deformed from the sensitivity measurements, especially with a higher nominal tip spring constant, and if the success rate is better than 30%, the user may consider themselves very lucky. To this end, typically force measurements are conducted with Si_3N_4 tips as these are tougher than bare silicon. However, even with these tips, success rate still hovers around 40-50%.

For quantitative values of modulus and adhesion with force imaging, the last step is to calibrate the spring constant. This is done with the tip on tip method in our lab (Figure 2-26).[32]

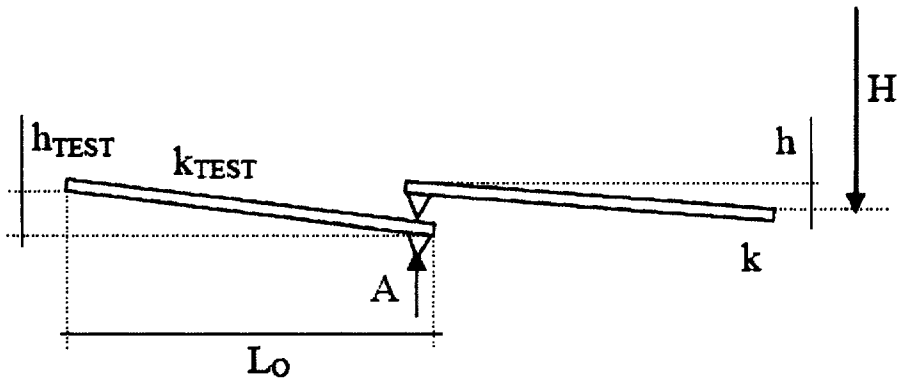

Figure 2-26. The bottom cantilevers is of 'known' spring constant, while the tip one is the one we are trying to calibrate. Taken from our MMA manual.

The tip with known constant (usually purchased from NTMDT at $50/tip, and they are rectangular in shape) is mounted in an extra AFM tip holder upside down, and the unknown cantilever with which force measurements are to be done with is brought into contact on the backside of the known cantilever. Force-distance curves are obtained and the processed in the MMA software, and the slope of the resulting load penetration (dh_{test}/dh) curves is needed. This value is multiplied by the known spring constant (equation below) to get the spring constant.

$$k \cong k_{TEST} \frac{dh_{TEST}}{dh}.$$

2.9.4 Thermal sensitivities with Atomic Force Microscopy and Optical Imaging

The thermal sensitivities of the microcantilever sensors were measured by determining their deflection per one degree temperature change (nm/°C). Sensitivities were measured over a small range and a large temperature range. The small range measurements were used to determine the extreme resolution of the sensors over a range of $\Delta T = 1$ or 2°C. Typically, this change in temperature corresponded to deflections anywhere from 100nm to 2μm, and while relatively large, this scale of deflection could be monitored by the photodiode in an AFM, which can measure deflections of a few angstroms with a straightforward optical detection scheme. In this case, the tip to be tested was placed in the AFM tip holder in the normal fashion with the laser aligned on the end of the tip. To calibrate the deflection of the system, the sensitivity of the modified cantilever (sensor) is measured on clean, bare silicon to get the calibration in nm/volt applied to the piezo.

For uniform thermal response, the cantilever was brought into a groove so that it would get an equal thermal flux from all sides. The groove was carved into the same mass of highly thermal conducting epoxy that was used to irreversibly adhere the thermistor to the Peltier temperature stage (Figure 2-27). The entire Peltier stage was then enclosed in a clear plastic chamber, along with the AFM piezo tube, in order to shield out all vibrations from air currents and noise (Fig. 2-27).

The thermistor was calibrated per manufacturer specifications[33], and the Peltier (Melcor) was fine tuned for the small temperature increments so that changes of 0.05°C could be made in less than one second with minimal temperature overshoot and quick settling time. At each temperature, the deflection of the cantilever was captured in force – distance mode. To ensure minimal artifacts from the instrument, the force-distance size was kept to 1nm with all triggering turned off. Z-rate was kept constant at 1 Hz for all measurements, data center was always kept at zero, and the force setpoint was always zeroed out before any data captures took place.

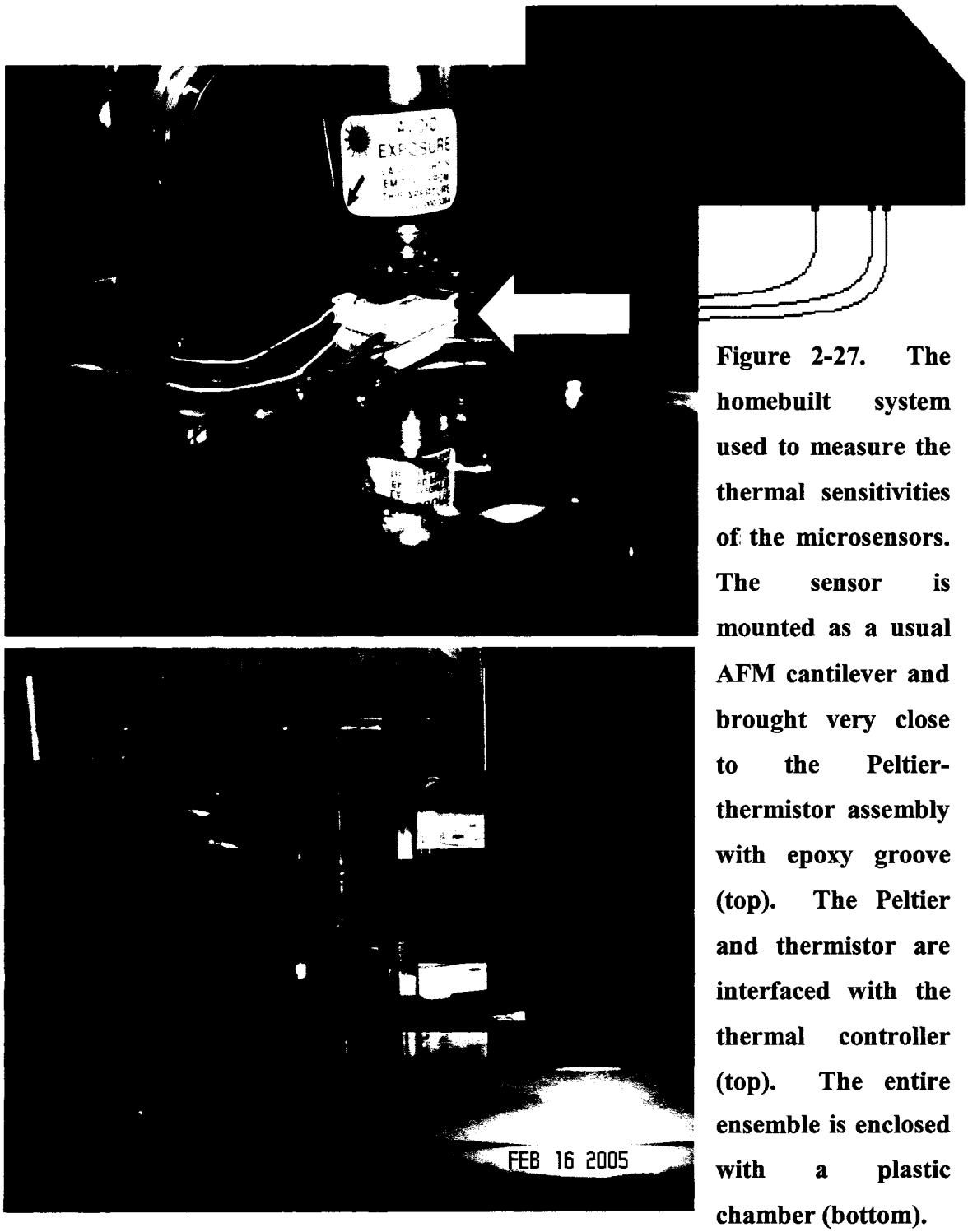

Figure 2-27. The homebuilt system used to measure the thermal sensitivities of the microsensors. The sensor is mounted as a usual AFM cantilever and brought very close to the Peltier-thermistor assembly with epoxy groove (top). The Peltier and thermistor are interfaced with the thermal controller (top). The entire ensemble is enclosed with a plastic chamber (bottom).

The response of the sensors to large scale temperature differences also needed to be determined. The deflections associated with this regime were too large for AFM, and were determined with a 400x optical microscope with a large focal length. In this case, the

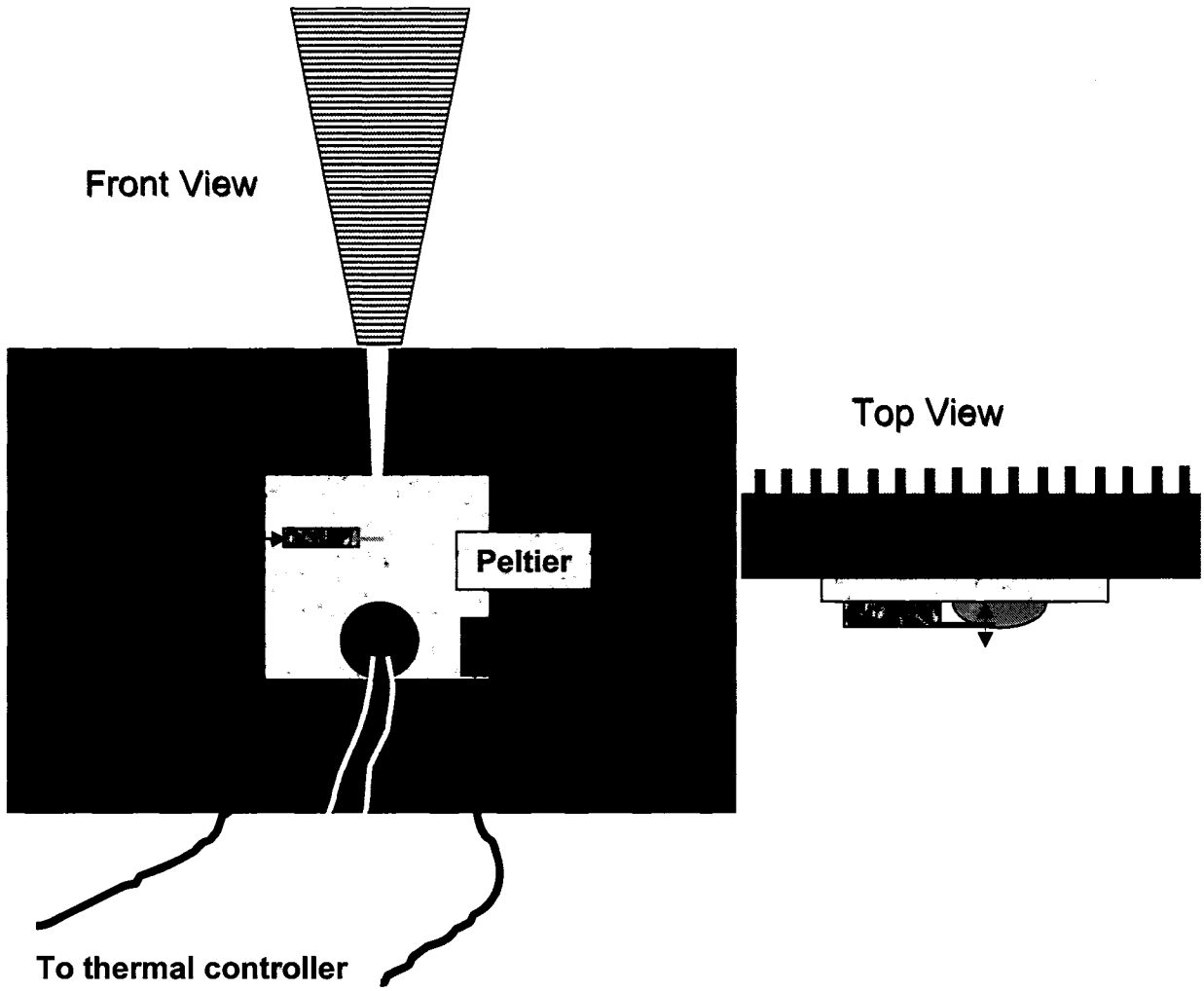

Figure 2-28. Front view (left) and top view (right) of the setup for optically recording the bending sensitivity of the microsensors to thermal response over large temperature range. The cantilever (mounted on the Peltier) motion is recorded by the optical microscope (top) and the signal is digitally recorded. Heat sink is mandatory for the wide temperature range or else Peltier will fail.

thermal setup (same thermistor, Peltier, and thermal controller) was mounted to a heat sink, and the tips were taped onto the end of the Peltier (Figure 2-28). Deflections at each temperature where digitally captured from the optical microscope, and converted into movies via Adobe Premier 1.5 software package. The scale bars were added by determining the number of pixels/μm of our homebuilt monitoring system.

2.9.5 Humidity Sensing

To test the response of the microcantilever sensors to water vapor, the sensors were placed inside an environmental chamber (Figure 2-29) in which humidity content could be controlled within 0.1% ('control' sensor mounted inside the humidity box, Fig. 2-29) and the setup for humidity monitoring is shown schematically in Figure 2-29. At the bottom of the Plexiglas chamber, an inlet valve allowed the controlled flow of water vapor by bubbling dry nitrogen through a glass bubbler containing roughly 50 mL of distilled water. The humidity sensor inside the chamber constantly monitored humidity, and the optical microscope recorded images at different humidity ranging from 5 – 70% Relative Humidity (RH).

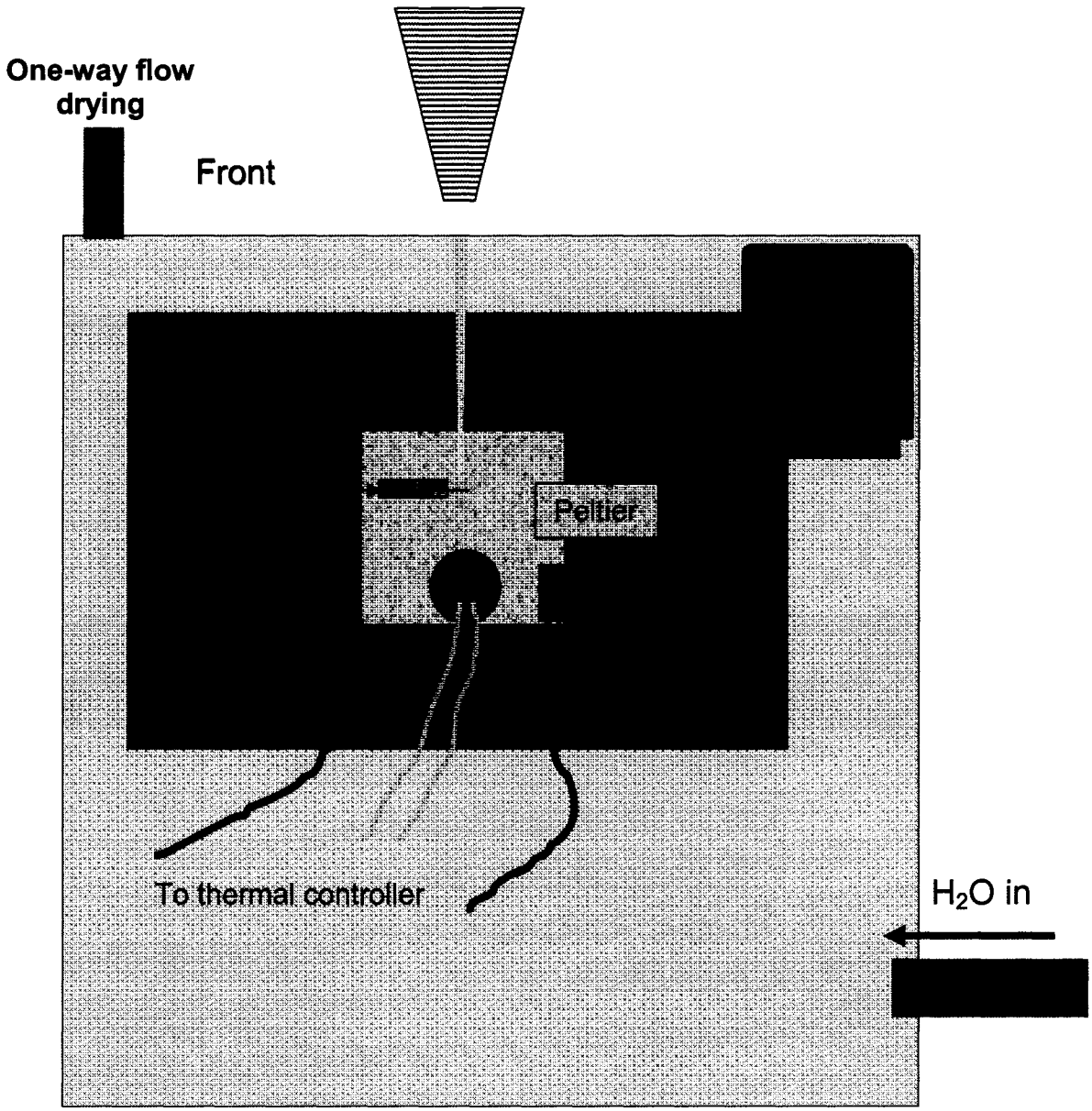

Figure 2-29. Front view (left) and top view (right) of the setup for optically recording the bending sensitivity of the microsensors to relative humidity response over large ranges. The cantilever (mounted on the Peltier) motion is recorded by the optical microscope (top) and the signal is digitally recorded.

2.9.6 Electric Field Testing

Response of SRM coated cantilevers to an electrical field was tested using AFM and custom built electrodes resembling parallel plate geometry (Figure 2-30). A copper substrate mounted on an insulating plastic platform was used as one of the electrodes, while the cantilever coated with the SRM forms the other electrode (as shown in the Fig. 2-30). The copper substrate was connected to a variable positive potential (Ominitron Electronics, XP-4A 0-15V) while the cantilever was grounded. The voltage applied was independently measured by a digital voltmeter connected in parallel across the cantilever and the copper plate. The copper plate under positive bias resulted in an electrical field equal to $E = v/d$ where v is the applied voltage and d is the distance between the cantilever and substrate. The distance of separation between the cantilever and copper substrate was controlled by the AFM Z-motor controls to be within 5μm. The deflection of cantilevers under various electrical fields was measured using force – distance mode, similar to the method described earlier for high resolution thermal sensitivity measurements with AFM.

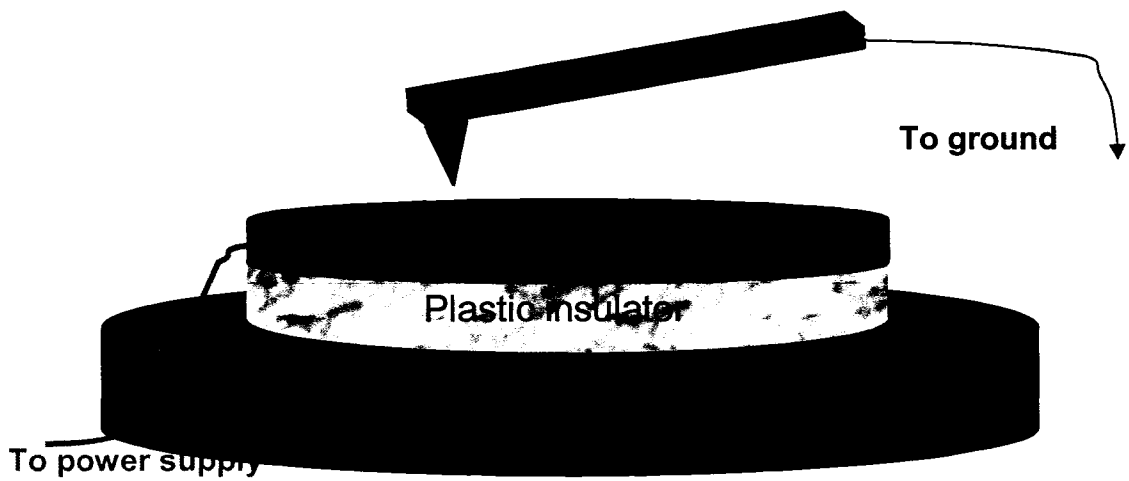

Figure 2-30. Diagram of the electric field testing of the microsensors. The entire ensemble was placed inside the MultiMode AFM, directly on the piezo tube as indicated.

Electrostatic force of interaction between two charges q_1 and q_2 is given by coulomb's inverse square law:

$$F = k\frac{q_1 q_2}{d^2}$$

where k coulomb's constant (= 9.0×10^9 $N\cdot m^2C^{-2}$). The electrostatic force was established using an uncoated cantilever (bare silicon) as a control. In the case of the polymer coated cantilevers the charged groups (if any) in the polymer layer are expected to contribute to additional forces thus leading to enhanced deflections. Furthermore, the electrostriction effects (conversion of the electrical energy to mechanical energy) in the polymer due to the electrical field also might lead to additional forces. It is important to note that the electrostriction effects become dominant in elastomers. Cantilevers coated with different polymers were tested to identify the presence of the charged groups.

2.9.7 μ-Raman mapping for stress distribution

The stress distribution along the length of the cantilever can be *directly* obtained by micro Raman mapping of the Silicon absorption peak at 521 cm^{-1}. Custom designed Raman setup based on a near-field scanning optical microscope (NSOM-Aurora-3 by Digital Instruments) was used for performing Raman mapping along the length of the cantilevers with resolution of 100nm. Excitation light from a Nd:Yag laser (532 nm) passes through variable attenuator and beam expander, and after reflecting off a 50:50 beam splitter is fed into the Aurora-3 NSOM. It is focused onto the sample surface by a high numerical aperture microscope objective (0.65NA). The final laser spot on the sample had a diameter of only 400 nm. The signal collected from the same objective passes through a notch filter and is focused on the entrance slit of an imaging spectrograph (SpectraPro SP-2558-W, Roper Scientific). The CCD camera (Spec-10:2KB, Roper Scientific) collects the spectra at every point of the sample. High-resolution spectra (0.32 cm^{-1} / pixel for 1800 mm^{-1} grating) were obtained from the Si surface of the cantilever along the length. The system was calibrated using a Neon lamp standard.

Raman spectroscopy is a unique technique for probing the stress in a material in a nondestructive manner as the lattice vibrations are sensitive to strain. The technique has been widely used for mapping internal stresses in materials such as silicon, carbon nanotubes.[34,35] It is well known that the Silicon peak occurs at 521 cm^{-1} which is sensitive to internal stress. The relation between stress and the Raman frequency is complicated, and a full explanation is beyond the scope of this thesis. However, as a rule of thumb, all non-zero strain tensor components influence the position of the Raman peak. A shift of 0.02 cm^{-1} in the Raman frequency equals a stress of 10 MPa for silicon. Compressive stress in the silicon results in up shift and a tensile stress results in a down shift of the Raman frequency. For each measurement, internal calibration (on the chip portion of the sensor with zero polymer and zero stresses) and spectrum for Si (100) material were obtained. The spectra were obtained along the length of the cantilever with a step of ~30μm and the spectra were recorded.

2.9.8 Other Techniques

Other supplemental techniques were used in this work outside of our research lab. These included FTIR, XPS, SEM, and Auger, and these techniques are explained in depth, were applicable, in the following chapters. Additionally, Finite Element Analysis was used in our lab (Comsol), and the details are explained in Chapters 8 and 9 were FEA was utilized.

2.10 References

1 Madou, M. *Fundamentals of Microfabrication.* CRC Press: Boca Raton, FL, **1997.**

2 Biebuyck, H.A.; Bain, C.D.; Whitesides, G.M. *Langmuir* **1994**, *10*, 1825.

3 Folkers, J.P.; Gorman, C.B.; Laibinis, P.E.; Buchholz, S.; Whitesides, G.M. *Langmuir,* **1995**, *11*, 813.

4 Tsukruk, V.V.; Lander, L.M., Brittain, W.J. *Langmuir,* **1994**, *10*, 996.

5 Tsukruk, V.V.; Luzinov, I.; Julthongpiput, D. *Langmuir* **1999**, *15*, 3029.

6 Nakagawa, T.; Ogawa, K.; Kurumizawa, T.; Ozaki, S. *Jpn. J. Appl. Phys.* **1993**, *32*, L294. Alley, R. L.; Komvopoulos, K.; Howe, R. T. *J. Appl. Phys.* **1994**, *76*, 5731.

7 Johnson, C. A.; Lenhoff, A. M. *J. Colloid Interface Sci.* **1996**, *179*, 587.

8 Tsukruk, V. V.; Bliznyuk, V. N.; Wu, J.; Visser, D. *Polym. Prepr.* **1996**, *37*, 575.

9 Bain, C. D.; Evall, J.; Whitesides, G. M. *J. Am. Chem. Soc.* **1989**, *111*, 7155. Bain, C. D.; Whitesides, G. M. *J. Am. Chem. Soc.* **1989**, *111*, 7164. Bain, C. D.; Troughton, E. B.; Tao, Yu.; Evall, J.; Whitesides, G. M.; Nuzzo, R. G. *J. Am. Chem. Soc.* **1989**, *111*, 321.

10 Frisbie, C. D.; Rozsnyai, L. F.; Noy, A.; Wrighton, M. S.; Lieber, C. M. *Science* **1994**, *265*, 2071.

11 Noy, A.; Frisbie, C. D.; Rosznyai, L. F.; Wrighton, M. S.; Lieber, C. M. *J. Am. Chem. Soc.* **1995**, *117*, 7943

12 Hafner, J. H.; Cheung, C. L.; Lieber, C. M. *J. Am. Chem. Soc.* **1999**, *121*, 9750.

13 Andrade, J.D.; Smith, L.M.; Gregonis, D.E. *In Surface and Interfacial Aspects of Biomedical Polymers, vol. 1.* Andrade, J.D., Ed. Plenum Press: New York, **1985**.

14 Elender, G.; Kuhher, M.; Sackmann, E. *Biosensors & Bioelectronics,* **1996**, *11*, 565.

15 Catalog, *Gelest, Inc.,* Tullytown, PA 19007, **1998**, p. 173.

16 www.veeco.com.

17 Binggeli, M.; Christoph, R.; Hinterman, H.E.; Colchero, J.; Marti, O. *Nanotechnology* **1993**, *4*, 59.

18 Maganov, S.N.; Cleveland, J.; Elings, V.; Denley, B.; Whangbo, M.H. *Surf. Sci.* **1997**, *389*, 201.

19 Berquand, A.; Mazeran, P.E.; Laval, J.M. *Surf. Sci.* **2003**, *523*, 125.

20 Magonov, S.N.; Cleveland, J.; Elings, V.; Denley, B.; Whangbo, M.H. *Surf. Sci.* **1997**, *389*, 201.

21 Sheller, N.B.; Petrach, S.; Foster, M.D.; Tsukruk, V.V. *Langmuir* **1998**, *14*, 453.

22 Ratner, B.; Tsukruk, V.V. *Scanning Probe Microscopy of Polymers.* Ratner, B.; Tsukruk, V.V., Eds.; ACS Symposium Series; American Chemical Society: Washington, D.C., **1998**; Vol. 694.

23 Tsukruk, V.V.; Wahl, K. *Microstructure and Microtribology of Polymer Surfaces.* Tsukruk, V.V.; Wahl, K., Eds. ACS Symposium Series: Washington, D.C., **1999**, Vol. 741.

24 Cappella, B.; Dietler, G. *Surface Science Reports* **1999**, *34*, 1.

25 MMA Manual from the SEMA Lab

26 Tsukruk, V. V.; Gorbunov, V.V. *Probe Microscopy* **2002,** *3-4*, 241. Huang, Z.; Chizhik, S. A.; Gorbunov, V.V. *J. Mat. Sci.* **1998**, *33*, 4905. Tsukruk, V. V.; Huang, Z. *Polymer* **2000**, *41*, 5541.

27 Hazel, J.L.; Tsukruk, V.V. *Thin Solid Films* **1999**, *339*, 249.

28 Hazel, J.L.; Tsukruk, V.V. *J. Tribol.* **1998**, *120*, 814.

29 Radmacher, M.; Tillmann, R.W.; Gaub, H.E. *Biophys. J.* **1993**, *64*, 735.

30 Tsukruk, V.V.; Gorbunov, V.V. *Microsc. Today* **2001**, *01-1*, 8.

31 Tsukruk, V.V.; Gorbunov, V.V.; Luzinov, I.; Huang, Z.; Fuchigami, N. In *Interfacial Properties on the Submicrometer Scale.* Frommer, J.; Overney, R. M. Eds. ACS Symposium Series: Washington, D.C., **2001**.

32 Radmacher, M.; Tillmann, R.W.; Gaub, H.E. *Biophys. J.* **1993**, *64*, 735.

33 ILX Lightwave Manual.

34 Hayazawa, N.; Motohashi, M.; Saito, Y; Kawata, S. *Appl. Phys. Lett.* **2005**, *86*, 263114.

35 Ko, H.; Pikus, Y.; Jiang, C.; Jauss, A.; Hollricher, O.; Tsukruk, V.V. *Appl. Phys. Lett.* **2004**, *85,* 2598.

Chapter 3

Single Functional Group Interactions with Sidewalls of Individual Carbon Nanotubes

A paper submitted to *Nature Materials*

Melburne C. LeMieux[*,1,2], *Raymond W. Friddle*[1,5], *Giancarlo Cicero*[3], *Alexander B. Artyukhin*[1,5], *Vladimir V. Tsukruk*[2,6], *Jeffrey C. Grossman*[4], *Giulia Galli*[5], *and Aleksandr Noy*[1]

[1] Chemistry and Materials Science Directorate, Lawrence Livermore National Laboratory, Livermore, CA 94550

[2] Materials Science & Engineering Department, Iowa State University, Ames, IA 50011

[3] University of Turin, Italy

[4] Center of Integrated Nanomechanical Systems, University of California, Berkeley

[5] University of California, Davis

[6] School of Materials Science and Engineering, Georgia Institute of Technology, Atlanta, GA

3.1 Introduction

Carbon nanotubes[1] display a consummate blend of geometry, material strength and electronic properties that impact a variety of applications ranging from nanoelectronic circuits[2, 3] and biosensors[4], to field emitters[5], membrane filters[6], and reinforcing fibers for composite materials[7-9]. A majority of these applications rely on non-covalent forces between the nanotubes and other materials[10]; yet we still lack understanding and molecular level control of these interactions that is vital for an efficient design of functional nanotube devices and composites. We have used chemical force microscopy[11] to measure the strength of the

[*] M.C.L.: Primary researcher, carried out all experiments, writer of all drafts

interactions of *single* chemical functional groups with the sidewalls of dispersed, vapor-grown individual single-wall carbon nanotubes. Surprisingly, the interaction strength does not follow conventional trends of increasing polarity, or hydrophobicity of the group; instead, we find that the interaction strength depends on the chemical nature of the group and in particular on the presence of lone pairs or –H atoms as terminal entities. *Ab-initio* calculations of the forces between single individual functional groups and single wall nanotubes confirm the experimentally observed trends and match the force distributions measured in the experiment. The calculations also demonstrate an unexpectedly strong sensitivity of the predicted adhesion force to the electronic charge of the nanotube and indicate that the external medium, e.g. a solvent, may play a key role in determining interaction forces through charge transfer mechanisms to or from the nanotube. These findings have wide-ranging implications for the design of carbon nanotube composites, devices, and functional materials.

Understanding the nature of the interaction forces between carbon nanotubes (CNT) and functional groups is an important step in the development of CNT devices. In principle, this goal can be accomplished by *a direct measurement* of the adhesion force experienced by an individual molecule at a SWCNT interface. However, the small size of the nanotubes makes such measurements challenging; therefore most researchers have relied either on theoretical models[12], indirect measurements involving large sample volumes[13], or large microscale tests[14].

Modern force spectroscopy, which use an atomic force microscope (AFM) tips covalently functionalized with specific functional groups[11], enables direct characterization of the interaction forces in nanoscale assemblies down to molecular levels. Still, very few experimental studies have attempted to measure interaction forces involving a *single* nanotube, and the nature of the interaction at a CNT/organic interface, which is crucial for practical CNT-based materials, remains largely unexplored.

Wagner et al. attached nanotubes to AFM tips and measured the pullout force from a polymer matrix after indentation[15]. However, the interpretation of these measurements was

complicated by the possibility of the nanotube buckling upon indentation and the chemical modification of carbon nanotubes required for tip attachment. Bottomley and coworkers measured the adhesion between thiol-modified AFM tips and nanotube filter "paper" composed of bundles of SWCNT[16, 17]. Those measurements were performed in atmosphere, rather than in a fluid, and this environment typically increases the contribution of capillary forces to the measured interaction strength, even at low humidity[18]. Moreover, randomly oriented nanotube "paper" samples interacting with relatively large gold-coated AFM tips generated large, uncontrollable variations in the tip-sample contact area as well as multiple probe-nanotube contacts.

3.2 Results and Discussion

In order to measure specific adhesion forces of individual functional groups interacting with the sidewalls of non-bundled, isolated SWCNT, we have designed a force spectroscopy experiment that minimizes tip-sample contact area (Fig. 1a). To eliminate capillary loads we have performed all measurement in fluid environment using an inert organic solvent (toluene). We have also used silane modification of the probe tips (Fig. 1a) that typically produces robust functionalization. Silane modification also does not degrade the probe sharpness as much as the gold/thiol modification, where a thicker gold layer is evaporated onto an AFM probe[19, 20]. A small probe radius is indeed the key to keeping the tip-sample area of contact small. Finally, our samples contained individual isolated carbon nanotubes instead of nanotube bundles. We used a catalytic CVD growth process yielding separated individual clean single-wall carbon nanotubes on the silicon wafer surface (Fig. 1b) with a relatively narrow distribution of sizes centered at 1.3 nm (Fig 1c). Consistent probe tip size[21] used in our measurements ensured tight control and reproducibility of the tip-sample contact area (and hence the number of the interacting groups) from one experiment to another.

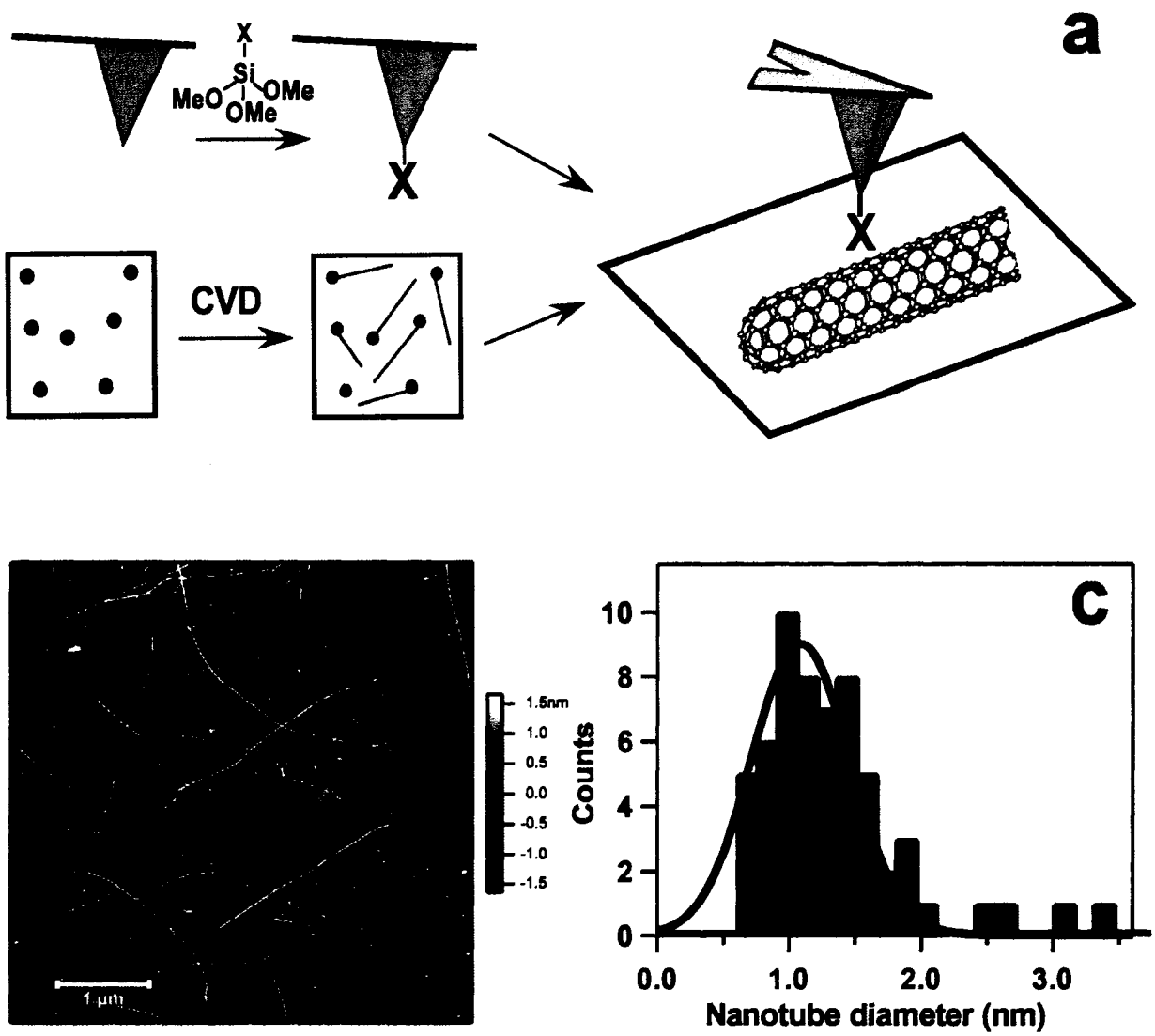

Figure 3-1. Measurement setup and nanotube characterization. (a) Schematics of carbon nanotube synthesis and AFM tip functionalization. (b) A tapping mode AFM image of the as-grown sample surface showing dense coverage of the isolated individual nanotubes. (c) Histogram of the diameters of carbon nanotubes measured from the AFM images. Solid line corresponds to the Gaussian fit of the histogram. The average diameter of the nanotubes is 1.3±0.5 nm.

Obtaining statistically-significant measurements of individual AFM force-distance curves on the tiny surface area of a SWCNT is challenging. A force volume approach could automate this task[16]; however, the overwhelming percentage of adhesion measurements would correspond to the "empty space" around the SWCNT; as an alternative we used closed-loop positioning capability of a modern AFM to position the probe tip repeatedly over the carbon nanotube[22] and measure the pull-off forces between the tip and the nanotube (Fig. 2). The adhesion forces collected on the carbon nanotube surface (Fig. 2c) are clearly distinct from the forces collected on the silicon oxide surface (Fig. 2b); these data demonstrate that we can perform site-specific force measurements on carbon nanotubes.

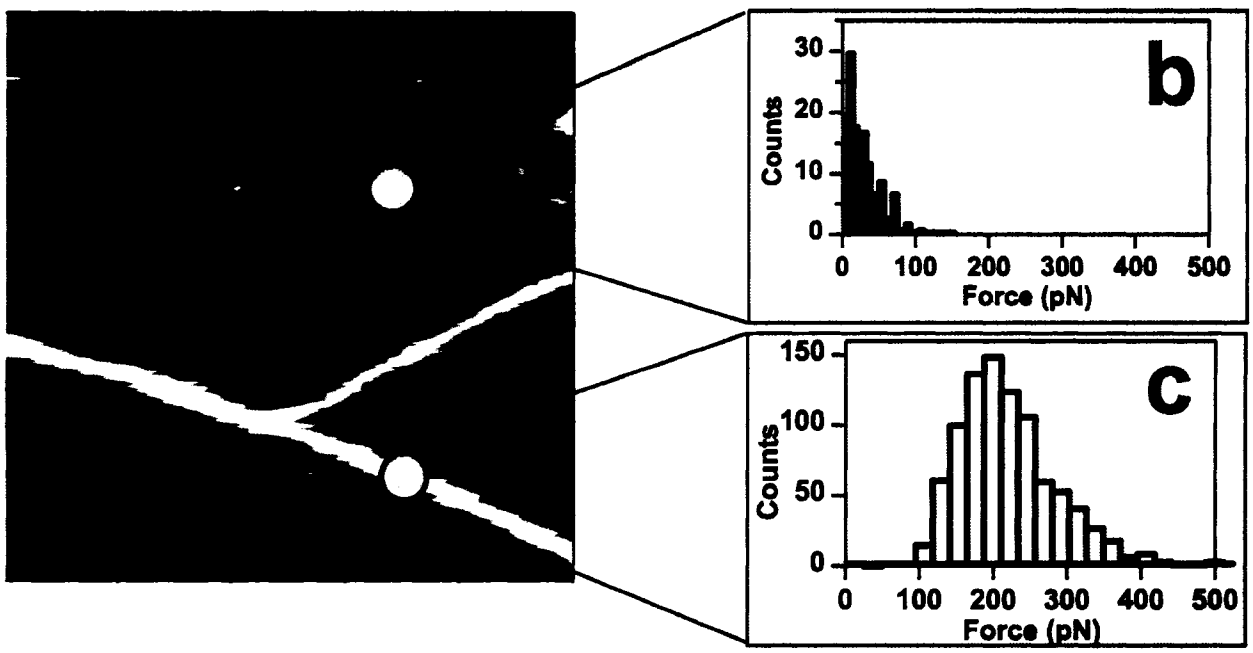

Figure 3-2. Site-specific force spectroscopy on carbon nanotubes. (a) Tapping mode image of a Y-junction of two single-wall carbon nanotube recorded under toluene using an -NH_2-terminated tip. (b) A histogram of adhesion forces collected at the area corresponding to the surface of the silicon substrate. (c) A histogram of adhesion forces collected on the carbon nanotube surface with the NH_2-terminated AFM tip.

We have used Hertzian mechanics to estimate the contact area for our measurements, which we modeled as a half-sphere (AFM tip) on a cylinder (nanotube) contact mating normal to each other[23, 24]. For this model, we assumed the value of the nanotube compression axial modulus of the nanotube to be approximately 150 GPa[25]. With this high in-plane strength, any compression of the nanotube will be negligible even under the highest load of 1.2 nN (corresponding to local pressures below 4GPa) used in our work. High compression strength also ensures that mechanical indentations do not induce *any* deformation and thus do not alter the electronic properties and overall structure of the SWCNT significantly in the course of the measurement.

Small probe radii and narrow carbon nanotube size distribution used in our experiments ensured nearly constant contact areas of the order of 0.33 ± 0.03 nm^2. If we assume that a silane molecule at the end of the AFM tip keeps the same density as in a close-packed monolayer on the flat surface[26], we can estimate that the contact area in our experiments corresponds to the interactions of only a single functional group. While researchers have measured interaction forces between single biological molecules[27], measurements of the interactions between *single functional groups* in condensed phases have not been reported. Such a small number of the interaction groups has profound consequences for the interpretation of our results. Force microscopy measurements in fluid environments are often dominated by entropic barriers arising from solvent-surface and solvent-solvent interactions[28-30]. These effects should disappear when the tip-sample contact area shrinks down to a few molecular contacts[28]. Our experiments operate in this regime, giving us the ability to measure with unprecedented precision the *interaction* of a *single* functional group on the AFM tip with the SWCNT sidewall.

Histograms of adhesion forces between carbon nanotubes and chemically-modified AFM tips show that interaction forces vary significantly from one functionality to the next (Fig. 3 and Table 1). Surprisingly, the interaction strengths observed for different functional groups do not follow any obvious trend, such as increasing functional group hydrophobicity or polarity.

Table 3-1. Adhesion force and contact area for the interactions of chemical functionalities with the carbon nanotube sidewalls.

Functional Group	**Contact Area** (nm^2)	**Mean Adhesion Force** (pN)
-CN	0.34	12±21
$-CH_3$	0.36	46±41
$-NH_2$	0.31	205±47

In order to explore the origin of the measured interaction forces, we have performed *ab-initio* simulations of the interactions of functional groups with the sidewall of a (14×0) ziz-zag carbon nanotube, which has a diameter d ~ 1.1 nm. We chose this nanotube because its size is close to the diameter of the nanotubes in our samples (Fig 1), and because it is semiconducting, similar to most of the nanotubes in our CVD-produced sample[31]. We modeled the AFM tip by a SiH_3CH_2-X molecule, where X- represents the terminal chemical functional group[32]. We simulated the pull-off experiments by slowly increasing the NT-silicon atom distance, while simultaneously optimizing the full structure of the nanotube and the functional group[33]. The structural simplicity of the attached molecules allowed us to fully explore functional group orientation and tip/NT alignment in our calculations, and to obtain an accurate potential energy curve for each functional group. From these curves we have also calculated the equilibrium distance and the interaction energy (minimum in energy curve) for each functional group (Table 2). For a neutral (uncharged) nanotube, our calculated interaction energies, show a different relative ordering compared to experiment (left column of Table 2). The $-NH_2$ tip has the largest energy, followed by the -CN, and then by the $-CH_3$ group. For the $-NH_2$ group the difference between exposing the lone-pair or the –H atom to the NT wall was negligible (Table 2).

To understand the discrepancy between experiment and theory we need to analyze the electronic structure of the interacting molecule/NT system. Note that the CN group is the only species that does not have H-atoms, and therefore can only interact with the CNT through a lone electron pair. Fig. 4 shows the electron density difference between

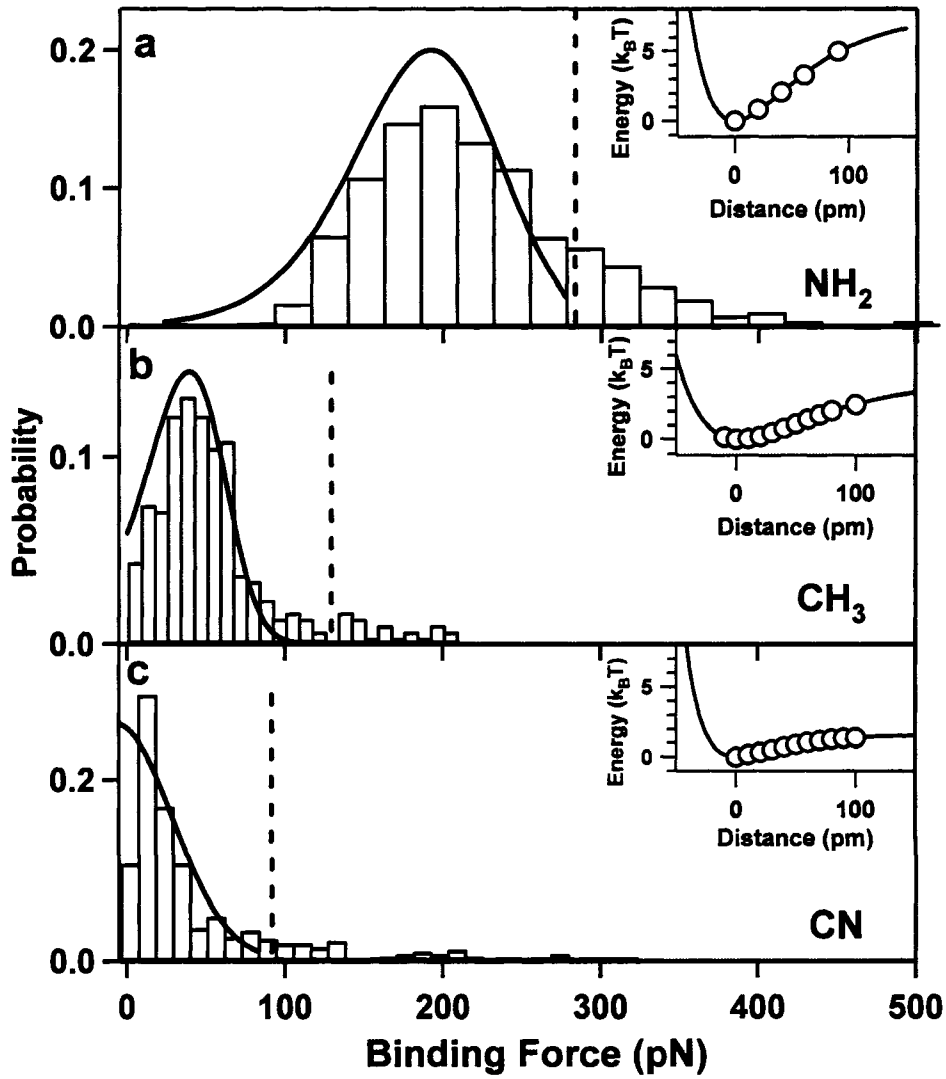

Figure 3-3. Comparison of the measured and calculated binding strength for the interactions of chemical functional groups with carbon nanotubes. Histograms of binding forces measured between individual carbon nanotubes and AFM tips functionalized with (a) NH2, (b) CH3, and (c) CN functionalities under toluene. Vertical dashed lines indicate the position of the "ideal force", corresponding to the maximum of the first derivative of the calculated interaction potentials with negatively charged carbon nanotubes. Solid blue lines correspond to the binding force distributions predicted by Equation 1 using the calculated interaction potentials. Insets show calculated interaction energies as a function of the tip distance (O) and Morse potential fits (solid black lines) for each system.

Table 3-2: Interaction energies (ΔE) and equilibrium distances (d_{eq}) for the AFM tips interacting with neutral (left), positively (center) and negatively (right) charged SWCNT. For the $-NH_2$ functionalized tip the interaction through their lone pair (LP) is explicitly indicated.

Functional group	Neutral SWNT		Positively Charged SWNT		Negatively Charged SWNT	
	ΔE (eV)	d_{eq} (Å)	ΔE (eV)	d_{eq} (Å)	ΔE(eV)	d_{eq} (Å)
-CN	-0.15	2.9	-0.21	2.9	-0.06	2.9
$-CH_3$	-0.09	2.5	-0.06	2.5	-0.09	2.4
$-NH_2$	-0.15	2.1	-0.09	2.1	-0.21	2.1
$-NH_2$ (LP)	-0.19	2.8	-0.25	2.8	-0.11	2.8

the interacting and isolated tip/NT systems in the case of the $-NH_2$ functionalization for two different orientations of the amino-group. The red and blue isosurfaces represent respectively charge depletion and accumulation when the tip is in 'contact' with the nanotube. In both cases the interaction has a strong electrostatic contribution, although the charge polarization depends on the $-NH_2$ group orientation. In particular, when a species with a lone-pair approaches the tube, a positive polarization charge appears in the NT: the interaction through the lone ē-pair induces a depletion charge in the underlying carbon ring, which in turn gives rise to an attractive force between the negatively charged lone-pair and the nanotube (right panel of Fig. 4). The opposite situation occurs when the tip interacts through the hydrogen atom, which is partially positively charged (Fig. 4 left panel).

This analysis suggests that small charge transfers from the functional group to the nanotube and thus electronic deviation of the CNT from perfect neutrality may be the key to understanding the results of the force spectroscopy measurements. An increase in the number of electrons per nanotube will discourage the interaction that leads to the localization of a positive polarization charge at the nanotube sidewall, as it is in case of the (-CN, $-NH_2$) groups interacting through the lone pairs. In these cases we expect to observe the weaker

interaction with the partially negatively charged nanotube than with the perfectly neutral nanotube. Interestingly, we will see the opposite effect if the functional groups interact through the hydrogen atom. The order of binding forces measured in our experiments argues against the possibility of having positive charges on the nanotube surface, since it would lead to an increasing of the interaction energy of the tips containing lone pairs, and, in particular, would not explain the very low binding forces measured for the –CN group.

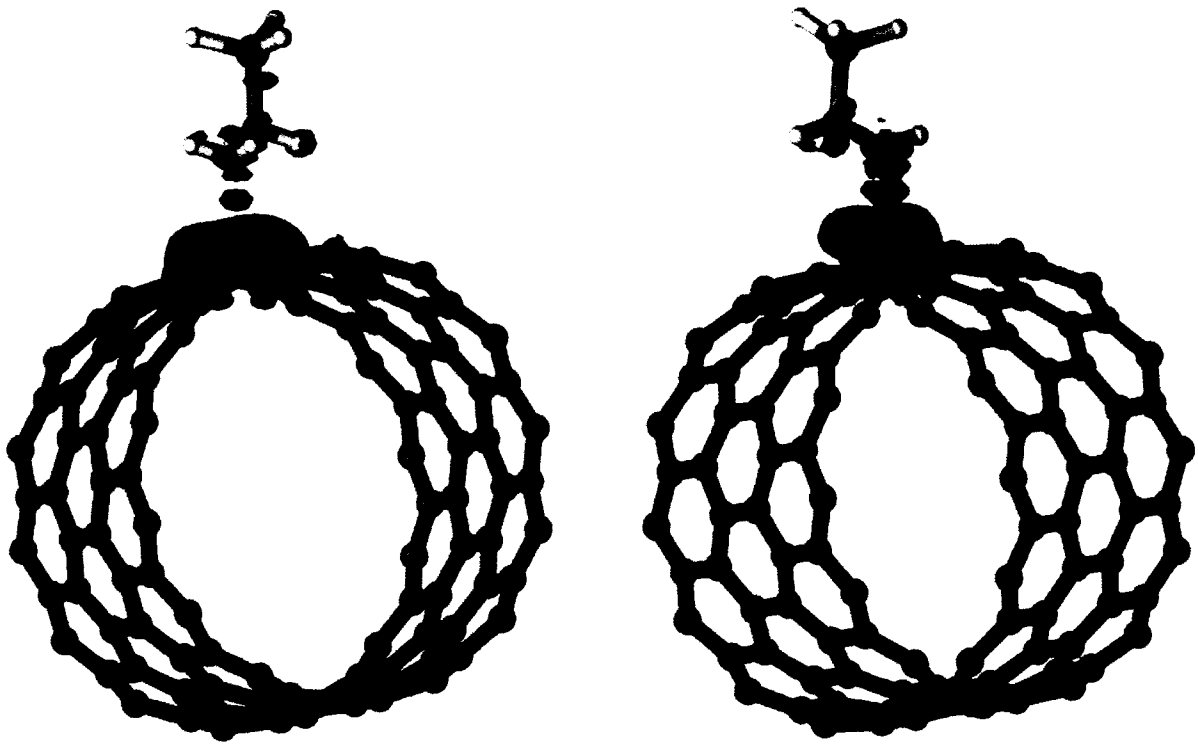

Figure 3-4. Electron density analysis of the $-NH_2$ functionalized tip interacting with a CNT sidewall. Ball and stick model of the equilibrium structure for the $-NH_2$ functionalized tip interacting through the lone-pair (left panel) and the H atom (right panel). Grey spheres correspond to C atoms, dark blue (light blue) correspond to nitrogen (silicon) atoms and white sphere to hydrogen. The iso-surfaces represent the electron density difference between the interacting and non interacting tip/NT system: blue (red) surfaces correspond to charge density increase (decrease).

To investigate the influence of the partial charge on the interaction strength we simulated interactions between functional groups and a negatively charged nanotube[33]. For the functional groups interacting through the lone electron pair the calculated binding energies were smaller than in the case of the neutral nanotube. However, when the functional groups interacted through the hydrogen atoms, the interaction energy increased slightly and the trend in the calculated forces matched the experimental results (Table 2).

The calculated interaction potentials provide a direct comparison between simulations and experiment (Figure 3). The naïve approach is to compute binding forces as maximum gradients of the interaction potentials (we call this value the "ideal force"). Evans showed[34] that thermal fluctuations cause the bond to break at forces below the "ideal force"; these kinetic effects also lead to the broadening of binding force distributions[35]. Recently Dudko et al. have developed a rigorous formalism that predicts the full rupture force distribution based on the shape of the interaction energy profile along the pulling coordinate[36].

$$P(F_{\max}) = P_0 \varepsilon^{1/2} \exp\left\{ -\frac{U_c}{k_B T} \varepsilon^{3/2} - \frac{k_B T \Omega_c^2 M F_c}{U_c 3\pi\gamma k v} e^{-\frac{U_c}{k_B T}\varepsilon^{3/2}} \right\} \qquad \text{Eq. 1}$$

Here k and v are respectively the cantilever spring constant and pulling velocity and γ is the damping coefficient of the system[37]. The parameters U_c, F_c, *and* Ω_c respectively denote the energy, force, and oscillation frequency at the critical point along the reaction profile; M is the particle mass, $\varepsilon = 1 - F_{max}/F_c$ is the reduced bias relative to the critical force, and P_o is a normalization constant. To compute the bond dynamics parameters for this model we follow Dudko et al.[36] and fit the interaction potentials obtained from the ab-initio simulations with a Morse potential function (Figure 3, Insets). We note that all parameters in Equation 1 except for the damping constant γ could be determined either directly from experiment or from the calculated interaction potentials. To determine the damping constant we fit the measured rupture force distributions to Equation 1 . Remarkably, the damping constant values that provide the best fits to the data all fall within one order of magnitude (Table 3), and match the damping constant values measured for an AFM cantilever in very close proximity to the surface[38,39]. Even more remarkable is the close fit of the calculated distributions for the negatively charged CNTs case to the experimental data: the calculated distributions closely

reproduce the experimental data for all functional groups (Figure 3). We note that this comparison provides additional evidence for the conclusion reached from our contact area analysis: our measurements are indeed probing the interactions of a *single* functional group with the nanotube sidewall.

Table 3-3. Interaction parameters for binding of functional groups to a negatively charged carbon nanotube sidewall. Theoretical parameters used in Eq 1 are calculated through a fit of the Morse potential $U(x) = U_0[1 - \exp(-2b(x-R_c)/R_c)]^2$ to the simulated interaction profiles.

Functional Group	Rupture Force (pN)	Morse Potential Parameters			Damping Constant, $\dot{\square}$ kg/s
		U_0 (k_BT)	b	R_c, (m)	
NH_2	189.8±79.5	7.60	1.60×10^{-4}	1.78×10^{-14}	$4.85 \pm 0.47 \times 10^{-4}$
CH_3	36.5±31.6	4.19	1.84×10^{-2}	2.47×10^{-12}	$4.33 \pm 0.28 \times 10^{-5}$
CN	9.0±15.1	1.56	4.00×10^{-4}	2.79×10^{-14}	$2.49 \pm 0.74 \times 10^{-4}$

A possible reason for a negative charge on the CNT is the solvent presence (toluene). In fact, recent experimental studies have shown that both the capacitance and the conductance of a SWNT network is sensitive to the presence of dilute concentrations of a wide range of vapors, and in specific cases n-doping has been reported[40, 41]. To study the effect of toluene on the nanotube electronic properties, we have analyzed the interaction of a single solvent molecule with the nanotube walls; we used the same *ab-initio* scheme discussed above. The toluene molecule can bind to a NT surface and the calculated interaction energy for the lowest energy configuration is 0.34 eV. The molecule resides flat at the NT wall; indeed, in this configuration, a π-π interaction between the delocalized π orbital

on the nanotubes and benzene ring takes place, and this stabilizes the complex. Analysis of the electronic structure of this complex shows that a small hybridization between the highest occupied molecular states of the nanotube and the toluene occurs (no hybridization was found when the molecule was at a non interacting distance of about 6 Å from the NT wall). The NT charge is thus affected by the presence of the solvent and polarization charges appear at the NT wall. While the qualitative effect of the solvent is clear, a quantitative conclusion on the final charge state of the NT as induced by the solvent is difficult to make, at this point, since the charge difference depends on the molecule orientation, which may continuously evolve and change in a liquid environment.

Our results strongly suggest that unlike most conventional materials, the interactions of carbon nanotubes with chemical functionalities strongly depend on exact electronic structure and partial charges at the molecule/nanotube interface. This conclusion is not entirely surprising, as electronic effects often determine the chemical reactivity of carbon nanotubes[42, 43, 44] and are also responsible for the unusual sensitivity of the carbon nanotube conductance to the nature of the surface adsorbates[45]. In addition, our simulations show that a solvent can influence the electronic structure of the nanotube; therefore different solvents can in principle modulate the efficiency and selectivity of carbon nanotube functionalization reactions. This conclusion could have important implications for the development of chemical functionalization strategies for carbon nanotubes as well as for the design of new generations of nanotube-reinforced composite materials and nanotube-based chemical and biological sensors.

3.3 Methods

Clean silicon AFM probes (sharpened microlevers, model MSCT from Veeco, Inc. (cantilever "A") were cleaned in piranha solution for 45 minutes and then incubated in anhydrous toluene solutions of (3-aminopropyl) trimethoxysilane, octadecyltrichlorosilane, and (3-cyanopropyl) trimethoxysilane under the nitrogen-purged glovebox to obtain–NH_2, -CH_3, and –CN functionalization. All silanes were distilled before use to ensure purity. The

probes were stored in anhydrous toluene and prior to mounting were rinsed with toluene and ethanol and dried under a nitrogen stream. Carbon nanotubes were synthesized using a 1-inch CVD system[46]. Briefly, we dip-coated colloidal iron catalyst particles onto piranha cleaned silicon wafers and grew carbon nanotubes at 850°C in a tube furnace using a 600sccm:400sccm:5sccm flow mixture of $Ar:H_2:C_2H_4$ feedstock gases. Immediately after the nanotube growth the samples were mounted into the fluid cell of an atomic force microscope (MFP-3D, Asylum Research, Santa Barbara) for force spectroscopy measurements.

To ensure accurate probe positioning during force spectroscopy measurements we first we performed progressively smaller tapping mode scans of the area of interest (typically until we reach 100nm x 100 nm scan size). We then switched the microscope to contact mode and collected force-distance curves at pre-positioned points along the nanotube.

3.4 Acknowledgments

We thank Louisa Hope-Weeks and Natalia Zaitseva (LLNL) and Sergey Peleshenko (ISU) for technical assistance and T. Sulchek (LLNL) for discussions. We also thank M. Urbakh for clarifying the conditions for using the Eq. 1. AN and GG acknowledge LLNL LDRD SI funding, VVT and MCL acknowledge funding from AFOSR, FA9550-05-1-0209 and NSF-NIRT-0506832 grants, and ABA and RWF acknowledge LLNL SEGRF Program support. JCG is grateful for partial support from NSF Grant No. EEC-0425914. This work was performed at the Lawrence Livermore National Laboratory under the auspices of the US Department of Energy under Contract No. W-7405-Eng-48.

3.5 References

1. Hu, J. T., Odom, T. W. & Lieber, C. M. Chemistry and physics in one dimension: Synthesis and properties of nanowires and nanotubes. Acc. Chem. Res. 32, 435-445 (1999).

2. Tans, S. et al. Individual single-wall carbon nanotubes as quantum wires. Nature 386, 474-477 (1997).

3. Dai, H. J. Carbon nanotubes: Synthesis, integration, and properties. Acc. Chem. Res. 35, 1035-1044 (2002).

4. Chen, R. J. et al. Noncovalent functionalization of carbon nanotubes for highly specific electronic biosensors. Proc. Natl. Acad. Sci. USA 100, 4984-4989 (2003).

5. Fan, S. S. et al. Self-oriented regular arrays of carbon nanotubes and their field emission properties. Science 283, 512-514 (1999).

6. Hinds, B. J. et al. Aligned multiwalled carbon nanotube membranes. Science 303, 62-65 (2004).

7. Mamedov, A. A. et al. Molecular design of strong single-wall carbon nanotube/polyelectrolyte multilayer composites. Nature Materials 1, 190-194 (2002).

8. Dai, L. M. & Mau, A. W. H. Controlled synthesis and modification of carbon nanotubes and C-60: Carbon nanostructures for advanced polymer composite materials [Review]. Adv. Mat. 13, 899 (2001).

9. Lin, Y. et al. Polymeric carbon nanocomposites from carbon nanotubes functionalized with matrix polymer. Macromolecules 36, 7199-7204 (2003).

10. Terrones, M. Science and technology of the twenty-first century: Synthesis, properties and applications of carbon nanotubes. Ann. Rev. Mat. Res. 33, 419-501 (2003).

11. Noy, A., Vezenov, D. & Lieber, C. Chemical Force Microscopy. Ann. Rev. Mat. Sci. 27, 381-421 (1997).

12. Liao, K. & Li, S. Interfacial characteristics of a carbon nanotube-polystyrene composite system. Appl. Phys. Lett. 79, 4225-4227 (2001).

13. Decossas, S. Interaction forces between carbon nanotubes and an AFM tip. Europhys. Lett. 53, 742 (2001).

14. Kharchenko, S. B., Douglas, J. F., Obrzut, J., Grulke, E. A. & Migler, K. B. Flow-induced properties of nanotube-filled polymer materials. Nature Materials 3, 564-568 (2004).

15. Barber, A. H., Cohen, S. R. & Wagner, H. D. Measurement of carbon nanotube-polymer interfacial strength. Appl. Phys. Lett. 82, 4140-4142 (2003).

16. Poggi, M. A., Bottomley, L. A. & Lillehei, P. T. Measuring the adhesion forces between alkanethiol-modified AFM cantilevers and single walled carbon nanotubes. Nano Lett. 4, 61-64 (2004).

17. Poggi, M. A., Lillehei, P. T. & Bottomley, L. A. Chemical Force Microscopy on Single-Walled Carbon Nanotube Paper. Chem. Mater. 17, 4289-4295 (2005).

18. Grigg, D. A., Russell, P. E. & Griffith, J. E. Tip-sample forces in scanning probe microscopy in air and vacuum. J. Vac. Sci. Technol. A, Vac. Surf. Films 10, 680-3 (1992).

19. Alley, R. L., Komvopoulos, K. & Howe, R. T. Self-assembled monolayer film for enhanced imaging of rough surfaces with atomic force microscopy. J. Appl. Phys. 76, 5731-7 (1994).

20. Tsukruk, V. V. & Bliznyuk, V. N. Adhesive and friction forces between chemically modified silicon and silicon nitride surfaces. Langmuir 14, 446-455 (1998).

21. Probe tip size used in our experiments was 18 ± 2 nm, as determined by scanning a reference gold colloid standard after each experiment.

22. We note that the diameter of our nanotubes was much smaller than the AFM tip diameter and consequently the nanotube "reverse-imaged" the probe tip. Such geometry relaxes the probe placement accuracy requirements: a simple geometrical calculation shows that if we approximate the probe by a hemisphere of radius R, and the nanotube a cylinder of radius r, then the probe only has to land within a distance of $2\sqrt{Rr}$ from the center of the nanotube. For our experiments this distance corresponds to 6.8nm.

23. Vu-Quoc, L. & Zhang, X. An elastoplastic contact force-displacement model in the normal direction: displacement-driven version. Proc. Royal Soc. A. 455, 4013-4044 (1999).

24. Johnson, K. L. Contact Mechanics (Cambridge University Press, Cambridge, 1987).

25. Srivastava, D., Menon, M. & Cho, K. J. Nanoplasticity of single-wall carbon nanotubes under uniaxial compression. Phys. Rev. Lett. 83, 2973-2976 (1999).

26. Ulman, A. Introduction to Ultrathin Organic Films (Academic Press, New York, 1991).

27. Clausen-Schaumann, H., Seitz, M., Krautbauer, R. & Gaub, H. E. Force spectroscopy with single bio-molecules. Curr. Opin. Chem. Biol. 4, 524-530 (2000).

28. Noy, A., Zepeda, S., Orme, C. A., Yeh, Y. & De Yoreo, J. J. Entropic Barriers in Nanoscale Adhesion Studied by Variable Temperature Chemical Force Microscopy. J. Am. Chem. Soc. 125, 1356 - 1362 (2003).

29. Vezenov, D. V., Zhuk, A. V., Whitesides, G. M. & Lieber, C. M. Chemical Force Spectroscopy in heterogeneous systems: Intermolecular Interactions involving Epoxy Polymer, mixed monolayers and polar solvents. J. Am. Chem. Soc. 124, 10578-10588 (2002).

30. Sinniah, S. K., Steel, A. B., Miller, C. J. & Reutt-Robey, J. E. Solvent Exclusion and Chemical Contrast in Scanning Force Microscopy. J. Am. Chem. Soc. 118, 8925-8931 (1996).

31. A random distribution of the nanotube chiralities produces 66% of semiconducting nanotubes. Electrical properties measurements in our laboratory indicate that an even higher percentage of the nanotubes produced by our CVD growth method (70-80%) is semiconducting (A. Artyukhin, A. Noy, unpublished 2005)

32. The Si atom represents the edge of the AFM tip, and the -CH2- represents the short alkyl chain connecting the functional group to the AFM tip

33. All pull-off computational experiments were carried out using the Density Functional Theory in the Local Density Approximation (LDA). The validity of LDA and comparisons with GGA functional and Diffusion Quantum Monte Carlo (QMC) to describe non-covalent interactions of nanotubes with simple molecules has been recently discussed by G.Cicero, J.Grossman and G.Galli (Phys. Rev. B., submitted). The calculations were performed using a pseudopotential plane wave formulation of ab-initio Molecular Dynamics (MD) [R. Car and M. Parrinello Phys. Rev. Lett. 55, 2471 (1985)], as implemented in the GP and Qbox codes written by F. Gygi (LLNL, 1998-2003). Electron/ion interactions are treated with norm conserving pseudopotentials of the Hamam type [Phys. Rev. B 40, 2980, (1989)], and Kohn-

Sham orbitals were expanded in plane waves up to an energy cutoff 60 R□. The integration over the Brillouin Zone was performed using only the Γ point. Systems representing positively and negatively charged NTs were obtained by removing or adding one electron per unit cell (eg. 0.009 el. per C atom), respectively.

34. Evans, E. & Ritchie, K. Dynamic strength of molecular adhesion bonds. Biophys. J. 72, 1541-1555 (1997).

35. It is also not surprising to see the tails of the distribution to exceed the "ideal force value" given the measurement uncertainty, as well as the possibility that a small fraction of the tip-sample contacts corresponds to the interactions of two or more functional groups instead of a single functional group.

36. Dudko, O. K., Filippov, A. E., Klafter, J. & Urbakh, M. Beyond the conventional description of dynamic force spectroscopy of adhesion bonds. Proc. Natl. Acad. Sci. USA 100, 11378 (2003).

37. Equation 1 is valid for force spectroscopy experiments carried out in the regime when the pulling velocity $v < \frac{k_B T \Omega_c^2 M F_c}{U_c 3\pi\eta k}$. The value of the expression at the right hand side of this relation is 1.25 – 4.23 μm/s for our system; this value is 3-10 times higher than the 400 nm/s pulling velocity used in the experiment.

38. Note that the average damping constant of 2.6×10^{-4} kg/s is 7 orders of magnitude higher than typical values for small molecules in aqueous solution. However, this damping constant matches the damping constant of an AFM cantilever located within 1 nm from a surface[39]. In CFM measurements the short alkane linker between the functional group and the AFM tip significantly restricts the mobility of the functional group; therefore it is reasonable to assume that damping is dominated by the AFM tip. [A. Sain, and M. Wortis. Phys. Rev. E 70, 031102 (2004)].

39. Jeffery, S. et al. Direct measurement of molecular stiffness and damping in confined water layers. Phys. Rev. B 70, 054114-8 (2004).

40. Someya, T., Small, J., Kim, P., Nuckolls, C. & Yardley, J. T. Alcohol Vapor Sensors Based on Single-Walled Carbon Nanotube Field Effect Transistors. Nano Lett. 3, 877-881 (2003).

41. Klinke, C., Chen, J., Afzali, A. & Avouris, P. Charge Transfer Induced Polarity Switching in Carbon Nanotube Transistors. Nano Lett. 5, 555-558 (2005).

42. Liu, J. et al. Controlled deposition of individual single-walled carbon nanotubes on chemically functionalized templates. Chem. Phys. Lett. 303, 125-129 (1999).

43. Strano, M. S. et al. Electronic structure control of single-walled carbon nanotube functionalization. Science 301, 1519-1522 (2003).

44. Usrey, M. L., Lippmann, E. S. & Strano, M. S. Evidence for a Two-Step Mechanism in Electronically Selective Single-Walled Carbon Nanotube Reactions. J. Am. Chem. Soc. 127, 16129-16135 (2005).

45. Kong, J. et al. Nanotube molecular wires as chemical sensors. Science 287, 622-625 (2000).

46. Artyukhin, A. B., Bakajin, O., Stroeve, P. & Noy, A. Layer-by-Layer Electrostatic Self-Assembly of Polyelectrolyte Nanoshells on Individual Carbon Nanotube Templates. Langmuir 20, 1442-1448 (2004).

Chapter 4

Ultrathin Binary Grafted Polymer Layers with Switchable Morphology

A paper published in *Langmuir*[♦]

Melburne C. LeMieux[*,1], *Duangrut Julthongpiput*[1], *Kathryn N. Bergman*[1], *Pham Duc Cuong*[2], *Hyo-Sok Ahn*[2], *Yen-Hsi Lin*[1], *Vladimir V. Tsukruk*[1]

[1] Materials Science & Engineering Department, Iowa State University, Ames, IA 50011

[2] Tribology Research Center, Korean Institute of Science and Technology, Seoul 136-791, South Korea

4.1 Abstract

Polymer surface layers comprised of mixed chains grafted to a functionalized silicon surface with total layer thickness *only* 1 – 3 nm are shown to exhibit reversible switching of their structure. Carboxylic acid terminated polystyrene (PS) and poly (butyl acrylate) (PBA) were chemically attached to a silicon surface that was modified with an epoxysilane self-assembled monolayer by a "grafting to" routine. While one – step grafting resulted in large, submicron microstructures, a refined, two – step sequential grafting procedure allowed for extremely small spatial dimensions of PS and PBA domains. By adjusting the grafting parameters such as concentration of each phase and molecular weight, very finely structured surfaces resulted with roughly 10 nm phase domains and less than 0.5 nm roughness. Combining the glassy PS and the rubbery PBA, we implemented a design approach to fabricate

---

♦ Reprinted with permission of *Langmuir*

* M.C.L.: Primary researcher, carried out sample prep and AFM experiments, writer of all drafts

a mixed brush from two immiscible polymers so that switching of the surface nanomechanical properties is possible. Post – grafting hydrolysis converted PBA to poly (acrylic acid) to amplify this switching in surface wettability. Preliminary tribological studies showed a difference in wear behavior of glassy and rubbery surface layers. Such switchable coatings have practical applications as surface modifications of complex nanoscale electronic devices and sensors, which is why we restricted total thickness for potential nanoscale gaps.

4.2 Introduction

Flexible polymer chains have long been known to respond and conform to subtle local changes in pH, temperature, and solvent quality. Thus, polymer surface modification, which inherently provides the ability to control and change surface composition allowing on – demand properties, is becoming increasingly significant for practical applications in fields like nanoscale lubrication, sensing and biocompatibility[1,2,3,4,5,6,7,8], or the exciting advancement of functional carbon nanotube devices.[9,10,11,12] Polymer brush layers are considered ideal choices in such applications for several reasons. They are chemically tethered to the surface at one end, virtually any chemistry can be designed into the layer depending on intended surface interactions, and the high grafting density combined with uniformity in composition and structure allows the *entire* surface to *quickly* respond to local environmental stimuli. These unique qualities have led to intense theoretical and experimental development of polymer brush systems.[13,14,15,16,17]

Aside from responsive coatings, a parallel approach is the development of nanocomposite polymer layers with heterogeneous surface properties. The design of molecular coatings with controllable size and shape of novel nanostructures is an important topic for nanotemplates and microelectronics.[18,19] Other approaches have used immiscible polymer blends and physisorbed layers, but dewetting is a prevalent problem in thin homopolymer blend films, and only chemisorbed layers possess practical robustness and stability. Chemically attached block copolymers have been widely exploited for this purpose as the periodicity and control of domains is well understood in these systems.[20,21] Recent

work has focused on using block copolymer systems as protective, or lubricating coatings for surfaces with repeated nanoscale contacts. It has been shown that triblock copolymers of poly[styrene-b-(ethylene-co-butylene)-b-styrene] (SEBS) formed fine domains of mechanically stiff PS and rubbery PEB chains with 30 nm interdomain spacing in a thin (9 nm) polymer film.[22] When this reinforced rubber layer was capped with a hard top layer, the resulting triplex coating provided an effective means of energy dissipation due to the large reversible elastic deformation possible, along with preventing penetration of sharp contacts to the surface via the hard top layer.[23] The main drawback with this coating is that it was relatively thick (within 20-50 nm), although it displayed exceptional surface nanomechanical heterogeneity and tribological properties.[24,25] Building on this approach, PS homopolymer was blended with SEBS to form a mechanically heterogeneous, non-dewetting film with the thinnest film still being around 10 nm thick.

Merging the responsive and sensing properties of grafted homopolymer brushes with the vast array of nanostructures and phase separations capable in block copolymer systems into a single polymer film is possible in binary (mixed) polymer brush layers.[26] In the case of binary brushes, the variety of surface morphologies possible greatly increases depending upon the chemical composition. Surface composition and hence properties such as surface energy, adhesion, friction, and wettability have the possibility of being "tuned" to the necessary state.[27,28] Current theory predicts, ideally, either complete lateral or complete vertical (layered) segregation of the two components within the binary assembly.[29,30,31,32]

Synthesis of binary brushes is a challenging issue with several factors considered. First, each homopolymer brush must be chemically attached to the substrate either with a grafting to or a grafting from approach. In general, grafting to is a more simple process although kinetically limited.[22] On the other hand, brushes grown from the surface (grafting from) are more dense and thicker, with the major drawbacks of having complicated synthesis and characterization procedures.[33,34,35] Secondly, to produce smaller, intriguing phases, two incompatible polymers should be immobilized randomly on the surface, which should be done in a two – step (sequential) grafting scheme to avoid agglomeration and dewetting.

Zhao reported synthesis of randomly mixed brushes by having mixed SAMs (co-adsorbed from one solution) on the surface, but the phase separation of the mixed SAMs can be a serious issue.[36] In another publication, to avoid preferential adsorption, a double-branched SAM was used that was selective to each monomer with the resulting surface morphology of the mixed brush showing nanoscale domain structure.[37] Recently, Julthongpiput et al. synthesized a novel Y-shape brush layer in which two incompatible polymer "arms" were attached at a single focal point, which in turn grafted to the surface.[38,39] The spatial constraints led to never before observed nanoscale phase separations of pinned micelles and crater – like structures. Poly (methyl acrylate) and fluorinated polystyrene (PSF) binary brushes were sequentially grown from the surface and could be completely and reversibly switched between the glassy, low energy PSF on the topmost layer, to the rubbery PMA occupying the top layer as a function of solvent exposure.[40] This resulted in having a surface with 2 nm RMS roughness and roughly 1 GPa elastic modulus in one state, and switching to a surface with 30 nm RMS and 40 MPa elastic modulus with two times higher adhesion in a *single* polymer film with total thicknesses ranging from 50 – 150 nm.[40,41] To date, this issue has not been addressed in sequentially grafted mixed brushes with total thickness less than 10 nm.

In this paper, we demonstrate how ultra thin (less than 3 nm) and stable nanocomposite grafted surface layers can be obtained from dissimilar functionalized polymers (Figure 4-1). For these layers, we observed the microstructural reorganization upon exposure to selective solvents for each component. Post – grafting hydrolysis was performed to induce amphiphilicity in these binary brushes. Here we discuss how molecular weight and type of grafting affect the resulting surface morphology and report preliminary results on their surface tribological properties.

4.3 Experimental

Materials and methods. Carboxyl acid – terminated polystyrene (M_n: PS 1 = 4,200 g/mol; PS 2 = 9,700 g/mol with very narrow polydispersity (M_w/M_n=1.08 for PS 1 and PS 2),

and carboxyl acid – terminated poly(butyl acrylate) (M_n: PBA 1 = 6,500 g/mol with M_w/M_n=1.06) polymers (Figure 4-1) were obtained from Polymer Source, Inc. The epoxysilane anchoring layer is (3-glycidoxypropyl)trimethoxysilane (Gelest Inc.), and fabricated according to the established procedure. [42,43] Anhydrous toluene was obtained from Aldrich, further dried with sodium, and stored in a nitrogen-filled glovebox with relative humidity not exceeding 2%. The silicon wafer {100} substrates were first cleaned in an ultrasonic bath for 30 minutes, placed in a hot (90°C) bath (3:1 concentrated sulfuric acid : 30% hydrogen peroxide) for 1 hour, and then rinsed with nanopure water (18 MΩ cm, Nanopure).

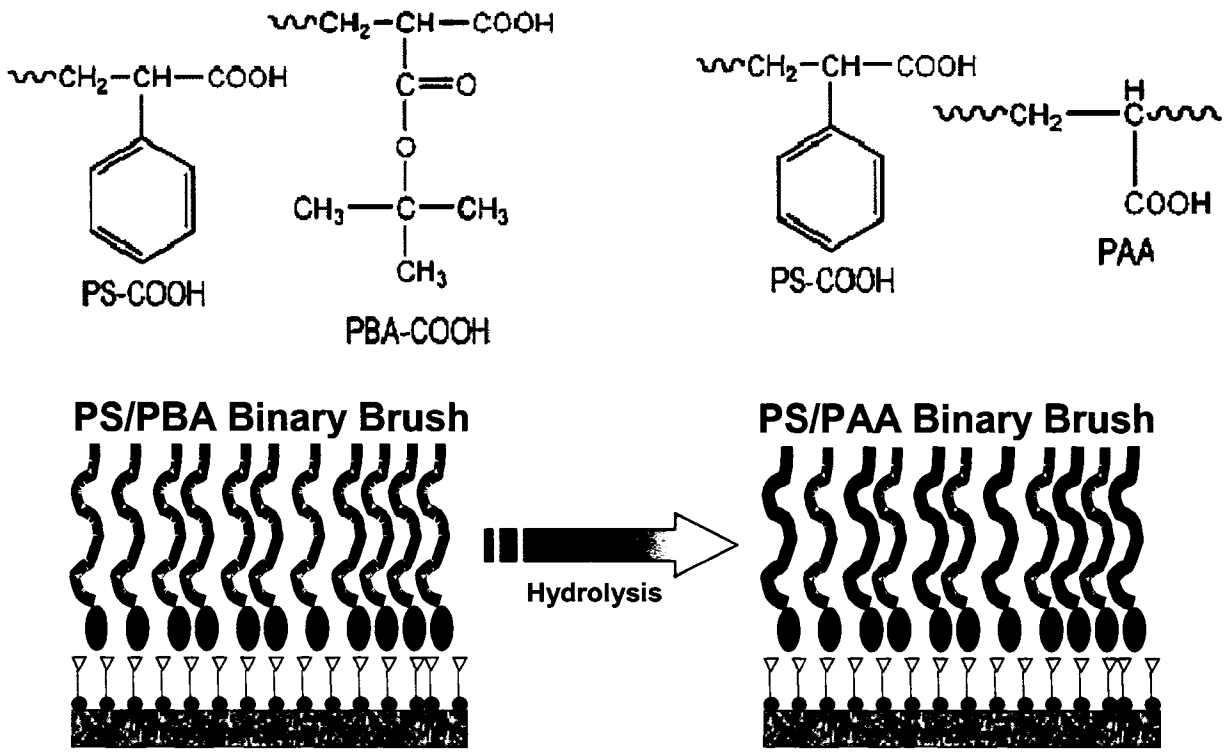

Figure 4-1. Chemical formulas for PBA, PS and PAA (top) along with schematics (bottom) of the binary brushes before and after hydrolysis.

Regarding the polymers solutions, we used two different approaches for grafting: concurrent grafting when a surface layer formed from the two mixed polymers at once, and sequential (one polymer after another) grafting. In the latter approach, after each grafting step, the sample was vigorously rinsed with toluene and additionally washed in an ultrasonic toluene bath to remove all ungrafted chains. The solutions were prepared in various concentrations of toluene ranging from 0.5 – 2.0 wt% polymer (Table 4-1), and spin coated onto the epoxysilane modified silicon wafers at 3000 RPM. The sample was then annealed to facilitate grafting between the epoxy and carboxyl acid groups [44], then spin coated with the second polymer (for the sequential grafting approach), then annealed again. All sample annealing was carried out under vacuum conditions. For the sequential approach, when PS was grafted as the first step (first polymer), unstable layers formed, thus, PBA was always grafted as the first polymer. Since PBA and PS have similar water contact angles, post – grafting hydrolysis was conducted to completely replace the PBA polymer with poly(acrylic acid) (PAA), which made the binary brush amphiphilic in nature with hydrophobic PS chains and hydrophilic PAA chains (Figure 4-1). The brush was hydrolyzed in a mixture of 30% tetrahydrofuran and 70% trifluoracetic acid for 48 hours, rinsed with nanopure water and toluene, then sonicated. All sample preparation was done inside a Class 100 Cleanroom facility.

Table 4-1. Grafting conditions for different samples.

Sample	SiO_2 Thickness (nm)	Epoxysilane Thickness (nm)	Binary Brush Step 1 (PBA grafting)	Binary Brush Step 2 (PS grafting)
1	1.10	0.75 ± 0.04	PBA 1 = 0.58 nm 20 min at 50° C 0.5% PBA in toluene	PBA 1 + PS 1 = 1.95 nm 18 hours at 150° C 2% PS 1 in toluene
2	1.10	0.75 ± 0.04	PBA 1 = 0.94 nm 20 min at 70° C 0.5% PBA in toluene	PBA 1 + PS 1 = 3.02 nm 18 hours at 150° C 2% PS 1 in toluene
3	1.10	0.72 ± 0.04	PBA 1 = 0.87 nm 20 min at 50° C 0.5% PBA in toluene	PBA 1 + PS 2 = 2.79 nm 18 hours at 150° C 2% PS 2 in toluene
4	1.10	0.72 ± 0.04	PBA 1 = 0.90 nm 20 min at 70° C 0.5% PBA in toluene	PBA 1 + PS 2 = 3.56 nm 18 hours at 150° C 2% PS 2 in toluene

All thickness measurements were obtained with a COMPEL Automatic Ellipsometer (InOm Tech, Inc.) with an incident angle of 70°.[45] Thickness of the spin coated films after each step (before annealing) was 36 ± 3 nm. Independent epoxysilane SAMs thicknesses were measured before polymer grafting to be 0.75 ± 0.1 nm. Thicknesses of the grafted layers were averaged over several sample locations and detailed in Table 4-1. The index of refraction for the SiO_2, epoxysilane, PBA, and PS are considered constant, and equal to the bulk values of 1.46, 1.429, 1.59, and 1.464, respectively.[46,47,48] Contact angle was measured with a sessile drop method using 2 μL droplets of nanopure water, which were captured with a custom-built digital microscope. Atomic force microscopy (AFM) (MultiMode and Dimension 3000, Veeco Metrology) was used for topographical and phase imaging in air according to the procedures adapted in our lab.[49,50] Unless otherwise noted, all AFM images were obtained using the light tapping regime, governed by the setpoint ratio (rsp), which is defined as the ratio of operating setpoint (amplitude) to the free oscillating amplitude of the cantilever. The attractive regime, or light tapping, is characterized by an rsp of 0.9 – 1, while the repulsive regime, or hard tapping, has rsp of 0.4 – 0.7. In light tapping, the tip sample interaction is strongly influenced by adhesion and the phase shift is greater on the surface with areas of higher attractive forces whereas in the, hard tapping regime the elastic response becomes predominant.[51] AFM tips were MikroMasch (Talin, Estonia) v-shaped, noncontact tips with nominal spring constant ranging from 30 – 100 N/m. For the high resolution (less than 1 x 1 μm) AFM imaging, care was taken to use a silicon tip with radius less than 15 nm, which was determined by scanning a gold nanoparticle reference sample.[52]

Switching of the brushes. To examine the chain reorganization and kinetics of reversible switching of surface properties in the binary brush, samples were exposed to selective solvents for each component. Selective good solvents for the PS and PBA system are trichloroethylene (TCE) for PS and n – butanol for PBA. After hydrolysis, for the PS/PAA binary brush, toluene was used as the selective solvent for PS, while water heated to 75°C was used for PAA. Samples were immersed in solvents for varying amounts of time, dried quickly under dry N_2, and contact angle measurements were done within 5 minutes of solvent drying, and the samples were quickly imaged with AFM.

Tribology testing. A custom-built microtribometer, an oscillating friction and wear tester, was used to characterize the frictional characteristics of the mono and binary brush layers. A planar specimen with a polymer brush was mounted on a platform and oscillated against a stationary glass ball with a smooth surface (microroughness less than 1nm as determined with AFM) with an applied load of 200 μN, which corresponded to the maximum Hertzian pressure of 34.3 MPa. Prior to test, the glass ball was subjected to an ultrasonic cleaning in acetone and methanol solutions for 15 minutes each to remove organic contaminants and residual debris originated from the polishing process. The glass ball was then rinsed in de-ionized water for 5 minutes and dried by compressed nitrogen gas flow. The sliding speed was 330 μm/s and the stroke length was 1.6 mm. The tests were conducted at 5 % and 80 % relative humidity in ambient environment.

The chemical composition of the surface was probed with Auger electron spectroscopy (AES) on a PHI-670 instrument. AES surface analysis was performed using a field emission gun with an accelerating voltage of 5 kV and a current of 0.0185 μA. The working potential for depth sputtering was 1 kV using Ar-ion. Under this working condition, the sputtering rate was 7A°/min. when calibrated against SiO_2.

4.4 Results and Discussion

One step grafting synthesis. One – step grafting for the synthesis of the binary layer resultedin heterogeneous surface morphology as shown in Figure 4-2. As can be seen, such a procedure leads to large surface domain structures in the resulting morphology caused by phase separation during grafting. As known, when grafting two polymers simultaneously from a mixed solution, the polymers can aggregate in solution before grafting, as well as one being preferentially adsorbed onto the silicon, and the other dewetting the surface.[53,54,55] Typical lateral dimensions of phase separated surface areas were several hundred nanometers with the surface microroughness exceeding 5 nm. Considering that we are focusing on the fabrication of surface layers with fine surface morphology, we concentrated mainly on the alternative sequential approach which produces desirable surface layers.

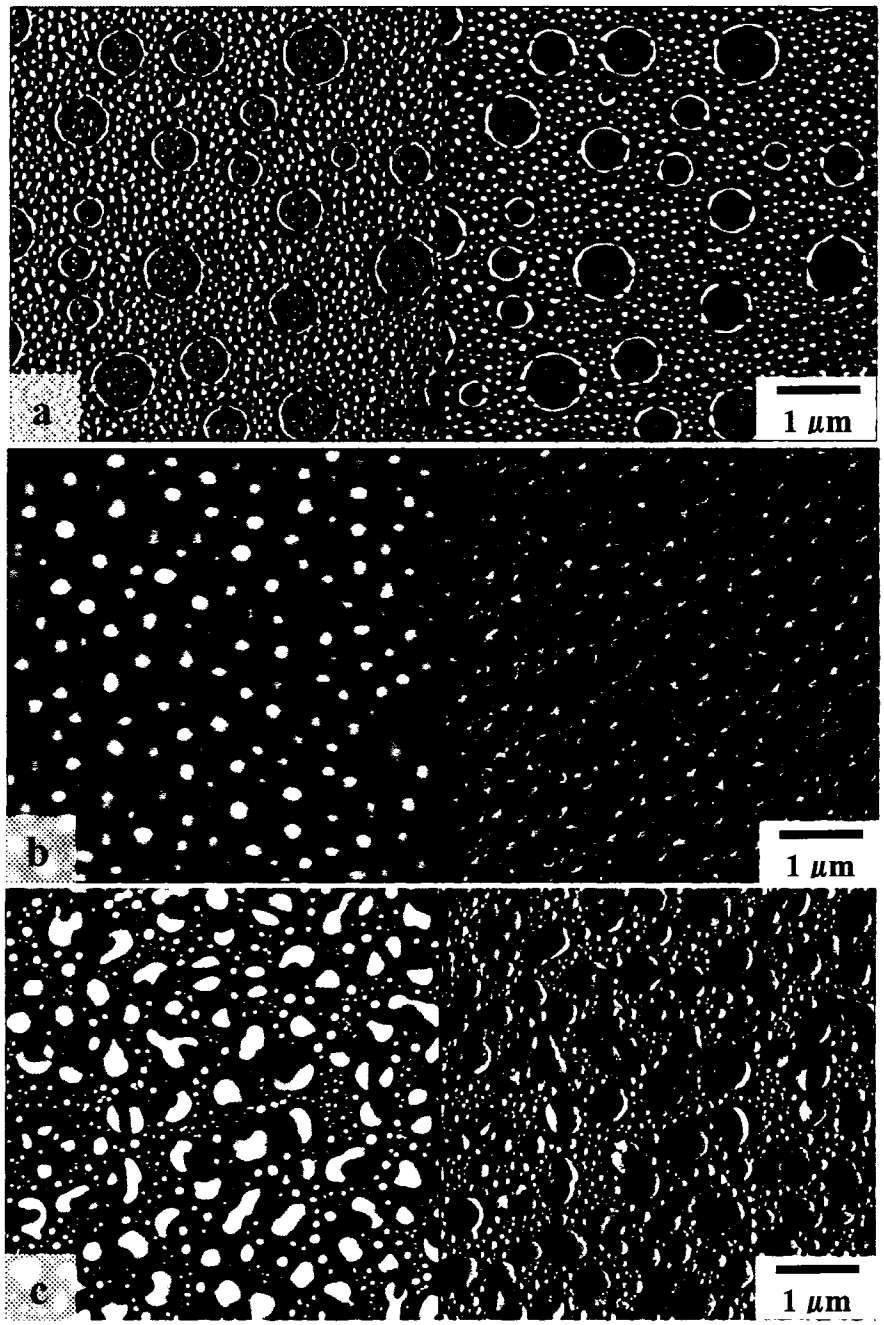

Figure 4-2. 5 x 5 μm AFM images of one–step grafting samples showing topography (left) and phase (right) with Z scale of 30 nm and 50°, respectively, while typical RMS roughness is greater than 5 nm. The three different images shown represent binary brushes with different PS molecular weight: (a) PS1, (b) PS2, and (c), M_n for PS = 28, 500 g/mol.

Two step grafting synthesis. The key to fabrication of binary polymer surfaces is to have control over the first step, in this case PBA. Allowing this first reaction to continue for too long will result in the majority of the grafting sites being consumed meaning that the second polymer (PS) will not be able to penetrate through the absorbed PBA chains. Prematurely terminating the reaction will have the opposite effect in which the binary layer will be highly asymmetric in favor of PS. When the brush binary layer is symmetric in terms of the grafted amount, it enhances the switching in surface composition of the layer.[56]

For the four samples studied here, we grafted PBA at the first step because the grafting of PS followed by PBA produced unstable results. The amount of PBA grafted onto the surface was controlled by altering the grafting (annealing) time and temperature. In a previous publication, we have fully characterized the kinetics of PBA layer formation.[57] The kinetics of layer formation for PBA revealed that half of the full achievable thickness occurs around 20 – 30 minutes, thus we chose 20 minutes as the grafting time, and varied the temperature as indicated in Table 4-1.[57] To compare, the theoretical maximum thickness for the PBA used in this work (M_n = 6,500 g/mol) is h = 3.3 nm, based upon well-known polymer brush models.[16,57,58] Thus, we have chosen our PBA grafting conditions using this model. We have characterized the grafting kinetics of both PBA and PS, and observed that the grafting conditions are highly reproducible.[57]

Surface layer properties. The parameters of the grafted layers are listed in Table 4-2. The grafting density (**D**, chains/nm^{-2}) of the brush layers was evaluated from M_n and the layer thickness (**d**, nm) according to the formula: $\mathbf{D} = d*\rho*N_a/(M_n*10^{21})$, where ρ (g/cm^3) is density of the polymer, and N_a=6.022*10^{23} (mol^{-1}) is the Avogadro's number.[59] The anticipated average distance between grafting points, **l**, calculated as $\mathbf{l} = 2(\pi D)^{-0.5}$. An indication of having polymer brush surfaces can be when the interchain distance is less than the radius of gyration of the corresponding free polymer chain.[14] For PS1, PS2, and PBA, the radius of gyration has been calculated as 1.80 nm, 2.73 nm, and 2.24 nm, respectively.[57] We have achieved high grafting densities for all samples, and the overall interchain grafting distance in all cases (except sample 1, with a difference of 0.33 nm) is less than the radius of gyration of these PS and PBA free polymer chains in solution, indicating that the chains are indeed in a stretched, brushlike conformation. This is summarized in Table 4-2 where the overall grafting distance considers both PS and PBA chains.

Large-scale representative AFM images of the as grafted binary surface layer obtained in two-step approach from toluene solutions shown in Figure 4-3 demonstrate overall uniformity of the surface layer without large-scale bumps and holes indicating dewetting, microscopic phase separation (compare with Figure 4-2), or contamination. All

binary surface layers have a fine nanostructured surfaces with phase sizes and interdomain spacing not more than a few tens of nanometers as can be seen on high-resolution AFM images (Figure 4-4). The surface RMS surface roughness does not exceed 0.3 nm, which is far less than the size of the free polymer chain indicating extremely homogeneous and uniform surfaces (Table 4-2). Higher molecular weight of the PS component and higher grafting density resulted in a slightly better defined domain morphology of binary layers.

Table 4-2: Properties of the grafted layers.

Sample	Polymer	Thickness (nm)	RMS roughness (nm)	Grafted amount (mg/m^2)	Graft density ($chains/nm^2$)	Interchain distance (nm)
1	**First Step**	0.58	NA	0.52	0.0483	5.14
	PBA 1 + PS 1	1.95 ± 0.2	0.23 ± 0.02	1.96	0.2809	2.13
2	**First Step**	0.94	NA	0.84	0.0782	4.04
	PBA 1 + PS 1	3.02 ± 0.2	0.19 ± 0.02	3.03	0.4342	1.71
3	**First Step**	0.87	NA	0.78	0.0724	4.19
	PBA 1 + PS 2	2.89 ± 0.2	0.18 ± 0.02	2.80	0.2592	2.22
4	**First Step**	0.9	NA	0.81	0.0749	4.12
	PBA 1 + PS 2	3.61 ± 0.3	0.20 ± 0.02	3.60	0.3336	1.95

The binary brush layer was immersed in TCE (good selective solvent for PS) and n – butanol (a good selective solvent for PBA) for 2 hours and rapidly dried so that the morphology under solvent is effectively frozen and retained in the dry state since the time for chain reorganization is much slower than solvent evaporation.[28] Figure 4-5 shows high-resolution AFM images of the binary brush surface after exposure to different selective solvents demonstrating some subtle changes in surface morphology. Change of contact angle went from 93° after TCE exposure to 80° after n – butanol exposure, which is very close to the values for pure PS and pure PBA, respectively.[48] However, this contact angle change is small due to the modest difference in amphiphilicity of PS and PBA chains. To amplify and better observe the changes in surface morphology, we conducted hydrolysis of PBA chains and their conversion to PAA chains (Figure 4-1).

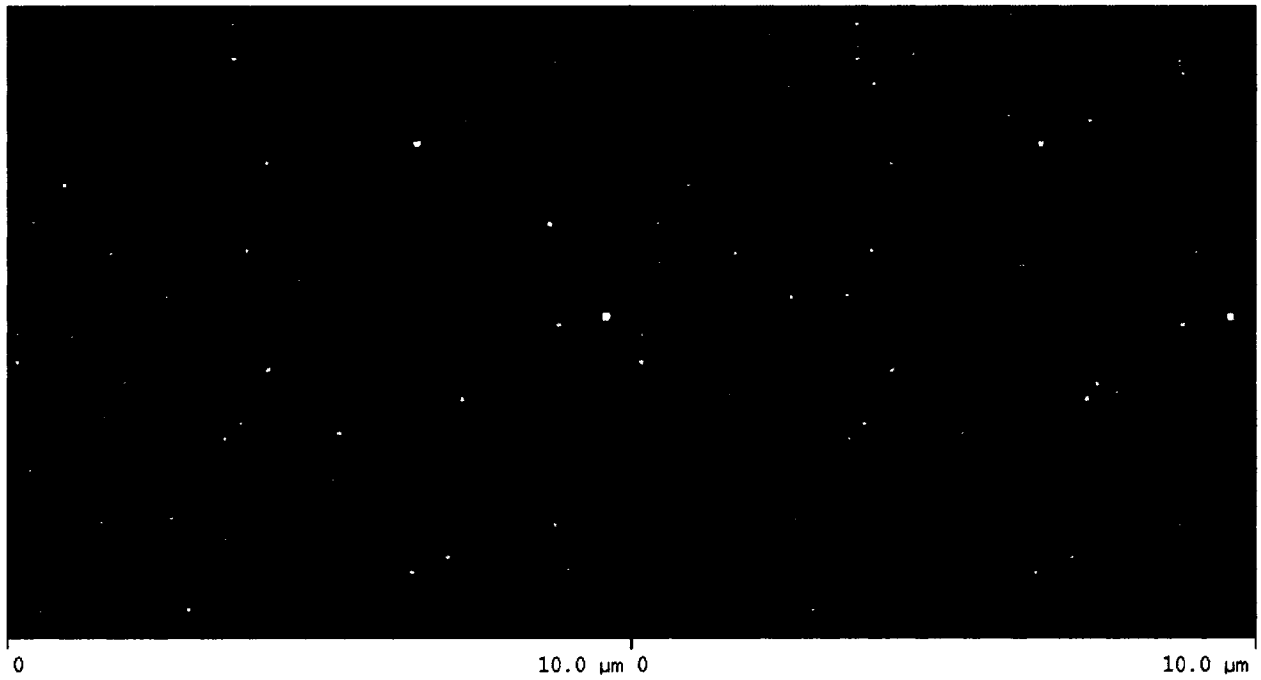

Figure 4-3. 10 x 10 μm AFM images for sample 4 listed in Table 4-2 with topography (left, scale is 10 nm) and phase (right, scale is 20°) showing the typical clean, large scale uniformity of the binary brush layer using the sequential, two-step grafting.

Treatment of PS-PAA binary brush layers in different selective solvents resulted in dramatic reorganization as seen in AFM images showing the switching of morphology after exposure to toluene and water (Figure 4-6).

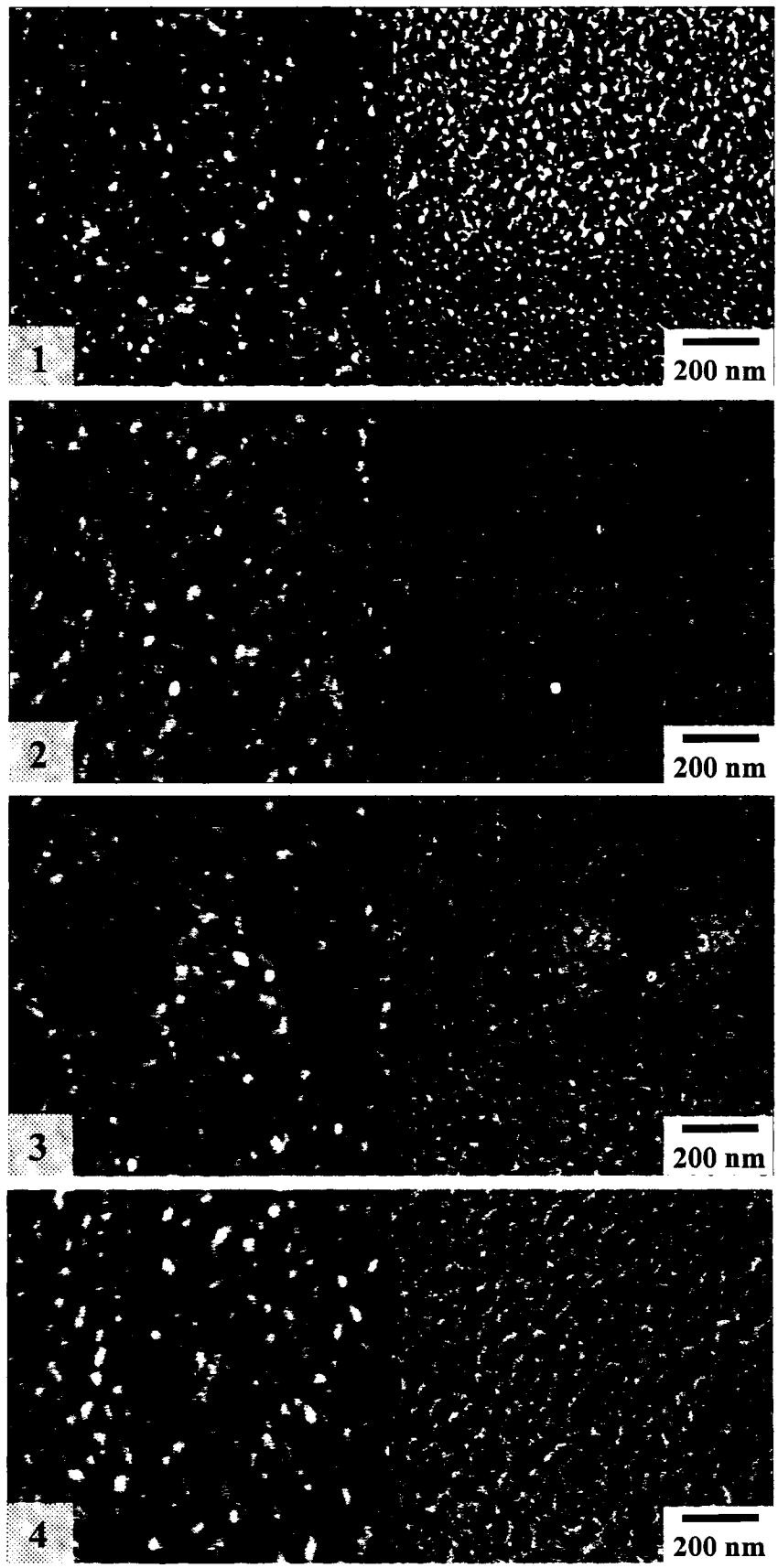

Figure 4-4. 1 x 1 μm AFM images, topography (left, scale is 3 nm) and phase (right, scale is 20°). Numbers correspond to sample numbers in Table 2.

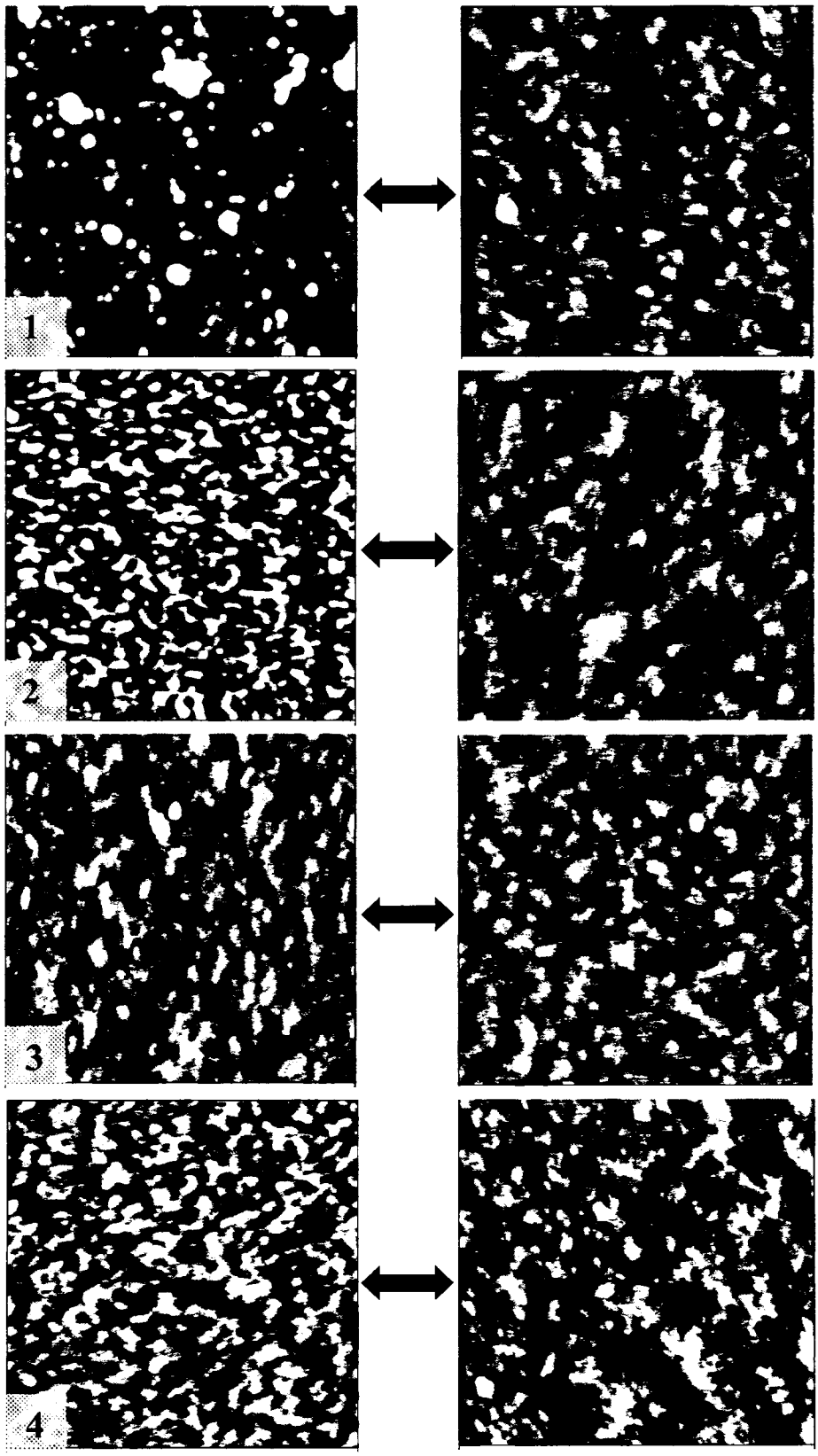

Figure 4-5. 400 x 400 nm topographical AFM images of different binary layers after exposure to n – butanol (left column) and TCE (right column). Z scale for topography is 3 nm and 20° for phase. Numbers correspond to sample numbers in Table 2.

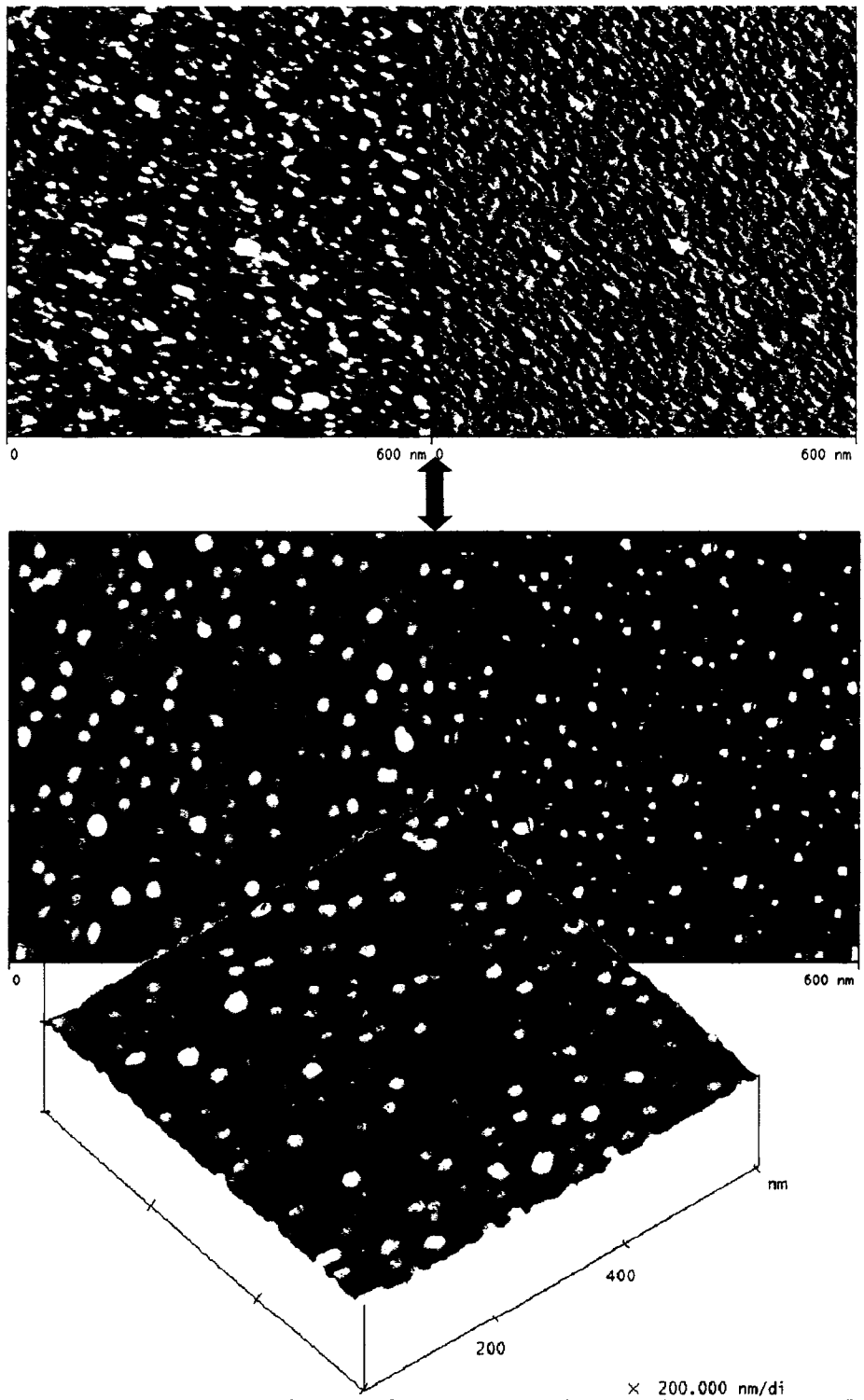

Figure 4-6. 600 x 600 nm AFM images for sample 3, (Table 2) topography (left) and phase (right), demonstrating switching after PBA hydrolysis to PAA. Top image is after exposure to toluene, middle is after water exposure, and bottom is 3D image of the binary layer after water exposure. Z scale for topography is 5 nm and 20° for phase.

Weakly ordered domain structure after toluene treatment is replaced with a well defined, dense packing of circular domains with 20 – 30 nm diameter after treatment with water. These lateral dimensions, much smaller than that typically observed for thick brush layers, result from the relatively low molecular weight and modest grafting density. The AFM tip instability on the top of these domains due to tip interaction with more than one material simultaneously resulted in apparent depletions of the tops and sharp change in phase contrast. This behavior indicates complex structure of the narrow domains with different composition in the center portion and along the edges of the domains, as was suggested for PS-PAA Y-shaped brushes.[38,39] Reorganization of surface morphology with predominant surface location of either PS or PAA chains resulted in more significant changes in the surface wettability than recorded for PS-PBA layers with contact angle changing from 60-65° to 85-90° in selective solvents (Figure 4-7). These contact angle changes by 15-20° for different binary brushes occur within the initial 100 minutes of treatment (Figure 4-7).

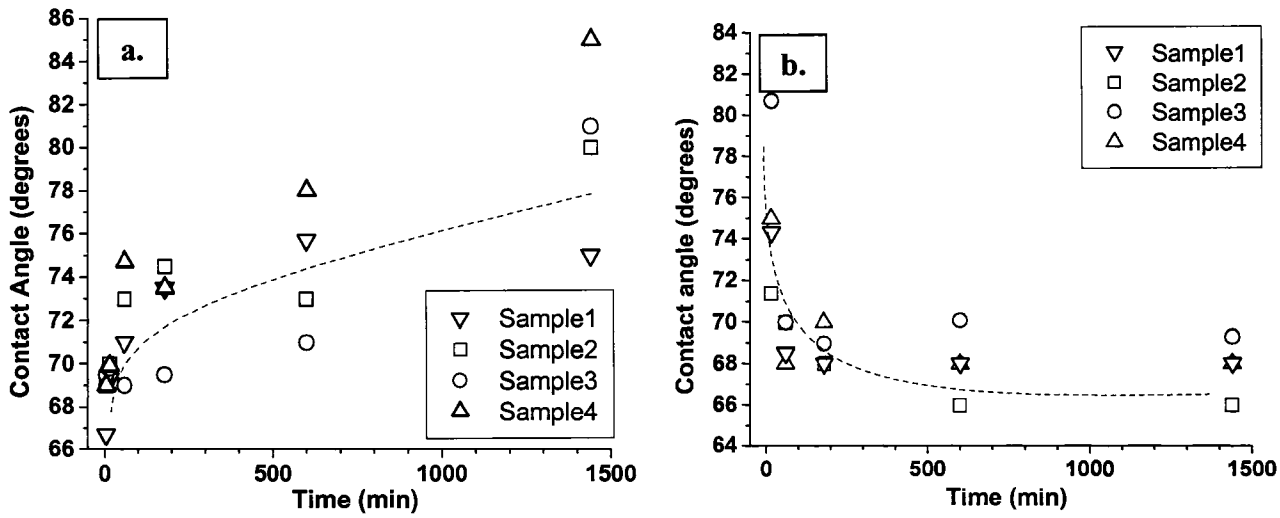

Figure 4-7. The kinetics for switching of surface wettability after toluene (a) and water (b) treatments, as measured by contact angle, for the binary brush layers (sample numbers correspond to Table 2) after hydrolysis. The time indicates the time immersed in solvent before measurement. The dashed lines are guides for the eye.

Preliminary studies of tribological properties. Tribological properties are greatly affected by the presence of thin polymeric surface layer with different chemical compositions and surface functionalities as demonstrated in Figure 4-8. The friction coefficient determined from repeating reciprocate sliding cycles is virtually constant for the hydrophobic glassy PS surface layers with different molecular weight and varies within 0.2-0.3 at low humidity (5%) with the lowest friction coefficient observed for **PS3** coating (Figure 4-8a). Increasing humidity resulted in lowering of the friction coefficient, especially in the initial stage (for number of cycles below 100) to below 0.2 that indicates an importance of the presence of thin water layer even on a hydrophobic glassy surface of the PS layer (Figure 4-

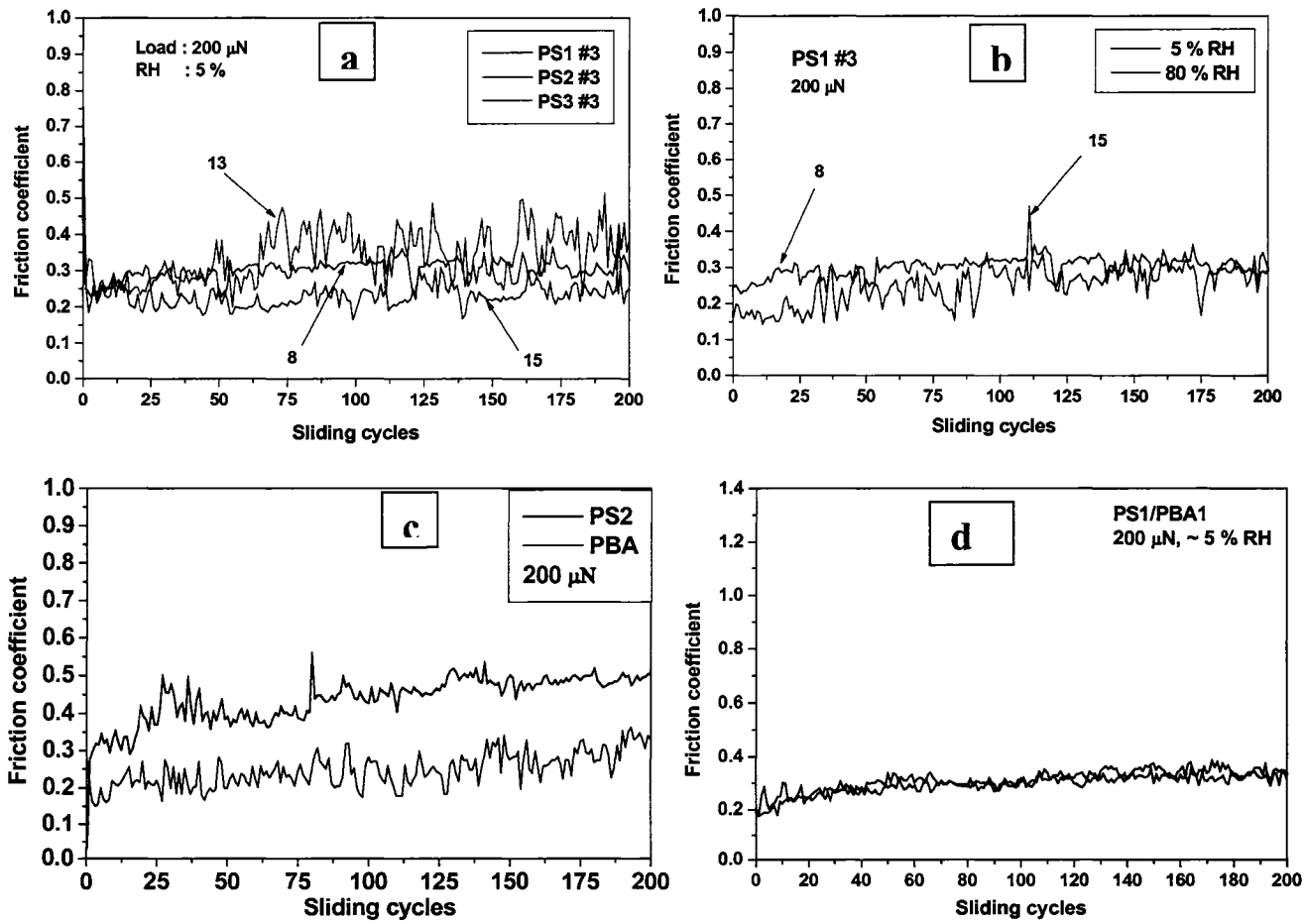

Figure 4-8. Friction coefficient versus number of sliding cycles for grafted PS# layers of different molecular weights at low humidity of 5% (a); for grafted PS1 layer at different humidity (b); for PS2 and PBA layers at low humidity (c); and for sample 1 (Table 2) of binary brush layer (d).

8b). The friction coefficient was higher for the rubbery surface layer of PBA reaching 0.38-0.44 for higher number of cycles at low humidity (Figure 4-8c) and even higher for increasing humidity (not shown). Both values are fairly similar to that observed for glassy and rubbery bulk polymers in macroscopic testing, and usually related to both stronger polar interactions and larger contact areas for rubbery materials. [60]

However, despite higher friction coefficient, grafted PBA rubbery layer with thickness of about 3 nm is much more wear resistant that the corresponding glassy layer. In fact, the worn track is less regular in PS coated silicon that in corresponding PBA coated silicon where no deep groves have been observed on SEM images (Figure 4-9). Moreover, the Auger electron spectroscopy shows striking difference in the wearing behavior of these surface layers (Figure 4-10). The original depth profile of all major chemical elements was very different for PS and PBA layers. Carbon concentration was the highest at the surface for the PS layer indicating a full coverage of the silicon surface with PS chains as was concluded from AFM data (Figure 4-10a). Oxygen concentrated mainly in the middle portion due to the presence of the silicon oxide layer of 1.1 nm as calculated from ellipsometry. Unlike, for the PBA layer significant oxygen presence was found directly on the surface due to the high

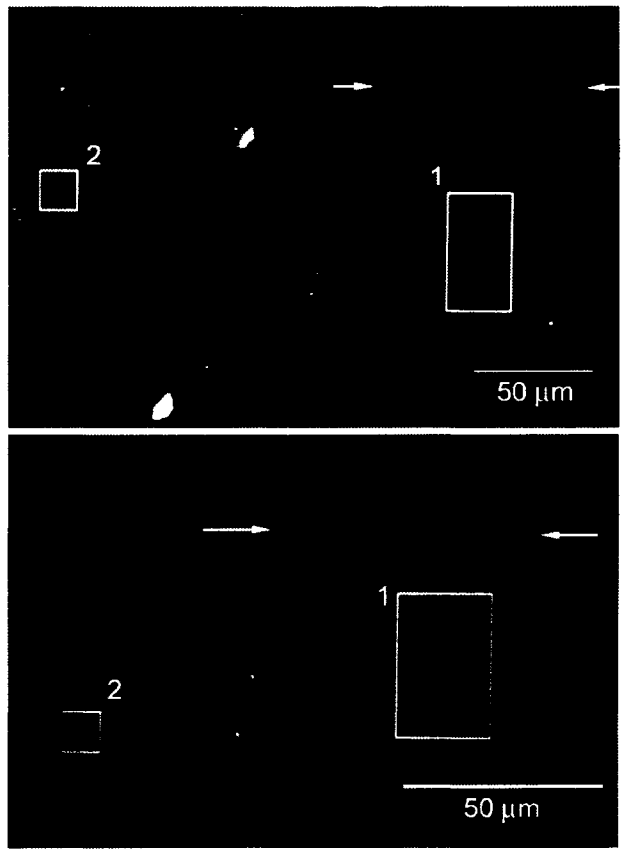

Figure 4-9. SEM images of intact and worn surface areas (vertical track on a right side as indicated by arrows) for PS1 (top) and PBA (bottom) grafted layers. Rectangular shapes show selected areas for AES analysis.

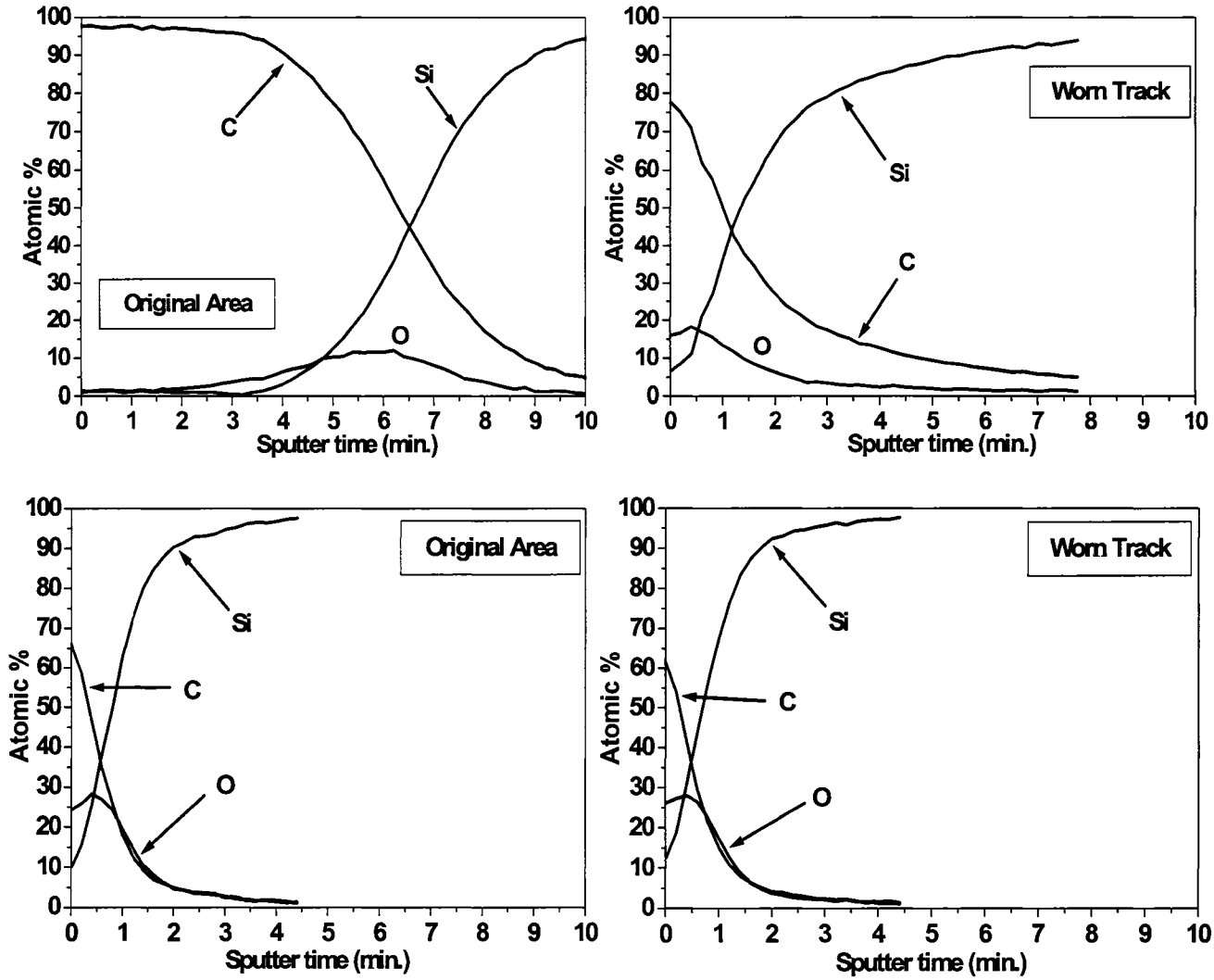

Figure 4-10. Auger analysis of an original, undamaged surface (a, b) compared to the worn areas (c, d) of the respective PS (a, c) and PBA (b, d) brush layers. The depth profile of C, O, and Si are shown in time-scale.

concentration of carboxylic groups in PBA backbones (Figure 4-10b). Wearing down the PS layer resulted in dramatic changes of the chemical composition indicating significant

deterioration of the PS layer and presence of oxidized polymer material and the exposed silicon oxide layer (Figure 4-10c). In contrary, signs of oxidation or the coating removal could not be found for the rubbery coating: the chemical composition of the PBA layer within the contact areas did not change at all as can be seen from elements profiles in Figure 4-10d. Thus, this layer demonstrated high recovery ability and restoration of its initial microstructure after being subjected to high normal and shear stresses due to large reversible elastic deformations of polymer chains below the glassy state.[61]

Finally, for the binary surface layer we observed very stable friction behavior at low humidity with the friction coefficient being very stable and low (within 0.2-0.3) despite the presence of rubbery phase (Figure 4-8d). The stability of the binary coatings can be associated with the presence of both stiff glassy microphase bearing the normal load and the rubbery domains providing elastic recovery. However, increasing humidity resulted in fast damaging of the binary coating due to increasing capillary forces as will be further addressed in forthcoming studies.

4.5 Acknowledgments

This research is supported by the National Science Foundation, grant CMS-0099868 and The National Research Laboratory Program of the Korean Ministry of Science and Technology. The authors thank Sergiy Peleshanko for worthy discussions and technical assistance.

4.6 References

1 Ionov, L.; Minko, S.; Stamm, M.; Gohy, J.-F.; Jérôme, R.; Scholl, A. *J. Am. Chem. Soc.* **2003**, *125*, 8302. Luzinov I.; Minko, S.; Tsukruk, V. V. *Prog. Polym. Sci.* **2004**, *29,* 635.

2 Bliznyuk, V. N.; Everson, M. P.; Tsukruk, V. V. *J. Tribology* **1998**, *120*, 489. Tsukruk, V. V.; Bliznyuk, V. N. *Langmuir* **1998**, *14*, 446. Sidorenko, A.; Houphouet-Boigny, C.; Villavicencio, O.; McGrath, D. V.; Tsukruk, V. V. *Thin Solid Films,* **2002**, *410,* 147. Peleshanko, S.; Sidorenko, A.; Larson, K., Villavicencio, O.; Ornatska, M.; McGrath, D. V.; Tsukruk, V. V. *Thin Solid Films,* **2002**, *406,* 233. Ahn, H.; Julthongpiput, D.; Kim, D. I.; Tsukruk, V. V. *Wear* **2003,** *255,* 801. Tsukruk, V. V.; Sidorenko, A.; Yang, H. *Polymer* **2002**, *43*, 1695. Sidorenko, A.; Julthongpiput, D.; Luzinov, I.; Tsukruk, V. V. *Tribol. Lett.* **2002**, *12*, 101.

3 Ito, Y.; Ochiai, Y.; Park, Y. S.; Imanishi, Y. *J. Am. Chem. Soc.* **1997**, *119*, 1619.

4 Galaev, I.; Mattiasson, B. *Trends Biotechnol.* **1999**, *17*, 335.

5 Jones, D. M.; Smith, R. R.; Huck, W. T. S.; Alexander, C. *Adv. Mater.* **2002**, *14*, 1130.

6 Aksay, I. A.; Trau, M.; Manne, S.; Honma, I.; Yao, N.; Zhou, L.; Fenter, P.; Eisenberger, P. M.; Gruner, S. M. *Science* **1996**, *273*, 892.

7 Dean, D.; Seog, J.; Ortiz, C.; Grdzinsky, A. J. *Langmuir* **2003**, *19*, 5526.

8 Rixman, M. A.; Dean, D.; Ortiz, C. *Langmuir* **2003**, *19,* 9357.

9 Qin, S. H.; Oin, D. Q.; Ford, W. T.; Resasco, D. E.; Herrera, J. E. *J. Am. Chem. Soc.* **2004**, *126*, 170.

10 Gomez, F. J.; Chen, R. J.; Wang, D. W.; Waymouth, R. M.; Dai, H. J. *Chem. Commun.* **2003**, 190.

11 Viswanathan, G.; Chakrapani, N.; Yang, H. C.; Wei, B. Q.; Chung, H. S.; Cho, K. W.; Ryu, C. Y.; Ajayan, P. M. *J. Am. Chem. Soc.* **2003**, *125*, 9258.

12 Artyukhin, A. B.; Bakajin, O.; Stroeve, P.; Noy, A. *Langmuir* **2004**, *20*, 1442.

13 Alexander, S.J. *J. Phys.* **1977**, *38*, 977.

14 de Gennes, P.G. *Macromolecules* **1980**, *13*, 1069.

15 Karim, A.; Tsukruk, V. V.; Douglas, J. F.; Satija, S. K.; Fetters, L. J.; Reneker, D. H.; Foster, M. D. *J. Phys. II* **1995**, *5*, 1441. Tsukruk, V. V. *Prog. Polym. Sci.* **1997**, *22*, 247. Tsukruk, V. V. *Adv. Mater.* **1998**, *10*, 253.

16 Zhao, B.; Brittain, W. J. *Prog Polym Sci* **2000**, *25*, 677. Zhao, B.; Brittain, W. J. *J. Am. Chem. Soc.* **1999**, *121*, 3557. Zhao, B.; Brittain, W. J.; Zhou, W. S.; Cheng, S. Z. D. *J. Am. Chem. Soc.* **2000**, *122*, 2407. Sedjo, R.; Mirous, B. K; Brittain, W. J. *Macromolecules* **2000**, *33*, 1492.

17 Wittmer, J.; Johner, A.; Joanny, J. F. *Colloids Surf., A* **1994**, *86,* 85.

18 Sidorenko, A.; Tokarev, I.; Minko, S.; Stamm, M. *J. Am. Chem. Soc.* **2003**, *125*, 12211.

19 **Bhushan, B. Ed. *Tribology Issues and Opportunities in MEMS* ; Kluwer Academic Publishers: Dordrecht, 1997.**

20 Bates, F. S.; Fredrickson, G. H. *Annu. Rev. Phys. Chem.* **1990**, *41*, 525.

21 Krausch, G.; Magerle, R. *Adv. Mater.* **2002**, *14*, 1579.

22 Luzinov, I.; Julthongpiput, D.; Tsukruk, V. V. *Macromolecules* **2000**, *33*, 7629.

23 Tsukruk, V. V.; Ahn, H. S.; Kim, D.; Sidorenko, A. *Appl. Phys. Lett.* **2002**, *80*, 4825.

24 Tsukruk, V. V.; Sidorenko, A.; Gorbunov, V. V.; Chizhik, S. A. *Langmuir* **2001**, *17*, 6715.

25 Sidorenko, A.; Ahn, H. S.; Kim, D. I.; Yang, H.; Tsukruk, V. V. *Wear* **2002**, *252*, 946.

26 Sidorenko, A.; Minko, S.; Schenk-Meuser, K.; Duschner, H.; Stamm, M. *Langmuir* **1999**, *15*, 8349.

27 Minko, S.; Patil, S.; Datsyuk, V.; Simon, F.; Eichhorn, K. J.; Motornov, M.; Usov, D.; Tokarev, I.; Stamm, M. *Langmuir* **2002**, *18*, 289.

28 Minko, S.; Usov, D.; Goreshnik, E.; Stamm, M. *Macromol. Rapid. Comm.* **2001**, *22*, 206.

29 Soga, K. G.; Zuckermann, M. J.; Guo, H. *Macromolecules* **1996**, *29*, 1998.

30 Marko, J. F.; Witten, T. A. *Phys. Rev. Lett.* **1991**, *66*, 1541.

31 Müller, M. *Phys. Rev. E* **2002**, *65*, 30802.

32 Minko, S.; Muller, M.; Usov, D.; Scholl, A.; Froeck, C.; Stamm, M. *Phys. Rev. Lett.* **2002**, *88*, 5502.

33 Boven, G.; Oosterling, M. L. C. M.; Challa, G.; Schouten, A. J. *Polymer* **1990**, *31*, 2377.

34 Prucker, O.; Ruhe, J. *Macromolecules* **1998**, *31*, 592.

35 Prucker, O.; Rühe, J. *Macromolecuels* **1998**, *31*, 602.

36 Zhao, B. *Polymer* **2003**, *44*, 4079.

37 Zhao, B.; He, T. *Macromolecules* **2003**, *36*, 8599. Zhao, B.; Haasch, R. T.; MacLaren, S. *J. Am. Chem. Soc.* **2004**, *126*, 6124.

38 Julthongpiput, D.; Lin, Y. H.; Teng, J.; Zubarev, E. R.; Tsukruk, V. V. *J. Am. Chem. Soc.* **2003**, 125, 15912.

39 Julthongpiput, D.; Lin, Y. H.; Teng, J.; Zubarev, E. R.; Tsukruk, V. V. *Langmuir* **2003**, *19*, 7832.

40 Lemieux, M.; Usov, D.; Minko, S.; Stamm, M.; Shulha, H.; Tsukruk, V. V. *Macromolecules* **2003**, *36*, 7244.

41 Lemieux, M.; Minko, S.; Usov, D.; Stamm, M.; Tsukruk, V. V. *Langmuir* **2003**, *19*, 6126.

42 Luzinov, I.; Julthongpiput, D.; Liebmann-Vinson, A.; Cregger, T.; Foster, M. D.; Tsukruk, V. V. *Langmuir* **2000**, *16*, 504.

43 Tsukruk, V. V.; Luzinov, I.; Julthongpiput, D. *Langmuir* **1999**, *15*, 3029.

44 Fisch, W.; Hofmann, W. *Macromol. Chem. Phys.* **1961**, *44-6*, 8.

45 Motschmann, H.; Stamm, M.; Toprakcioglu, C. *Macromolecules* **1991**, *24*, 3681.

46 Xie, R.; Karim, A.; Douglas, J. F.; Han, C. C.; Weiss, R. A. *Phys. Rev. Lett.* **1998**, *81*, 1251.

47 Koneripalli, N.; Singh, N.; Levicky, R.; Bates, F. S.; Gallagher, P. D.; Satija, S. K. *Macromolecules* **1995**, *28*, 2897.

48 Handbook of fine chemicals and laboratory equipment, Aldrich®, **2003**. *Polymer Handbook*, 4th ed.; Brandrup, J., Immegurt, E. H., Grulke, E. A., Eds.; John Wiley & Sons: New York, 1999.

49 Ratner, B.; Tsukruk, V.V. Eds. *Scanning Probe Microscopy of Polymers.*; ACS Symposium Series; American Chemical Society: Washington, D.C., **1998**; Vol. 694.

50 Tsukruk, V. V. *Rubber Chem. Technol.* **1997**, *70*, 430.

51 Magonov, S. N.; Cleveland, J.; Elings, V.; Denley, D.; Whangbo, M. H. *Surf. Sci.* **1997**, *389*, 201.

52 Radmacher, M.; Tilmann, R. W.; Gaub, H. E. *Biophys. J.* **1993**, *64*, 735.

53 Henn, G.; Bucknall, D. G.; Stamm, M.; Vanhoorne, P.; Jerome, R. *Macromolecules* **1996**, *29*, 4305.

54 Higgins, A. M.; Jones, R. A. L. *Nature* **2000**, *404*, 476.

55 Lu, G.; Li, W.; Yao, J. M.; Zhang, G.; Yang, B.; Shen, J. C. *Adv. Mater.* **2002**, *14*, 1049.

56 Minko, S.; Luzinov, I.; Luchnikov, V.; Muller, M.; Patil, S.; Stamm, M. *Macromolecules* **2003**, *36*, 7268.

57 Julthongpiput, D.; LeMieux, A.; Tsukruk, V. V. *Polymer* **2003**, *44*, 4557.

58 Siqueira, D. F.; Kohler, K.; Stamm, M. *Langmuir* **1995**, *11*, 3092.

59 Luzinov, I.; Julthongpiput, D.; Malz, H.; Pionteck, J.; Tsukruk, V. V. *Macromolecules* **2000**, *33*, 1043.

60 Bhushan, B. Ed. *Micro/Nanotribology and Its Applications*; Kluwer Academic Publishers: Dordrecht, The Netherlands, 1997. Luzinov, I.; Julthongpiput, D.; Gorbunov, V.; Tsukruk, V. V. *Tribol. Int.* **2001**, *34*, 327.

61 Tsukruk, V. V. *Adv. Mater.* **2001**, *13*, 95.

Chapter 5

Adaptive Nanomechanical Response of Stratified Polymer Brush Structures

A paper submitted to *Langmuir*

M. C. LeMieux[*1], *S. Peleshanko*[1,2], *K. D. Anderson*[1], *V. V. Tsukruk*[1,2]

[1] Department of Materials Science and Engineering, Iowa State University, Ames, IA 50011

[2] School of Materials Science and Engineering, Georgia Institute of Technology, Atlanta, GA 30332

5.1 Abstract

We have fabricated a stratified polymer brush architecture through facile, room temperature UV-initiated polymerization using a UV-sensitive SAM with temperature-sensitive pNIPAAM layer confined beneath hydrophobic layer. AFM morphology and ellipsometry measurements were measured at each grafting step, along with XPS measurements of the overall layer to verify layer growth. The strong characteristic LCST behavior of pNIPAAM was observed in water, with a 100% change in thickness above and below this transition. The AFM nanomechanical results demonstrate vertical gradients in the depth profiling of the elastic modulus with the elastic behavior tunable to a desired state by environment temperature. These temperature-sensitive, adaptive polymer layers with pNIPAAM layer "hidden" beneath the rubbery, hydrophobic PBA topmost layer represent and interesting example of the nanoengineering surfaces with their properties such as

[*] M.C.L.: Primary researcher, helped with sample prep, all AFM/characterization experiments, writer of all drafts

adhesion, elastic modulus and multi-level structural reorganization responsive to fluidic and temperature variations which can be important when designing polymer surfaces for biological purposes such as implant coatings, cell-surface mimicry, or drug delivery vehicles.

5.2 Introduction

Highly complex biomaterials research is currently a very intense field requiring polymer scientists to develop synthetic replicas to mimic biological internal structures. Nearly all important biological structures have evolved through a bottom-up "synthesis", in which the final *nanoscaffolds* have a common feature of possessing a hierarchal structure with each level performing a separate, different function.[1,2] Engineering new polymer surfaces involves designing complex architectures with features such as graded branching and composition that will lead to novel material properties in terms of mechanical behavior, adaptability, and functionality. Polymer brushes, which possess an intrinsic remarkable stimuli responsive nature, represent one area of intense research in polymer science regarding adaptive surfaces.[3,4] Another area that will be key for expounding the nanotechnology frontier from the polymer science aspect is macromolecular architecture engineering.[5,6,7,8] The combination of the two will lead to new surfaces imperative for next generation nanoscale devices with novel conformations (confinements) inducing secondary intramolecular interactions leading to unusual nanomechanical and nanotribological properties.[9,10,11,12,13,14,15,16]

Nanoscale devices and their operating environments require adaptive surfaces constructed with "smart" properties that can not only sense or respond to environmental stimuli, but also be robust and possess tailored, on-demand physical properties.[17,18,19,20] Thus, polymer surface modification, which inherently provides the ability to control and change surface composition, allowing on – demand properties, is becoming increasingly significant for practical applications in fields like nanoscale lubrication, sensing and biocompatibility[21,22,23,24,25,26,27,28], or the exciting advancement of functional carbon nanotube devices.[29,30,31,32] Polymer brush layers are considered ideal choices in such applications for

several reasons. They are chemically tethered to the surface at one end, virtually any chemistry can be designed into the layer depending on intended surface interactions, and the high grafting density combined with uniformity in composition, thickness, and structure allows the *entire* surface to respond to local environmental stimuli.[3,9,33,34,35,36,37,38]

On the other hand, it is recognized that the stretched conformation of brush chains due to overlapping is the origin of intrinsic properties such as high compression resistance and excellent mechanical response.[35,39,40,41] Grafted multi-component (mixed) brush layers allow for supreme interfacial manipulation.[42] Polymer brush layers with vertically graded branching/properties normal to the surface would be an ideal candidate in both cases. Rather than grafting two homopolymer brushes to create a mixed binary brush, an alternative route to responsive surfaces is grafting block copolymers of two chemically different blocks. These systems are attractive due to the very rich and interesting surface morphologies that are possible depending on block length ratios and interactions between the two blocks relative to each other, and with the local environment.[43,44] The main difference between these brushes and binary brushes is that the phase domain structure is usually well ordered and periodic allowing them to be useful in applications of nano-patterning and templates.[45,46]

One type of brushes that is receiving intense interest consists of an architecture in which one block serves as a backbone filled with initiators (macromonomer) from which other polymer chains can be attached to[47] via a "grafting through" process[48]. These are known in the literature as comb-graft copolymers. The vast majority of research dealing with these molecules has been in solution where they adopt a cylindrical configuration, thus they are labeled as bottle-brushes, or cylindrical brushes. The interest here in taking this a step further and developing complex macromolecular architectures *within* grafted brush layers is related to the potential of controlled vertical gradients in brush composition and branching, and thus forward logic for nanomechanical design. Moreover, by using a macromonomer approach not only can extremely high branching densities be achieved, but also *selective* branching. Selective branching here implies attachment only at the top of the main backbone chain (not its entire length as in a cylindrical brush), leading to a brush-block-coil

copolymer.[49] This can lead to uniquely enhanced backbone strengthening due to steric crowding, increased intramolecular interactions, and tailor-made chemical incompatibility between polymer segments.[50] Not until very recently have such complex brushes been able to be grown from the surface of silicon substrates due to advancements in polymerization methods such as ATRP, and the breakthrough RAFT polymerization technique.[51, 52] Furthermore, dense, uniform grafted brush layers consisting of these molecules have yet to be reported in the literature. Luzinov et al. have grafted binary brushes to a PGMA layer that serves as a "carpet" of functional epoxy grafting sites.[53] However, this is an extremely thin layer (monolayer, 1.5 nm thick) with a lack of physical properties and response mechanism. Sheiko et al. have established methods to graft side chains to a macroinitiator backbone with a gradient in spacing intervals along the backbone.[54] The authors are not concerned with fabricating grafted layers of these molecules as they just deposit individual molecules on the surface and observe their structure.[55,56]

Our aim is to build on this approach by fabricating novel polymer architectures in which one block is some environmentally responsive polymer (strong response to thermal or pH fluctuations) that is capped with a macroinitiator (macromonomer) in which other polymer chains can be *grown from,* or attached to. However, the intention here is to have a very asymmetrical backbone in terms of length of the surface block (very long), and the macroinitiator block (very short), which will result in a "palm-tree" like polymer (Figure 5-1). The main points we address in this paper are: (1) To synthesize *vertically-segregated brush layers* using facile UV-initiated polymerization; (2) To characterize the morphology at each synthesis step, and the overall morphology of the complex layer; (3) To design a vertically graded nanomechanical response, which can be tuned by external temperature. With the "palm-tree" configuration, it is anticipated that due to the relatively high chain density at the top of the layer, a multi-layer type structure can result with varying degrees of vertical gradient.

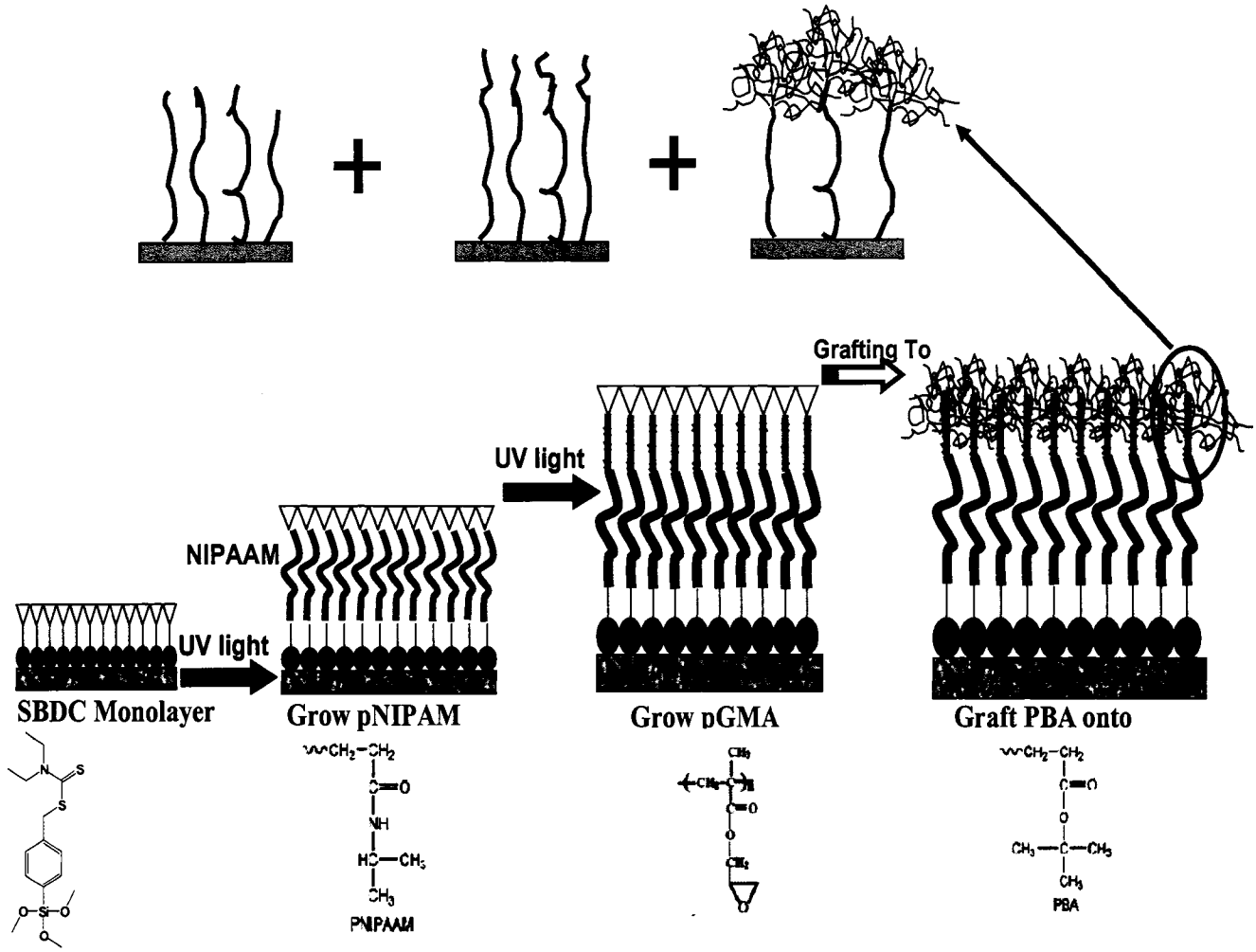

Figure 5-1. Schematic representation showing overall layer construction and chemical structures starting with the SBDC monolayer, UV-initiated polymerization of pNIPAAM, UV-initiated polymerization of pGMA, and finally, grafting of COOH-PBA.

5.3 Experimental

Materials. N,N – (Diethylamino)dithiocarbamoylbenzyl(trimethoxy) silane (SBDC) was purchased from Gelest with 95% purity, and were further distilled. The monomers N-isopropylacrylamide (NIPAAM), glycidyl methacrylate (GMA) were purchased from

Aldrich (Milwaukee, WI) with >99% purity. NIPAAM was recrystallized from hexane, and vacuum dried for 24 hours. GMA was distilled and stored under argon at -15°C. Carboxyl acid – terminated poly(butyl acrylate) (M_n: PBA = 42,500 g/mol with M_w/M_n=1.06) was obtained from Polymer Source, Inc. Anhydrous toluene and DMF were obtained from Aldrich, further dried with sodium, distilled off prior to use, and stored in a nitrogen-filled glovebox with relative humidity not exceeding 2%. All other solvents were used as received. The silicon wafer {100} substrates were first cleaned in an ultrasonic bath for 30 minutes, placed in a hot (90°C) bath (3:1 concentrated sulfuric acid: 30% hydrogen peroxide) for 1 hour, and then rinsed with nanopure water (18 MΩ cm, Nanopure).

Layer Fabrication. An overall schematic of multi-step layer fabrication is presented in Figure 5-1. The freshly cleaned silicon wafers were submerged in 4% toluene solutions of SBDC inside a nitrogen glovebox (RH < 1%) for 2 hours to form the UV-initiating self-assembled monolayer (SAM). The wafers were transferred to individual custom-made rectangular quartz test tubes. NIPAAM (wt10% in water) was transferred to the sealed test tube by syringe, and the solution with wafer was further purged with argon for at least 1 hour. At the next step, NIPAAM was polymerized at room temperature by exposing the tube to UV irradiation at 5 mW/cm^2. This was found to be optimal as higher power resulted in immediate crosslinking and gelation of the solution, while less power resulted in extremely slow or completely suppressed growth. The growth rate was found to be roughly 10nm/hour as verified by a series of data from ellipsometry and atomic force microscopy (AFM). After polymerization, the pNIPAAM layer was rinsed three times in ethanol, sonicated for 30 minutes in ethanol, and rinsed three more times. At the next step, the wafer was put into a fresh sealed test tube, and GMA (wt10% in DMF) was added by syringe. Polymerization took place after UV-exposure of $3mW/cm^2$ for 1 hour, which corresponded to 1-2nm of pGMA as verified by ellipsometry and AFM. Afterwards, the sample was cleaned as in the previous step, except with DMF in this case. Finally, the PBA layer was added via a grafting to process with the available epoxy groups in pGMA. The PBA solutions were prepared in DMF at 5.0 wt% polymer, and spin coated onto the brush modified silicon wafers at 3000

RPM. The samples were then annealed to facilitate grafting between the epoxy and carboxyl acid groups [57], and rinsed and sonicated in the same fashion as described above with DMF.

Characterization. All thickness measurements were obtained with a COMPEL Automatic Ellipsometer (InOm Tech, Inc.) with an incident angle of 70° at λ=532nm.[58] Contact angle was measured with a sessile drop method using 2 μL droplets of nanopure water, which were captured with a custom-built digital microscope. XPS was done with a Perkin-Elmer Multitechnique Chamber, model 5500. The etching rate was measured to be 1nm/min as measured against a SiO_2. AFM (MultiMode and Dimension 3000, Veeco Metrology) was used for topographical and phase imaging in air according to the procedures adapted in our lab.[59,60] Unless otherwise noted, all AFM images were obtained using the light tapping regime, governed by the setpoint ratio (rsp), which is defined as the ratio of operating setpoint (amplitude) to the free oscillating amplitude of the cantilever. The attractive regime, or light tapping, is characterized by an rsp of 0.9 – 1, while the repulsive regime, or hard tapping, has rsp of 0.4 – 0.7. AFM tips were MikroMasch (Talin, Estonia) V-shaped, contact tips with nominal spring constant ranging from 1 – 6 N/m. We used softer contact tips in the noncontact regime in order to get suitable scans of the soft NIPAAM surface at room temperature. The tips had radius less than 30 nm, which was determined by scanning a gold nanoparticle reference sample.[61] AFM scratch tests at each temperature were conducted with a sharp needle. After the scan of the scratched area was obtained, the average thickness in fluid was obtained over a 10x10μm area with height histogram distribution.

Force volume mode, which utilizes the collection of the AFM force distance curves (FDC) over selected surface areas, was used for nanomechanical analysis of the brush layers. A single FDC obtains the forces acting on the tip as it approaches to and retracts from a point on the sample surface.[62] Obtaining arrays of FDCs allows for the micromapping of the mechanical properties of polymer surfaces with nanometer scale resolution, while obtaining topographical information simultaneously.[63,64] Typically, we collected 16x16 arrays over a 3x3 μm^2 surface areas to do micromapping. Data collected were processed using an MMA software package developed in our lab which provides means for calculation of localized

elastic modulus.[65] The loading curves, the elastic modulus, reduced adhesive forces, and surface histograms of elastic moduli and adhesive forces were obtained from experimental images as described elsewhere.[65,66] Spring constants of cantilevers were determined from the resonant frequencies and the tip-on-tip method according to the procedures described earlier.[67, 68] The tips used for MMA probing were silicon nitride with radius of 60 – 90 nm, and spring constant ranging from 0.1 to 0.8 N/m.

Switching of the brushes. The brushes were switched to drive the strong collapse/swelling of NIPAAM sub-layer above and below LCST (32°). The brushes had to be placed in a fluid environment (water) to drive this phase transition. The samples were placed on a Peltier heating/cooling stage (Melcor Co.) that was heated to the desired temperature via the interfaced thermal controller (ILX Lightwave) with resolution of 0.001°C, and stability of ± 0.0005°C over 24 hours. The fluid (water) was injected into the system by taking advantage of capillary forces between AFM tip and sample. After adding water, the system was allowed two hours to reach equilibrium after temperature change.

5.4 Results and Discussion

Study of layer growth. The foundation of the branched hierarchal polymer brush is the stable formation of the SBDC monolayer, which is the UV initiating SAM (Fig. 5-1). It should be noted here that this initiator is advantageous for a few reasons, the main reason being that is nonreactive with nearly all vinyl monomers.[69] Furthermore, the "living" nature of the dithiocarbamyl radical has been well documented and shown to be reversible[70], allowing easy reinitiation for polymerization of different monomers, making it ideal to use in these complex multicomponent brushes. Most importantly, this photoiniferter technique leads to the ability to conduct RAFT polymerization at room temperature without the need for an elaborate setup.

The monolayer was optimized with several iterations of coating parameters (concentration and assembly time). Once the reaction was terminated with rinsing, the wafers were either kept in solution and protected from light, or immediately scanned with

AFM. AFM images of the SBDC monolayer reveal a highly uniform and clean layer formation on the large scale, with surface RMS roughness measured over a 1x1 μm^2 area of 0.2 nm (Figure 5-2). Theoretical estimates SBDC SAM thickness for an ideal close-packed monolayer is about 1.4 nm.[71] This thickness was confirmed with ellipsometry, which along with very smooth surface morphology indicated the formation of uniform SAM with up-right orientation of molecules (Table 5-1). This result is critical as it represents that this particular dithiosilane as been used in UV initiated RAFT polymerization.

Table 5-1. Characteristics of the surface layers.

Layer	Thickness (nm)	Microroughness (nm)	Contact angle (°)	Elastic modulus (MPa)
SBDC SAM	1.4	0.2	60	NA
pNIPAM	19	0.9	70	NA
pGMA	2	0.3	54	NA
PBA-COOH	5	0.6	75	NA
Total film				
Dry state	25	0.6	NA	60
Water, 10°C	34	1.8		15
Water, 50°C	17	1.3		45

At a UV light intensity of 5mW/cm^2, an optimal layer growth of roughly 10nm/hour was achieved. The process used here was more empirical; a suitable medium between gelation and reasonable layer growth, that was monitored at each iteration with ellipsometry. Higher intensities resulted in quick gelation in the system due to excessive crosslinking between side chains or formations in the bulk solution. On the other hand, lower intensities resulted in extremely slow and non-uniform growth. The kinetics involving the polymerization on a silicon surface from this iniferter monolayer are beyond the scope of this

paper and it had been studied before.[69] It was instrumental to keep the initial pNIPAAM layer to around 20 nm in order to observe a vertical gradient.

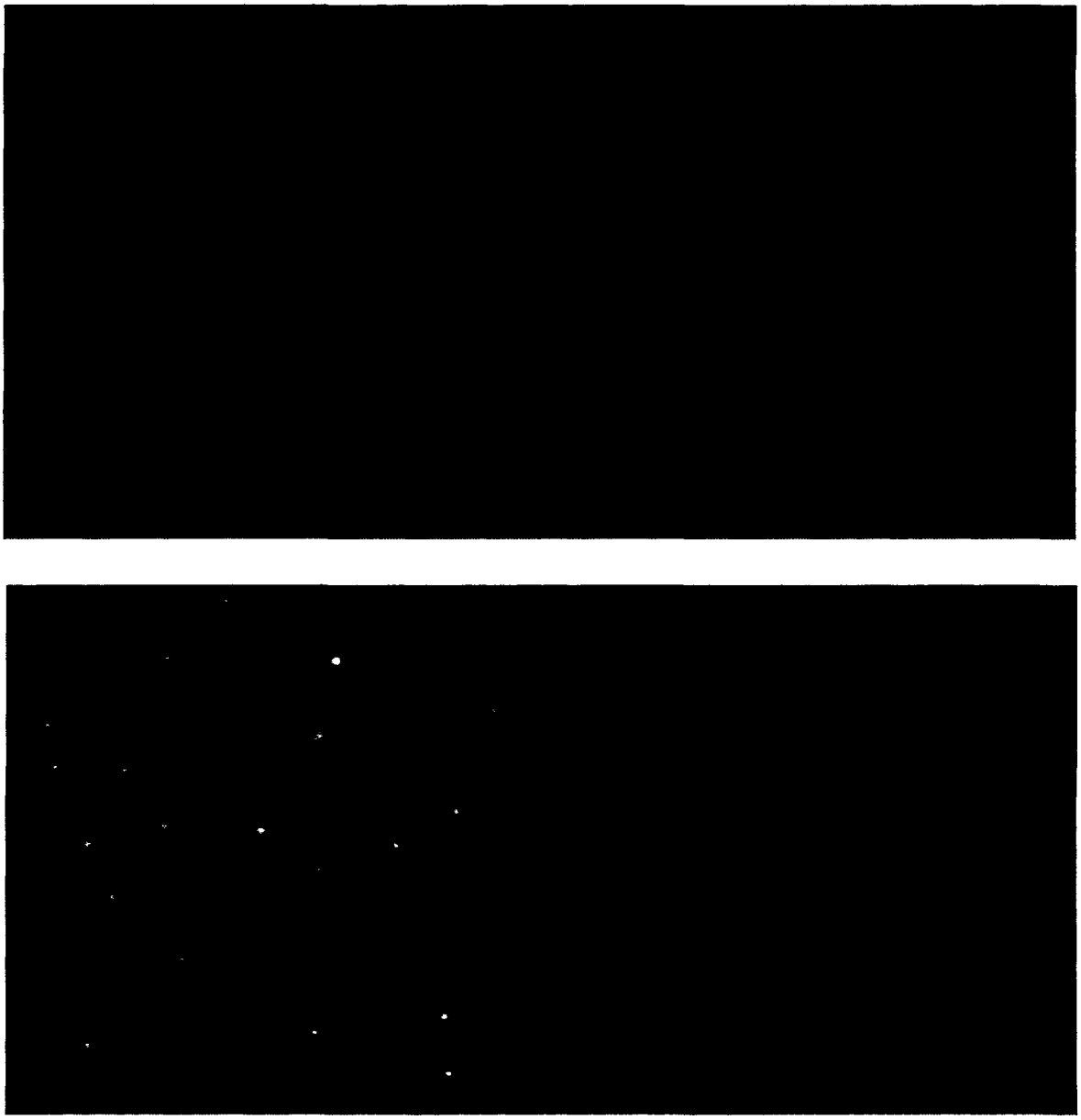

Figure 5-2. AFM tapping mode images (topography and phase) of the SBDC monolayer at 10x10μm (top) and 1x1μm (bottom). Z-scale is 5nm for topography and 30° for phase.

The presence of pNIPAAM was verified with ellipsometry measurements, AFM, and XPS (see below). The pNIPAAM dry thickness of all samples was within 19 ± 1 nm (Table 1). The dry state AFM images reveal a fine, contamination free morphology with surface RMS roughness around 1 nm (Figure 5-3). In addition, the light tapping regime during scanning was necessary to avoid instabilities while scanning the extremely soft pNIPAAM below LCST, another characteristic proving the presence of a strongly attached pNIPAAM layer.[72]

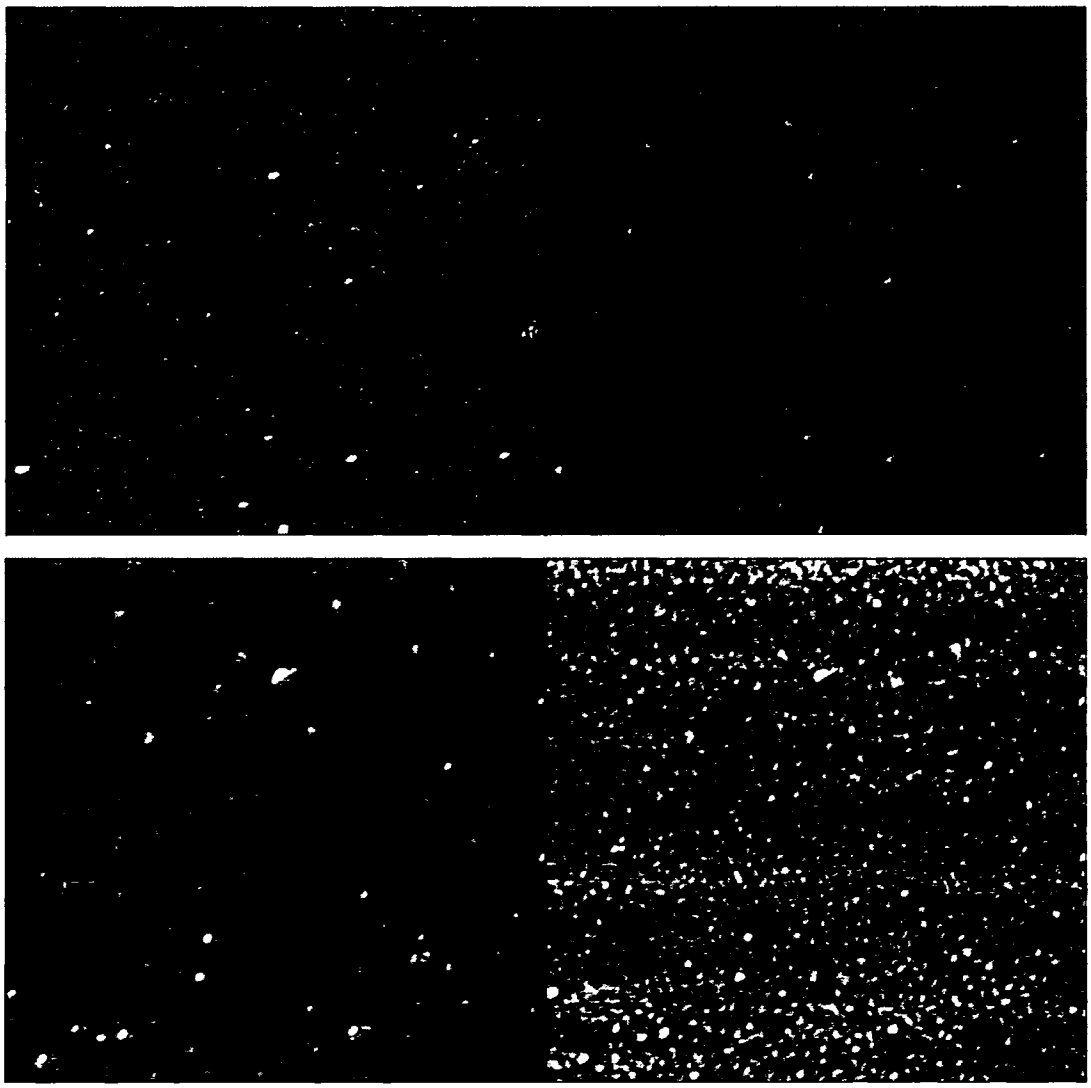

Figure 5-3. AFM tapping mode images (topography and phase) at room temperature of the as grown first grafted layer (NIPAAM) by UV-RAFT polymerization. Top is 10x10 μm and bottom is 1x1μm; Z-scale is 5nm for topography and 30° for phase.

The next step was deposition of GMA to act as a macroinitiator (Fig. 5-1). Polymerization was carried out below pNIPAAM LCST to keep the chains swollen in the solvent making them more accessible to GMA monomer. Figure 5-4 represents the brush after copolymerization of the GMA macroinitiator with pNIPAAM. As can be seen, although the surfaces remain relatively smooth on the large scale (RMS roughness is 1.2 nm), the morphology changes significantly from the pure pNIPAAM layer. In addition, contact angle dropped from 70° with the pure pNIPAAM layer, to 54° with the addition of pGMA. The thickness of 2 ± 0.5nm indicated that each pGMA chain attached to a pNIPAAM has 6-7 grafting sites available for incoming polymer in the subsequent 'grafting-to' stage to complete the topmost layer (Fig. 5-1). Thus, an important aspect of these complex brushes realized by grafting onto a macroinitiator is that by incorporating a 2nm thick "grafting plane", the availability of grafting sires can be much better than that typical for a monolayer of anchoring SAMS on a stiff substrate.[73,74]

The final fabrication step was to attach PBA to the available grafting sites (Fig. 5- 1). When preformed COOH terminated PBA polymer was grafted to the pGMA macromonomer, the measured thickness was 5 ±1nm (Table 1). This value is higher than the 3nm typical for this molecular weight PBA via the grafting to epoxy-terminated SAMs.[75,76] An indication of having high neighboring chain interaction and potentially significant entropic effects is to be in the polymer brush regime, in which the interchain distance is substantially less than the radius of gyration of the corresponding free polymer chain.[35] For the PBA used here, the radius of gyration has been calculated as 2.2 nm.[75] Thus, the grafting distance was less than the radius of gyration of these PBA chains, indicating that the chains are indeed in a stretched, brush-like conformation. AFM images of the final topmost PBA layer shown in Figure 5-5 demonstrate a clean and homogenous surface with microroughness not exceeding 1.5 nm, indicating extremely homogeneous and uniform grafting.

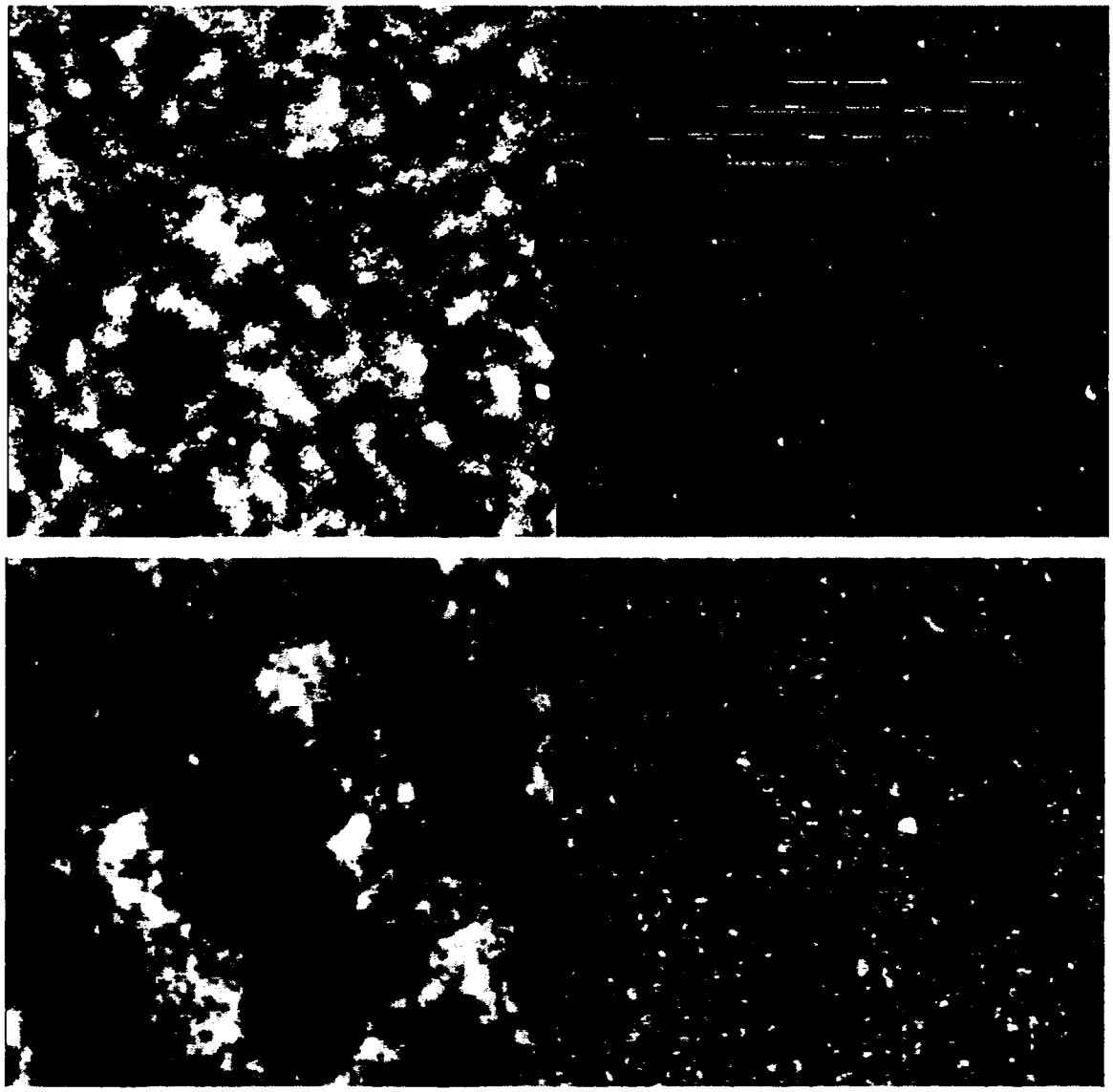

Figure 5-4. AFM tapping mode images (topography and phase) at room temperature of pGMA macromonomer. Top is 10x10 μm and bottom is 1x1μm; Z-scale is 5nm for topography and 30° for phase.

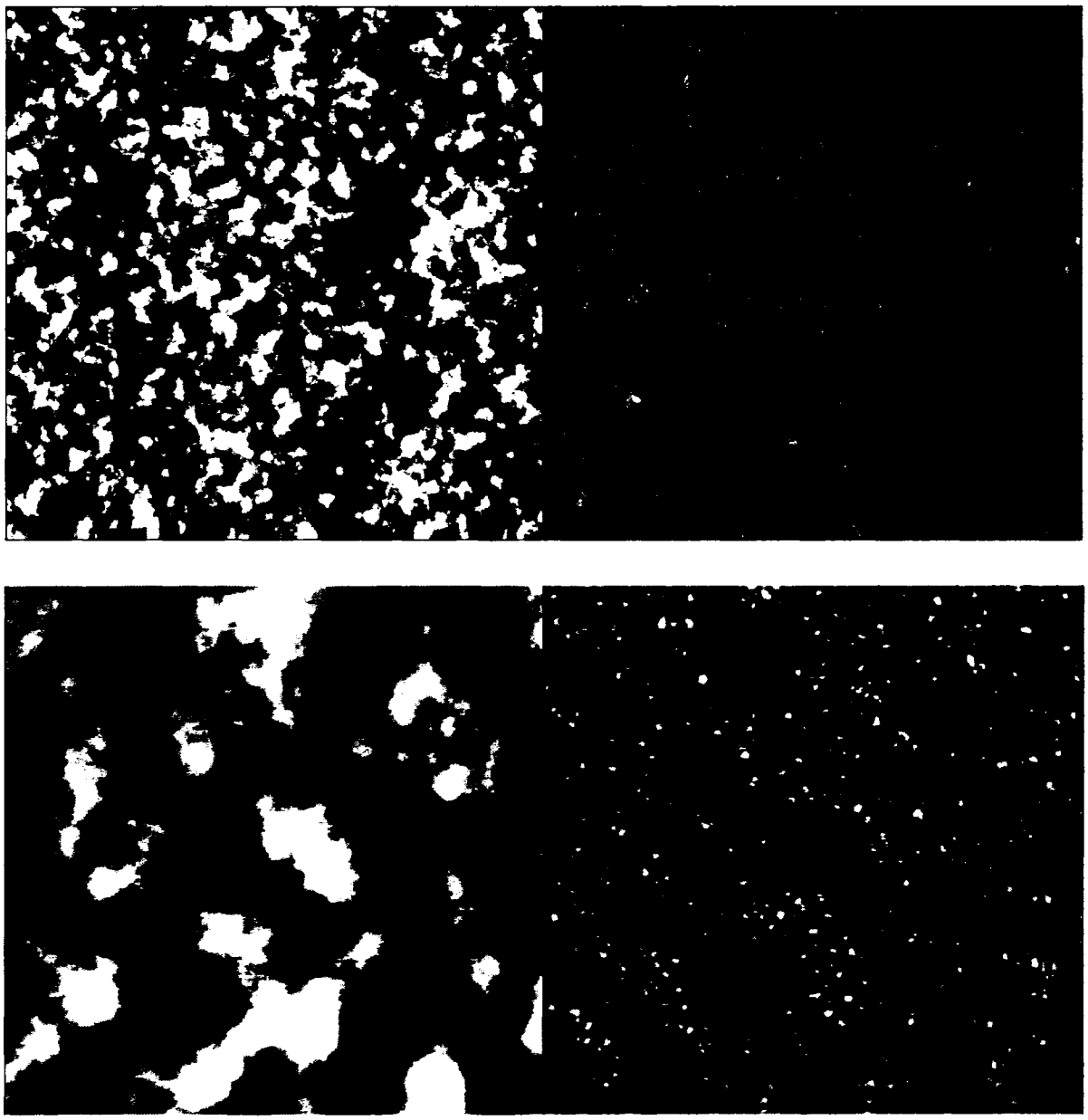

Figure 5-5. AFM tapping mode images (topography and phase) at room temperature of the topmost grafted layer, COOH-PBA. Top is 10x10 μm and bottom is 1x1μm; Z-scale is 5nm for topography and 30° for phase.

This data monitored at each grafting step clearly shows that a complex, multicomponent multilayered branched brush can be constructed, using "grafting from" and "grafting to" processes in series, and the overall dry thickness was around 25 nm (Fig 5-1, Table 5-1). To confirm vertical distribution of different layers, we conducted XPS surveys taken allow for depth profiling of the brush layer (Figure 5-6). At a rate of 1nm/min, a signature from the full top two layers should be observed, as well as a fraction of the pNIPAAM bottom layer (Fig. 5-6).

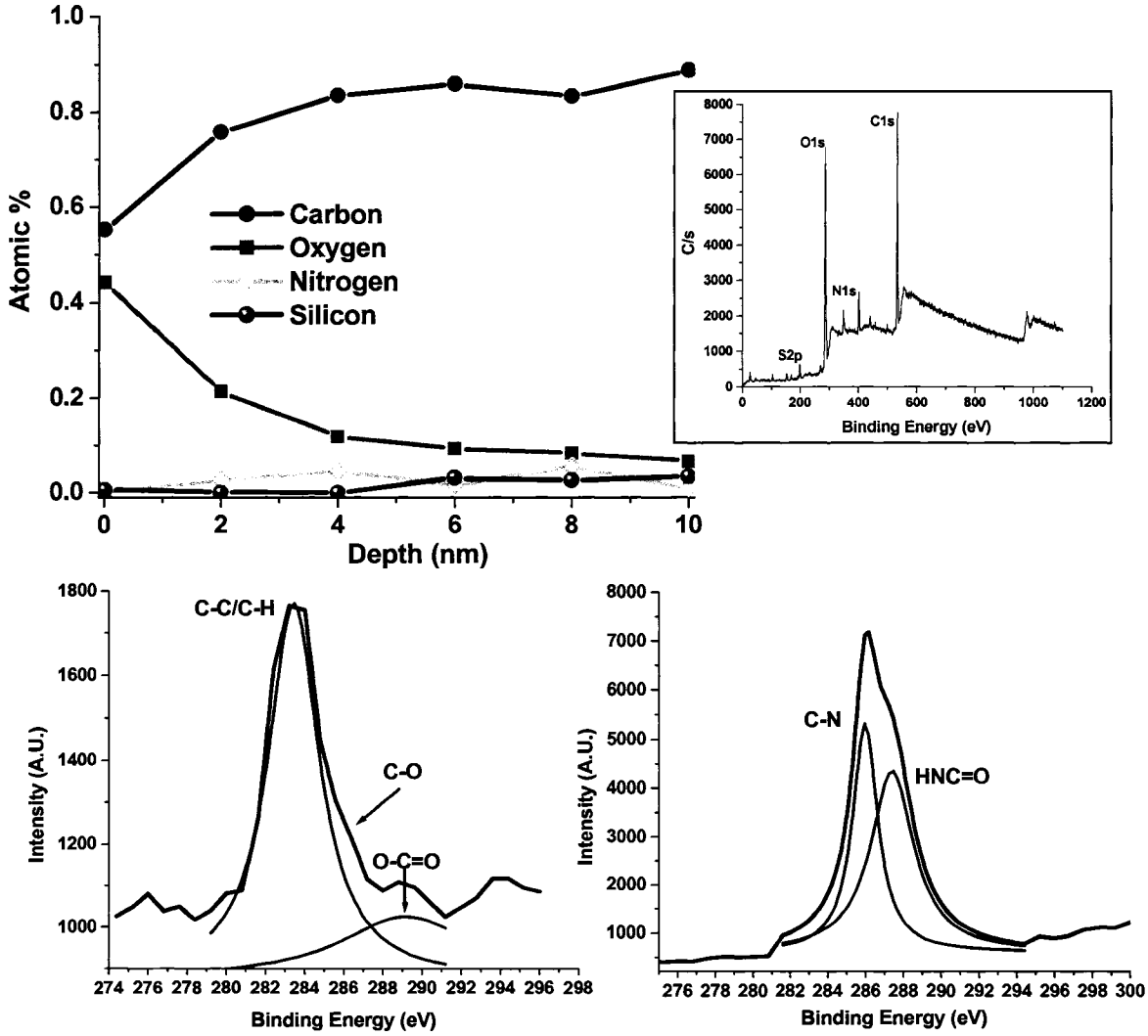

Figure 5-6. XPS data on the overall branched polymer brush layer. At top is depth profiling results over the probing of the first 10nm of the layer, which is deep enough to probe all layers in this brush. The inset is the overall survey showing characteristic peaks. At bottom are extracted data showing specific group binding energies for the polymers making up the grafted brush layer.

This variation corresponds to the overall drop in oxygen concentration as the ratio of oxygen in pNIPAAM is much lower as compared with PBA and pGMA. The peak at 289 eV is a clear indication of the O-C=O bond in PBA and GMA, along with the shoulder at 286 eV (Fig 5-6).[77,78] The peak at 285.8 eV can be assigned to the C-N bond, while the HNC=O is represented at 287.4 eV.[79] The sulfur peak represents residual initiator remaining from the SBDC. Therefore, XPS along with previously discussed AFM and ellipsometry results confirmed layered composition of the fabricated polymer films.

LCST transition within grafted film. After layer fabrication, it was imperative to test the LCST phase behavior pNIPAAM confined within the layered structure. It is well known that pNIPAAM undergoes a strong response to temperature around temperature of 32°C, and our hypothesis here is that this collapse/swelling will change overall vertical layering leading to distinct variation of elastic response. To monitor this, we measured thickness of the overall layer above and below LCST with *in-situ* AFM scratch tests. Initial AFM scratch tests done in air at 50°C and 10°C showed no change in thickness. In fact, several recent reports claim that pNIPAAM layers only respond strongly if they are also in a favorable solvent (such as water), and that the transition is not apparent in the ambient.[80,81] Indeed, the same measurements in water revealed significant changes (Figure 5-7). The layer reached an overall thickness of around 34 nm at 10°C and the layer thickness collapsed to 17 nm above LCST (Fig. 5-7, Table 5-1).

Along with this change in thickness, there is a marked change in the morphology of the topmost PBA layer at the different temperatures with the appearance of long, wavy surface at 50°C (Figure 5-8). Such a change can only result from variations in the underlying pNIPAAM layer because separate studies of PBA surface at these different temperatures resulted in no change of morphology. This is an important result revealing that at 10°C, with a swollen underlying brush layer, the PBA chains adopt a random structure. However, at 50°C, where the underlying layer strongly collapses above LCST reducing overall thickness by 50%, the PBA top layer adopts a constrained morphology with distinct elongated cluster domains (Fig. 5-8). These types of change should be sufficient to induce distinct density

gradients within the layer and thus overall nanomechanical properties as was tested with MMA approach.

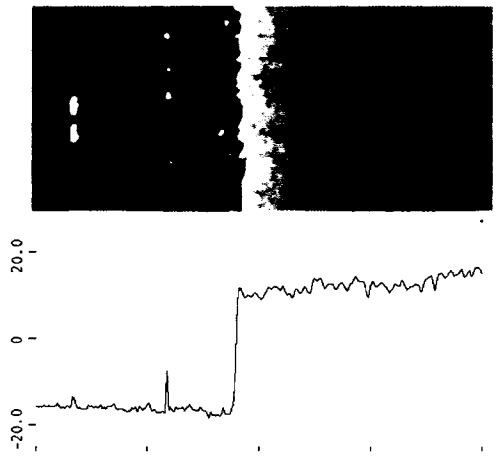

As grown: d_{avg} = 25 nm

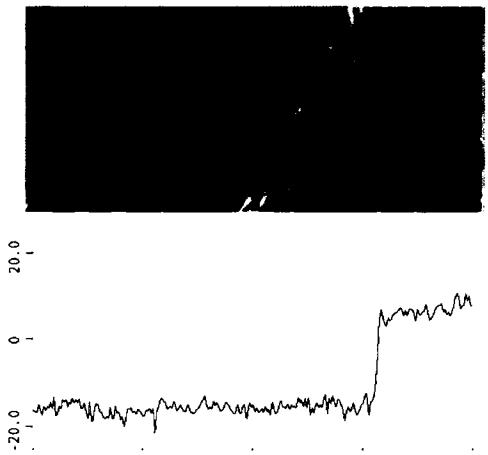

50°C: d_{avg} = 17 nm

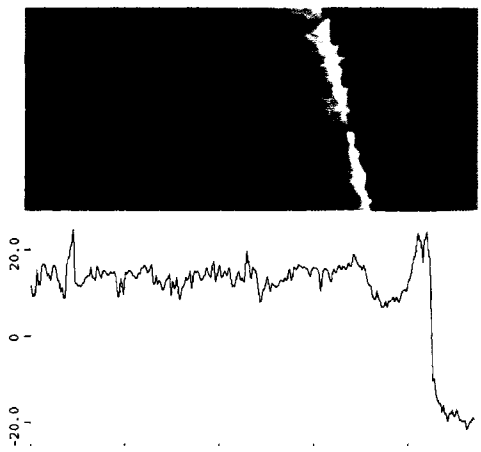

10°C: d_{avg} = 34 nm

Figure 5-7. AFM analysis of scratch tests of the overall layer done in water at different temperatures compared with the as grown, dry state condition (left). As can be seen, the layer undergoes dramatic changes in thickness going from 50°C (middle) to 10°C (right), as well as noticeable changes in overall layer morphology.

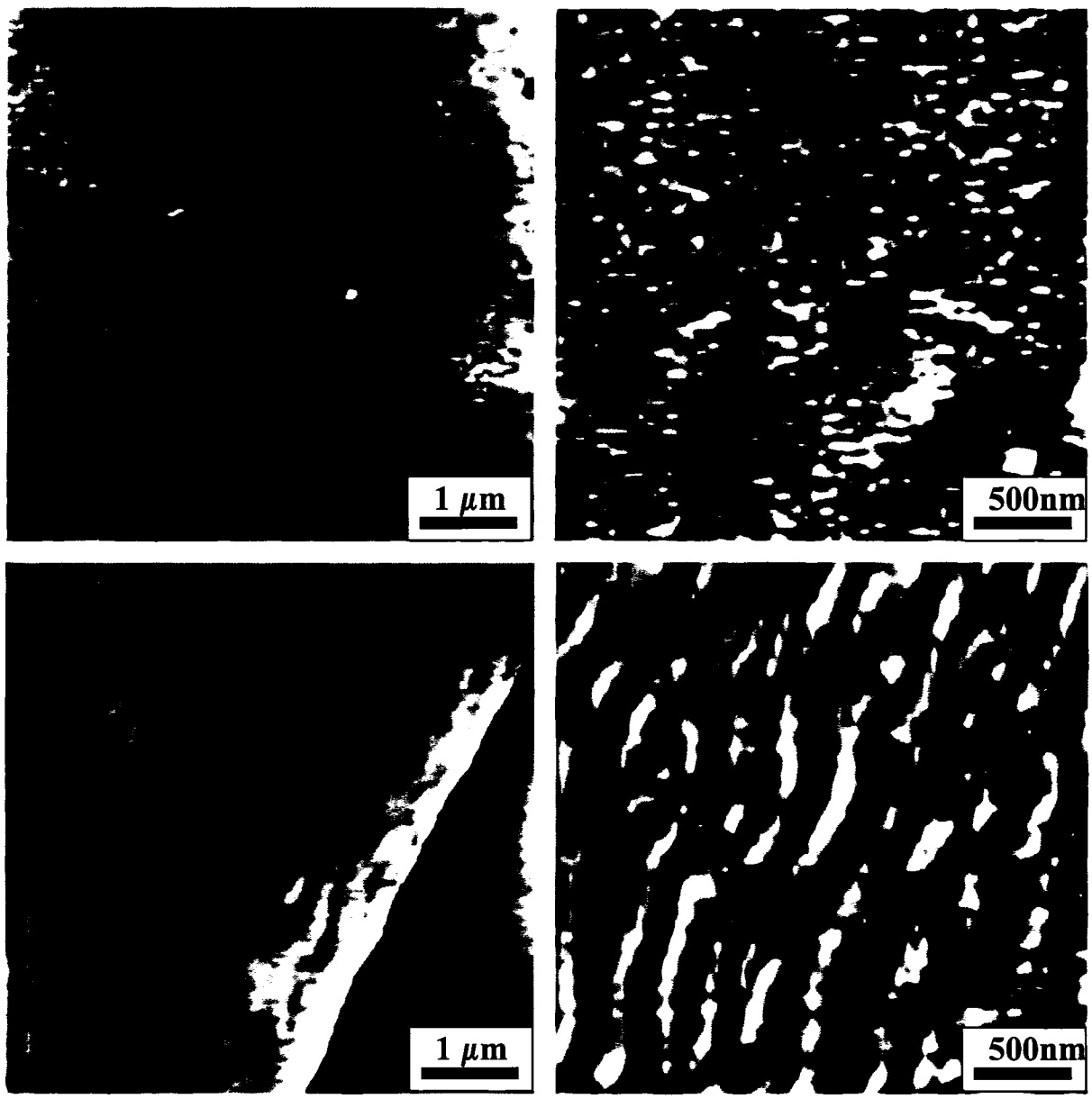

Figure 5-8. AFM tapping mode topography images in water of the overall brush at different temperatures. The top row is the brush layer at 10°C (at 5x5 and 2.5x2.5 μm), and bottom row is at 50°C (at 5x5 and 2.5x2.5 μm).

Temperature-dependent nanomechanical properties. This MMA analysis can determine modulus of the surface layers with nanoscale resolution *directly* in fluid at specific temperature, at 10°C (below LCST) and at 50°C (above LCST) (Figure 5-9). The resulting surface histograms of the elastic modulus presented shows a unimodal distribution of the

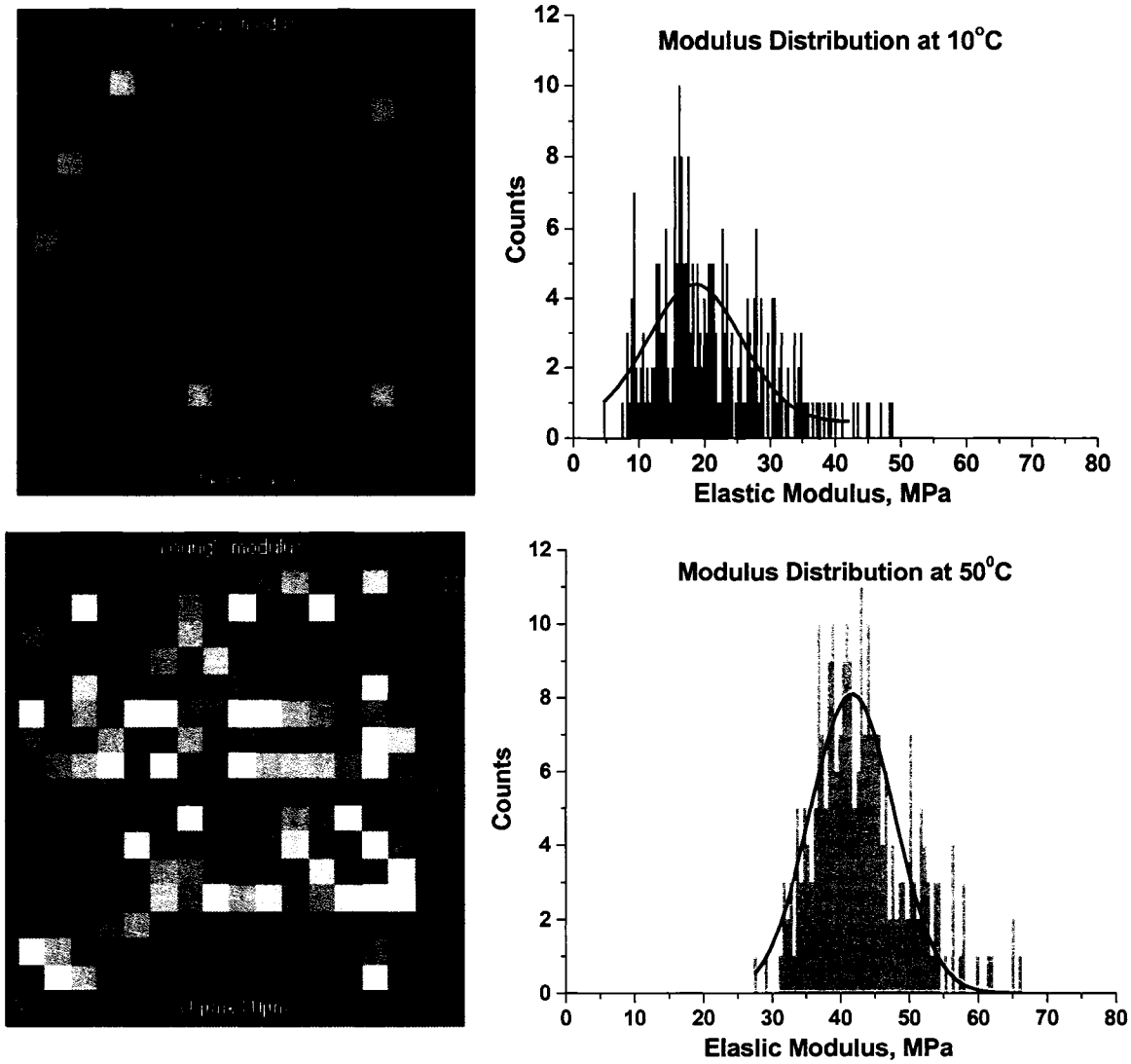

Figure 5-9. The left column represents force-volume resulting images with 16x16 nanomechanical probing resolution mapping overall layer elastic modulus over a 3x3 μm area. Brighter areas correspond to higher modulus values. This mapping results from nanomechanical probing in water at 10°C (top) and 50°C (bottom). The right column is the resulting modulus histograms from the corresponding modulus maps. The elastic modulus is the average value for each data point over the entire indentation range, and the data are fitted with a Lorentzian curve.

elastic modulus that is expected for a surface with homogeneous top phase. The average value is close to 15 MPa which is lower than a modulus of 50 – 100 MPa for PBA in the collapsed state above T_g =-5°C.[75,76] For temperature above LCST, the elastic modulus has a higher value around 45 MPa despite PBA (Fig. 5-9).

Examination of individual FDCs show that the overall adhesion is very similar at both temperatures with slightly higher adhesion for 50°C, which is expected for a PBA top layer well above its glass transition temperature (Figure 5-10). The overall close of FDC at 10°C is slightly lower which corresponds to more compliant state as concluded from the elastic modulus histograms (Fig. 5-9). Conversion of the FDCs into load – penetration curves further confirms that a more compliant surface is associated with the 10°C state (Fig. 5-10). For 50°C the loading curve is virtually linear indicating a unform elastic compression for the penetration reaching 10 nm. However, below LCST (10°C) the loading curve shows two distinct regions of different slopes implying the AFM tip is feeling non-uniform compliancy from the brush layer related to its stratification below LCST. Very compliant behavior is observed for initial 8-10 nm of deformation with much stiffer response followed (Fig. 5-10).

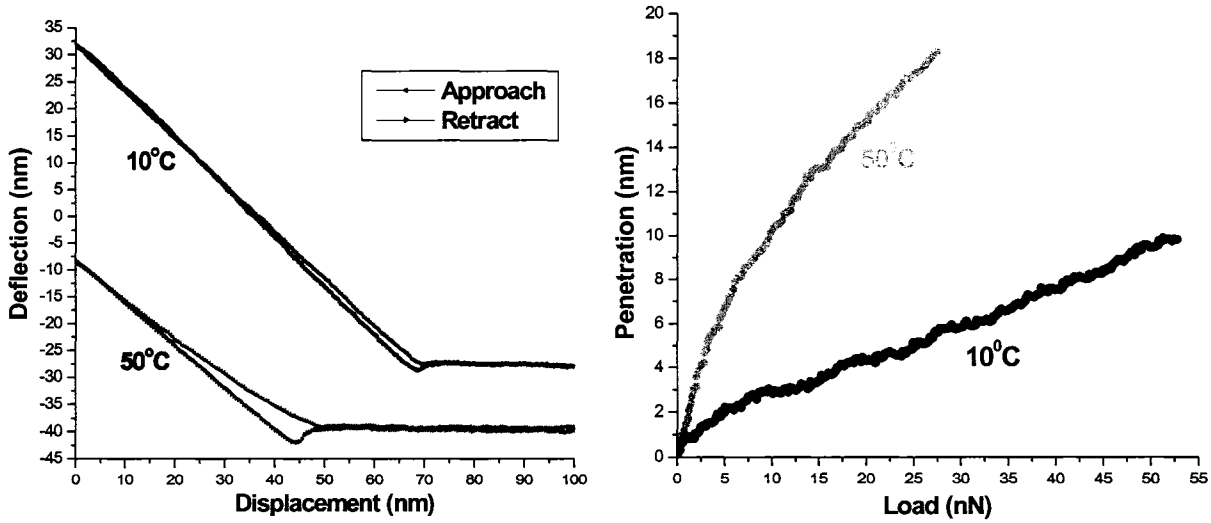

Figure 5-10. Typical force-distance curves (top) and resulting load-penetration curves (bottom) obtained at each pixel in the nanomechanical analysis at the indicated temperature in water.

Considering these results, we suggest the schematics of temperature-dependent vertical stratification in our surface film (Fig. 5-11). First, we suggest that at elevated temperature above LCST, the central, temperature-sensitive pNIPAAM layer is in its collapse state which results in compact overall structure with two major layers forming the 17 nm film. The uniform elastic deformation with relatively high elastic modulus, 45 MPa, is caused by comparable elastic properties of PBA above T_g (50-100 MPa) and pNIPAAM above LCST (20 – 100 MPa).[76,82] Below LCST when pNIPAAM chains become swollen in water, a completely different nanomechanical is observed. Here, the initial elastic modulus is much lower because of overall deformation of the film

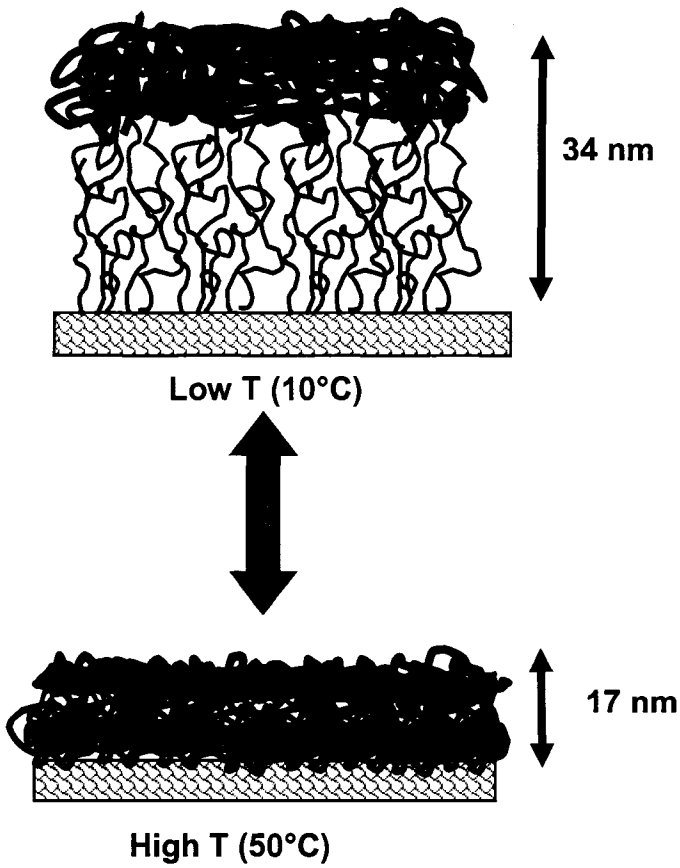

Figure 5-11. Schematic depicting the structure reorganization of the overall branched polymer brush in water at the two temperatures indicated above and below LCST. Below LCST, pNIPAAM chains are highly swollen while PBA is collapsed (bad solvent conditions) while above LCST, NIPAAM is collapsed into tight clusters towards the substrate. As this occurs, due to the high density of PBA at the top layer, PBA is pulled into tighter clusters, because it is still in a bad solvent (water) as NIPAAM collapses strongly (more than 100% as indicated by scratch tests in water). However, because of this high grafting density of PBA, steric constraints limit this collapse and effective voids are formed at the PBA-pNIPAAM interface resulting in the observed depth profile.

under the AFM tip is controlled by the most compliant component, a highly swollen pNIPAAM layer with 30 nm thickness with the extremely low modulus around 1 MPa (Fig. 5-11).[82] Only at very high deformation, the overall resistance of PBA layer and compressed pNIPAAM layer becomes more significant with the elastic modulus increasing to 35 MPa. The overall behavior of the stratified polymer layer designed here reminiscents the non-linear elastic response of tri-layered surface film composed of soft, rubbery block-copolymer layer sandwiched between SAM and photopolymerized acrylate topmost layer reported previously. However, in the study, the peculiar elastic response is responsive and can be tuned by varying external temperature.[83] Moreover, it is completely reversible and can be turned on/off on-demand by lowering/rising temperature in the vicinity of LCST point. These temperature-sensitive, adaptive polymer layers with pNIPAAM layer "hidden" beneath the rubbery hydrophobic PBA topmost layer represent and interesting example of the nanoscale engineering surfaces with their properties such as adhesion, and elastic modulus and multi-level structural reorganization responsive to various fluidic and temperature fluctuations.

5.5 Acknowledgments

Funding from AFOSR, FA9550-05-1-0209 and the National Science Foundation, DMR-00308982 is gratefully acknowledged. The authors would like to kindly thank Jim Anderegg for technical support with XPS measurements.

5.6 References

1 Tomalia, D.A.; Mardel, K.; Henderson, S.A.; Holan, G.; Esfand, R. *in Goddard III, W. A. et al., Eds. Handbook of nanoscience, engineering, and technology.* Boca Raton, FL: CRC Press; **2003**, p. 1-34.

2 Goodsell, D.S. *Am. Sci.* **2000,** *88*, 230.

3 Luzinov, I.; Minko, S.; Tsukruk, V.V. *Prog. Polym. Sci.* **2004**, *29,* 635. Zhao, B.; Brittain,W.J. *Prog. Polym. Sci.* **2000**, *25*, 677.

4 Advincula, R.C.; Brittain,W.J.; Caster, K.C; Ruhe, J. *Polymer Brushes.*; Wiley: Weinheim, **2004**.

5 Matyjaszewski, K. *Prog. Polym. Sci.* **2005**, *30*, 858.

6 Frauenrath, H. *Prog. Polym. Sci.* **2005**, *30*, 325.

7 Hadjichristidis, N.; Pitsikalis, M.; Iatrou, H.; Pispas, S. *Macromol. Rapid. Commun.* **2003**, *24*, 979.

8 Nakayama, Y.; Sudo, M.; Uchida, K.; Matsuda, T. *Langmuir* **2002**, *18*, 2601.

9 Tsukruk, V.V. *Adv. Materials,* **2001**, *13,* 95.

10 Romiszowski, P.; Sikorski, A. *J. Chem. Inf. Comput. Sci.* **2004**, *44*, 393.

11 Percec, V.; Ahn, C.H.; Ungar, G.; Yeardley, D.J.P.; Möller, M.; Sheiko, S.S. *Nature*, **1998**, *391*, 161.

12 Pakula, T.; Minkin, P.; Matyjaszweski, K. *ACS Symp. Ser.* **2003**, *854*, 366.

13 Tian, P.; Uhrig, D.; Mays, J.W.; Watanabe, H.; Kilbey, S.M. *Macromolecules* **2005**, *38*, 2524.

14 Ye, M.; Zhang, D.; Han, L.; Tejada, J.; Ortiz, C. *Soft Matter*, **2006**, *2*, 243.

15 Zhang, D.; Ortiz, C. *Macromolecules*, **2005**, *38*, 2535.

16 Zhang, D.; Ortiz, C. *Macromolecules*, **2004**, *37*, 4271.

17 Muller, R.S. in *Micro/Nanotribology and Its Applications*, Bhushan, B., Ed.; Kluwer Academic Press: Dordecht, **1997**: p 579. *Tribology Issues and Opportunities in MEMS,* Bhushan, B., Ed.; Kluwer Academic Publishers: Dordrecht, **1997**. Tsukruk, V.V. in: *Nanotribology*, Hsu, S.M.; Ying, C. Z.; Eds.; Kluwer Academic Press: Boston, **2002**, p 347.

18 Santer, S.; Kopyshev, A.; Donges, J.; Yang, H–K.; Rühe, J. *Macromolecules* **2006**, *22*, 4660. Genson, K.L.; Holzmuller, J.; Villacencio, O.F.; McGrath, D.V.; Vaknin, D.; Tsukruk, V.V. *J. Phys. Chem. B* **2005**, *109,* 20393. Julthongpiput, D.; Lin, Y.H.; Teng, J.; Zubarev, E.R.; Tsukruk, V.V. *Langmuir* **2003**, *19*, 7832. Julthongpiput, D.; Lin, Y-H.; Teng, J.; Zubarev, E. R.; Tsukruk, V.V. *J. Am. Chem. Soc.* **2003**, *125*, 15912. Lin, Y.-H.; Teng, J.; Zubarev, E.R.; Shulha, H.; Tsukruk, V.V. *Nano Lett.* **2005**, *5*, 491. Xu, C.; Fu, X.; Fryd, M.; Xu, S.; Wayland, B.B.; Winey, K.I.;

Composto, R.J. *Nano Lett.* **2006**, *6*, 282. Gunawidjaja, R.; Peleshanko, S.; Tsukruk, V.V. *Macromolecules* **2005**, *38*, 8765

19 Lemieux, M.; Usov, D.; Minko, S.; Stamm, M.; Shulha, H.; Tsukruk, V. V. *Macromolecules* **2003**, *36*, 7244.

20 Tsukruk, V.V.; Luzinov, I.; Larson, K.; Li, S.; McGrath, D.V. *J. Mater. Sci. Let.* **2001**, *20*, 873. Sidorenko, A.; Minko, S.; Schenk-Meuser, K.; Duschner, H.; Stamm, M. *Langmuir* **1999**, *15*, 8349. Peleshanko, S.; Sidorenko, A.; Larson, K.; Villavicencio, O.; Ornatska, M.; McGrath, D.V.; Tsukruk, V.V. *Thin Solid Films* **2002**, *406*, 233. Sidorenko, A.; Houphouet-Boigny, C.; Villavicencio, O.; McGrath, D.V.; Tsukruk, V.V. *Thin Solid Films* **2002**, *410*, 147. Larson, K.; Vaknin, D.; Villavicencrio, O.; McGrath, D.V.; Tsukruk, V.V. *J. Phys. Chem.* **2002**, *106*, 7246; Genson, K.L.; Vankin, D.; Villavicencio, O.; McGrath, D.V.; Tsukruk, V.V. *J. Phys. Chem.* **2002**, *106*, 11277.

21 Ionov, L.; Minko, S.; Stamm, M.; Gohy, J.-F.; Jérôme, R.; Scholl, A. *J. Am. Chem. Soc.* **2003**, *125*, 8302. Liu, Y.; Klep, V.; Zdyrko, B.; Luzinov, I. *Langmuir* **2005**, *21*, 11806.

22 Bliznyuk, V.N.; Everson, M.P.; Tsukruk, V.V. *J. Tribology* **1998**, *120*, 489. Tsukruk, V.V.; Bliznyuk, V.N. *Langmuir* **1998**, *14*, 446. Sidorenko, A.; Houphouet-Boigny, C.; Villavicencio, O.; McGrath, D.V.; Tsukruk, V.V. *Thin Solid Films,* **2002**, *410,* 147. Ahn, H.; Julthongpiput, D.; Kim, D.I.; Tsukruk, V.V. *Wear* **2003**, *255,* 801. Tsukruk, V.V.; Sidorenko, A.; Yang, H. *Polymer* **2002**, *43*, 1695. Sidorenko, A.; Julthongpiput, D.; Luzinov, I.; Tsukruk, V.V. *Tribol. Lett.* **2002**, *12*, 101.

23 Ito, Y.; Ochiai, Y.; Park, Y.S.; Imanishi, Y. *J. Am. Chem. Soc.* **1997**, *119*, 1619.

24 Galaev, I.; Mattiasson, B. *Trends Biotechnol.* **1999**, *17*, 335.

25 Jones, D.M.; Smith, R.R.; Huck, W.T.S.; Alexander, C. *Adv. Mater.* **2002**, *14*, 1130.

26 Aksay, I.A.; Trau, M.; Manne, S.; Honma, I.; Yao, N.; Zhou, L.; Fenter, P.; Eisenberger, P.M.; Gruner, S.M. *Science* **1996**, *273*, 892.

27 Dean, D.; Seog, J.; Ortiz, C.; Grodzinsky, A.J. *Langmuir* **2003**, *19*, 5526.

28 Rixman, M.A.; Dean, D.; Ortiz, C. *Langmuir* **2003**, *19,* 9357.

29 Qin, S.H.; Oin, D.Q.; Ford, W.T.; Resasco, D.E.; Herrera, J.E. *J. Am. Chem. Soc.* **2004**, *126*, 170.

30 Gomez, F.J.; Chen, R.J.; Wang, D.W.; Waymouth, R.M.; Dai, H.J. *Chem. Commun.* **2003**, *2*, 190.

31 Viswanathan, G.; Chakrapani, N.; Yang, H.C.; Wei, B.Q.; Chung, H.S.; Cho, K.W.; Ryu, C.Y.; Ajayan, P.M. *J. Am. Chem. Soc.* **2003**, *125*, 9258.

32 Artyukhin, A.B.; Bakajin, O.; Stroeve, P.; Noy, A. *Langmuir* **2004**, *20*, 1442.

33 Murat, M.; Grest, G.S. *Phys. Rev. Lett.* **1989**, *63*, 1074.

34 Alexander, S.J. *J. Phys.* **1977**, *38*, 977.

35 de Gennes, P.G. *Macromolecules* **1980**, *13*, 1069.

36 Karim, A.; Tsukruk, V.V.; Douglas, J.F.; Satija, S.K.; Fetters, L.J.; Reneker, D.H.; Foster, M.D. *J. Phys. II* **1995**, *5*, 1441. Tsukruk, V.V. *Prog. Polym. Sci.* **1997**, *22*, 247. Tsukruk, V.V. *Adv. Mater.* **1998**, *10*, 253.

37 Zhao, B.; Brittain, W.J. *J. Am. Chem. Soc.* **1999**, *121*, 3557. Zhao, B.; Brittain, W.J.; Zhou, W.S.; Cheng, S.Z.D. *J. Am. Chem. Soc.* **2000**, *122*, 2407. Sedjo, R.; Mirous, B. K; Brittain, W.J. *Macromolecules* **2000**, *33*, 1492.

38 Wittmer, J.; Johner, A.; Joanny, J.F. *Colloids Surf., A* **1994**, *86*, 85.

39 Woodcock, S.A.; Chen, C.; Chen, Z. *Langmuir* **2004**, *20*, 1928.

40 Gunari, N.; Schmidt, M.; Janshoff, A. *Macromolecules* **2006**, *39*, 2219.

41 Zhang, Q.; Archer, L.A. *Langmuir* **2006**, *22,* 717.

42 *Responsive Polymer Materials: Design and Applications;* Minko, S.; Ed.; Blackwell Publishing: Ames, IA, **2006**.

43 Krausch, G., Magerle, R.G. *Adv. Mater.* **2002**, *14*, 1579.

44 Zhulina, E.B.; Birshtein, T.M.; Priamitsyn, V.A.; Klushin, L.I. *Macromolecules* **1995**, *28*, 8612.

45 Park, M., Christopher H., Chaikin, P.M., Register, R.A., and Adamson, D.H. *Science* **1997**, *276*, 1401.

46 Sidorenko, A.; Tokarev, I.; Minko, S.; Stamm, M. *J. Am. Chem. Soc.* **2003**, *125*, 12211.

47 Sheiko, S.S.; Möller, M. *Chem. Rev.* **2001**, *101*, 4099.

48 Wintermantel, M.; Gerle, M.; Fischer, K.; Schmidt, M.; Wataoka, I.; Urakawa, H.; Kajiwara, K.; Tsukahara, Y. *Macromolecules* **1996**, *29*, 978.

49 Neiser, M.W.; Muth, S.; Kolb, U.; Harris, J.R.; Okuda, J.; Schmidt, M. *Angew Chem Int. Ed.* **2004**, *43*, 3192.

50 Rathgeber, S.; Pakula, T.; Wilk, A.; Matyjaszewski, K.; Beers, K.L. *J. Chem. Phys.* **2005**, *122*, 124904.

51 McCormick, C.L.; Lowe, A.B. *Acc. Chem. Res.* **2004**, *37*, 312.

52 Edmonson, S.; Osborne, V.; Huck, W.T.S. *Chem. Soc. Rev.* **2004**, *33*, 14-22.

53 Iyer, K.S.; Zdyrko, B.; Malz, H.; Pionteck, J.; Luzinov, I. *Macromolecules* **2003**, *36*, 6519.

54 Borner, H.G.; Duran, D.; Matyjaszewski, K.; da Silva, M.' Sheiko, S.S. *Macromolecules* **2002**, *35*, 3387.

55 Lord, S.J.; Sheiko, S.S.; LaRue, I.; Lee, H.; Matyjaszewski, K. *Macromolecules* **2004**, *37*, 4235.

56 Borner, H.G.; Beers, K.; Matyjaszewski, K.; Sheiko, S.; Moller, M. *Macromolecules* **2001**, *34*, 4375.

57 Fisch, W.; Hofmann, W. *Macromol. Chem. Phys.* **1961**, *44-6*, 8.

58 Motschmann, H.; Stamm, M.; Toprakcioglu, C. *Macromolecules* **1991**, *24*, 3681.

59 Ratner, B.; Tsukruk, V.V. Eds. *Scanning Probe Microscopy of Polymers.*; ACS Symposium Series; American Chemical Society: Washington, D.C., **1998**; Vol. 694.

60 Tsukruk, V.V. *Rubber Chem. Technol.* **1997**, *70*, 430.

61 Radmacher, M.; Tilmann, R. W.; Gaub, H. E. *Biophys. J.* **1993**, *64*, 735.

62 Cappella, B.; Dietler, G. *Surface Science Reports* **1999**, *34*, 1.

63 *Scanning Probe Microscopy of Polymers.* Ratner, B.; Tsukruk, V.V. Eds.; ACS Symposium Series; American Chemical Society: Washington, D.C., **1998**; Vol. 694.

64 *Microstructure and Microtribology of Polymer Surfaces.* Tsukruk, V.V.; Wahl, K. ACS: Washington, D.C., **1999**, Vol. 741.

65 Tsukruk, V.V.; Gorbunov, V.V. *Probe Microscopy* **2002,** *3-4*, 241. Huang, Z.; Chizhik, S. A.; Gorbunov, V.V. *J. Mat. Sci.* **1998**, *33*, 4905. Tsukruk, V.V.; Huang, Z. *Polymer* **2000**, *41*, 5541.

66 Kovalev, A.; Shulha, H.; LeMieux, M.C.; Myshkin, N.; Tsukruk V.V. *J. Mater. Res.* **2004**, *19*, 716. Shulha, H.; Kovalev, A.; Myshkin, N.; Tsukruk, V. V. *Eur. Polym. J.*, **2004**, *40,* 949.

67 Hazel, J.L.; Tsukruk, V.V. *Thin Solid Films* **1999**, *339*, 249.

68 Hazel, J.L.; Tsukruk, V.V. *J. Tribol.* **1998**, *120*, 814.

69 de Boer, B.; Simon, H.K.; Werts, M.P.L.; van der Vegte, E.W.; Hadziioannou, G. *Macromolecules*, **2000**, *33*, 349.

70 Otsu, T.; Matsunaga, T.; Doi, T.; Matsumoto, A. *Eur. Polym. J.*, **1995**, *31*, 67.

71 Rahane, S.B.; Kilbey, S.M.; Metters, A.T. *Macromolecules* **2005**, *38*, 8202.

72 Harmon, M.E.; Kuckling, D.; Frank, C.W. *Langmuir*, **2003**, *19*, 10660.

73 Iyer, K.S.; Zdyrko, B.; Malz, H.; Pionteck, J.; Luzinov, I. *Macromolecules*, **2003**, *36*, 6519.

74 Tsukruk, V.V.; Luzinov, I.; Julthongpiput, D. *Langmuir,* **1999**, *15*, 3029. Luzinov, I.; Julthongpiput, D.; Liebmann-Vinson, A.; Cregger, T.; D. Foster, M.; Tsukruk, V.V. *Langmuir*, **2000**, *16*, 504.

75 Julthongpiput, D.; LeMieux, M.C.; Tsukruk, V.V. *Polymer*, **2003**, *44*, 4557.

76 LeMieux, M.C.; Julthongpiput, D.; Bergman, K.N.; Cuong, P.D.; Ahn, H-S.; Lin, Y-H.; Tsukruk, V.V. *Langmuir*, **2004**, *20*, 10046.

77 Matrab, T.; Chehimi, M.M.; Perruchot, C.; Adenier, A.; Guillez, A.; Save, M.; Charleux, B.; Cabet-Deliry, E.; Pinson, J. *Langmuir* **2005**, *21*, 4686.

78 Zhang, Y.; Tan, K.L.; Liaw, B.Y.; Liaw, D.J.; Kang, E.T. *Thin Solid Films* **2000**, *374*, 70.

79 Ying, L.; Kang, E.T.; Neoh, K.G. *Langmuir* **2002**, *18*, 6416.

80 Kuckling, D.; Hoffmann, J.; Plötner, M.; Ferse, D.; Kretschmer, K.; Adler, H-J.P.; Arndt, K-F.; Reichelt. R. *Polymer* **2003**, *44*, 4455.

81 Kim, S.; Healy, K.E. *Biomacromolecules* **2003**, 4, 1214.

82 Harmon, M.E.; Kuckling, D.; Pareek, P.; Frank, C.W. *Langmuir* **2003**, *19*, 10947.

83 Tsukruk, V.V.; Ahn, H.-S.; Sidorenko, A.; Kim, D., *Appl. Phys. Lett.* **2002**, *80,* 4825.

Sidorenko A.; Ahn, H.-S.; Kim, D.-I.; Yang, H.; Tsukruk, V.V. *Wear* **2002,** *252*, 946.

Chapter 6

The Elastic Properties and Plastic Behavior of Two-Dimensional Polymer Structures Fabricated with Laser Interference Lithography

A paper published in *Advanced Functional Materials*♦

Ji-Hyun Jang[1], *Chaitanya K. Ullal*[1], *Taeyi Choi*[1], *Melburne C. LeMieux*[*,2], *Vladimir V. Tsukruk*[2] *and Edwin L. Thomas*[1,*]

[1]Institute for Soldier Nanotechnologies, Department of Materials Science and Engineering, Massachusetts Institute of Technology, Cambridge, Massachusetts 02139

[2]Department of Materials Science and Engineering, Iowa State University, Ames, Iowa 50011

6.1 Abstract

The elastic and plastic properties within a two-dimensional polymer structure with six-fold symmetry fabricated via interference lithography have been studied. We observed a non-uniform spatial distribution in the elastic modulus with higher elastic modulus measured for nodes and lower elastic modulus observed for beams of the photopatterned films. We suggest that such a non-uniformity and unusual plastic behavior observed are related to the variable material properties "imprinted" with interference pattern.

♦ Reprinted with Permission of *Advanced Functional Materials*

* M.C.L.: Assistant researcher, did AFM experiments, assistant writer of all drafts, revised final figures and final inside cover image

6.2 Introduction

An epoxy-based negative photoresist from the Novolak-resin family, named SU8, has become a common material for the fabrication of complex microelectromechanical (MEMS) structures due to its mechanical durability, thermal stability, and dielectric properties combined with easy processability.[1,2,3] SU8 is easily solution spun to form a uniform glassy and transparent film on various substrates. Its chemical structure with eight epoxy-cycles allows fast thermal and light-initiated crosslinking resulting in a rigid network polymer with excellent chemical stability. Various MEMS devices such as microgears, microcoils, and pumps,[4,5] microvalves and grippers,[6] microchannels and high-aspect ratio beams,[7,8,9] microcantilevers and tribological coatings,[10,11] phononic and photonic crystals and light waveguides[12,13,14,15] have been recently fabricated from SU8. Yield strength and elastic properties of microfabricated structures are critical for reliable performance of these microdevices. The current design of MEMS assumes the preservation of mechanical properties of materials within microscopic parts of MEMS structures with the elastic modulus remaining close to that measured for the bulk state.[10] However, in practice, the damping of dynamic properties of some microfabricated devices points toward a more complex distribution of elastic and viscoelastic properties.[16]

To date only few studies address the question of the resultant mechanical properties of SU8 under complex microfabrication conditions. Feng and Farris reported the value 3.2 GPa for in-plane tensile elastic modulus and 5.9 GPa for out-of plane elastic modulus for UV-cured material with the ultimate strain reaching 8%.[17] Reducing the post-exposure bake time results in decreasing cross-linking density and, thus, a lower elastic modulus (down to 0.7 GPa) with an increase in elongation to break (up to 30%).[7,18]. The glass transition temperature of SU8 is 55°C in the uncured state and increases to 230°C for fully cured material with a linear relationship found between glass transition temperature and crosslinking density and the degree of conversion of the epoxy groups reaching 90% for e-beam curing.[18,19]

The recent application of advanced optical microfabrication methods such as holographic or interference lithography (ITL) for the creation of complex 2D and 3D microstructures poses the question of the actual distribution of crosslink density and, thus, the corresponding spatial distribution of mechanical and thermal properties within these structures.[2,5] In accordance with usual consideration of MEMS structures, current approaches simply treat these complex porous microstructures as a two-phase (polymer-air) composite with properties of the epoxy material identical to that for the corresponding bulk state.

In order to investigate the actual material properties of the complex photopatterned materials fabricated by interference lithography, here we focus on the elucidation of the spatial distribution of elastic and plastic properties of a relatively simple 2D microstructure. Using atomic force microscopy (AFM), we conduct high-resolution nanomechanical studies of the thin SU8 film having a hexagonal pattern of cylindrical air holes fabricated via three-beam laser interference lithography. A spatial distribution of the local elastic modulus, which can be directly related to the symmetry of light intensity distribution within the original interference pattern in the photoresist, is found with higher elastic modulus observed for nodes. Extremely plastic behavior of the films in the course of their fracturing was related to the essentially composite nature of 2D perforated films with higher crosslink density of nodes and lowered crosslink density of the beams.

6.3 Results and Discussion

Uniform thin films

Uncured and cured uniform SU8 films (laser exposure with a dose close to ITL conditions followed by development without thermal hardbaking, see Experimental) fabricated here for comparative purposes showed a very smooth surface topography with the RMS microroughness of 0.3 nm for uncured films and the 0.9 nm for cured films (measured within 3x3 μm^2 areas). This similarity demonstrates a little surface alternation after laser beam expose and curing procedure used in this study (Figure 6-1a and 6-2a). No significant

wrinkling of the polymer film after crosslinking procedure indicates very small shrinkage and insignificant residual stresses developing in the bilk SU8 material as was reported in previous studies.[20,21]

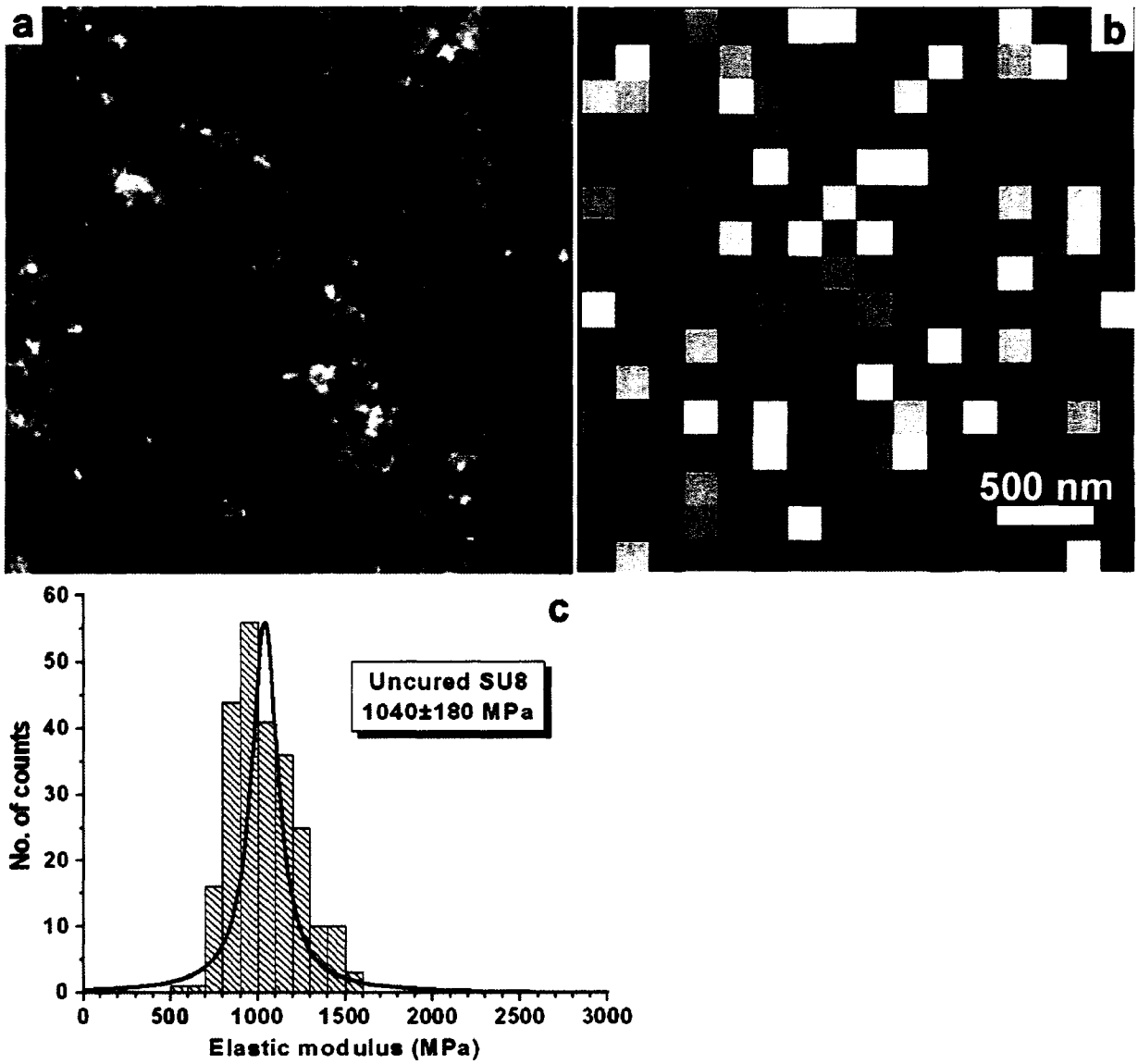

Figure 6-1. AFM data for uncured SU8 film: a) AFM topography image; b) the surface distribution of the elastic modulus (3x3 μm2) and c) the histogram of the elastic modulus distribution.

The surface distribution of the elastic modulus data of the uncured SU8 film obtained with static AFM force volume micromapping with spatial resolution of below 0.2 μm shows relatively uniform distribution and indentation depth not exceeding 3 nm (Figure 6-1b).[22] The histogram of the surface distribution of the elastic modulus confirms the uniform spatial distribution with virtually all values obtained in the range from 500 to 1500 MPa and the average elastic modulus measured of about 1 GPa (Figure 6-1c). This value is fairly close to that reported for bulk SU8 films from tensile experiments for bulk specimens and confirms virtually identical microscopic elastic response of thin films studied here and macroscopic elasticity of the bulk material.[18]

The surface distribution of the elastic moduli obtained with microscopic spatial resolution (below 0.1 μm) for cured SU8 films was very uniform as well (Figure 6-2b). The standard deviation for different surface areas was well below 20% indicating the absence of any significant spatial and chemical inhomogeneities at a microscale, which can be generated by light-initiated crosslinking and chemical developing (Figure 6-2c). However, the average elastic modulus after curing increased significantly as compared with the uncured film reached 3-4 GPa (Figure 6-2c). This value is fairly close to that obtained from macroscopic tensile experiment for the bulk SU8 material.[17]

The lateral compression of the films on an elastomeric substrate was used to generate the bucking instability and make independent evaluation of the in-plane macroscopic elastic modulus.[23] Such a deformation produced a very uniform buckling pattern with the spacing of 100-180 μm expanding over several squared centimeter of the SU8 films (Figure 6-3). This spacing of the buckling pattern obtained from the 2D FFT analysis of the deformed films was used for independent estimation of the elastic modulus of the films (Figure 6-3). The elastic modulus measured by the buckling method (2-3 GPa) was similar to but slightly higher of those obtained from both AFM and macroscopic tensile measurements which probably indicates differences related to measuring routine with in-plane compression of thin polymer films. Similarly, some higher elastic moduli have been recently measured for ultrathin multilayered polymer films in the buckling experiments.[24] However, despite some

discrepancies in the absolute values the buckling measurements confirmed significant (by a factor of 2-4) increase of the elastic modulus upon curing.

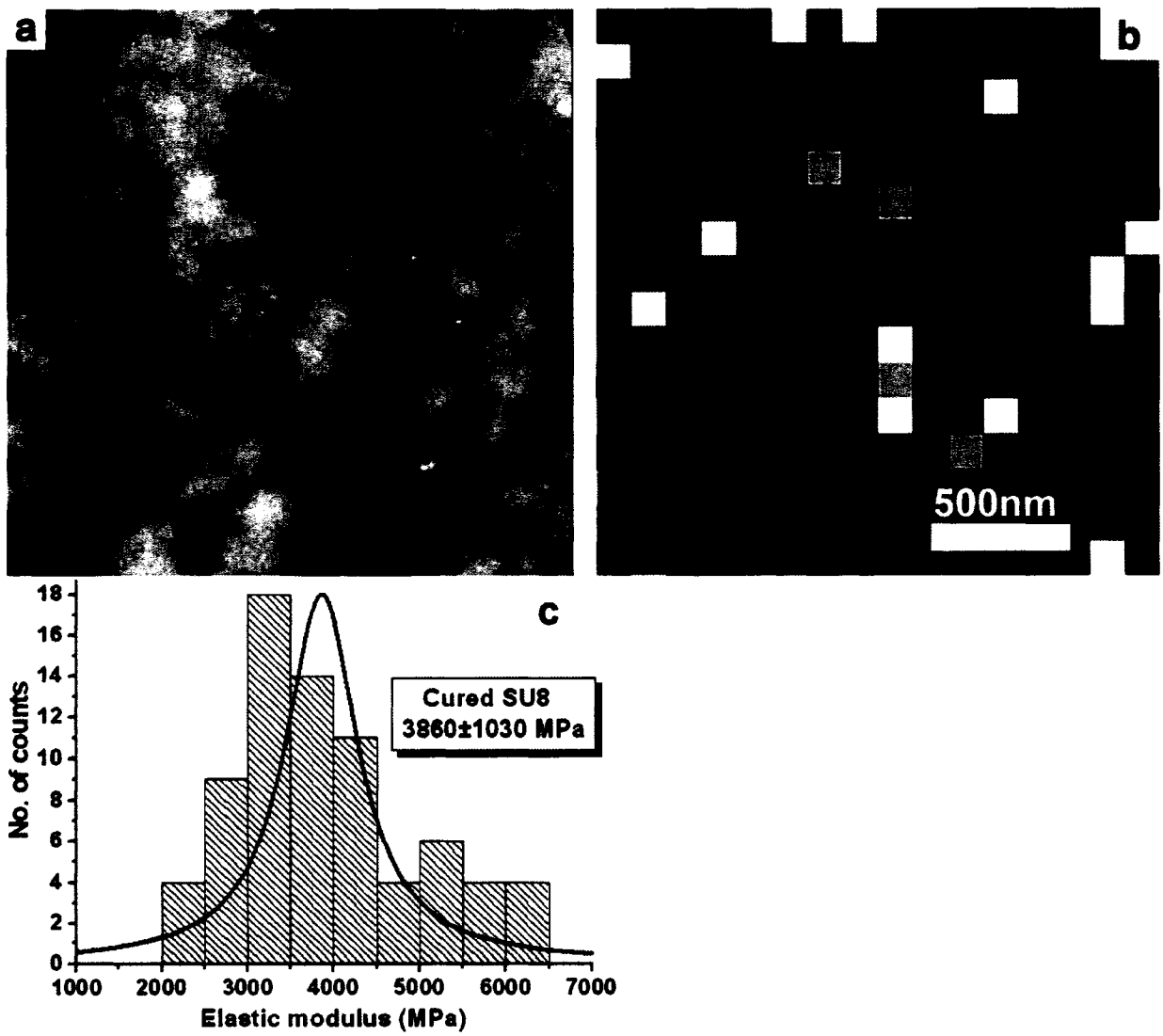

Figure 6-2. AFM data for cured SU8 film: a) AFM topography image; b) the surface distribution of the elastic modulus (2x2 μm2) and c) the histogram of the elastic modulus distribution.

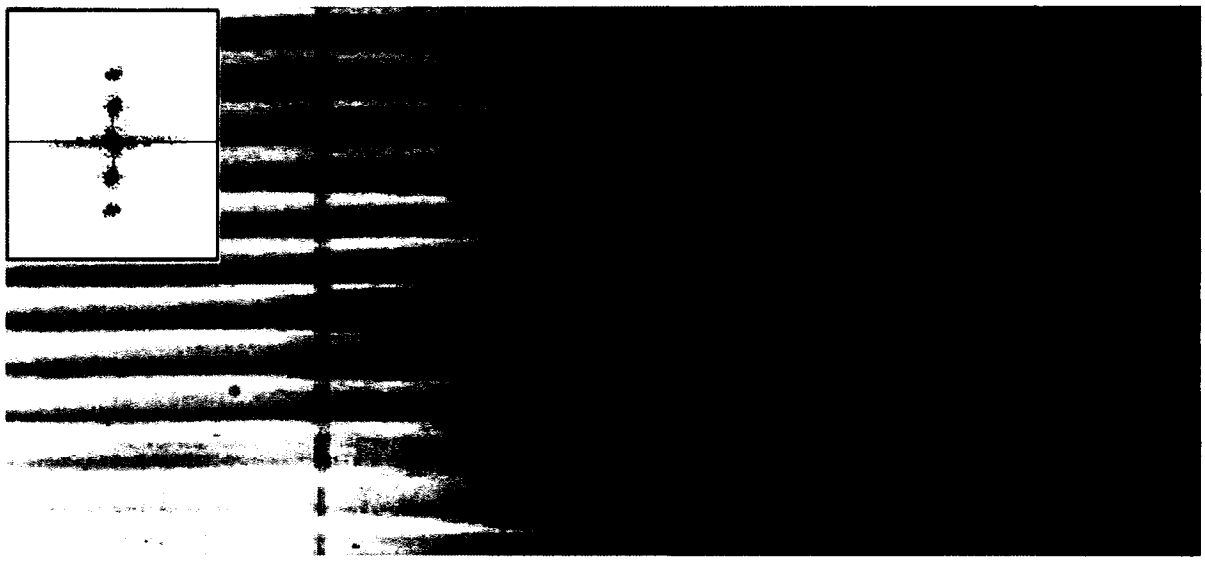

Figure 6-3. The elastic buckling instability measurement of the uncured SU8 film on the PDMS substrate. The buckling wavelength is 174 μm from the inset Fourier transform.

Microscopic distribution of the elastic response.

The interference pattern was designed to create a 2D lattice with hexagonal symmetry and pre-defined spacing and porosity level. The two-dimensional distribution of light intensity created by three-beam interference is presented in Figure 6-4a, along with a sketch of a unit cell and primary lattice vectors if the 2D lattice. The brighter spots present the nodes (**N**) with the highest intensity and the somewhat darker regions are called beams (**B**) (as marked in Figure 6-4a). The actual surface morphology of the photopatterned film showed a well-ordered, long-range, two-dimensional lattice with a hexagonal array of air holes closely resembling the theoretical light "template" as can be seen in SEM image (Figure 6-4b). The theoretical light distribution between nodes and beams is shown in Figure 6-4c,d with one-dimensional distribution along the [11] direction and along the [10] direction. The intensity of light distribution along [11] direction is a simple periodic function although more complex intensity distribution is observed along the [10] direction with

intensity slightly lower for beams (marked B) between two neighboring nodes (marked N) (Figure 6-4c,d).

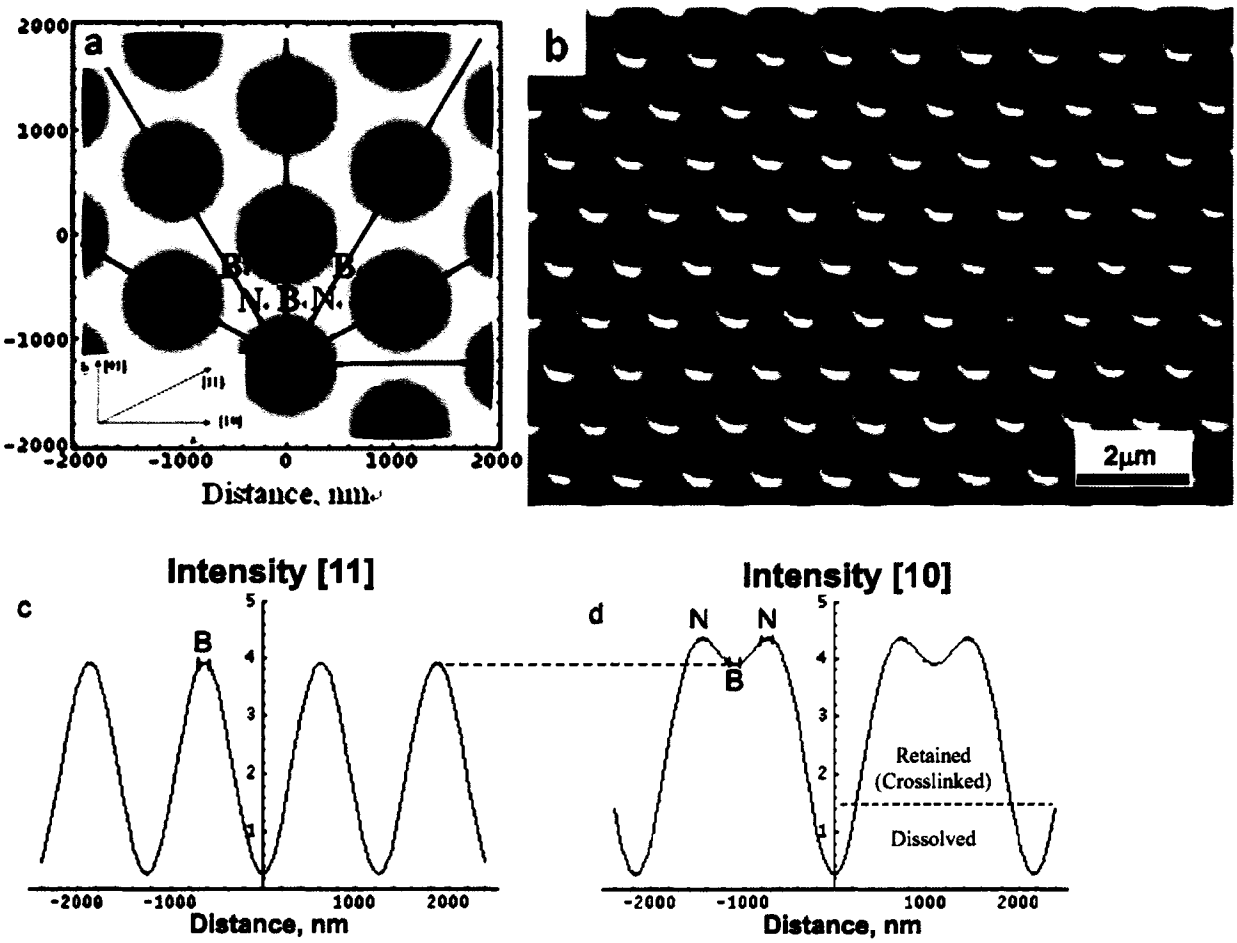

Figure 6-4. a) 2D light intensity distribution for three-beam interference used for the fabrication of the patterned specimen along with primary lattice vectors for corresponding 2D lattice; B and N stand for regions of beams and nodes of lattice, inset shows primary lattice vectors; b) Scanning electron microscopy (SEM) image shows long-range ordered 2D hexagonal lattice; c) one-dimensional light intensity distribution along the [11] direction (y axis in arbitrary values, DC offset is removed by amine); d) one-dimensional light intensity distribution along the [10] direction.

The surface morphology of the 2D polymer films with higher resolution was obtained by applying the tapping mode AFM (Figure 6-5). The AFM images revealed a well-developed topography with an array of round holes penetrating through the polymer film (Figure 6-5a). A porosity level of about 40% and a spacing of 1220 nm were estimated from the bearing analysis and 2D Fourier transforms of the AFM images, respectively. A diameter of the through, nearly cylindrical holes of 700 nm was obtained from AFM cross-sections (see Figure 6-5b, the shape is smeared by the convolution with the AFM tip). The polymer surface between these round holes was relatively smooth with the local microroughness not exceeding 1 nm within 500x500 nm^2 surface areas.

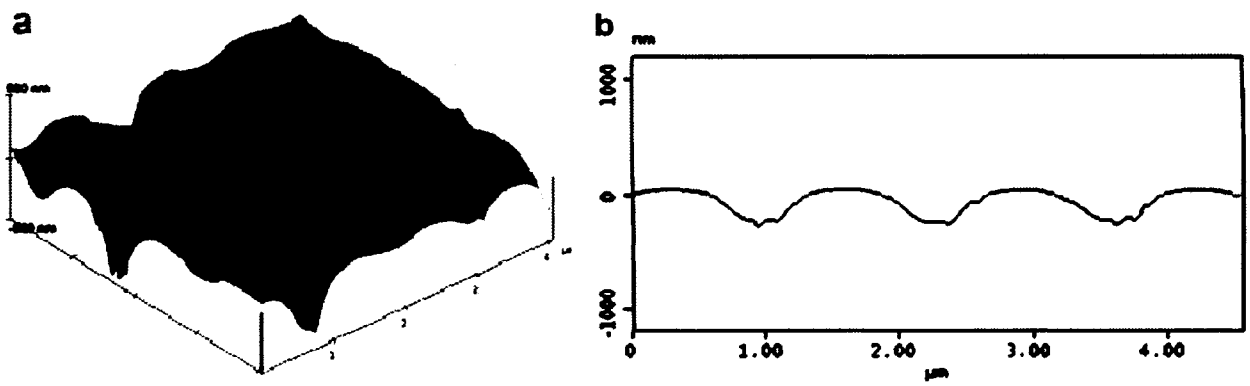

Figure 6-5. a) 3D surface topography of the specimen with the hexagonal pattern (4x4 μm2, the tapping mode); b) corresponding height profile along the [11] direction.

The nanomechanical measurements were conducted in the elastic regime with an indentation depth of less than 2 nm allowing full elastic recovery of the tested surface areas after probing. The estimated contact area for a single nanoprobing experiment did not exceed 1 nm which is much smaller than the distance between two consequential indentations (80 nm) thus precluding interference related to stress generation. High-resolution topographical images obtained simultaneously with nanomechanical probing

shown as a 32x32 array of small square pixel were very similar to those obtained with conventional tapping mode scanning (Figure 6-6a). Each pixel at this image with 80 nm x 80 nm lateral dimensions represents the entire surface area for a single force measurement. In the course of AFM micromapping, the AFM tip indented the surface in the center of this area, pulled off, and moved to a neighbor surface area for the next nanoprobing.

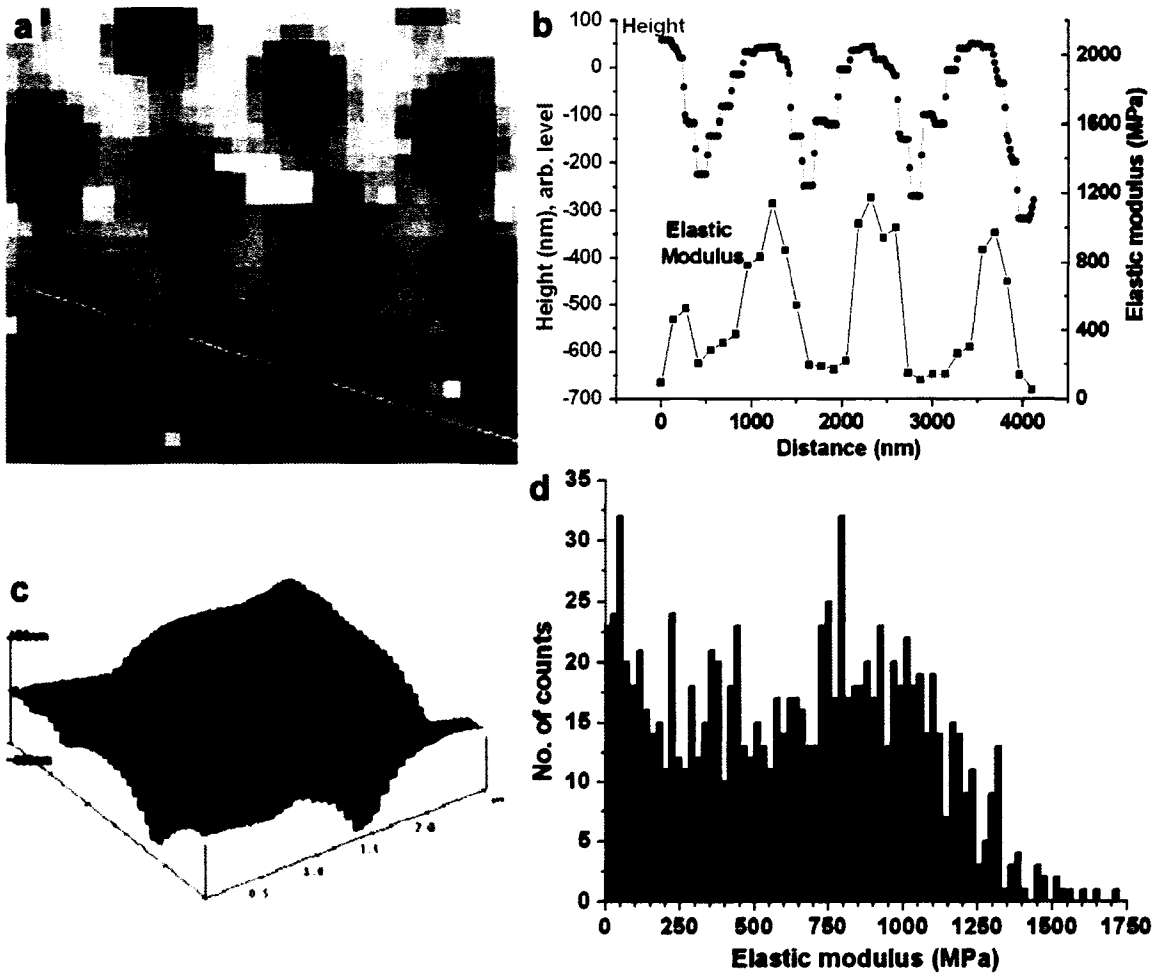

Figure 6-6. a) Topview 4x4 μm2 AFM topography collected in force-volume mode with 32x32 resolution and b) corresponding height (compiled from topographical image of this area with obtained with higher resolution, left axis) and elastic modulus (right axis) cross-sections along the [11] direction (gray line in (a)). Dark line in (a) is caused by probing instabilities; c) 3D topography of the surface areas mapped with 32x32 force spectroscopy (2.5x2.5 μm2); d) The surface distribution of the elastic modulus obtained from (c) (1024 data points).

The force-distance data obtained were converted to the loading curve (indentation vs. load) for the evaluation of the surface stiffness and calculation of the elastic modulus by applying the Hertzian model of the elastic deformation by a semi-spherical indenter interacting with a planar elastic solid. This approximation is acceptable for small penetration depths and intermediate loading rates used in this work, as well as uniform surface morphology. Under these probing conditions, the viscoelastic contribution and auxiliary instrumentation contributions are negligible as was demonstrated for variety of polymers in our previous publications. [25,26,27,28] The application of the Hertzian approximation to AFM nanoprobing is based on the relationship between normal pressure, P, and indentation depth, h, in the form [29]:

$$P = \frac{4}{3} R^{\frac{1}{2}} h^{\frac{3}{2}} E'$$

where R is tip radius and E' is the composite modulus of the two contacting bodies. Thus, the composite elastic modulus (which is identical to the elastic modulus of the polymer for silicon tips) at an incremental depth (between i-1 and i) can be derived from:

$$E_i = \frac{3}{4}(1-\nu^2)\frac{k_n}{R^{\frac{1}{2}}}\frac{Z_{defl,i,i-1}}{h_{i,i-1}^{3/2}}$$

where k_n is the normal spring constant of the cantilever, ν is the Poisson's ratio, Z_{defl} is the incremental vertical deflection of the cantilever derived from force-distance data and calibrated by the sensitivity measurement (since $h=Z_{pos}-Z_{defl}$ and Z_{pos} is the displacement of the AFM piezoelement).

The representative histogram of the elastic moduli for the surface area of the hexagonal patterned film (1024 force-distance curves collected over a 4x4 μm^2 area) showed a clear bimodal distribution of the elastic response (Figure 6-6b). The spatial distribution of the surface stiffness (not shown) possessed very similar, bi-modal character. A broad distribution of moduli ranging from 300 MPa to 1.7 GPa corresponded to the wide distribution of the AFM probed locations (nodes, beams, sidewalls and slope regions). Very

low (close to zero) effective modulus values were detected for hole regions with almost no resistance to AFM tip. Underestimated values of "apparent" elastic modulus were also generated along the edges where actual slope of the surface corrupted force probing due to side contact, non-normal load, and tip sliding instead of indenting. However, this type of topological contribution was significant only in the vicinity of the holes and inside the holes.

The surface distribution of the elastic moduli collected for larger surfaces areas of the patterned polymer film with lower resolution (130 nm x 130 nm per pixel) demonstrates the expected six-fold symmetry known from AFM imaging (Figure 6-6c). A regular variation of the "apparent" elastic modulus on this spatial scale is determined by the surface topography as clear from the corresponding height and elastic modulus cross-sections along the [11] direction (gray line in 6c) (Figure 6-6d). The value of the elastic modulus is high and close to 2 GPa between holes where relatively flat polymer surface area is probed but drops to near zero values inside the holes.

To address the question of the elastic modulus distribution on polymer surface on/between nodes and far from the holes, the higher-resolution micromapping (pixel size down to 60 nm x 60 nm) was implemented (Figure 6-7). The selected surface areas which included a complete set of nodes and beams with six-fold symmetry were used to calculate elastic moduli separately for node and beam areas averaged over six locations (Figure 6-7a and 7b). A statistically significant difference in the average elastic modulus between nodes and beams was derived from this analysis. Considering that the selected surface areas very reasonably flat (maximum slope angle was within 10-20°) the topological contribution can be neglected within the areas of interest. Considering that the estimated contact area is only about 1 nm and potential tip downhill sliding should not exceed 20%, we can essentially assume spherical indenter on a plane with small correction on indentation, thus, applying the Hertzian model. Furthermore, adhesion histograms (not shown) did not show a significant gradient through this area, indicating the virtually constant contact area.

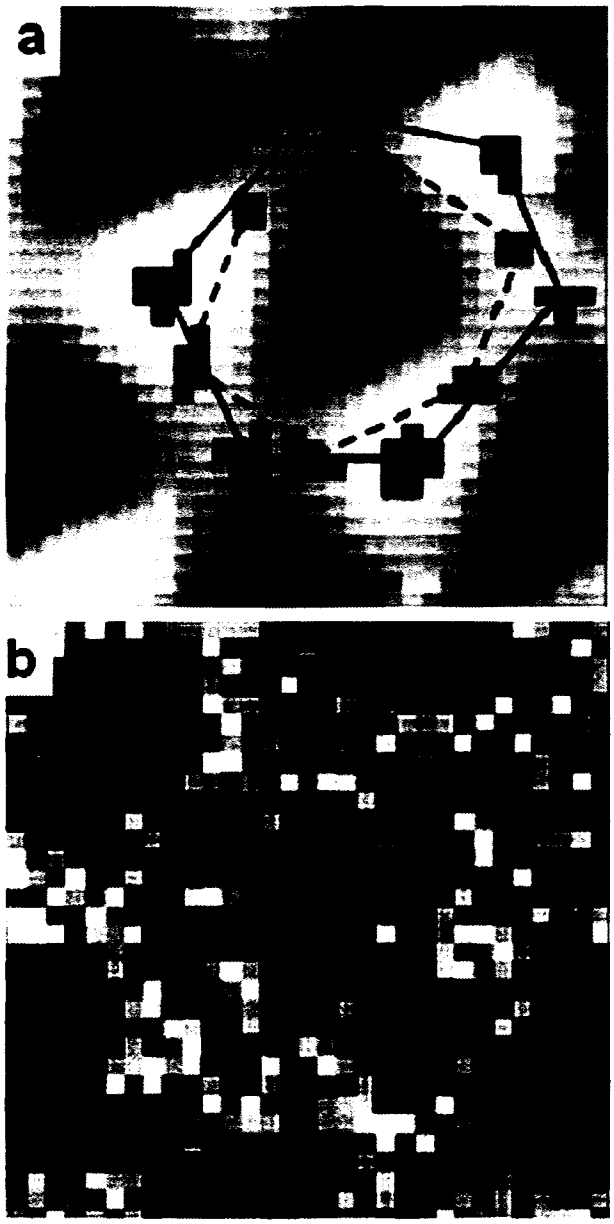

Figure 6-7. High resolution AFM micromapping of the photopatterned SU8 film: a) 32x32 topography and b) elastic modulus collected during force micromapping of the 2.5x2.5 μm^2 surface area (two designated areas are marked by squares of pixels (blue for nodes (N) and red for beams (B)).

The difference between elastic moduli for different locations was consistently observed for multiple nodes and beams probed independently (see blue and red marks in Figure 6-7). On the other hand, we calculated histogram of the elastic modulus distribution for different smooth surface areas. We selected two surface areas representing beams and nodes which excluded the surface areas in the vicinity to the holes (Figure 6-8a). For these areas, we calculated statistical distribution of the elastic moduli (Figure 6-8b). The average elastic modulus obtained from these histograms for the nodes was 1480 ± 460 MPa, which was higher (beyond standard deviation) than that calculated value for the beam areas, 1120 ± 590 MPa.

We suggest that the observed location-dependent variation of the elastic moduli is caused by the spatial variation of the material properties "templated" by the light distribution within the interference pattern.[30] The variable light distribution results in variable crosslinking density and hence

corresponding materials properties such as elastic modulus, glass transition, or plasticity behavior.[17, 31, 32] In interference lithography, crosslinking density depends on both dose and the distribution of the amine compensator. In fact, the close to linear relationship between the illumination dose and the crosslinking density above the dissolution threshold is confirmed in this study by microprobing SU8 materials exposed to light doses from 0.38 to 3.8 J/cm^2 (not shown). The 2D interference pattern produces higher intensity in the spots of constructive interference (nodes) with a decrease of intensity down to the zero level in the spots of destructive interference (holes) (Figure 6-4c). Regions with the highest intensity define lattice nodes with the highest crosslinking density (marked as N in Figure 6-4). The locations of holes (air holes after removing uncured material) correspond to the intensity minima confirming close correlations between spatial distributions of

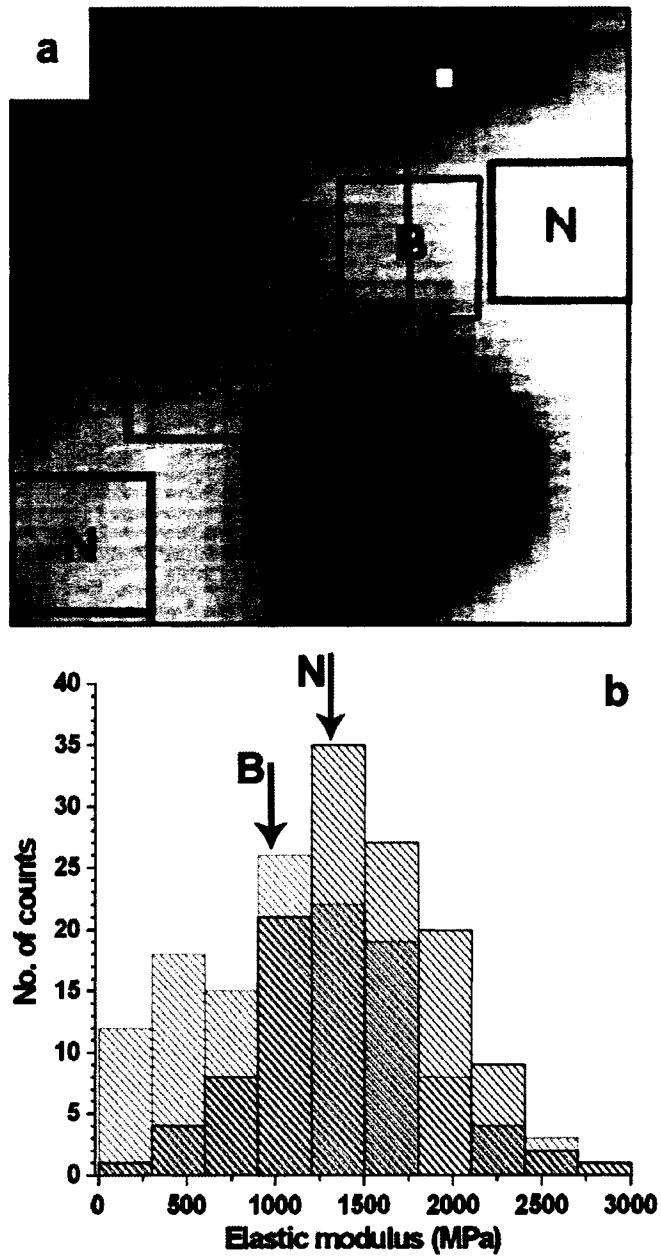

Figure 6-8. a) 32x32 high-resolution AFM topography during force micromapping of the 2x2 μm^2 surface area and b) combined surface histograms collected for selected surface areas (500x500 nm^2) for nodes (black boxes) and beams (gray boxes).

intensity and the elastic modulus distribution. Less dramatic but still significant variation of the elastic modulus observed here for the beams and nodes of the photopatterned films also follows closely the light intensity distribution in the interference pattern can reflect a complex combination of spatial variation of crosslinking density, local glass transition temperatures, and amine compensator distribution. The precise nature of the behavior observed should be addressed in future studies.

The 2D photopatterned films fabricated here can be also considered as "natural" composite networks with potentially peculiar properties associated with non-uniform distribution of internal elastic properties. In fact, in our preliminary studies, we observed very peculiar deformational behavior of these perforated films (Figure 6-9). The SU8 film was fractured with external stresses by pulling the grafted film with a sticky tape and a variety of deformational modes was observed by applying SEM. In two selected images presented here, one can see that the perforated SU8 are capable of highly plastic behavior with significant local deformation of individual cells and

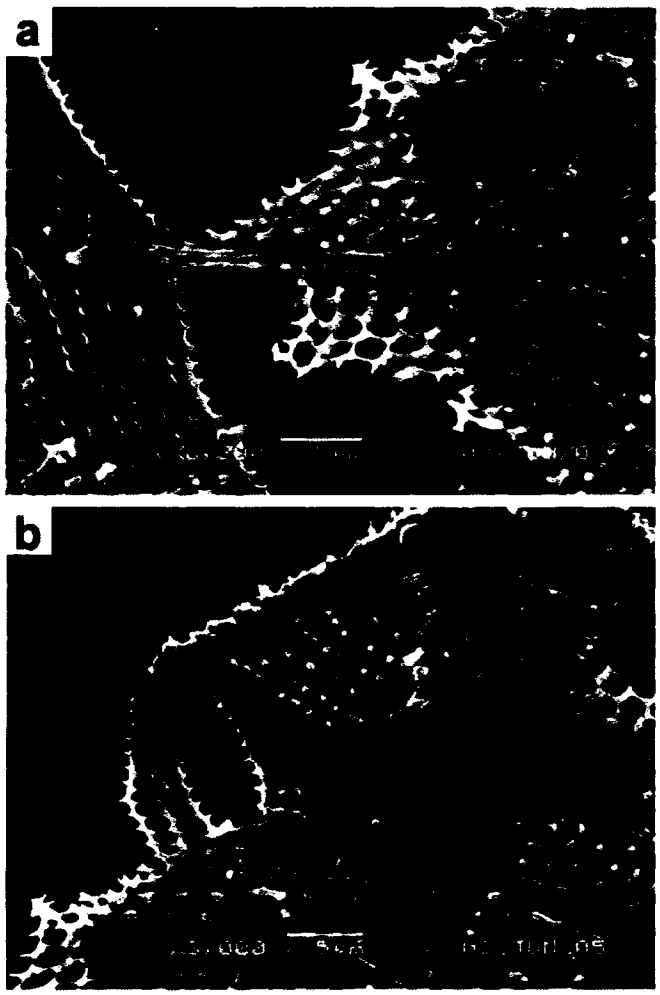

Figure 6-9. SEM micrographs of stretched and twisted polymer 2D hexagonal pattern demonstrating extreme plasticity and unique fracturing behavior.

large-scale deformation of the whole net (Figure 6-9). High shearing and bending was observed for large film regions, which is completely uncharacteristic for glassy polymeric materials. Although this unusual behavior requires further investigation, we can speculate that the precise control of the non-uniform internal elastic properties within ITL microfabricated polymer structures makes these structures highly deformable and opens potential paths for the photopatterned polymeric materials with efficient energy absorption on a submicron scale.

6.4 Experimental

2D patterns were fabricated using multi-beam holographic interference lithography that allows generation of periodic structures over large areas with high resolution.[33,34] The fabrication procedure involved the interference of three equal intensity laser beams and the transfer of the resultant intensity pattern into an SU8 photoresist platform via laser-initiated cationic polymerization.[35] The materials platform consisted of Epon-SU8 (Shell) as a photoresist (a multifunctional epoxy derivative of a bisphenol-A Novolac), cyclopentanone (Aldrich) as a solvent for spin-on of the film, rubrene (Aldrich) as a photosensitizer which absorbs the visible light and electron transfers to an onium salt, octoxyphenylphenyliodonium hexafluoroantimonate (OPPI) (UCB Radcure) as a photoacid generator, and tributylamine to compensate the non-zero background of the interference intensity. These compounds were first dissolved in cyclopentanone and then mixed with SU8 in a weight ratio of rubrene:OPPI:SU8=0.2:2:100, respectively. To increase the adhesion between the glass substrate and SU-8 layer, a 1 μm thick buffer layer of SU8 was spin-coated (2,000 rpm, 1 min) and baked (5 min, 95°C). It was then flood-exposed under the UV lamp and hard-baked at 180°C for 15 min. This layer effectively improved adhesion of the patterned SU-8 layer to the substrate and prevented delamination during the developing process. Next, the SU-8 solution in cyclopentanone was spin-coated on top of this existing SU-8 film at a spin speed of 1000 rpm. The coated photoresist was then soft baked at 95°C for 10 min. The exposure was done using a 532 nm Nd:YAG laser with an intensity of 0.3 W for 10 seconds to give a total exposure dose of 5-10 J/cm^2 over areas with diameter larger than 4 mm. After baking

the 6 μm thick film at 65 °C for 5 min, the resultant cationic photopolymerization only takes place in regions that were exposed to high intensities of light. The uncured regions were developed away in PGMEA (propyleneglycol monomethylether acetate) and the film was finally rinsed with isopropyl alcohol to yield the 2D porous photopatterned structure.

AFM studies were performed on a Multimode Nanoscope IV microscope (Digital Instruments, Inc.).[36] Probing of the surface nanomechanical properties was conducted with static surface force spectroscopy using cantilevers with independently characterized spring constants (from 6 to 30 N/m) and tip radii (from 40 to 200 nm). Force-Volume mode was applied to selected surface areas by collecting 32x32 point arrays of force-distance curves.

The cantilever calibration, data processing and the evaluation of the loading behavior (indentation depth vs normal load), calculation of the surface stiffness and the elastic modulus by fitting loading curves, and the evaluation of the surface distribution of the elastic moduli were carried out in accordance with the usual approach by using the Hertzian contact mechanic model as described in detail previously.[37,38] Briefly, the AFM tip with known shape (deconvoluted by scanning a gold nanoparticles reference specimen) indents the polymer surface with probing frequency of 1 Hz. The indentation depth is selected to avoid any plastic deformations (within 2-4 nm for SU8 material). The nanoscale contact diameter within 1-2 nm limits stress field distribution to only several nanometers in the vicinity of the probed point, thus preventing influence of consequential measurements and the hole presence. The known bulk Poisson's ratio was used for these calculations and possible deviation would not affect significantly the outcome of calculations. The nanoscale structure of the SU8 films is considered to be uniform and thus the model with local uniform distribution of the elastic modulus was applied for a single indentation within the 60 nm x 60 nm surface area. More complex models can be applied if evidences of the non-uniform nanoscale distribution will be available as discussed in a separate publication.[37] SEM images were obtained with a JEOL-6060 microscope. The strain-induced elastic buckling-instability measurements were carried out of uncured and cured SU8 films spun-on the oxygen treated polydimethylsiloxane (PDMS) substrate.[21,39]

6.5 Acknowledgments

We thank S. Kooi for technical assistance and A. D. Nolte for buckling instability test. This research was supported by the U.S. Army Research Office through the Institute for Soldier Nanotechnologies, under Contract DAAD-19-02-D-0002 and AFOSR, F496200210205 Grant.

6.6 References

[1] K. Y. Lee, N. LaBianca, S. Zolgharnain, S. A. Rishton, J. D. Gelorme, J. M. Shaw, T. H. Chang, *J. Vac. Sci. Techn.* **1995**, *B13*, 3012.

[2] G. Hong, A. S. Holmes, M. E. Heaton, *Microsyst. Technol.* **2004**, *10*, 357.

[3] T. Staedler, K. Schiffmann, *Surf. Sci.* **2001**, *482*, 1125.

[4] H. Lorenz, M. Despont, N. Fahrni, N. LaBianca, P. Renaud, P. Vettiger, *J. Micromech. Microeng.* **1997**, *7*, 121.

[5] N. T. Nguyen, T. Q. Truong, *Sens. Actuators B-Chem.* **2004**, *97*, 139.

[6] V. Seidemann, S. Bütefisch, S. Büttgenbach, *Sens. Actuators A Phys*, **2002**, *97-98*, 457.

[7] H. Yu, O. Balogun, B. Li, T. W. Murray, X. Zhang, *J. Micromech. Microeng.* **2004**, *14*, 1576.

[8] H. Lorenz, M. Laudon, P. Renaud, *Microelectron. Eng.* **1998**, *41-42*, 371.

[9] R. G. Alargova, K. H. Bhatt, V. N. Paunov, O. D. Velev, *Adv. Mater.* **2004**, *16*, 1653.

[10] M. Calleja, J. Tamayo, A. Johansson, P. Rasmussen, L. M. Lechuga, A. Boisen, *Sensor Lett.* **2003**, *1*, 20.

[11] R. Bandorf, H. Lüthje, A. Wortmann, T. Staedler, R. Wittorf, *Surf. Coat.* **2003**, *174-175*, 461.

[12] T. Gorishnyy, C. K. Ullal, M. Maldovan, G. Fytas, E. L. Thomas, *Phys. Rev. Lett.* **2005**, *94*, 115501.

[13] D. N. Sharp, M. Campbell, E. R. Dedman, M. T. Harrison, R. G. Denning, A. J. Turberfield, *Opt. Quantum. Electon.* **2002**, *34*, 3.

[14] M. De Vittorio, M. T. Todaro, T. Stomeo, R. Cingolani, D. Cojoc, E. Di Fabrizio, *Microelectron. Eng.* **2004**, *73-74*, 388.

[15] M. Nathan, *Appl. Phys. Lett.* **2004**, *85*, 2688.

[16] F. E. H. Tay, J. A. V. Kan, F. Watt, W. O. Choong, *J. Micromech. Microeng.* **2001**, *11*, 27.

[17] R. Feng, R. J. Farris, *J. Mater. Sci.* **2002**, *37*, 4793.

[18] R. Feng, R. J. Farris, *J. Micromech. Microeng.* **2003**, *13*, 80.

[19] S. K. Rath, F. Y. C. Boey, M. J. M. Abadie, *Polymer Int.* **2004**, *53*, 857.

[20] A. Plepys, M. S. Vratsanos, R. J. Farris, *Comp. Struct.* **1993**, *23*, 51.

[21] K. K. Seet, V. Mizekis, S. Matsuo, S. Juodkazis, H. Misawa, *Adv. Mater.* **2005**, *17*, 541.

[22] S. A. Chizhik, Z. Huang, V. V. Gorbunov, N. K. Myshkin, V. V. Tsukruk, *Langmuir* **1998**, *14*, 2606.

[23] C. M. Stafford, C. Harrison, K. L. Beers, A. Karim, E. J. Amis, M. R. Vanlandingham, H. C. Kim, W. Volksen, R. D. Miller, E. E. Simonyi, *Nat. Mater.* **2004**, *3*, 545.

[24] A. J. Nolte, M. F. Rubner, R. E. Cohen, *Macromolecules* **2005**, *38*, 5367.

[25] V. V. Tsukruk, Z. Huang, S. A. Chizhik, V. V. Gorbunov, *J. Materials Science,* **1998**, *33*, 4905.

[26] V. V. Tsukruk, V. V. Gorbunov, Z. Huang, S. A. Chizhik, *Polymer Intern.* **2000**, *49*, 441.

[27] A. Kovalev, H. Shulha, M. LeMieux, N. Myshkin, V. V. Tsukruk, *J. Mater. Res.* **2004**, *19*, 716.

[28] V.V. Tsukruk, V.V. Gorbunov, *Probe Microsc.* **2002**, *2*, 241.

[29] V. V. Tsukruk, A. Sidorenko, V. V. Gorbunov, S. A. Chizhik, *Langmuir* **2001**, *17*, 6715.

[30] C. Decker, T. N. T. Viet, D. Decker, E. Weber-Koehl, *Polymer* **2001**, *42*, 5531.

[31] J. Zhang, M. B. Chan-Park, S. R. Conner, *Lab Chip* **2004**, *4*, 646.

[32] L. Simonin, J. J. Hunsinger, J. P. Gonnet, D. J. Lougnot, *SPIE* **1996**, *2775*, 207.

[33] M. Campbell, D. N. Sharp, M. T. Harrison, R. G. Denning, A. J. Turberfield, *Nature* **2000**, *404*, 53.

[34] C. K. Ullal, M. Maldovan, G. Chen, Y. Han, S. Yang, and E. L. Thomas., *Appl. Phys. Lett.* **2004**, *84*, 5434.

[35] S. Yang, M. Megens, J. Aizenberg, P. Witzius, P. M. Chaikin, W. B. Russell, *Chem. Mater.* **2002**, *14*, 2831.

[36] V. V. Tsukruk, *Rubber Chem. Technol.* **1997**, *70*, 430.

[37] J. L. Hazel, V. V. Tsukruk, *Thin Solid Films*, **1999**, *339,* 249.

[38] H. Shulha, A. Kovalev, N. Myshkin, V. V. Tsukruk, *Eur. Polym. J.* **2004**, *30*, 949.

[39] A. L. Volynskii, S. Bazhenov, O. V. Lebedeva, N. F. Bakeev, *J. Mater. Sci.* **2000**, *35*, 547.

Chapter 7

3D Polymer Microframes that Exploit Length-Scale Dependent Mechanical Behavior

A paper published in *Advanced Materials*♦

Ji-Hyun Jang[1], *Chaitanya K. Ullal*[1], *Taeyi Choi*[1], *Melburne C. LeMieux*[*,2], *Vladimir V. Tsukruk*[2] *and Edwin L. Thomas*[1,*]

[1] Institute for Soldier Nanotechnologies, Department of Materials Science and Engineering, Massachusetts Institute of Technology, Cambridge, Massachusetts 02139

[2] Department of Materials Science and Engineering, Iowa State University, Ames, Iowa 50011

7.1 Abstract

Holographic interference lithography is used to create a 3D polymer microframe with submicron periodicity, low density and 200 nm feature size. Due to their length scale dependent mechanical behavior these structures exhibit interesting deformational characteristics with ultimate strains reaching ~ 300 %, much higher than the strains attainable in bulk films of either the fully crosslinked solid polymeric material or the uncrosslinked glassy monomer precursor.

♦ Reprinted with permission of *Advanced Materials*

* M.C.L.: Assistant researcher, did AFM experiments, assistant writer of all drafts.

7.2 Introduction

Materials science, especially metallurgy has long exploited the relationship between microstructural scale arising from various processing routes and resultant properties with increasing emphasis on the benefits of ultra-fine scale structures. Critical elements for the design of lightweight materials for mechanical applications include means for stiffening, strengthening as well as providing energy absorption and controlled crack propagation [1, 2, 3, 4]. Combinations of hard and soft components, control over component size, shape, and arrangement, and attention to interfacial strength are widely used to design composite materials with superior properties. Man-made ordered composites are typically assembled via machine or hand lay-up and generally rely on macroscopic components. On the other hand, load bearing structures in nature are much more complex, often using a combination of hard (e.g. calcite) and soft (e.g. proteins) components and importantly, feature elegant self organized hierarchical designs extending from the nanometer to the mm scale [5]. Moreover, nature has evolved certain structures into nearly optimized mechanical designs [6]. Most current man-made sub-micron scale composites provide little control over the detailed microstructure of the respective components [7].

For example, recent efforts with polymer-carbon nanotube composites currently lack the processing ability to pattern the components at various length scales to create optimally designed materials. Patterning by self assembly is one means to mimic nature but at present most ordered structures occur more by happenchance than by purposeful design and the pattern is achieved normally only at one length scale. Taking advantage of length-scale dependent mechanical properties is another strategy used by nature to tailor mechanical behavior [5]. Polymeric materials in particular are also sensitive to the influence of sample dimensions on properties, for example, below a critical film thickness, brittle polymers can exhibit increased strain to break and improved toughness [8, 9].

Lightweight microframe structural materials possessing load bearing capabilities approaching theoretical limits have recently been constructed from millimeter size metallic

assemblies [10]. Their open architecture provides for a density well below 10 % of that for the corresponding bulk materials [11]. Several structures have been fabricated, tested, and theoretically analyzed. However, for feature sizes at the millimeter scale, the material's mechanical properties are not size dependent, indeed, theoretical models that rely only on inputting a constitutive equation based on bulk material behavior along with the particular truss geometry do a very good job of capturing the experimentally observed behavior. Designs that provide conditions such that beams are under compression or tension while avoiding bending are desired. In particular pyramidal and octahedral frame structures provide maximum stiffness and strength at a given density [12]. In addition to outstanding specific mechanical properties, the open structure and high surface area ($\sim m^2 g^{-1}$) of microframes add additional functionality such as the ability to cool by flowing a continuous fluidic phase through the structure [13].

Recent developments in laser interference lithography (IL) demonstrate the ability for fast fabrication of complex polymeric structures with long-range periodic order [14]. IL can create connected sub-micron sized elements in complex 2D and 3D networks [15] with micron to sub-micron spacings. Such periodic structures created with IL are being pursued for photonic [14, 15, 16] and phononic [17] applications. Periodic high porosity polymeric structures are also attractive candidates for mechanical applications, provided the polymeric material used for the "skeleton" network of members exhibits appropriate mechanical properties, and the chosen geometry of the 3D structure provides proper mechanical load distribution.

7.3 Results and Discussion

Here, we report the use of holographic interference lithography to create a 3D polymer microframe having a four-functional network geometry with submicron periodicity, low density (~ 0.3 gm cm^{-3}) and 200 nm feature size. These large area, periodic, porous polymer/air structures are fabricated from negative Novolak-resin photoresist and due to their length scale dependent mechanical behavior, exhibit interesting deformational characteristics (e.g. necking of crosslinked struts and their evolution into long fibrils) with ultimate strains

reaching ~ 300 %, much higher (~ 10X) than the strains attainable in bulk films of either the fully crosslinked solid polymeric material or the uncrosslinked glassy monomer precursor. The unique deformation and fracture behavior of the polymer networks reported here demonstrates the promise of rational design and fabrication via interference lithography of lightweight bicontinuous network nanocomposite materials.

As a first attempt to fabricate and mechanically test a 3D polymer microframe, we used multiple interference lithography to pattern Novolak-resin (SU8). This cross-linkable material is widely used as a robust negative photoresist for microelectromechanical devices [18]. Fabrication involved the interference of four laser beams and the transfer of the resultant intensity pattern into the photoresist via laser-initiated cationic polymerization [19]. The Gaussian output from the laser was converted into a top hat function using a refractive beam shaper. The light intensity distribution throughout the photoresist depends on the relative directions and polarizations of the interfering beams. The 3D microstructure targeted here is an elongated IL variant of the classic Yablonovite photonic structure [20]. The final directions and polarizations of the beams inside the photoresist are given by:

$\vec{k}_0 = [0.0112, 0.0112, 0.0112]$ $\vec{E}_0 = [0, -5.74, 5.74]$

$\vec{k}_1 = [0.0164, 0.0073, 0.0073]$ $\vec{E}_1 = [0, -2.45, 2.45]$

$\vec{k}_2 = [0.0073, 0.0164, 0.0073]$ $\vec{E}_2 = [0.97, -1.75, 2.97]$

$\vec{k}_3 = [0.0073, 0.0073, 0.0164]$ $\vec{E}_3 = [-0.97, -2.97, 1.75]$

The structure is a four-functional network and can be envisioned as a type of continuously joined set of polymer nodes and members, having a basic unit comprised of a thick vertical post (L/D ~ 2.3) supporting three thinner struts (L/D ~ 3.2) where L is the length and D is the diameter (see Fig. 7-1) [21]. This modification, we believe, could provide for better compressive stability to normal loads. The structure is defined by the distribution of crosslinks in the photoresist arising from the light intensity distribution determined by the laser beam parameters (directions, polarizations, amplitudes and phases). For the present IL

defined network members having aspect ratios of only 2-3, transverse loads create shear stresses across the members in addition to bending.

To gain a better understanding of our structure, the theoretical light distribution at different sections of the unit cell as well as the corresponding schematic views of different orientations of the theoretical 3D structure are presented in Fig. 7-1. The highest intensity regions of the interference pattern result in regions with the highest crosslink density, while the darker regions correspond to regions with the lowest crosslink density. The non-zero background of generated acid due to the non-zero background of light intensity is offset by fine-tuning of beam polarization and small amount of additional base[19]. During the development process, the weakly crosslinked material is removed, leaving a connected pore space between the more highly crosslinked epoxy regions.

The unit cell of our structure is comprised of three layers illustrated by the different colors in Fig. 7-1c. The section at 2c/3 shows the successive lateral shift of the basic motif. The view along [0 0 0 1] shows a 3-fold pattern of members and nodes with the color indicating the height in the unit cell (see Fig. 7-1b). SEM images of planes perpendicular to [1 1 2bar 0] and [0 0 0 1] show good correspondence between the SU8 structure and the theoretical model (compare Figs. 7-1b, 1c with the insets in 1e). The overall 8.5 μm-thick microframe polymer film includes 2 unit cells with six sub layers composed of staggered vertical posts with average height of 1400 nm, diameter of 500 nm and spacing of 980 nm as evaluated from the side view (Fig. 7-1e). We estimate sample porosity at about 70 % by comparison of SEM images with various level set representations of the structure and from assigning sizes to the struts and computing the volume fraction occupied by the epoxy network in the unit cell.

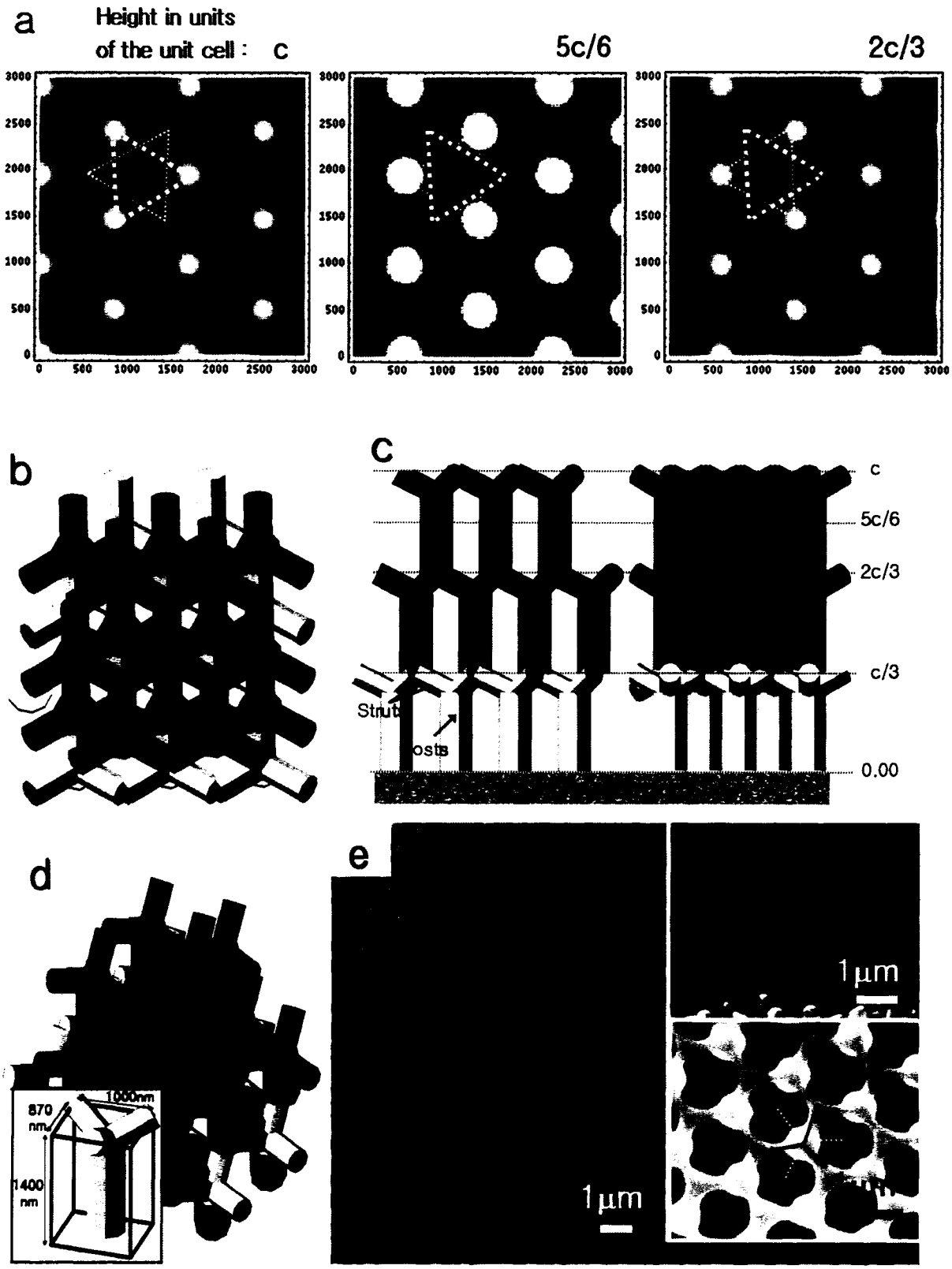
a
Height in units
of the unit cell : c
5c/6
2c/3
b
c
c
5c/6
2c/3
c/3
0.00
Strut
Posts
d
870 nm
1000nm
1400 nm
e
1μm
1μm

Figure 7-1. Microframe polymer structures fabricated by 3D interference lithography. (a) Theoretical 2D light intensity distributions at various heights within the unit cell (the middle image is binarized to correspond to the final developed structure). The triangles are for locating the same region in each image (b) View normal to the (0001) plane of the microframe structure. The colors correspond to struts at c/3, 2c/3 and c. (c) Views normal to the (1 1 bar2 0) and (1 0 bar1 0) planes of the microframe structure. (d) Perspective view of the structure with the basic four-functional element as the inset. The sub cell dimensions are ~ 1400 nm x 1000 nm x 870 nm. The three thinner struts have a diameter about 200 nm and length of 640 nm and the thicker vertical post has a diameter of 500 nm and length of 1100 nm. (e) SEM image of the 3D-microframe fabricated in SU8. The insets show magnified views of the top and cross sectional surfaces corresponding to the schematic views in b and c.

In order to make a preliminary assessment of the deformation behavior of the microframe film, we employed a simple peeling process that involves adhering adhesive tape to the structure and peeling off a portion of the film. The remaining film is then transferred onto carbon tape and mounted in a SEM holder. Peeling involves a complex interplay of forces and allows us to observe the mechanical response of the microframe structure in a wide variety of deformational modes. We thus see the effect of tension, bending, compression, and shearing on our sample. Inspection of the film (see Fig. 7-2, 7-3) reveals a host of interesting morphologies related to fracture and various types of deformation.

Features associated with failure include long, straight, micron-wide cracks following high symmetry, easy fracture directions (Fig. 7-2a, 7-2b) and penny shaped cracks extending inwards from the surface towards the substrate (Fig. 7-2c). The planes of easy fracture are parallel to the direction of the thick posts and always involved the failure of the thin, transversely oriented struts in accordance with the 3-fold symmetry normal to the (0 0 0 1) planes (e.g. see boxed region in Figure 7-2a and facets visible in Figure 7-2b).

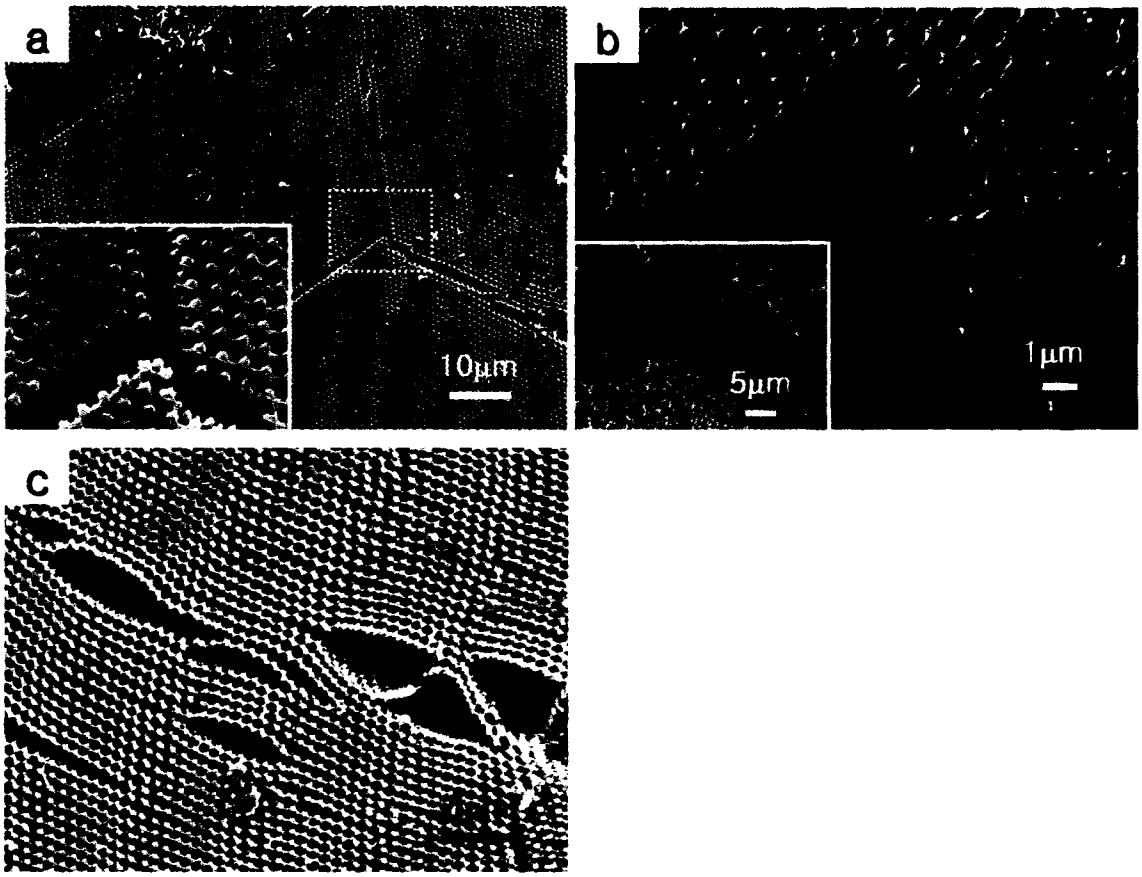

Figure 7-2. SEM images of fracture within the polymer microframe. (a) Region where cracks are guided by planes of easy fracture. (b) View showing a region with intersecting {1 1 2bar 0} facets with an apex angle of 60 degrees. The inset is the low magnification picture. (c) Region where surface-initiated cracks penetrate towards the substrate.

Unusual behavior is observed while examining the modes of failure of the thin members. Here we observe portions of microframe bridging across wide cracks (Fig. 7-3a), highly stretched members in front of arrested cracks (Fig. 7-3b), and crushed and densified areas in regions of compression (Fig. 7-3c). The diameter of the most highly stretched members decreases to approximately 70 nm. By comparison, of the strut length in unperturbed unit cells with those in deformed regions, member strain can be estimated and is upwards of 300 % (see elongated members in Fig. 7-3b). The strain to failure of the 100 nm

features is about an order of magnitude higher than that observed for uncrosslinked monomer films ($\varepsilon_f \sim 30$ %) and for fully crosslinked (exposed plus a hard bake) Novolak resins ($\varepsilon_f \sim 8$-10 %)[22]. The plasticity of the fine scale structure is further evidenced in the formation of fibrils in regions of high extension, due to pull out and alignment of posts and struts (see Fig. 7-3d, 7-3e).

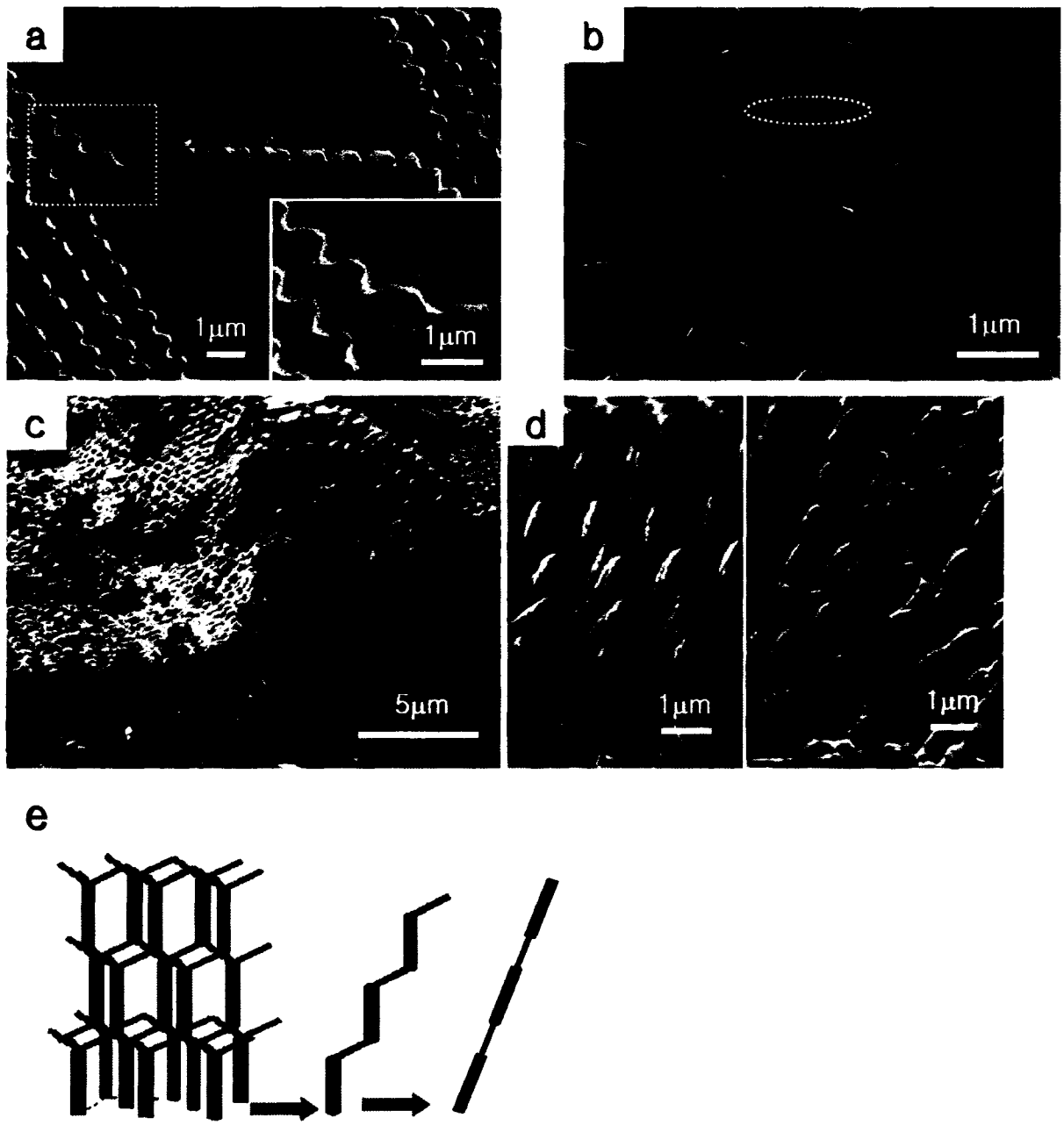

Figure 6-3. SEM images of microframe structure showing large amounts of plastic deformation. (a) Area with a microframe bridge extends from one side of a crack to the other. The inset shows extensive shear, bending, and microplastic deformation of the structure near the left terminus of the bridge. (b) Evidence of tensile deformation and fracture of transverse struts with up to several hundred % strain (e.g. circled strut) in the vicinity of a crack. The local strain can be estimated based on the departure of the strut and node pattern from the initial undeformed unit cell structure (right side of image). (c) Portion of film that was compressed, showing the collapsed microframe region at left. (d) (left) Cross section of a region of the film where the structure has been plastically deformed (right). Fibrils formed due to peeling of microframe from substrate. (e) Schematic depicting how long fibrils form via stretch-alignment of vertical and transverse struts.

We can explain the unusual highly ductile failures of the normally brittle SU8 epoxy primarily as a result of two effects: the creation of the very small diameter epoxy members and attainment of an intermediate crosslink density. Kramer's group has shown for glassy amorphous polymers that below a critical film thickness (~ 100 nm-1000 nm), the strain to break can approach the maximum expected draw ratio of the entanglement network [8] or crosslinked network [23]. Van der Sanden and Meijer [24] investigated a thermosetting polymer and found a similar critical ligament thickness, below which the strain to failure greatly increased. For highly crosslinked SU8 material, the glass transition temperature is 230 °C [25], compared to 55°C for the uncured, uncrosslinked monomer [22]. The glass transition temperature determined by DSC of our structured polymer film was approximately 100 °C consistent with partially crosslinked material. In order to eliminate the possibility of the behavior being due to the presence of solvent, we conducted FTIR studies, which revealed no detectable residual solvent after developing and drying (supercritical CO_2). The nature of the crosslink gradients in the structure can be understood by examining the intensity variation used to expose the photoresist. The intensity pattern that is created by IL is a sum of a few Fourier terms. In the case of a negative photoresist such as SU8, the resultant crosslink

density follows this same intensity variation. We compensate for the DC IL signal by addition of a base.

A previous study of the localized small strain mechanical properties via nanoindentation experiments of 2D structures created by IL in SU8 has established this correlations between the spatial distribution of the light intensity and the distribution of the crosslinking density[26]. The elastic modulus for the nodes (brightest regions in the interference pattern) was 1.3X that for the beams (darker regions in the interference pattern).

To access a greater span of mechanical properties, additional types of microframe materials other than photoresists can be made by infiltration of these polymeric templates with for example, a sol-gel to create polymer-ceramic composites, or after a suitable etch, air-ceramic structures. Alternatively, photoetchable glasses may in the future be directly patterned to create microframes [27]. Periodic microframe structures can direct crack propagation along certain crystallographic directions and also exhibit enhanced plastic response. The remarkable high plastic deformation exhibited in our microframe structure derives from the hundred nm length scale of the individual members, facilitated by crosslink density gradients in the epoxy, with the more highly crosslinked nodes being less deformable than the less densely crosslinked struts. Deformation mechanisms characteristic to a nanoscale structure combined with a purposeful mechanical design suggest a pathway for creating new ultra light, mechanically dissipative structures.

7.4 Experimental

3D microframe structures with four-functional topology were fabricated using multi-beam holographic interference lithography according to the procedure described in detail elsewhere [28]. The glass support was treated with a thin (700 nm) buffer layer of pre-crosslinked SU8 material to assure firm attachment of the structured polymer film to the substrate via chemical grafting to enable subsequent mechanical peeling experiments. The exposure was done using a 532 nm Nd:YAG laser and the Gaussian output was converted

into a top hat function using a refractive beam shaper. By post exposure bake of the 8.5 μm-thick film, the resultant cationic photopolymerization takes place in regions that were exposed to high intensities of light. To avoid collapse of the 3D microframe structure, CO_2 supercritical drying is applied after developing the uncured region to yield the final 3D porous microframe structure over areas as large as 5 mm in diameter. Sample morphology was analyzed with SEM (JEOL 6060 and FESEM JSM-7401). The modulation of the frame structure evident in the lower magnification SEM images is due to the slight noncoplanarity of the (0001) plane of the interference pattern and the upper surface of the photoresist.

Thermal properties and average extent of crosslinking were evaluated by a TA instruments Differential Scanning Calorimeter (Q 1000) by scanning from 30 °C to 250 °C with a heating rate of 20 °C min^{-1} under a nitrogen purge. Samples for DSC were collected by scraping the crosslinked film from the substrate.

Total Reflectance Fourier Transform Infrared Spectra (ATR FT-IR mode) was obtained from SU8 structure on glass substrate using NEXUS 870 FT-IR (Thermo Nicolet). The film thickness was measured with a profilometer (P10 Tencor Surface Profiler).

7.5 Acknowledgments

We thank S. Kooi for technical assistance, T. Kanazawa (JEOL) for some SEM images and L. Gibson for helpful discussions. This research was supported by the U.S. Army Research Office through the Institute for Soldier Nanotechnologies, under Contract DAAD-19-02-D-0002 and AFOSR, Grant F496200210205.

7.6 References

[1] L. J. Gibson, M. F. Ashby in *Cellular Solids: Structure and Properties* 2nd Ed., Cambridge Univ. Press **1999**.

[2] M. F. Ashby in *Materials Selection in Mechanical Design* 2nd Ed., Butterworth-Heinemann **1999**.

[3] R. J. Young in *Crack Propagation in Thermosetting Polymers: Developments in Reinforced Polymers.* Applied Science **1980**.

[4] C. Creton, E. J. Kramer, H. R. Brown, C. Y. Hui, *Adv. Polym. Sci.* **2002**, *156*, 53.

[5] J. Aizenberg, J. C. Weaver, M. S. Thanawala, V. C. Sundar, D. E. Morse, P. Fratzl, *Science* **2005**, *309*, 275.

[6] V. S. Deshpande, M. F. Ashby, N. A. Fleck, *Acta. Mater.* **2001**, *49*, 1035.

[7] J. Kim, Y. W. Mai, *Comp. Sci. Technol.* **1991**, *41*, 333.

[8] E. J. Kramer, L. L. Berger, *Adv. Polym. Sci.*, **1990**, *91/92*, 1.

[9] M. C. M. Van der Sanden, H. E. H. Meijer, P. J. Lemstra, *Polymer* **1993**, *34*, 2148.

[10] H. N. G. Wadley, N. A. Fleck, A. G. Evans, *Comp. Sci. Technol.* **2003**, *63*, 2331.

[11] J. Tian, T. Kim, T. J. Lu, H. P. Hodson, D. T. Queheillalt, H. N. G. Wadley, *Int. J. Heat Mass. Tran.* **2004**, *47*, 3171.

[12] S. Hyun, A. M. Karlsson, S. Torquato, A. G. Evans, *Int. J. Solids Struct.* **2003**, *40*, 6989.

[13] D. J. Sypeck, H. N. G. Wadley, *J. Mater. Res.***2001**, *16*, 890.

[14] M. Campbell, D. N. Sharp, M. T. Harrison, R. G. Denning, A. J. Turberfield, *Nature* **2000**, *404*, 53.

[15] C. K. Ullal, M. Maldovan, M. Wohlgemuth, E. L. Thomas, C. A. White, S. Yang, *J. Opt. Soc. Am.* **2003**, *A/20*, 948.

[16] D. C. Meisel, M. Wegener, K. Busch, *Phys. Rev.* **2004**, *B 70*, 165104.

[17] T. Gorishnyy, C. K. Ullal, M. Maldovan, G. Fytas, E. L. Thomas, *Phys. Rev. Lett.* **2005**, *94*, 115501.

[18] H. Lorenz, M. Despont, N. Fahrni, N. LaBianca, P. Renaud, P. Vettiger, *J. Micromech. Microeng.* **1997**, *7*, 121.

[19] S. Yang, M. Megens, J. Aizenberg, P. Wiltzius, P. M. Chaikin, W. B. Russel, *Chem. Mater.* **2002**, *14*, 2831.

[20] E. Yablonovitch, T. J. Gmitter, K. M. Leung, *Phys. Rev. Lett.* **1991**, *67*, 2295.

[21] C. K. Ullal, Ph.D. Thesis, Massachusetts Institute of Technology **2005**.

[22] R. Feng, R. J. Farris, *Micromech. Microeng.* **2003**, *13*, 80.

[23] L. L. Berger, E. J. Kramer, *J. Mater. Sci.* **1998**, *23*, 3536.

[24] M. C. M. Van der Sanden, H. E. H. Meijer, *Polymer* **1993**, *34*, 5063.

[25] R. Feng, R. J. Farris, *Mater. Sci.* **2002**, *37*, 4793.

[26] T. Choi, J.-H. Jang, C. K. Ullal, M. C. Lemieux, V. V. Tsukruk, E. L. Thomas, *Adv. Funct. Mater.* **2006**, in press.

[27] P. Fuqua, S. W. Janson, W. W. Hansen, H. Helvajian, *Proc. SPIE* **1999**, *3618*, 213.

[28] C. K. Ullal, M, Maldovan, E. L. Thomas, G. Chen, Y.-J. Han, S. Yang, *Appl. Phys. Lett.* **2004**, *84*, 5434.

Chapter 8

Trilayered Ceramic-Metal-Polymer Microcantilevers with Dramatically Enhanced Thermal Sensitivity

A paper published in *Advanced Materials*♦

By Y-H. Lin, M. McConney, M. C. LeMieux, S. Peleshanko, C. Jiang, S. Singamaneni, and V. V Tsukruk**

Materials Science & Engineering Department, Iowa State University, Ames, IA 50011

8.1 Introduction

The highly sensitive microcantilever sensors have a broad range of applicability for detecting diverse physical phenomena such as temperature, heat, magnet fields, mass, and stress.[1,2,3,4,5] The applications of microcantilever sensors exploit the advantages which are offered by their microscopic dimensions, high sensitivity, easy fabrication, batch processing, and direct transduction.[6,7] Although microcantilevers themselves are fabricated via conventional photolithography from silicon and silicon nitride, to assure specific chemical and biological interactions, surface modification is required to detect and absorb appropriate chemical groups. At present, different techniques have been reported to modify silicon-based microcantilevers with an organic or polymer coating for different sensing capabilities. For example, microcantilever modification was conducted by using spin coated films[8] self-assembled monolayers,[9] layer-by-layer assembly[10,11], hydrogel layers[12,13]and polymer brush layers[14].

♦ Reprinted with permission of *Advanced Materials*

* M.C.L.: Directed research, co-advisor in all drafts of paper, revised final version of paper

Microcantilever sensors designed for thermal detection have been recently introduced for IR detection and imaging.[15,16,17,18,19] The design uses the well-known phenomenon of temperature-induced bending of bilayered beams composed of two materials with very different thermal expansion coefficients. The most common approach utilizes a silicon-based substrate with a metallic coating (bimetallic beams), which is usually gold or aluminum, as these materials are readily processed with microfabrication assemblies.[20,21] Thermally induced stresses result in reversible bending of microcantilevers with measurements of cantilever deflections detected via various readout schemes such as laser beam deflection (Fig. 8-1). [4] Previous studies have reported that bimetallic microcantilevers had high sensitivity to ambient temperature changes as well as to absorbed IR photons.[22,23] These bimetallic microcantilevers are considered to be a promising platform for the microfabrication of highly sensitive uncooled IR detectors.[20] Polymers as layer with high thermal expansion have been considered but not applied because their perceived low mechanical strength and poor chemical affinity to metal surfaces. Moreover, polymer processing of cantilevers leads to damage, and large stresses within the polymer-silicon beams.

With sensitive optical or electrostatic readouts, the microcantilever-based devices can show resolution of several tens of mK with thermal sensitivity, S, (beam deflection per K) reaching hundred nm/K for microcantilevers with the length around hundred microns. These characteristics are sufficient for the fabrication of medium resolution uncooled IR imaging arrays with promising spatial, thermal, and temporal characteristics.[24,25] However, to make significant progress in the miniaturization of these devices and, most importantly, increasing their sensitivity below the limits of modern cooled solid state sensors (below 10 mK), thermal sensitivity should be increased significantly. Considering that the difference of thermal expansion coefficients between the two materials constituting the bimorph is limited and the thickness of metal layer cannot be increased significantly without compromising sensitivity and uniformity, other materials should be envisioned to enhance thermal bending ability of metal-silicon beam microstructures.

Therefore, we suggest a novel approach to design thermally-sensitive microcantilevers by fabricating *trilayer* ceramic-metal-polymer beams with enhanced thermal bending ability by adding the topmost strong polymer nanocomposite layer chemically grafted to original silicon nitride-gold microcantilever (Fig. 8-1). The topmost polymer nanocomposite layer with thermal expansion about two orders of magnitude higher than that for the gold layer in conjunction with its low thermal conductivity should provide for enhanced thermal sensitivity according to theoretical estimation.[21] To increase mechanical strength of this layer beyond usual limits, it has been reinforced with silver nanoparticles and carbon nanotubes and to increase stress transfer to underlying beam polymer nanocomposite nanolayer was chemically grafted to the gold surface via a bi-functional self-assembled monolayer (SAM) as discussed in literature.[26,27,28,29,30]

8.2 Results and Discussion

For this study, we utilized rectangular and V-shaped silicon nitride-gold microcantilevers with the length 200 and 310 μm and spring constants in the range 0.02-0.03 N/m (as measured by thermal tuning) coated with the gold layer (Table 8-1). As polymeric materials we used end-functionalized poly(acrylonitrile) (PAN) and polystyrene (PS) with the thermal expansion coefficient of 68-100 $x10^{-6}$/K grafted to the gold layer via the cysteamine SAM and reinforced with highly dispersed single-walled carbon nanotube (SWCNTs) bundles and Ag nanoparticles (see Experimental, Fig. 8-1). PAN with high chemical and solvent resistance is commonly used with activated carbon for variety applications with the enhanced interaction with SWCNTs.[31]

Table 8-1. Characteristics of microcantilever sensors studied.

Sensor	Layer composition	Cantilever shape	Cantilever dimensions (L/W/T) μm	Spring constant (N/m)	Resonant frequency (kHz)	Sensitivity before modification (nm/°C)	Sensitivity after modification (nm/°C)	Theoretical sensitivity after modification (nm/°C)
A	PAN/Ag	rectangular	200/20/0.6	0.031	14.1	65	73	132
B	PS/Ag/PAN	rectangular	200/20/0.6	0.028	13.3	102	140	174
C	PAN/SWNT	rectangular	200/20/0.6	0.027	15.6	93	193	220
D	SWNT/PS/Ag /PAN	V- shaped	320/22/0.6	0.016	6.5	86	417	452
E	Gold/Si_3Ni_4 (Unmodified)	rectangular	200/20/0.6	0.027	13.0-14.8	67-107	N/A	110
F	Gold/Si_3Ni_4 (Unmodified)	V-shaped	320/22/0.6	0.017	6.1-7.3	73-103	N/A	117

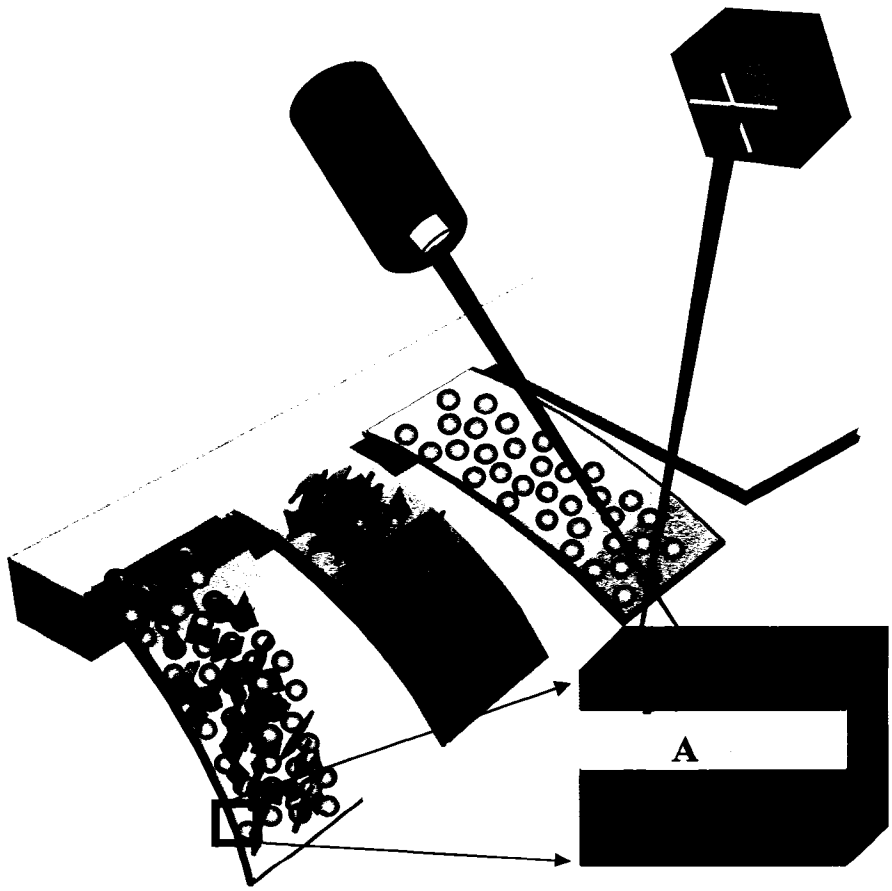

Figure 8-1. A schematic of a microcantilever array with optical readout and trilayered composition. Silicon nitride-gold microcantilever cantilevers modified with thin polymeric film reinforced with silver nanoparticles and carbon nanotubes, producing enhanced thermal bending of the cantilevers.

Figure 8-2 shows AFM topographic images of different nanocomposite layer directly scanned on the chip part of the microcantilevers. The microroughness of the topmost gold layer for uncoated microcantilevers was 3 nm (within a 10x10 μm surface area) and the microroughness of the polymer modified microcantilever increased to 10-12 nm but the surface morphology remained uniform with fine grainy nodes caused by Ag nanoparticles aggregation (Fig. 8-2b). SWCNT formed dispersed aggregates at SAM surface the final nanocomposite layer showed relatively smooth and uniform morphology (Figs. 8-2c,d). The thickness of the polymer nanocomposite layers was obtained from micropatterned layers and was found to be in the range of 10-14 nm for all polymer layers fabricated here.

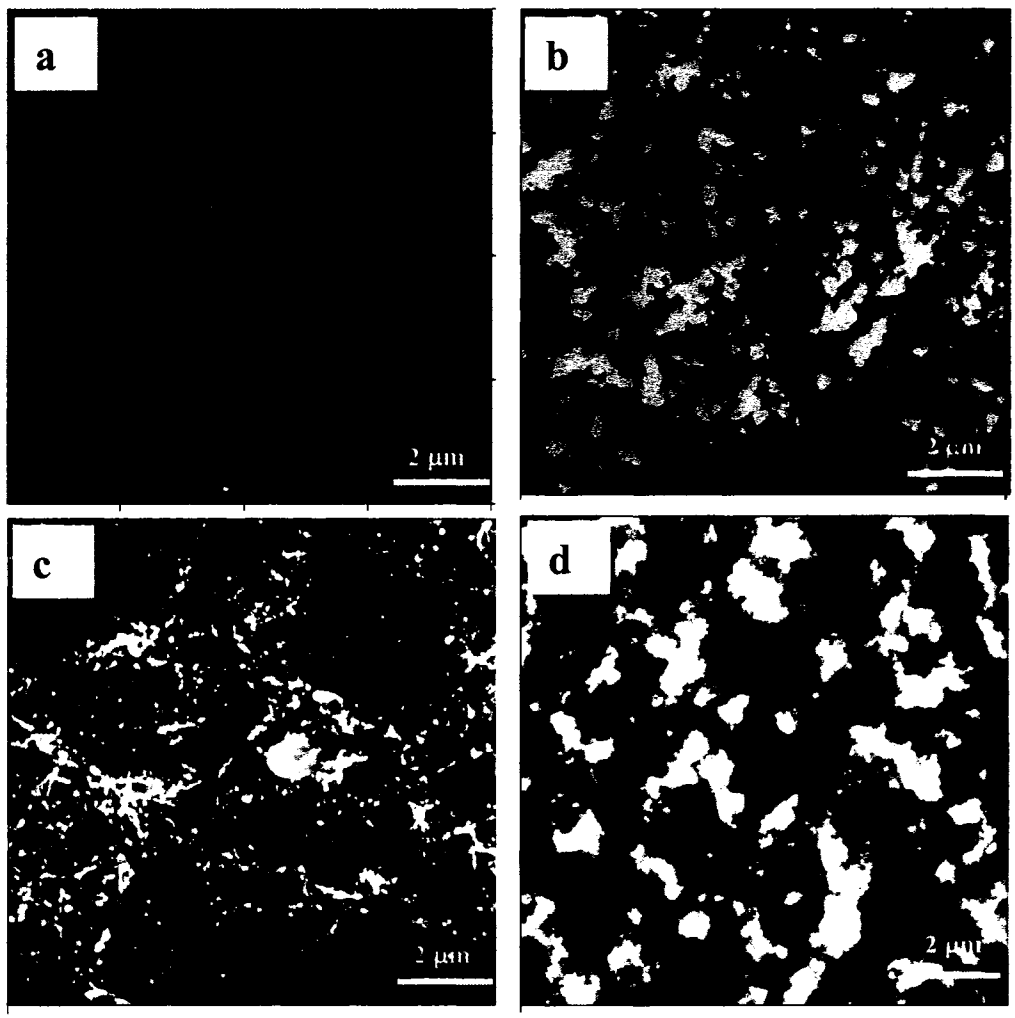

Figure 8-2. AFM images of (a) gold surface of an unmodified microcantilever (b) Ag/PAN layer (c) Cysteamine/SWNT layer (d) SWNT/PS/Ag/PAN layer. Z-scale is 60 nm.

Raman spectroscopy with a confocal microscope conducted for the polymer composite layer was used to confirm independently the chemical composition of the topmost layer. As an example, we present a Raman image for the polymer layer containing SWNT on the triangular microcantilever with optical contrast caused by strong Raman scattering from the carbon nanotubes (Fig. 8-3). Raman micromapping was conducted by integrating intensity at 1590 cm^{-1} (a G-mode and a main resonance peak for carbon nanotubes) (Fig. 8-3c).[32,33] The footprint shows the triangular shape caused by the surface distribution of the SWNTs embedded in the polymer matrix in the vicinity of the microcantilever end.

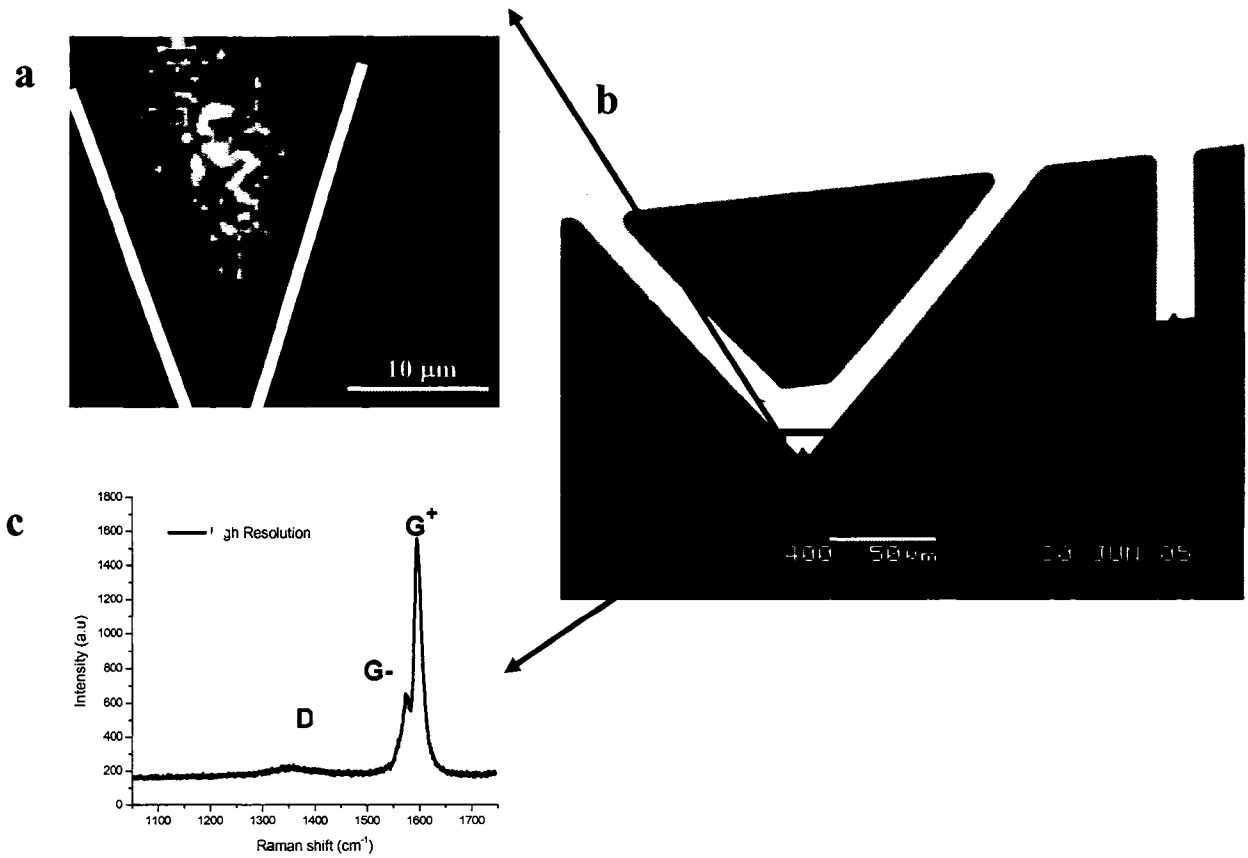

Figure 8-3. (a) Raman mapping of microcantilever end area as marked on an SEM image of silicon nitride-gold microcantilever (b); (c) Raman spectra of carbon nanotubes embedded into the microcantilever.

The microcantilever deflection as a function of the temperature variation for four different microcantilevers is presented in Fig. 8-4 and corresponding characteristics are given in Table 8-1. First, it is worth to note that the grafting procedure and added topmost polymer layer do not compromise the general microcantilever characteristics. E.g., for the rectangular cantilevers a spring constant stays within 0.027-0.031 N/m, resonance frequency varies within 13.3-15.6 kHz, and the quality factor is within 23-26 (Table 8-1). However, thermal bending ability changed dramatically after adding the polymer composite layer (Fig. 8-4).

In fact, the silicon nitride-gold microcantilever bends downward by about 100 nm due to mismatch of thermal expansion coefficient of gold (14 $x10^{-6}K^{-1}$) and silicon nitride (0.8 $x10^{-6}$ K^{-1}) (Fig 8-4a). The deflection of the microcantilever end versus temperature is linear, reversible, and can be repeated hundreds of cycles with identical results. The thermal sensitivity calculated from the linear fit of the data was in the range 65-105 nm/K for microcantilevers presented depending upon specific characteristics of individual microcantilevers which is within the typical range reported for gold-coated microcantilevers (Table 8-1).[23,34] Considering this microcantilever-specific variations, we conducted thermal sensitivity measurements for each individual microcantilevers initially and repeated them after modification.

Adding the PAN-Ag nanocomposite layer as the topmost layer (microcantilever **A**) changed thermal bending behavior insignificantly (Fig. 8-4a). Much larger effect was observed for microcantilever **B** with PAN-Ag embedded in a PS matrix (Figs. 8-4b, Table 8-1).

However, the largest increase in the thermal sensitivity was achieved for the microcantilevers **C** and **D** with the topmost coating containing carbon nanotubes (Figs. 8-4c, d, Table 8-1). Two-fold increase was observed after adding carbon nanotubes to the PAN matrix and even higher, *four-fold increase* was observed for the microcantilevers with a polymer nanocomposite layer containing both carbon nanotubes and silver nanoparticles embedded into PS matrix (Table 8-1). All bending cycles were reproducible and similar bending behavior was obtained for other temperature intervals (not shown).

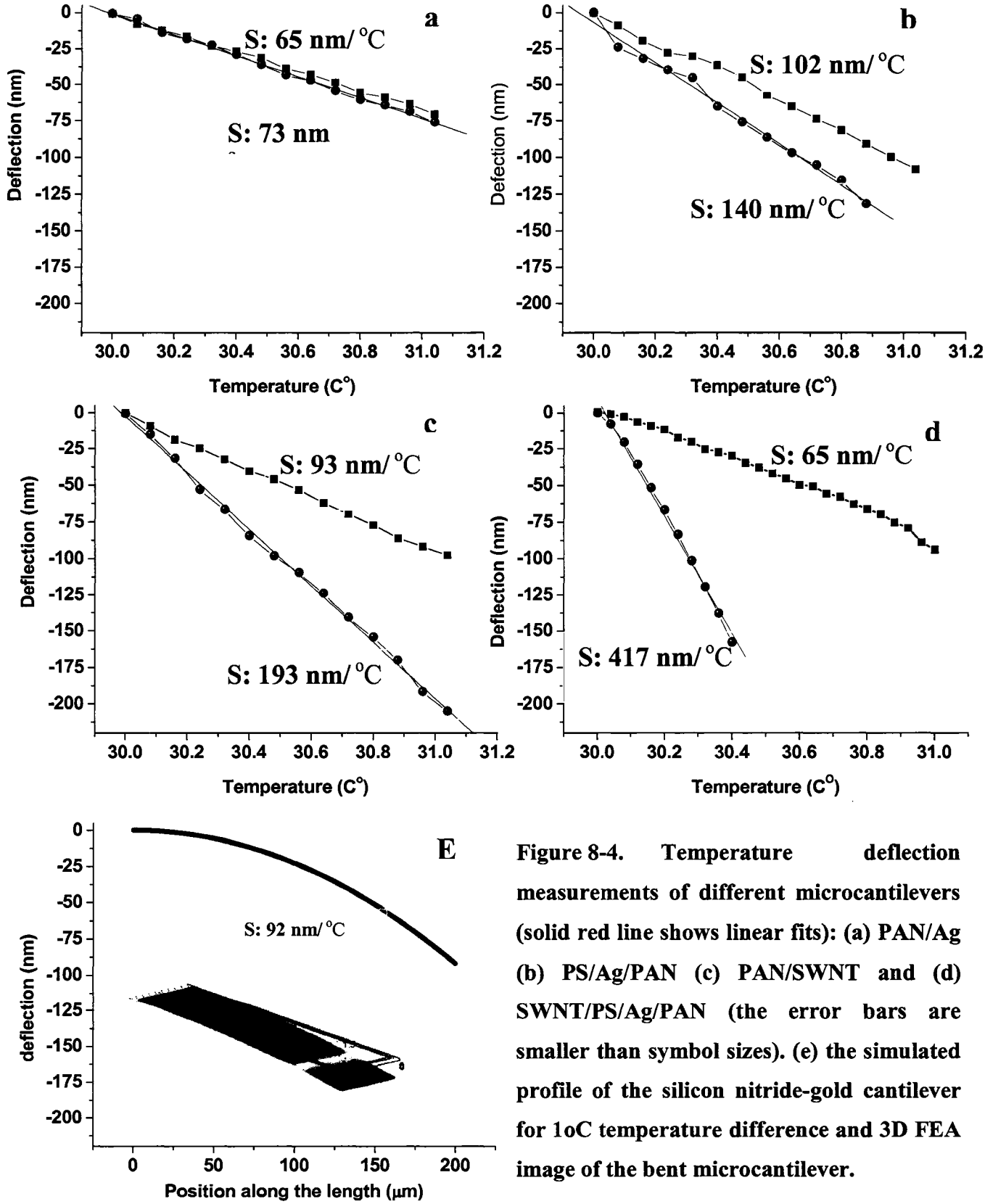

Figure 8-4. Temperature deflection measurements of different microcantilevers (solid red line shows linear fits): (a) PAN/Ag (b) PS/Ag/PAN (c) PAN/SWNT and (d) SWNT/PS/Ag/PAN (the error bars are smaller than symbol sizes). (e) the simulated profile of the silicon nitride-gold cantilever for 1oC temperature difference and 3D FEA image of the bent microcantilever.

The thermal sensitivity for the microcantilever **D** reached 400 nm/K, which is a very high value for biomaterial microcantilever sensors. This suggest that in fact the nanocomposite layers of PAN/Ag/SWNT with high elastic modulus (estimated to be 50 GPa and higher for the carbon nanotubes with random in-plane orientation) are firmly grafted to the metal surfaces to transfer thermally induced stresses and enhance bending ability despite slightly reduced thermal expansion coefficient due to negative thermal expansion of carbon nanotubes in axial direction.

The thermal bending scenarios for various polymer composite nanolayers was modeled with finite element analysis simulation accounting for the thermally-induced stresses caused by mismatch in thermal expansion of different layers and full stress transfer across the interfaces (see a representative example in Fig. 8-4e). For silicon nitride and gold layers we used standard literature values for the thermal expansion coefficients and elastic moduli and for the polymer composite layer we evaluated the corresponding composite values from chemical composition (volume fractions of polymer, carbon nanotubes, and silver nanoparticles) assuming isostrain conditions.[35,36] The thermal sensitivity for different microcantilevers obtained with FEA showed excellent agreement with experimental observations for microcantilevers **B-D** as well as for un-modified microcantilevers **E** and **F** with difference within 20% (Table 8-1). Only in the case of the microcantilever **A** with PAN-Ag layer we observed lower experimental value which can be related to poor adhesion between gold and PAN matrix.

In summary, we have presented a novel *trilayered (ceramic-metal-polymer) approach* for designing thermally sensitive microcantilevers with the topmost *polymer nanocomposite layers* chemically grafted to the gold layer reinforced with carbon nanotubes and metal nanoparticles. Such a combination of materials with the strong polymer composite topmost layer provides for high bending stresses developed as a result of large thermal expansion of the polymer nanocomposite layer that results in significant (*up to fourfold*) increase in the thermal sensitivity as compared with conventional ceramic-metal bilayered microcantilevers. These trilayered microcantilevers with dramatically enhanced thermal sensitivity can serve as

basis for the next generation of un-cooled IR sensor arrays with the thermal and spatial resolution manifold higher than those currently available.

8.3 Experimental

A. Modification and characterization of microcantilevers

We used commercially available of six similar (one rectangular and five V-shaped) bimaterial Si_3N_4-Au cantilevers with a 60 nm gold layer sputtered on a 600 nm thick silicon nitride beam (Veeco, CA). PAN with carboxylic terminal groups was synthesized according established procedure, reported by Matyjaszewski et al.[37] , but using S-1-dodecyl-S'-(α,α'-dimethyl-α''-acetic acid) trithiocarbonate[38] as the RAFT agent. The M_n measurements were performed with a Varian 300MHz at 25 °C using dimethylsulfoxide-*d* (DMSO-d_6) as the solvent and tetramethylsilane (TMS) as an internal reference. The experimental molecular weight of PAN, M_n(NMR)=3 500, was calculated by comparing the area of peak corresponding to polymer backbone -CH_2 protons with those corresponding to -CH_3 protons from dodecyl of RAFT group , similar to procedure describe in literature.[39] Cystamine and α,ω-dicarboxy terminated PS, (93.8K) were used as received from Aldrich and Polymer Source Inc.

The polymer composite nanolayer was immobilized via a self-assembled monolayer of cystamine-functionalized Au surface.[40,41] Single-walled carbon nanotubes (Carbolex, Texas) produced by the arc discharge method with COOH groups achieved by oxidation in nitric acid. Casting was conducted by drop drying of nanotube solution on cystamine-functionalized Au surface of microcantilever for about 24 h dried in air, and then rinsed with Nanopure water. The solution of 2% (w/w) of α,ω-dicarboxy terminated PS, in toluene were used for "grafting to" modification of the cantilever surface from melt.[27] The coated microcantilever were annealed at grafting temperatures ranging from 120°C to 130°C for 8 hours to enable the end groups to graft to the microcantilever. The un-grafted polymer was removed by multiple washings with toluene. Amine terminated silver nanoparticles (diameter of 10-20 nm, Nanohorizons) were cast onto the modified microcantilever over

night before the last polymer layer build up. The last polymer layer of PAN in N,N-dimethylformamide were grafted to from melt to coated microcantilever by using spin coating followed by gentle thermal backing and drying with the same condition of grafting PS. The overall layer microstructure is described as (A) PAN/Ag (volume fraction 70:30) (B) PS/Ag/PAN (43:14:43) (C) PAN/SWCN (90:10) and (D) SWNT/PS/Ag/PAN (5:40:15:40) (Table 8-1).

B. Sensitivity measurements and thermal tune

The thermal sensitivity of microcantilevers was measured by utilizing the AFM optical detection system with angstrom resolution (Dimension 3000). The microcantilevers with spring constant 0.016-0.031 N/m was brought into within 1μm of the surface of the thermal stage (a Peltier heater, 1x1 cm, ±0.001°C). An acoustic/isolation hood was placed over the entire set-up to block out outside fluctuations. A laser beam was be focus on the end of the microcantilever and reflected onto the AFM photodiode detector. The deflection of microcantilever was obtained with precision of 0.3 nm (limited by the amplitude of thermal vibrations) after the sensitivity of the photodiode detector of the AFM was independently calibrated. At each temperature step (usually, 0.04-0.05C°), the microcantilevers were kept for about a minute to reach an equilibrium.

The cantilever spring constants were measured using a Multimode AFM equipped with a Picoforce module, which used the well-known thermal tuning. Before each measurement the tip was allowed to equilibrate before the photodetector was carefully calibrated. Then, after taking precautions to minimize environmental noise, the photodetector signal was sampled at frequencies from 0-35 kHz. The signal was filtered with a lock-in amplifier to optimize the signal to noise ratio. Then using the Picoforce software a Lorentzian equation was used to fit the power vs. frequency curves and to obtain the spring constant value.[42]

C. Finite Element Analysis

Theoretical values for the deflections of the cantilever have been estimated with Finite Element Analysis (FEA) using Structural Mechanics module of a commercial package COMSOL Multiphysics 3.2.[43] A typical FEA involves the reduction of the Energy Functional (***E***) of individual elements of the model. The minimization is attained by setting the derivative of ***E*** with respect to the displacement of the mesh element (***D***) to zero. Principle of Virtual work has been opted as the implementation method for minimizing the ***E***. The FEM was solved in non-linear mode to account for the probable pinch-off effects in the deformation. The structure was meshed into ~40,000 elements. The ultra thin polymer layers and the gold layer have been mesh more finely compared to the thick Si_3N_4 so that the number of elements in each layer closely matched. The finer structure (increasing the element number twofold) caused less than 1% change in the deflection. Critical areas of the structure like the interfacial boundary between different layers and the edges were meshed finely to ensure small convergence parameter. The model accounts the material properties including Poisson's ratio, elastic modulus, thermal expansion coefficient, and density.

8.4 References

[1] R. Raiteri, M. Grattarola, H. J. Butt, P. Skladal, *Sens. Actuators, B* **2001**, *79,* 115.

[2] N. V. Lavrik, M. J. Sepaniak, P. G. Datskos, *Rev. Sci. Instrum.* **2004**, *75*, 2229.

[3] C. Ziegler, *Anal. Bioanal. Chem.* **2004**, *379*, 946.

[4] J. R. Barner, R. J. Stephenson, M. E. Welland, C. Geberr, J. K. Gimzewski, *Nature* **1994,** *372*, 79.

[5] T. Thundat, R. J. Warmack, G. Y. Chen, D. P. Allison, *Appl. Phys. Lett.* **1994**, *64*, 2894.

[6] M. Sepanicak, P. Datskos, N. Lavrik, C. Tipple, *Anal. Chem.* **2002**, *74*, 568.

[7] P. G. Datskos, P. I. Oden, T. Thuandat, E. A. Watchter, R. J. Warmack, S. R. Hunter, *Appl. Phys. Lett.* **1996,** *69*, 2986.

[8] M. Calleja, J. Tamayo, A. Johansson, P. Rasmussen, L. Lechuga, A. Boisen, *Sens. Lett.* **2003**, *1*, 1.

[9] L. A. Pinnaduwage, V. Boiadjiev, J. E. Hawk, T. Thundat, *Appl. Phys. Lett.* **2003**, *83*, 1471.

[10] X. Yan, Y. Lvov, H. Ji, A. Singh, T. Thundat, *Org. Biomol. Chem.* **2003**, *1*, 460.

[11] X. Yan, X. K. Xu, H. Ji, *Anal. Chem.* **2005**, *77*, 6197.

[12] K. Liu, H. F. Ji, *Anal. Sci.* **2004**, *20*, 9.

[13] Y. F. Zhang, H. Ji, D. Snow, R. Sterling, G. M. Brown, *Instrum.Sci. Technol.* **2004**, *32*, 361.

[14] G. G. Bambu, G. Kircher, M. Wolkenhauer, R. Berger, J. S Gutmann, *Macromol. Chem. Phys.* **2004**, *205*, 1713.

[15] T. Perazzo, M. Mao, O. Kwon, A. Majumdar, J. B. Varesi, P. Norton, *Appl. Phys. Lett.* **1999**, *74*, 3567.

[16] C. Jongeun, J. Yamaguchi, S. Morales, R. Horowitz, Y. Zhao, A. Majumdar, *Sens. Actuators, A.* **2003**, *104*, 132.

[17] L. R. Senesac, J. L. Corbeil, S. Rajic, N. V. Lavrik, P. G. Datskos, *Ultramicroscopy* **2003**, *97*, 451.

[18] Y. Zhao, M. Mao, R. Horowitz, A. Majumdar, J. Varesi, P. Norton, J. Kitching, *J. Microelectromech. Syst.* **2002**, *11*, 136.

[19] C. Escriba, E. Campo, D. Estève, J. Y. Fourniols, *Sens. Actuators, A* **2005**, *120*, 267.

[20] P. G. Datskos, M. J. Sepaniak, C. A. Tipple, N. Lavrik, *Sens. Actuators, B* **2001**, *76*, 393.

[21] P. G. Datskos, N. Lavrik, S. Rajic, *Rev. Sci. Instrum.* **2004**, *75*, 1134.

[22] E. A. Wachter, T. Thundat, P. G. Datskos, P. I. Oden, S. L. Sharp, R. J. Warmack, *Rev. Sci. Instrum.* **1996**, *67*, 3434.

[23] J. L. Corbeil, N. V. Lverik, S. Rajic, *Appl. Phys. Lett.* **2002**, *81*, 1306.

[24] J. R. Barnes, R. J. Stephenson, C. N. Woodburn, S. J. O'Shea, M. E. Welland, T. Rayment, J. K. Gimzewski, Ch. Gerber. *Rev. Sci. Instrum.* **1994**, *65*, 3793.

[25] J. K. Gimzewski, C. Gerber, E. Meyer, R. R. Schlitter, *Chem. Phys. Lett.* **1994,** *217,* 589.

[26] V. V. Tsukruk, *Prog. Polym. Sci.* **1997**, *22*, 247.

[27] I. Luzinov, D. Julthongpiput, H. Malz, J. Pionteck, V. V. Tsukruk, *Macromolecules* **2000**, *33*, 1043.

[28] V. V. Tsukruk, A. Sidorenko, H. Yang, *Polymer* **2002**, *43,* 1695.

[29] I. Luzinov, S. Minko, V. V. Tsukruk, *Prog. Polym. Sci.* **2004**, *29,* 635.

[30] D. Julthongpiput, M. LeMieux, V. V. Tsukruk, *Polymer* **2003**, *44*, 4557.

[31] T. V. Sreekumar, T. Liu, B. G. Min, H. Guo, S. Kumar, R. H. Hauge, R. E. Smalley, *Adv. Mater.* **2004**, *16*, 58.

[32] H. Ko, Y. Pikus, C. Jiang, A. Jauss, O. Hollricher, V. V. Tsukruk, *Appl. Phys. Lett.* **2004**, *85*, 2598.

[33] C. Jiang, H. Ko, V. V. Tsukruk, *Adv. Mater.* **2005**, *17*, 2127.

[34] B. Li, *Sens. Actuators, A* **2004**, *112*, 351.

[35] J. L. Hazel, V. V. Tsukruk, *Thin Solid Films* **1999**, *339,* 249.

[36] J. Hazel, V. V. Tsukruk, *J. Tribology* **1998**, *120,* 814.

[37] C. Tang, T. Kowalewski, K. Matyjaszewski, *Macromolecules* **2003**, *36,* 8587.

[38] J. T. Lai, D. Filla, R. Shea, *Macromolecules* **2002**, *35*, 6754.

[39] A. Quanfu, J. Qian, L. Yu, Y. Luo, X. Liu, *J. Polym.Sci., Part A: Polym. Chem.* **2005**, *43*, 1973.

[40] A. Ulman, *Chem. Rev.* **1996**, *96*, 1533.

[41] V. V. Tsukruk, V. N. Bliznyuk, *Langmuir* **1998**, *14*, 446.

[42] J. L. Hutter, J. Bechhoefer, *Rev. Sci. Instrum.* **1993**, *64*, 1868.

[43] *Structural Mechanics Module Model User's Guide for Femlab3*, COMSOL AB, **2004.**

Chapter 9

Alternative Materials Platform for Uncooled Hybrid Infrared Sensors

A paper submitted to *Nature Nanotechnology*

Melburne C. LeMieux[*1], *Michael McConney*[1], *Jiang Hao*[2], *Srikanth Singamaneni*[1], *Kyle Anderson*[1], *Yen-Hsi Lin*[1], *Timothy Bunning*[2], *and Vladimir V. Tsukruk*[1]

[1] Department of Materials Science and Engineering, Iowa State University, Ames, IA, 50011

[2] Air Force Research Laboratory, Materials and Manufacturing Directorate/MLP, Wright Patterson Air Force Base, Ohio 45433

9.1 Introduction

After several decades of research and development, improving the sensitivity of infrared (IR) detectors now by more than an order of magnitude seems almost improbable. However, this technology, critical for many civilian applications such as medical imaging and environmental surveys, as well as human or weapons sensing/tracking for military related purposes, has reached a plateau due to intrinsic limitations in the current design. Irregardless of signal transduction type and detection schemes, the heart of any infrared sensor is the sensing element, and improving the overall sensitivity involves a change at the most fundamental level: altering the materials design of the sensing element itself. Here, we introduce polymeric nanolayers into bimaterial microcantilevers (BMC), as BMCs are the typical sensing element in uncooled IR detectors. Due to manufacturability considerations, BMCs, which rely upon mismatch of materials properties to induce thermal stresses that result in bending, have been designed with a ceramic-metal combination. With a microfab-

* M.C.L.: Primary researcher, did all sample prep and most characterization, writer of all drafts.

compatible process that deposits polymer (plasma polymerization) with controllable residual stresses, the result here is an organic-inorganic hybrid BMC with a maximized bimaterial bending effect. In fact, the sensitivity of our polymer-ceramic BMC approaches 0.2 mK, which is about two orders of magnitude better than the current metal-ceramic design. This new hybrid platform suggested here overcomes the inherently limited sensitivity of current sensor designs, and provides the basis to develop the ultimate uncooled IR sensor with unsurpassable sensitivity. Furthermore, due to the unique physical properties of the plasma polymers here, the sensors also exhibit remarkable response to humidity at a sensitivity of 400 ppt (parts per *trillion*), more than *three orders* of magnitude better than current humidity sensors. Dual ultrasensitive thermal and humidity sensing combined with supreme ease and flexibility in fabrication makes these BMC with nanoscale hybrid structures the ultimate multifunctional microscale sensor.

IR detectors[1] may be sorted into two general classifications based on the detection mechanism: photon detection and thermal detection. Typical IR sensors employing cooled photon detectors whereby the radiation is absorbed by the sensing element (typically a semiconductor material) and the observed output arises from a change in the electronic energy distribution, exhibit excellent performance with sensitivities that are very high[2,3]. Unfortunately, they require cryogenic cooling to around 80°K to eliminate thermal generation of the charge carriers, and the bulky cooling unit drives up the cost of IR devices and severely limits portability. On the other hand, for IR sensors based on uncooled thermal detectors, the noise varies as $\sqrt{(k_bT)}$, so cooling does not significantly enhance performance, and thus they are operated at room temperature[4].

The mechanism behind the operation of uncooled IR detectors is absorbed incident radiation changes the sensing element temperature, which changes some physical property that is detected and displayed through a desired transduction mechanism. Essentially, we are constrained by the sensing element choice of a microcantilever beam, which is acceptable as it is the simplest and least expensive approach for large-scale implementation[5]. However, the sensitivity of current uncooled IR sensors are not only lagging well behind their cooled

counterparts, but also inherently limited due to the design approach of the materials platform for the sensing element. The design suggested here, which is fabricating bimorph microsensors comprised of plasma polymer nanolayers on hard ceramic substrates, is inspired by an existing efficient and ultra-sensitive thermomechanical transduction found in nature. Indeed, the best example of an IR 'eye' comes to us from the jewel beetle (*Melanophila acuminata*), which can sense heat from a forest fire 80 km away[6]. The beetle accomplishes this through micron scale thermal sensors comprised of alternating hard/compliant nanolayers exploiting a thermomechanical mechanism[7,8]. Ideally, man-made IR sensors should be miniaturized and uncooled, with an efficient thermomechanical signal transduction mechanism similar to those in nature.

Long perceived to possess poor sensitivity compared to cooled units, uncooled IR technology has only received appreciable attention in the past 10 years because it is now recognized that to be practical for advanced applications, IR devices need to be compact and batch processed for cost reduction. However, it also needs to possess extreme sensitivity, and this is the obstacle that must be overcome. Theoretical studies based on current technological limitations predict that the sensitivities of uncooled thermal based detection can approach that of cooled photonic detection.[9,10,2] Primarily, this equivalency has been facilitated in the last decade by microfabrication technology advances, and there has been a recent trend to implement uncooled IR sensors onto microelectromechanical systems (MEMS) chips, resulting in unprecedented and traditionally unexpected opportunities for IR technology.[11] Such optical MEMS are focal plane arrays (FPAs) of IR sensing pixels. Uncooled arrays are based on several different types of thermal detection. Currently, changes in electrical conductivity (bolometer), by gas expansion (Golay cell), pyroelectricity (pyroelectric detectors) are used in various versions of IR detectors.[10] Obviously, shrinking the pixel size thereby increasing the array size will increase sensitivity, but this is finite, and the key towards advancement of IR technology is to maximize the sensitivity of each micro sensor, or pixel, in uncooled micro IR devices.

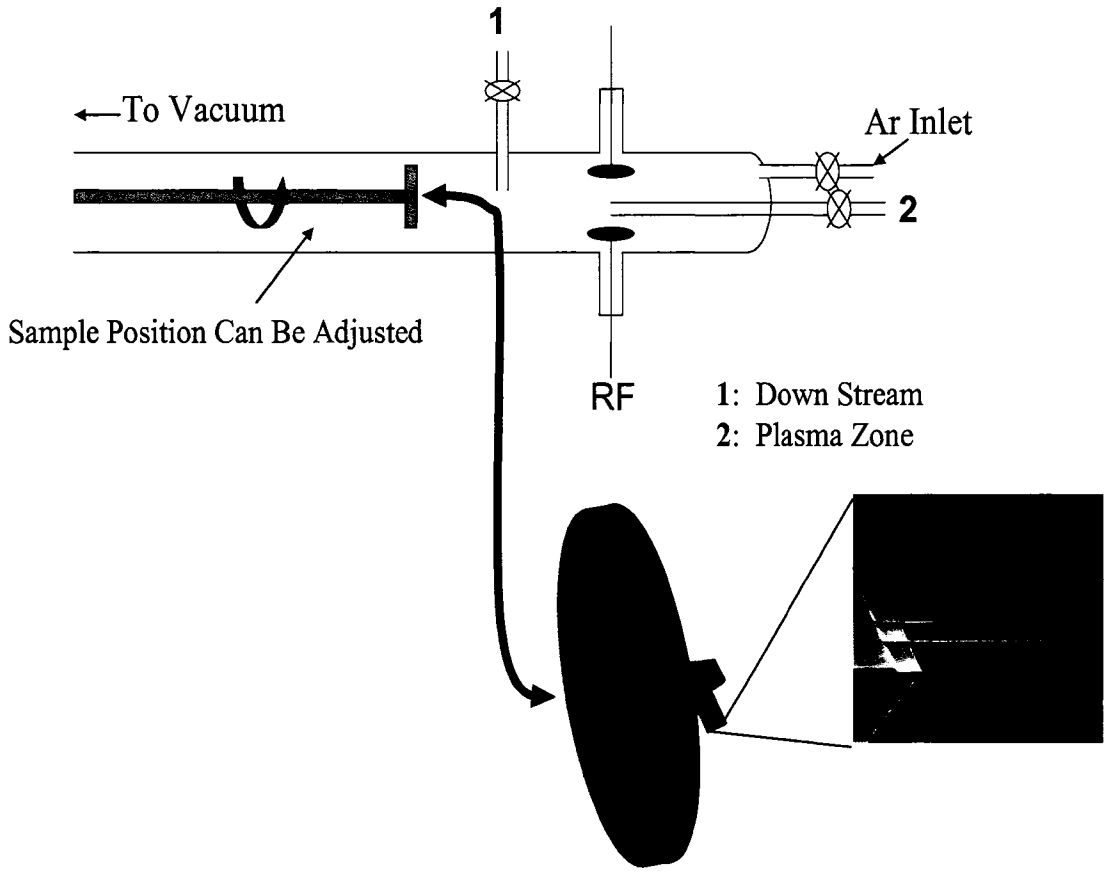

Figure 9-1. Schematic of the PECVD chamber showing the downstream position of the wafer. The microsensor was mounted on the corresponding wafer so that only one side was coated. This wafer was then mounted inside the chamber such that the sensor was directly perpendicular to the flow, being constantly rotated to ensure a uniform deposition. The SEM image is of the original microcantilevers before modification.

9.2 Results and Discussion

Here, we attack this issue by using microcantilever beams as model sensing elements, or 'pixels' in IR sensors. The cantilevers to be modified, initially composed only of polysilicon, possess a simple rectangular geometry (Figure 1, Table 1) and are extremely flexible (nominal spring constant around 0.01 N/m) to ensure extreme sensitivity. The

measured Brownian amplitude of these microcantilevers is around 2 nm, which thus is the fundamental limit of deflection sensitivity. This model was used for a couple of reasons. First, considering signal detection methods, mechanical deformations of a microcantilever beam can be detected optically down to 0.1 Å of deflection (in ambient or fluidic environments), as in an atomic force microscope (AFM). Compared to other detection methods, the optical route is optimal, combining low noise and lowest fabrication costs, both of which are negative aspects of electronic detection schemes.[12,13] Secondly, the most promising design choice for each pixel is the easily accessible and miniaturized microcantilever similar to those used in AFM.[14,15] In fact, microcantilever sensors are now being heavily exploited as miniaturized sensors[16] in gas monitoring[17,18], explosive detection[19,20], and biological[21,22] and chemical sensors[23] based on the signal transduction method of bending (deflection). Very often, to increase bending sensitivity, a *sensing* active layer is typically coated onto the silicon based microcantilever. The principal behind this is that the bending of the microcantilever originates from differential surface stress generated between the active layer and substrate. In the case of gas, biological, and chemical sensors, for example, the absorption of target molecules will cause the differential stress, inducing cantilever bending.

Table 9-1: Microcantilever properties

Tip	Dimensions (LxWxT)	K (N/m)	F (kHz)	Δd/°C
ppPAN	300μm x 20μm x 700nm	0.058	17.1	1800nm
ppPS	300μm x 20μm x 700nm	0.061	17.6	900nm
ppPSF	300μm x 20μm x 700nm	0.058	16.8	600nm

This bimaterial effect can be exploited for IR detection by fabricating microcantilevers whereby bending of a cantilever upon incident IR radiation results from a mismatch in thermal expansion coefficients (α) of the materials.[24,25] This approach was

pioneered by Barnes and Gimzewski when they coated microfabricated cantilevers with a metal (as the sensing active layer) to form the bimorph[24]. Later, Datskos et al. made the point that 2D arrays of these heat sensitive cantilevers can serve as thermal imaging devices.[26,27] The ideal bimaterial properties for IR sensing include: large mismatch of α and thermal conductivity (λ) between the two materials, one of the materials needs to have extremely low λ, there must be low residual stresses to eliminate non-thermal bending, and one of the materials may have to absorb in the infrared, depending upon the design. Quate et al. used silicon cantilevers exotically shaped in a flat spiral with an aluminum coating to complete the bimorph.[28] Datskos et al. developed a microcantilever bimorph with silicon as substrate, and a 150 nm gold layer coating as the high α component that exhibited temperature sensitivity of 0.4°C.[29] Majumdar et al. applied bimaterial cantilevers of silicon nitride and gold into a complicated comb-like MEMS structure, which resulted in sensitivity of 3 – 5° K.[30] Sarcon Microsystems in combination with Oak Ridge National Laboratory (ORNL) have developed bimaterial cantilevers with sensitivity approaching 5mK, which is the lowest value reported for uncooled IR detectors based on bimaterial cantilevers.[11] In their design, SiC was the low (α) component, again being combined with gold as the high (α) layer.

Rather than continually tweaking the shape of the microsensor or optimizing the metallic coating, we introduce polymers, or at least soft matter, into the mix, fostering the opportunity to reach unprecedented sensitivities with a new design paradigm. Common, industrially important polymers were used as the sensing layer: polystyrene (PS), fluorinated polystyrene (PFS), and acrylonitrile (PAN). Amazingly, until now, polymers have not been exploited in this critical application, and we immediately understood why this is the case. Traditionally, polymer coatings are implemented via "wet" deposition techniques, as in self-assembly, spin coating, or grafting. Such a deposition, especially when speaking in terms of large-scale processing is extremely expensive, requires high purity, is time consuming (often with several steps). Furthermore, wet processing of microdevices renders them unusable due to stiction, and casting/spin coating methods can easily cause micro fractures in the silicon[31]. However, diverse and elaborate coatings can be deposited in this way, made up of

multicomponent polymer and polymer nanocomposite layers, such as nanoparticles and carbon nanotubes that are known to enhance IR absorption.[32] This work was undertaken in our lab, and while the results published[33] show both the excellent proof of principal that complex layers can in fact be infiltrated into microsensors, as well as a strong response to temperature change, it is difficult to imagine large scale implementation of such a coating process in batch fabricated MEMS sensors.

Another matter impeding the exploitation of hybrid cantilevers becomes apparent upon realizing that the thermal sensitivity of such bimorphs, *S*, defined as a beam deflection (δ) per a temperature difference depends upon geometrical parameters and, most importantly, difference in thermal expansion coefficients of the two materials, *as well as elastic modulus*[30,24] (eq1):

$$S_{Th} = \frac{\delta}{\Delta T} = 3(\alpha_{bimat} - \alpha_{sub})(\frac{n+1}{K})(\frac{L_{cant}^2}{d_{sub}}) \qquad \text{Eq. 1}$$

where L, n, d are parameters related to beam geometry and K is a structure factor accounting for mechanical properties.:

$$K = 4 + 6n + 4n^2 + \phi n^3 + \frac{1}{\phi n}$$

and: $$n = \frac{d_{bimat}}{d_{sub}} \qquad \phi = \frac{E_{bimat}}{E_{sub}}$$

Clearly there is a tradeoff as the modulus of the coating needs to be high enough to bend the substrate and generate high enough stresses, but materials with high elastic modulus typically have low thermal expansion. Eq. 1 is plotted in Figure 2 where the thickness and modulus of our microcantilever substrate is kept constant at 700nm and 160 GPA, respectively. In the hybrid regime, with modulus ratio ϕ roughly 0.03, it seems evident that the polymer/ceramic bimorph cannot compete, although key issues not taken into account in this equation is the

effect of controllable residual stresses (discussed below), and thermal conductivities, which are extremely low in soft matter enabling more absorption of the thermal energy.

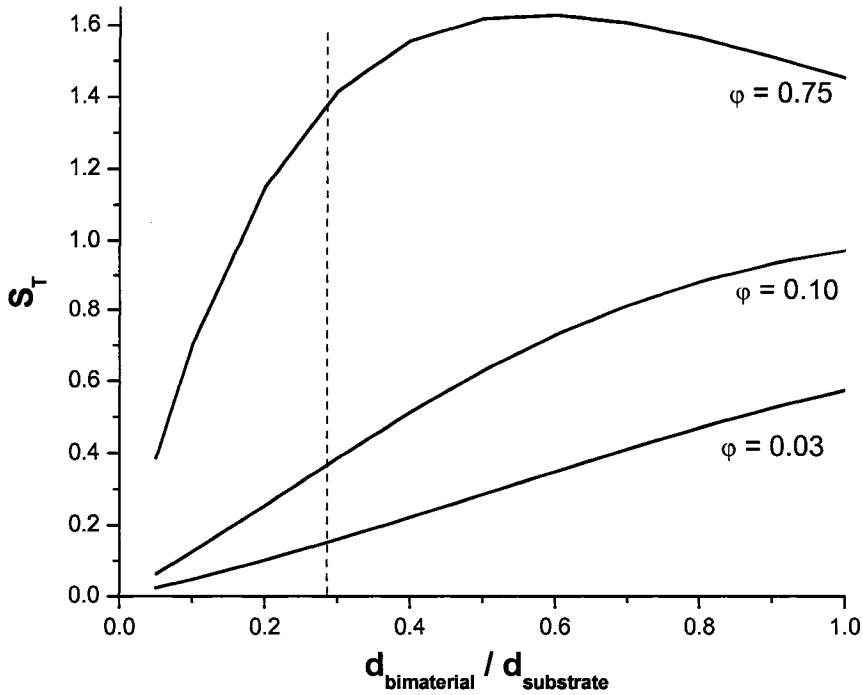

Figure 9-2. Theoretical bending sensitivities versus thickness ratio of the coating (bimaterial) and substrate at different modulus ratio. Our coatings averaged about 200nm thick on a roughly 700nm – 1μm thick substrate (~0.28) represented by the dashed line. The modulus ratio of our hybrid ceramic-polymer cantilevers corresponded to ϕ = 0.03.

With this in mind and considering especially in a technological field not well-represented by materials engineers, it is clear why bimaterial microcantilevers for IR sensing have been predominately comprised of a ceramic-metal combination of materials. On the other hand, this approach of using soft matter should not be abandoned, but refined since organic or polymeric layers have the potential to increase the sensitivity of IR detection

because there thermal expansion coefficient is more than two orders of magnitude higher than the current high α components in these bimaterial cantilevers. Considering that the difference in α ($\Delta\alpha \approx 20 \times 10^{-6}\ K^{-1}$) for current metal-ceramic bimaterial designs is inherently limited[29], the novel design of *polymer-ceramic* microcantilevers is suggested here with dramatically enhanced thermally induced bending. The strongly adhered polymer nanolayer on ceramic, with $\Delta\alpha \approx 500 \times 10^{-6}\ K^{-1}$ combined with low thermal conductivity allows for the ultimate sensitivity of uncooled thermal microsensors. However, by definition, to create the differential stress, absorption can take place *only on one side* of the microcantilever or this bimaterial effect will be cancelled.

To overcome these issues and be compatible with microfabrication techniques[34], an unexplored route of building IR responsive polymeric coatings using plasma enhanced chemical vapor deposition (PECVD)[35] is studied here. PECVD provides excellent control over polymer film parameters such as uniformity, density, thickness (10 nm – several micron thick films have been produced), and composition, as well as allowing high adhesion between polymer and any substrate.[36,37,38] A main advantage of PECVD, especially considering polymeric systems and potential unwanted stresses in microcantilevers, is that the deposition can be done at room temperature. In addition, PECVD polymer films will result in films with a high degree of cross-linking leading to higher modulus values than typical polymers, ideal for enhancing bending of the microcantilever.[39]

The monomers to be plasma polymerized were chosen for their IR absorption range and mechanical properties (Table 2), and we refer to these as plasma polymerized PAN (ppPAN), PFS (ppPFS), and PS (ppPS). In terms of absorption bands, cyano groups strongly absorb in the black body NIR (3-5μm), while fluoro groups strongly absorb in the hot body MIR (8-12μm).[40] Both of these ranges are especially interesting for military and civilian applications, since these are the two atmospheric windows of IR radiation. The sensors where mounted inside the chamber in such a way so that only one side would be coated (Figure 1) on top of a larger silicon wafer so that XPS, AFM, and FTIR measurements could be done to examine the exact same coating on the sensor, which is too small to get suitable

data from. This is critical because plasma polymers often are very different structurally than their bulk linear counterparts. In this case, FTIR spectra (Figure 3) reveal that the characteristic cyano group stretching mode (2250 – 2230 cm^{-1}) in ppPAN remains[40]. For ppPFS, the peaks at 980 and 1550 cm^{-1} correspond to CF stretching modes[40]. Furthermore, XPS measurements (Table 2) obtained from the wafers indicate a compositional ratio close to the bulk monomer value (excess oxygen results from impurities) indicating the plasma polymers should have reasonably similar physical properties as their linear counterpart.

Table 9-2: Physical properties of the plasma polymer coating.

Material	Modulus (GPa)	α (10^{-6} K^{-1})	AFM RMS roughness (nm)
Silicon	160	2.6	0.1
ppPAN	4	-310	2
ppPS	2	190	2
ppPSF	3	90	2

The electronic energy generated in the plasma afterglow (around 11eV), is suitable to break most organic bonds and produce plasma polymerized film.[41,42] Depending upon the vapor pressure of the monomers, deposition rates varied from 3 to 90 nm/min, as verified by ellipsometry (Table 3). The resulting layers, as measured by AFM, were quite smooth (RMS roughness less than 2nm, Table 3) with uniform topography (Figure 4). The morphology displayed here indicates a fine granular surface, with small variations distinct to each monomer, and it is well known that the chemistry of plasma polymers can effect the morphology of these films.[43] Because "after glow" (downstream) PECVD was used, the plasma density is lower, and thus the final polymerized polymer very much resembles the chemistry of a conventional polymer (as verified also by FTIR and XPS). Consequently, there is a lower degree of cross linking, longer polymer chains, and the granular topography is due to actual polymer chain aggregation.[44]

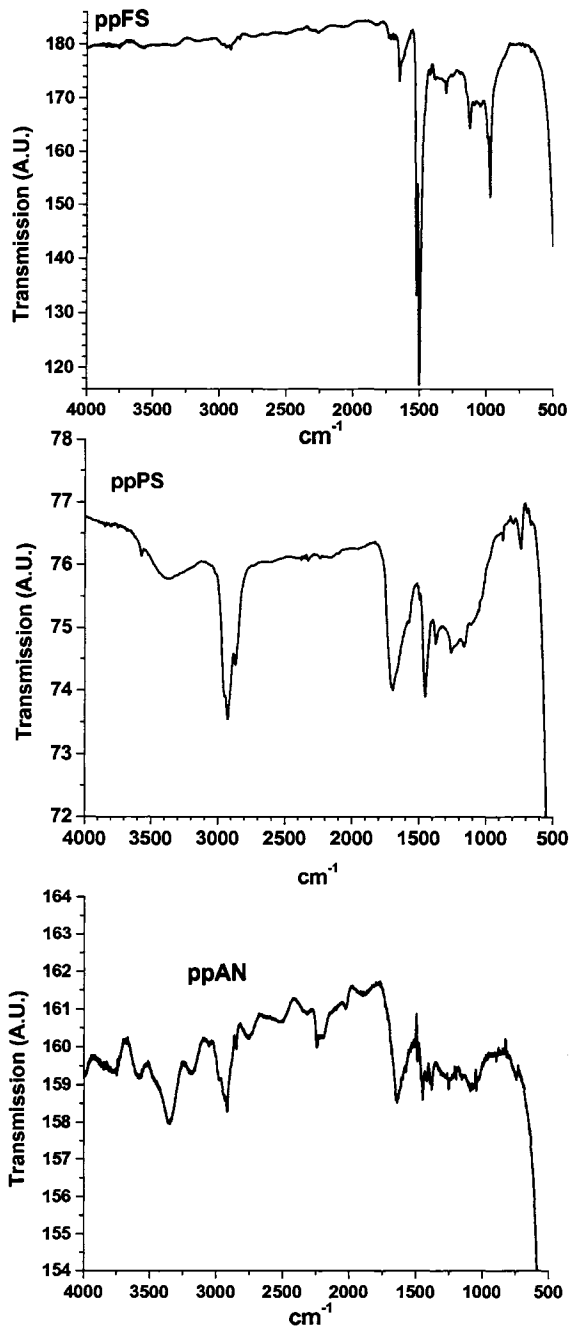

Figure 9-3. FTIR spectra of the plasma polymerized polymers deposited in this study. Top is ppPAN, middle is ppPFS, bottom is ppPS.

We aimed for coating thickness of about 200 nm that corresponded to a time of less than 10 min for the entire deposition. To verify, SEM images clearly show the level of thickness to be close to 200nm on a typical coated cantilever along the entire length (Figure 4), and demonstrate the uniformity and large-scale smoothness of the PECVD coating, and the thickness of the coatings is exactly what was anticipated based on our calculations of the deposition parameters. Thus, we have proven that we can easily control the PECVD deposition process to fabricate smooth, uniform, thick, robust, and most importantly, *one-sided* coatings, on these microcantilevers. And this is an important point for the microelectronics community, as well as towards the design of multifunctional sensors. As mentioned, while organic layers have been used in microcantilever bio/chemical analyte sensors as described above, limited work has been accomplished incorporated highly sensitive polymer molecules as the high α component in IR/temperature sensing due to processing conditions. Furthermore, examples of analyte microsensors using organic sensing layers are based on silane/thiol grafting methods where a very

thin polymer layer or monolayer is deposited by *wet* grafting techniques.[45] However, the thin layer is not optimal for maximized bending deflection (Figure 2), and the wet grafting techniques will be detrimental to MEMS devices.[31] Other *dry* methods such as the "airbrush technique" or polymer "spray coating" are not compatible with MEMS fabrication (requires additional steps off the "assembly line"), offer poor adhesion to the substrate, as well as high porosity within the coating, and are material limited.[46]

Table 9-3: Structure Properties of the Plasma Polymers

Tip Wafer	Monomer Structure	Ellipsometry Data: Thickness (Tip Thickness)	XPS Data: Carbon	Nitrogen	Oxygen	Fluorine
PSF	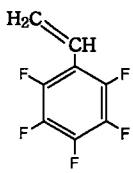	166	51%	3%	4%	42%
Styrene	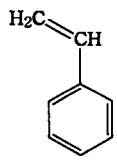	206	87%	3%	10%	--
Acrylonitrile	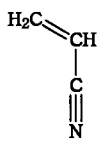	294	77%	20%	3%	--

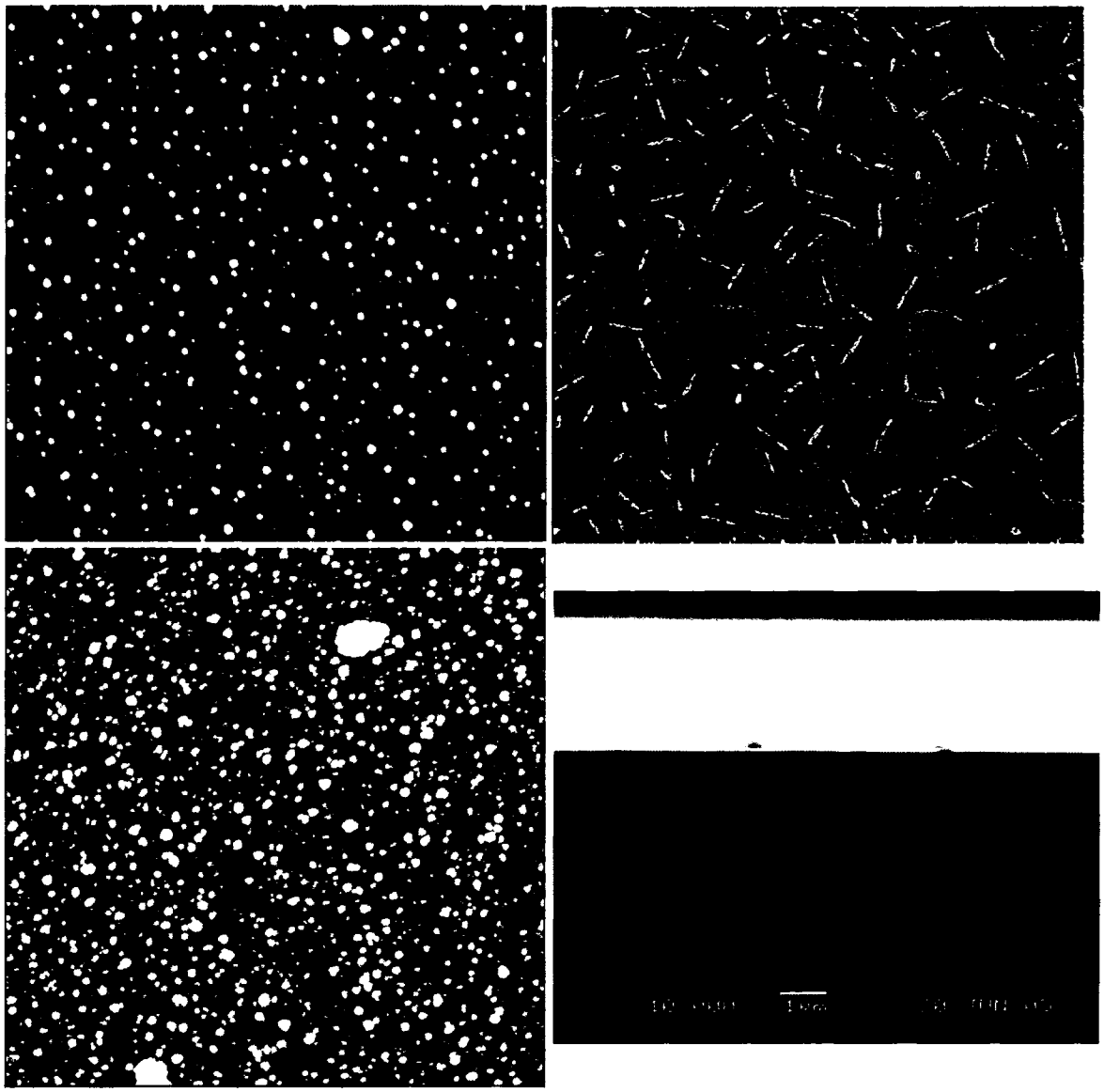

Figure 9-4. 5 x 5 μm^2 tapping mode AFM topography images of the plasma polymers with z range = 10nm. Top left is ppPAN, top right is ppPS, bottom left is ppPFS. At bottom right is 10,000X SEM image of the modified cantilever showing a roughly 200nm thick uniform coating on one side of the microsensor.

The hybrid sensor response versus temperature is summarized in Figure 5, along with a bare Si control sensor, as well as a gold-coated sensor (60nm coating as stated by manufacturer) as a reference for the current design standard. Upon heating, the polymer-polysilicon hybrid beams bend downward, reaching a planar state around 40°C as demonstrated in side-view optical images (Figure 5). Evidently, an initial pre-bent state is introduced (Figure 5, at ~25°C) in the course of plasma polymer deposition due to the chemical cross linking in the glassy state (as discussed above) inducing the usual compressive residual stresses of PECVD polymers on one side (bottom in Fig. 4) of the microsensor which favorably creates additional tensile stresses. Such a phenomenon leads to a pre-bent and pre-stressed bimorph beam with the initial parameters controlled by deposition conditions.[47,48]

To quantify this deflection, we conducted precise measurements of the microcantilever deflections (with accuracy ± 0.05 nm) within a narrow temperature interval and small temperature increments of 50 mK (Fig. 5). We compared these data to the reference ceramic-metal microcantilever. As obvious from this plot, the thermomechanical bending of the hybrid microsensors are *many times* higher than the deflection of the reference ceramic-metal microcantilever due to thermomechanical induced stresses (Figure 6). The thermal sensitivity approaches 2 nm/mK, which is far higher than that for the corresponding gold-polysilicon microcantilever (0.056 nm/mK). The ppPAN modified microsensor exhibits the best sensitivity at *over* 1800nm/K (slope in Fig. 5), followed by ppPS (900nm/K) and ppPSF (600nm/K). The thermal sensitivity achieved here for the polymer-polysilicon bimorph is an order of magnitude beyond the value 0.12 nm/mK achieved for the best published uncooled IR detector employing microcantilevers.[11] Moreover, for all microsensors reported here, the direction of thermally initiated deflection is *opposite* to that detected for the gold-polysilicon reference microcantilever, which points out the complex yet remarkable nature of bending of polymer-silicon composite beams as will be discussed below.

For any discussion of results, the modulus and the (α) of the plasma polymers ideally should be quantified, and unfortunately, not only are these types of values lacking in the

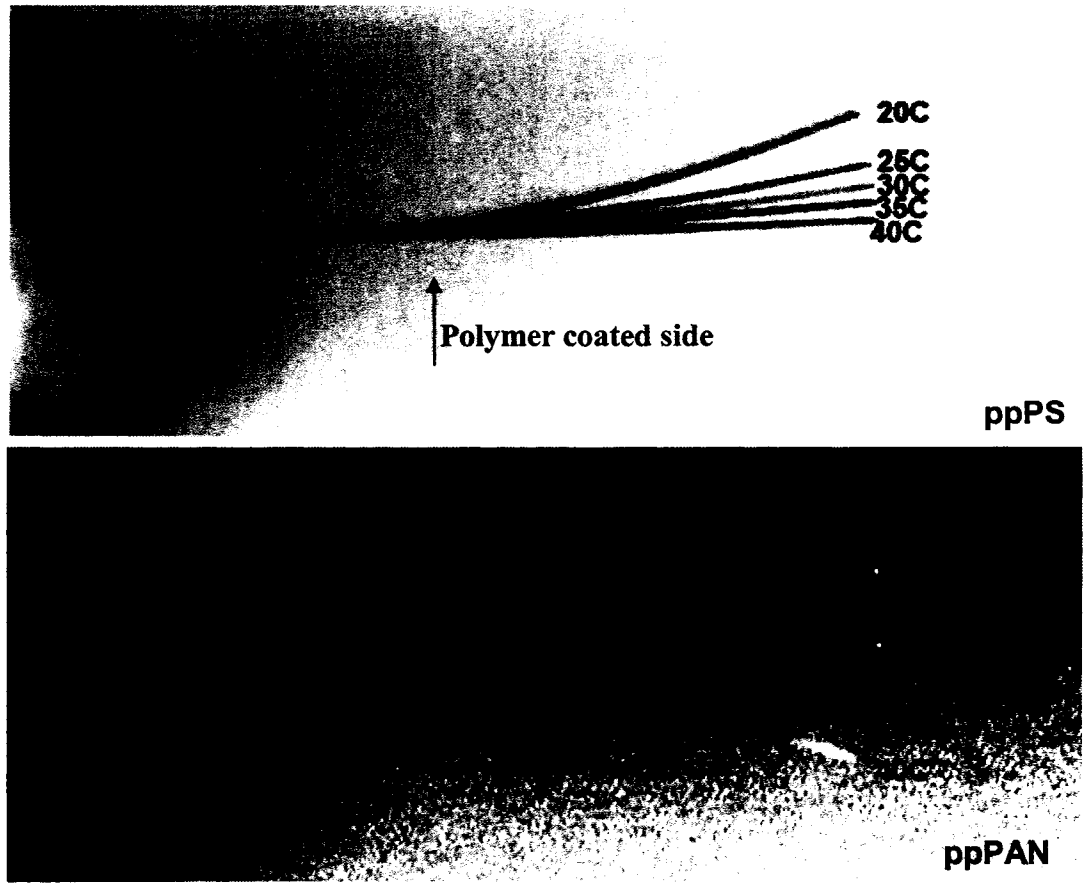

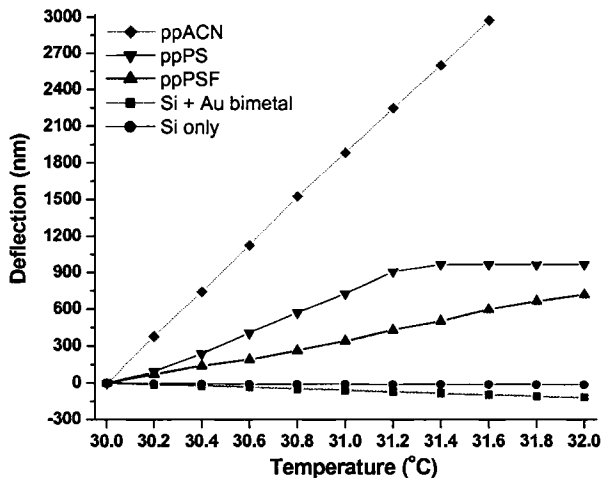

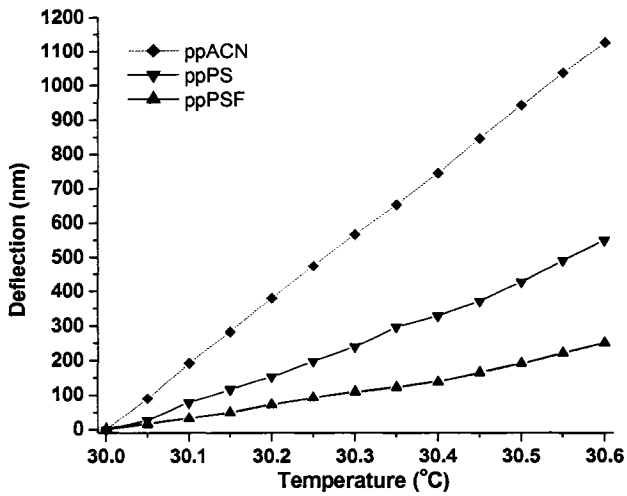

Figure 9-5. At top is a series of superimposed optical images taken at the indicated temperature showing the large magnitude of bending for ppPS and ppPAN modified hybrid microsensors. Bottom left is an overall deflection versus temperature compilation of the three plasma polymer hybrid sensors compared to a control bare Si sensor, along with the gold-ceramic bimaterial sensor reference standard. Bottom right is deflection versus temperature of the three plasma polymerized sensors at high resolution (50mK).

literature for plasma polymer films, but they can be very different depending upon deposition conditions. For this testing, we focused on the best two results ppPAN and ppPS, and discarded ppPSF. The modulus and (α) of the plasma polymer deposited on the microsensors was determined by measuring these values on the corresponding "tip wafer". AFM based nanomechanical measurements[49] revealed an elastic modulus of 2-4 GPa (Table 2, Figure 6) for ppPAN that is much higher than the bulk values of the corresponding conventionally polymerized material, and this is due to the higher crosslinking. The average value of modulus for ppPS was 1-2 GPa (Table 2, Fig. 6), which is close to conventionally polymerized PS. However, the modulus vs. temperature curve for ppPS is very different than for ppPAN, and it actually resembles conventional PS below T_g. This is an indication that the level of cross-linking is much lower in the ppPS than ppPAN, reflected in the modulus disparity. The FTIR data further supports this claim as the ppPS trace (Fig. 3) is very similar to bulk PS[50]. The ppPAN spectrum (Fig. 3) shows the characteristic C≡N stretch at 2240 cm^{-1} corresponding to the cyano group. The spectrum also displays a much stronger C=N stretching mode at 1650 cm^{-1} and N-H stretching at 3300 cm^{-1} suggesting a much higher degree of cross linking in the polymer film.

With these higher than typical values of modulus, the (α) values would be expectantly lower than bulk values. The linear expansion coefficient was measured by taking ellipsometry measurements at increasing temperatures, before and after annealing (results did not differ with annealing). These measurements were done on slightly thinner films under the same deposition conditions in order to get better accuracy. Remarkably, the (α) values consistently ranged between 200 – 400 $x10^{-4}K^{-1}$ for ppPS and ppPAN, which is even higher than bulk polymers, a bonus as we obtain the best trade off between modulus and (α). However, most astounding is the highly *negative* value for ppPAN. This is a very puzzling, yet exciting result, and emphasizes the potential of plasma polymers in advanced applications, especially functional surfaces, because such a vast array of properties is possible via a relatively simple deposition procedure in which almost any organic precursor can be used.

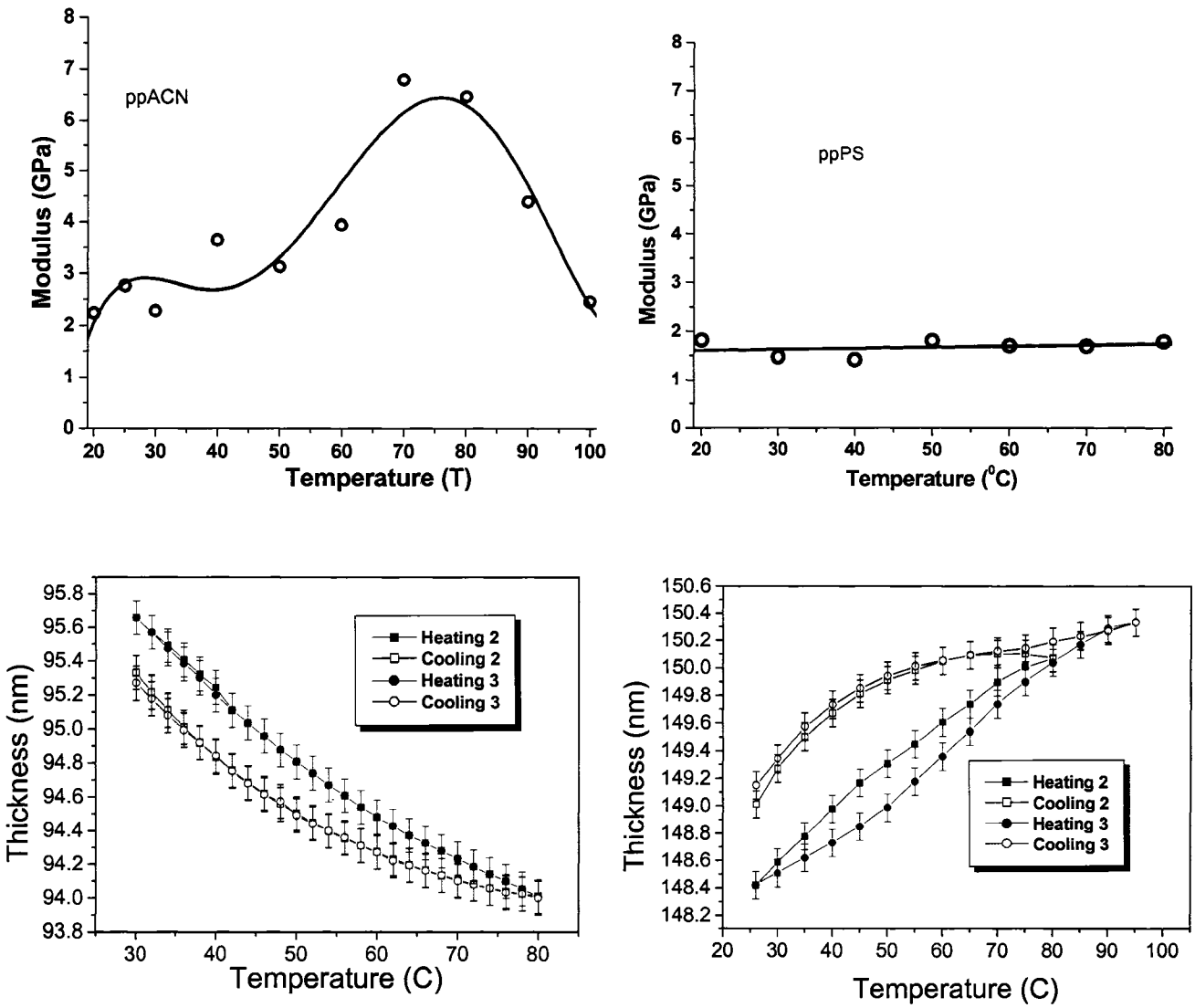

Figure 9-6. At top is the AFM measured elastic modulus of ppACN (left) showing a very non-linear response with temperature. At top right is the modulus vs. temperature of ppPS with linear fit. Bottom row is ellipsometry measured thermal expansion showing the highly negative expansion of ppACN (bottom left), while ppPS is at right. Error bars are averaged from three separate cycled experiments.

A full discussion of the negative expansion phenomenon is given in a separate forthcoming publication. Briefly, this is due to metastable states caused by a high degree of cross-linking and trapped free radicals in the plasma polymer being 'frozen' into the layer due to the room temperature deposition.[51] This leads to a level of residual stresses during the deposition procedure, and it has been recently suggested that these 'favorable' residual stresses can lead to non-equilibrium conditions in a polymer layer leading to unusual physical properties such as negative thermal expansion.[52] In general, the overall high values of these plasma polymers results from the layer essentially being composed of oligomers of polymer like chains or charged organic oligomers depending upon the plasma deposition procedures.[53,54]

The fact that the ppPAN cantilever bends down upon increase in temperature is primarily from the negative thermal expansion. On the other hand, for ppPS, this phenomenon is due to residual stresses and thermal relaxation as discussed earlier[55] and touched upon below. The residual stresses can be seen in Figure 5 for ppPS clearly; however, there is a very minimal prebent state associated with ppPAN indicating a much lower level of residual stresses associated with the acrylonitrile deposition than the styrene deposition.

In fact, the presence of the polymer layers generates a bending stresses (σ_s) given by a modified Stoney's Equation[56,57]:

$$\sigma = \frac{E \cdot t_s^{\,2}}{6R(1-\upsilon)t_f} \qquad \text{Eq. 2}$$

where E is the elastic modulus, t_s is the substrate thickness, R is the radius of curvature, υ is Poisson's ratio, and t_f is the polymer layer thickness. This equation is valid for bicomposite beams and describes interfacial stresses in bent beams. To expand upon this, we look at the case specific to the ppPS modified microsensor as PS layers are readily comparable in the literature. The PECVD-deposited polymer layer creates intrinsic stress associated with grafting, chemical reaction, and growth of a polymer layer, σ_i, which is always

compressive.[58] At room temperature, the microcantilevers is in *stable* pre-bent (non-equilibrium) state with balanced stresses:

$$\sigma_s - \sigma_i - \sigma_T = 0 \qquad \text{Eq. 3}$$

where σ_T is the thermal stress (generating additional compression on polymer layer) caused by mismatch of the thermal expansion coefficients of polymer and silicon layers. Considering that $\sigma_T = 0$ at room temperature (PECVD was conducted at room temperature), we can conclude that $\sigma_s = \sigma_I$, and thus use Eq. 2 for the estimation of the intrinsic compressive stresses. This estimation gives $\sigma_i = 85$ MPa which is a very high value indicating high compression of the polymer layer at room temperature caused by preparation conditions.

Restoring the planar shape of the microcantilevers at elevated temperature (40°C for the microcantilever in Fig. 5) indicates balanced stresses (Eq. 3) with $\sigma_s = 0$ (no bending in this state) but non-zero thermal stresses σ_T. This result leads us to the conclusion that the intrinsic stress at the elevated temperature should compensate for both initial intrinsic stress and thermally induced stress. Considering that both stresses are compressive in nature and act in the same direction, we must conclude that the intrinsic stress within the polymer layer actually *reverses sign* at elevated temperature and becomes tensile, a very intriguing phenomenon.

In Figure 7, the bending of the cantilever upon change in 1°C was simulated using FEA. The best result of the ppPAN hybrid microsensor is compared to the reference gold-silicon bimaterial sensor. The model was set with values of modulus, α, thickness from values that are well know, or in the case of ppPAN, values that we measured independently as discussed above. As shown, the ppPAN hybrid sensor is expected to deflect nearly 1400nm/°C. Although this is very large, the observed value is much higher, and thus the added deflection experimentally observed is due to a small residual stress component

associated with the ppPAN. The larger theoretical bending of the gold-silicon sensor is because we modeled both coatings here with 200nm coating, even though the gold-metal sensor in the experiment had a 60nm layer. Analysis of the cross-sectional stress through the thickness of the cantilevers (Fig. 7) shows similar values for ppPAN and gold meaning that indeed the resulting huge sensitivity of the ppPAN layer is due to the huge negative thermal expansion combined with high modulus (thermomechanical effect), with the remaining amount (around 1MPa) due to intrinsic stress in the cantilever. However, for the ppPS, much higher values are observed in accordance to the above equation. Overall, typically with plasma polymers a higher level of intrinsic stress coincides with a higher degree in cross-linking. However, this also depends upon chemical nature of the monomers, and consider that ppPS is composed of large bulky units. Combine this with the fact that the construction of plasma polymer layers can be summarized as a wedging process of reactive species (oligomers of excited molecules and free radicals) to a nascent layer, and thus it is feasible to conclude that the wedging of these particles containing large phenyl groups will cause much higher intrinsic stress. The internal compressive stress is directly dependent upon the size and steric factors of the 'wedging' species.[59] Furthermore, it is well know that in plasma polymerization, a higher deposition rate generally means lower internal stress[60], and here ppACN was deposited at 90 nm/min, while ppPS was deposited at a rate of 50 nm/min.

Although a full understanding of this complex thermomechanical behavior requires further detailed studies, it is worth noting that, indeed, a similar phenomenon of changing from compression to tensile stress was observed for PECVD layers and was associated with the changing radical density within the layer leading to material contraction at elevated temperatures.[58] However, in our case, the phenomenon observed is completely reversible as will be demonstrated below.

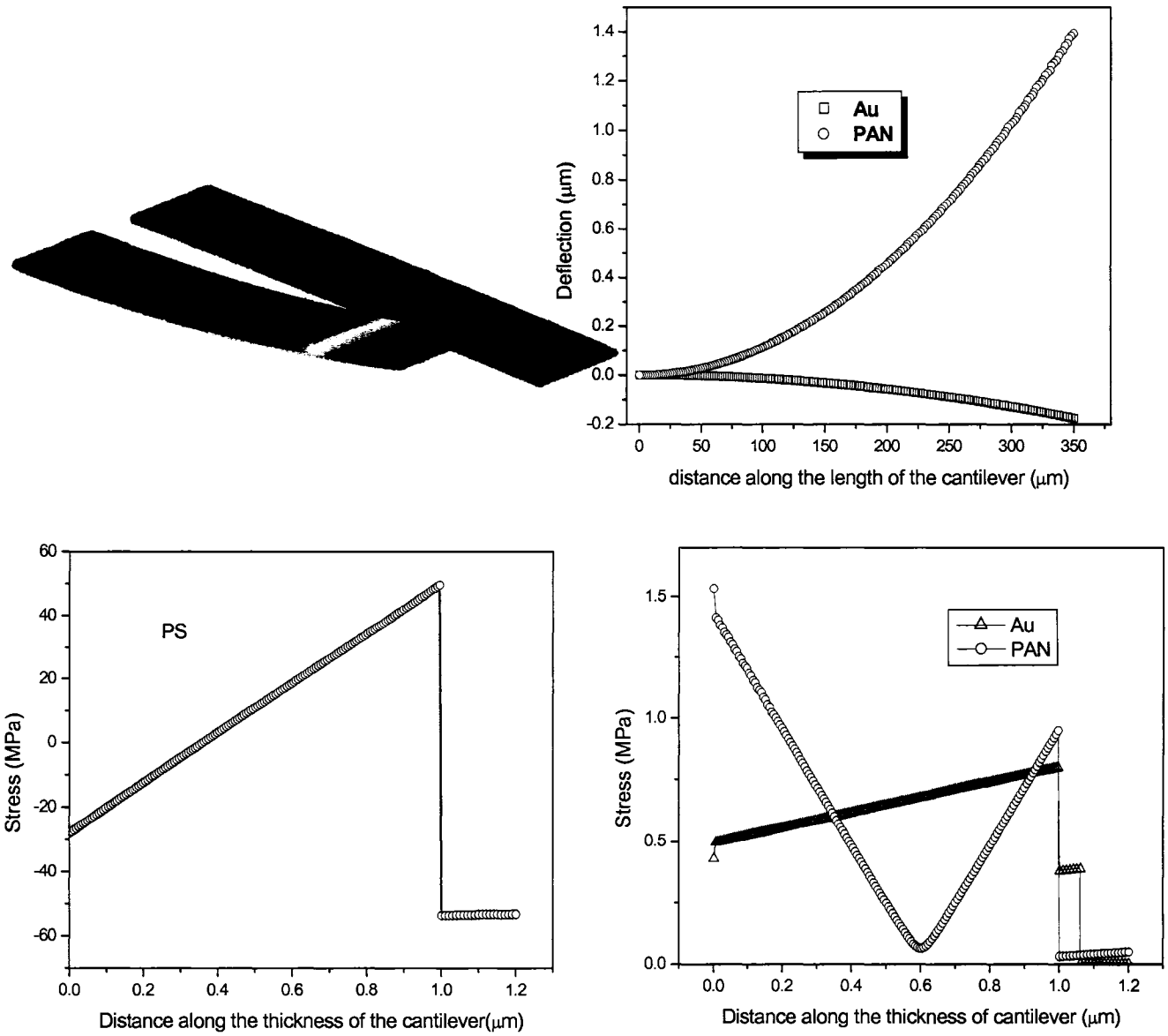

Figure 9-7. Stress analysis of the bending in response to a 1 degree temperature change using FEA. At top right is the bending comparison in a 200nm ppACN and gold coated cantilever with the resulting simulated image at top left (ppACN bending up, gold coated cantilever bending down) with color brightness corresponding to relative deflection. At bottom right is the stress comparison from a cross-sectional analysis of the indicated cantilevers. Notice the much larger stresses involved with the ppPS case (bottom left) due to the intrinsic stresses (larger pre-bent).

For reliable use in a MEMS based IR sensor application, the microcantilever deflection must be reversible through the course of cycling. This test was done over a large temperature range to ensure the device could sustain large, repeatable deformations. Due to the large bending, the deflections were out of the AFM detector range and were monitored with a home built video system. The reversibility and limits of the polymer-ceramic microcantilever performance measured by multiple thermal cycling tests were done with the ppPS hybrid microsensor over the large temperature range with the microcantilevers subjected to 100 heat-cool cycles (Fig. 8). Real-time video of microcantilever deflections in the course of thermal cycling presented in the Supporting Information demonstrates a high level of reversible bending across a wide temperature range with 50 μm reversible deflection occurring. The reproducibility of thermal bending under these conditions was quite convincing, as the overall fluctuation between the first and last (100^{th}) cycle was less than 5%. The overall thermal sensitivity (slope of the plot in Fig. 4) remains constant within 1%. This stability is excellent considering that the total microcantilever deflections reached nearly 50 μm, corresponding to a 1.1% strain that is quite high for silicon. Remarkably, over this temperature range, the thermal sensitivity was found to be 1.86 nm/mK. This sensitivity value is *more than 30 times higher* than for the reference gold-silicon microcantilever. Moreover, the temperature resolution or minimum detectable temperature difference of these microcantilevers is 0.2 mK, which is an order of magnitude better that of the best uncooled IR sensors.[2,11] The sensitivity is limited by thermal vibrations, which have amplitudes of 0.4±0.1 nm as measured by thermal tuning in air.[61]

Owing to the stimuli responsive nature of polymeric materials, another potential advantage of organic/inorganic hybrid sensors is the ability to possess multi-sensing capabilities. Indeed, if a sensor with a simple design such as that proposed here composed with a microfabrication compatible *single* active organic sensing layer could transduce *two* distinctly strong signals to very different physical conditions of the local environment, such a sensor would be quite valuable. The same microcantilever sensors showing unprecedented thermal response also show humidity response on the order of parts per trillion (ppt), or three orders of magnitude better than results reported in the literature.[62,63] This value is found with

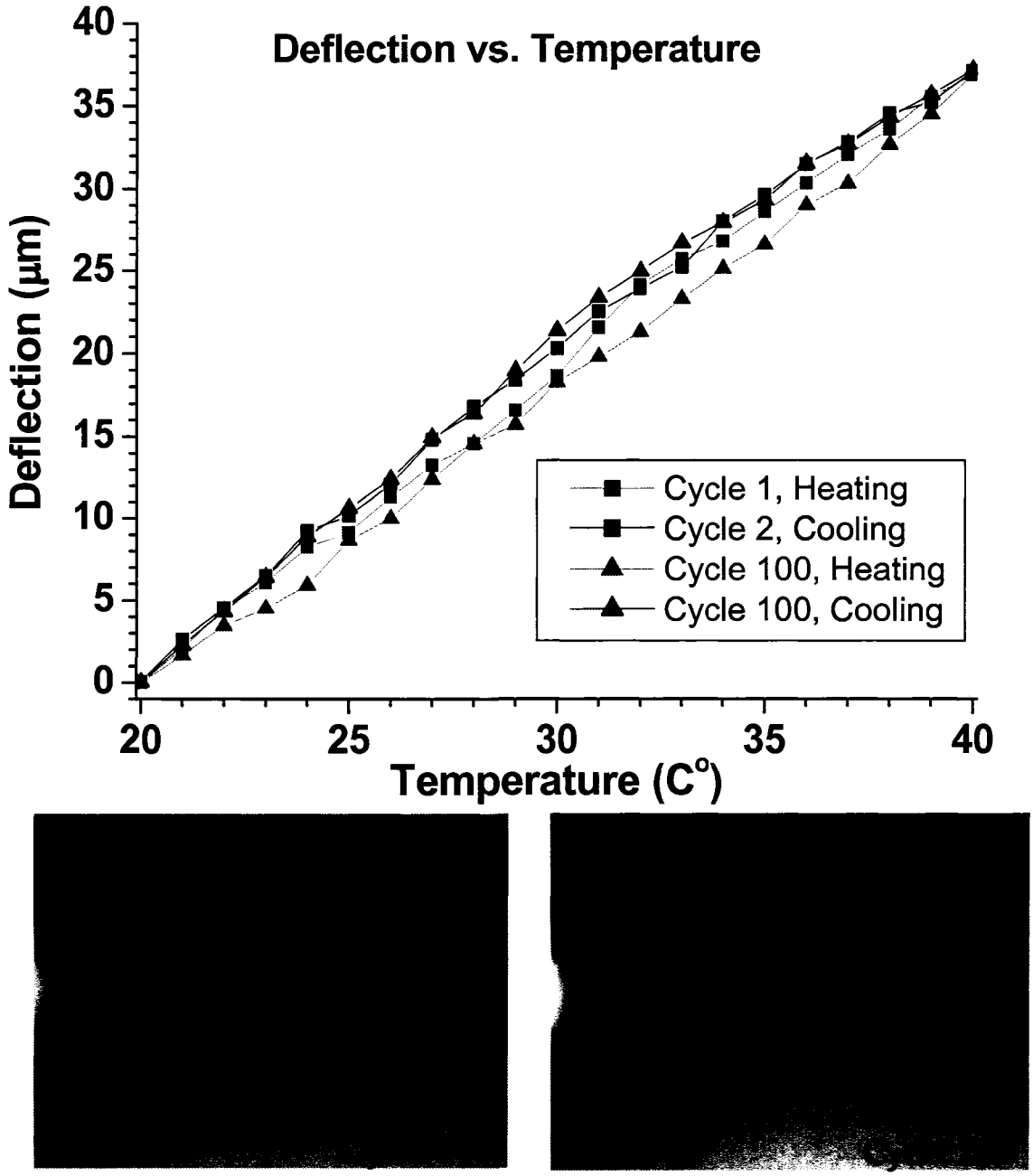

Figure 9-8. The thermal deflection of the microcantilevers over a larger temperature range showing the high reproducibility upon heating and cooling over a 100 cycles. Shown below the plot are the initial run and the 100th (final) cycle.

the ppPAN hybrid sensor, while ppPS showed a much lower sensitivity. Based on the FTIR analysis and modulus results described above, it was concluded that ppPS had a more regularity structure correlation with conventional PS, thus, ppPAN has a more cross-linked structure. Furthermore, it has been clearly demonstrated that a more tightly cross-linked plasma polymer will also have a higher number of free radicals trapped in the network.[64,65] Water will absorb stronger on the hybrid sensor with a larger density of free radicals[66], and this explains the superior performance of the ppPAN in this case.

Humidity sensors are important for measuring the relative humidity in a variety of environments, and our critical in biomedical analysis and medical equipment such as respiratory devices.[67] Currently, capacitive sensors are the most commonly used with 70% of the current sensors relying on capacitive transduction.[68] The water vapor of the environment is absorbed or desorbed causing a change in the capacitance. Capacitive sensors are suitable for applications requiring a high degree of sensitivity at low humidity levels, where they will provide a relatively fast response. However, one of the common problems with the capacitive sensors is the tendency to saturate and become non-linear at higher RH. In terms of sensitivities, Salonen et al have reported a capacitive sensor based on carbonized porous silicon with a sensitivity of 0.2 ppm.[69] Chakraborthy et al have demonstrated a FET based humidity sensor with a sensitivity of ~1 ppm.[70] Decres et al have demonstrated an optical humidity sensor based in Nafion crystal violet films with a sensitivity of 4.37 ppm.[71]

In this case, the hybrid sensor was exposed to a RH range of 6-66%, and assuming a linear variation over the entire range the sensitivity was calculated to be 1.6 μm/%. With assumptions of Brownian motion, we assumed a smallest detectable change of 3nm, and thus a change in humidity of 2.0×10^{-3} RH. Since the experiment was performed at room temperature (25°C) from the saturation vapor pressure the 1% RH corresponds to 0.23 g/m^3 of absolute humidity. The detection resolution of the cantilever was estimated to be 400 ppt. To our knowledge, there is no technique with such high sensitivity.

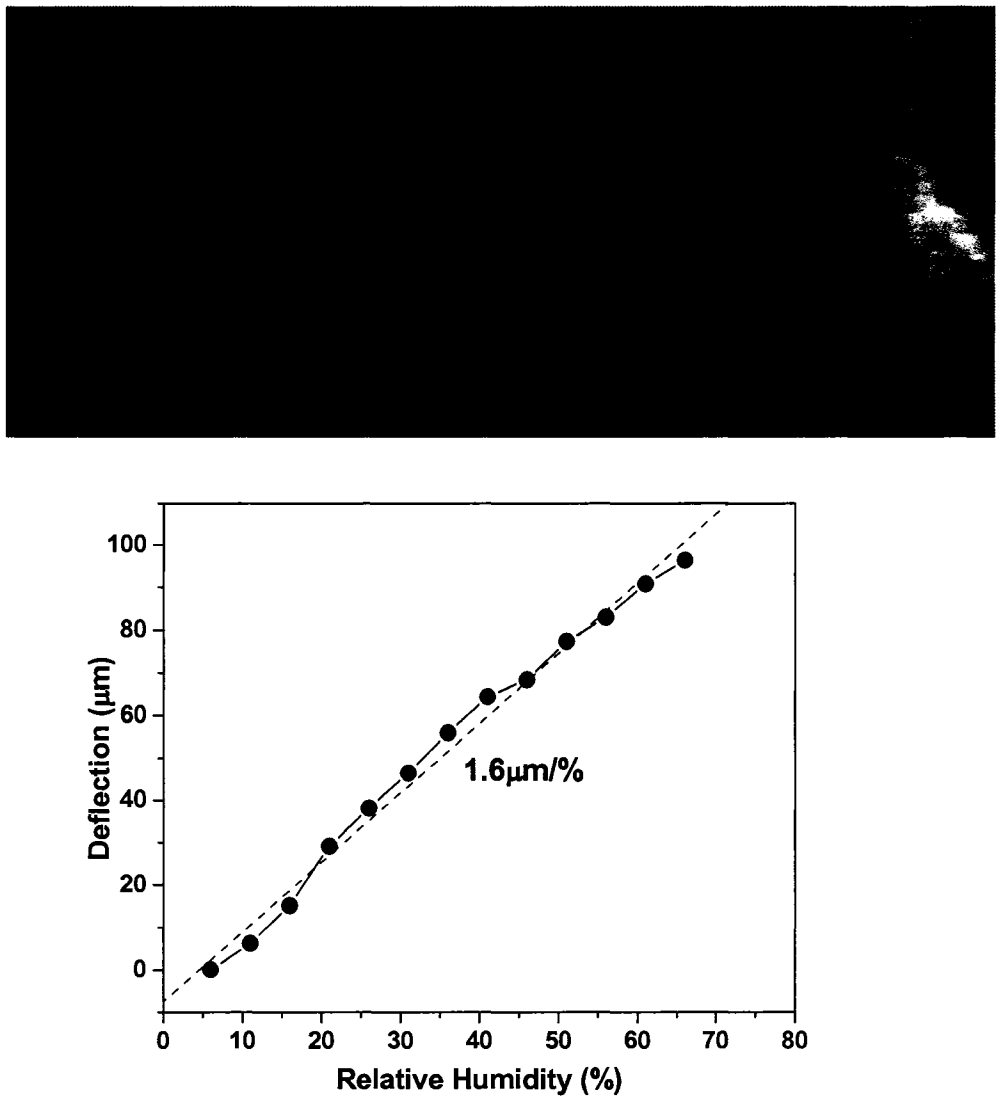

Figure 9-9. Optical images (top) of the deflection of ppPAN cantilever in response to humidity from 6 – 66%, and corresponding plot (bottom).

In summary, the focus of the work is to show that polymer coated microcantilever hybrid sensors can be produced undamaged, with remarkable thermal sensitivity (amount of deflection/temperature change) compared to similar bimetal cantilevers, and to establish the concept that this type of design approach can lead to a new class of uncooled IR sensor arrays surpassing the ultimate sensitivity offered by even cooled photon detectors. The

approach described here clearly opens the way for the microfabrication of highly sensitive microscale thermal arrays for miniature thermal imagers with record thermal sensitivity of about 2 nm/mK, and the lowest limit of temperature detection of about 0.2 mK. As it turns out, the unique process of PECVD nanolayers unexpectedly led to peculiar properties, such as the high modulus/high thermal expansion combination, as well as enhanced bending due to a pre-bent state, which essentially implies residual stresses can be tuned based upon deposition parameters. To this end, we believe PECVD polymers is the optimal route for such sensor applications because almost any monomer can be easily deposited with controllable stresses (and thus chemical structure) in a dry, microfabrication friendly procedure leading to further chemical modification towards multifunctional chemical-thermal microsensor arrays with tunable spectral response, as well as unprecedented humidity sensors as demonstrated here.

9.3 Methods

PECVD polymer materials and coating.

Styrene, acrylonitrile, and pentafluorostyrene were purchased from Aldrich (purity greater than 99%), and were directly used for the plasma polymerization. Because it is impossible to characterize the polymer sensing layer while on the cantilever, both microcantilevers and a corresponding large silicon wafer were coated simultaneously for each deposition condition. The microcantilevers (MicroMasch USA) were rectangular shaped with the following dimensions: L = 300μm; W= 20μm; T = 0.7 – 1.3μm as verified by SEM. The tips were uncoated silicon, or silicon with a 60 nm Au layer. Spring constants varied from 0.01 to 0.2 N/m, measured by the thermal tune method.[61] The cantilevers were reversibly mounted on the corresponding wafer, and placed in the PECVD reaction chamber so that only one side of the cantilever was coated. The PECVD chamber is custom built, and schematic is presented in Figure 1. Details of the system are published elsewhere.[72] Briefly, Argon (50-200 cm^3/min, 99.999%), used as the noble gas for generating a plasma, flows into a 10-cm diameter reactor at 0.02-0.5 Torr vacuum through a capacitively coupled radio frequency (RF, 13.56 MHz) discharge of 20 to 45W power. The plasma density is controlled

to approximately 108 cm^{-3} in the afterglow region. The precursor gas/vapor is added 10 cm downstream from the plasma generation zone. The substrate is located about 1-3 cm further downstream from the precursor inlet. The distance between the substrates and the inlet of precursor materials can be changed as the requirements of the resulting films change. Precursor flow rates of 0.5 and 1.125 cm^3/min were utilized for the coatings. Films of each polymer were deposited on the microcantilevers, silicon wafers (for ellipsometry, XPS, and AFM characterization), and IR transparent salt plates for FTIR measurements.

AFM topography and roughness characterization was carried out on a Dimension 3000 Nanoscope (Veeco) in usual tapping mode.[73] Ellipsometry, FTIR, and XPS analysis were done according to previous protocols.[74]

Sensitivity Testing of the microcantilevers.

The response to thermal flux was monitored using a custom built heating stage to heat the mounted tip, and the corresponding deflection was measured by the AFM optical system. The tip was brought into a grooved Peltier heating element (Supercool, Göteborg) that was 1.2 cm^2. This was controlled by an ILX Thermo-Controller (ILX, Bozeman, MT) that had 0.001°C resolution, range of -50°C to 250°C, and 24 hour thermal stability of ± 0.005°. The entire setup was enclosed in a small (5 x 5 x 10 cm) plastic enclosure to prevent heat dissipation, and to shield against wind forces and noise. The corresponding deflection was measured in voltage deflection on the photodiode, and converted into nanometers after the sensitivity of the system (tip, piezo, photodiode) was measured in contact mode AFM. The effect of the laser beam was tested on an unmodified microcantilever and only long-time random deflections on a nanometer scale have been observed confirming minimum influence of the laser beam. On the other hand, all deflection measurements have been taken at a given temperature after several minutes of equilibration and even long (hours) waiting did not affected deflection despite exposure to the laser beam. Theoretical thermal deflections have been estimated with Finite Element Analysis (FEA) using Structural Mechanics module of a package COMSOL Multiphysics 3.2.[75] A typical FEA involves the reduction of the Energy

Functional (E) of individual elements of the model. The bimaterial structure was meshed into ~40,000 elements.

9.4 Acknowledgements

The authors thank Kyle Anderson for technical assistance and Dr. L. Zhang (Agiltron, Woburn, MA) for technical discussions. Support is provided by AFOSR, F49620-03-C-0069 Grant via Agiltron, Inc. and the AFRL.

9.5 References

1. Kayes, R. J. Optical and Infrared Detectors (Springer-Verlag, Berlin, 1977).
2. Rogalski, A. Infrared detectors: status and trends. Prog. Quant. Elect. 27, 59 (2003).
3. Henini, M. and Razeghi, M. Handbook of Infrared Detection Technologies (Oxford, New York, 2002.
4. Wood, R. A. Uncooled Infrared Imaging Arrays and Systems, Semiconductors and Semimetals, Vol. 47. Eds. Kruse, P. W. and Skatrud, D. D. (Academic, San Diego, 1997).
5. Lai, J., Perazzo, T., Shi, Z. and Majumdar, A. Sens. Actuators 58, 113 (1997).
6. Schmitz, H., Murtz, M. and Bleckmann, H. J. Comp. Physiology, A: Sensory, Neural, and Behavioral Physiology 186, 543 (2000).
7. Schmitz, H., Bleckmann, H. and Murtz, M. Nature 386, 773 (1997).
8. Gorbunov, V., Fuchigami, N., Stone, M., Grace, M. and Tsukruk, V.V. Biomacromolecules 3, 106 (2002).
9. Malyarov, V. G. J. Opt. Technol. 69, 750 (2002).
10. Kruse, P. W. Inf. Phys. Technol. 36, 869 (1995).
11. Hunter, R. S. Proc. SPIE 5074, 469 (2003).
12. Datskos, P. G., Lavrik, N.V. and Rajic, S. Rev. Sci. Instrum 75, 1134 (2004)
13. Sarid, D. Scanning Force microscopy (Oxford University press, New York, 1991).

14. Sze, S. M. Semiconductor Devices: Physics and Technology, 2nd ed. (Wiley, New York, 2002).
15. Madou, M. Fundamentals of Microfabrication (CRC, Boca Raton, FL, 1997).
16. Lang, H.P., Hegner, M. and Gerber, C. Materials Today 8, 30 (2005).
17. Hagleitner, C., Hierlemann, A. et al. Nature 414, 293 (2001).
18. Fadel, L. et al. J. Micromech. Microeng. 14, S23 (2004).
19. Pinnaduwage, L.A. et al. Nature 425, 474 (2003).
20. Pinnaduwage, L.A. et al. Langmuir 20, 2690 (2004).
21. Ziegler, C. Anal. Bioanal. Chem. 379, 946 (2004).
22. Hilt, J.Z., Gupta, A.K., Bahir, R. and Peppas, N.A. Biomed. Microdev. 5, 177 (2003).
23. Datskos, P.G. et al. J. Vac. Sci. Technol. B 19, 1173 (2001).
24. Barnes, J.R., Stephenson, R.J., Welland, M.E., Gerber, C. and Gimzewski, J.K. Nature 372, 79 (1994).
25. Varesi, J., Lai, J., Perazzo, T., Shi, Z. and Majumdar, A. Appl. Phys. Lett. 71, 306 (1997).
26. Datskos, P.G., Oden, P.I., Thundat, T., Wachter, E. A., Warmack, R.J. and Hunter, S.R. Appl. Phys. Lett. 69, 2986 (1996).
27. Oden, P.I., Datskos, P.G., Thundat, T. and Warmack, E.A. Appl. Phys. Lett. 69, 3277 (1996).
28. Manalis, S.R., Minne, S.C., Quate, C.F., Yaralioglu, G.G. and Atalar, A. Appl. Phys. Lett. 70, 3311 (1997).
29. Corbeil, J.L., Lavrik, N.V., Rajic, S. and Datskos, P.G. Appl. Phys. Lett. 81, 1306 (2002).
30. Zhao, Y., Mao, M., Horowitz, R., Majumdar, A., Varesi, J., Norton, P. and Kitching, J. J. MEMS 2, 136 (2002).
31. Komvopoulos, K. Wear 200, 305 (1996).
32. Kam, N.W.S., O'Connell, M., Wisdom, J.A., Dai, H. Proc. Nat. Acad. Sci. 102 11600 (2005).
33. Lin, Y.-H. et al. Adv. Mater. 18, 1157 (2006).

34. Hierlemann, A., Brand, O., Hagleitner, C. and Blates, H. Proc. IEEE 91, 839 (2003).
35. Biederman, H. Plasma Polymer Films (Imperial College Press, London, 2004).
36. Tamirisa, P., Liddell, K.C., Pedrow, P.D. and Osman, M.A. J. Appl. Poly. Sci. 93, 1317 (2004).
37. Shi, F. Surf. Coat. Technol. 82, 1 (1996).
38. Biederman, H. and Slavinska, D. Surf. Coat. Technol. 125, 371 (2000).
39. Cicala, G., Milella, A., Palumbo, F., Rossini, P., Favia, P. and d'Agostino, R. Macromolecules 35, 8920 (2002).
40. Lin-Vien, D. The handbook of infrared and raman characteristic frequencies of organic molecules (Boston, Academic Press, 1991).
41. Denes, F. Trends Polym. Sci. 5, 23 (1997).
42. Haaland, P., Ibrani, S. and Jiang, H. Appl. Phys. Lett. 64, 1629 (1994).
43. Zou, X.P. et al. Polym. Adv. Technol. 12, 583 (2001).
44. Fu, G.D., Kang, E.T. and Neoh, K.G. J. Phys. Chem. B. 107, 13902 (2003).
45. Ulman, A. Chem. Rev. 96, 1533 (1996).
46. Biederman, H.J. Vac. Sci. Technol. A. 18, 1642 (2000).
47. Kim, H. et al. Polymer 45, 3175 (2004).
48. McFarland, A.W., Poggi, M.A., Doyle, M.J., Bottomley, L.A. and Colton, J.S. App. Phys. Lett. 87, 053505 (2005).
49. Tsukruk, V.V., Sidorenko, A., Gorbunov, V.V. and Chizhik, S.A. Langmuir 17, 6715 (2001).
50. Sigma Aldrich Catalog (2006).
51. Reiter, G. and de Gennes, P.G. Eur. Phys. J. E. 6, 25 (2001).
52 Reiter, G. et al. Nat. Mater. 4, 754 (2005).
53. Guerin, D.C. et al. Langmuir 18, 4118 (2002).
54. Denes, F. et al. J. Photopolym Sci. Technol. 93, 1141(1997).
55. LeMieux, M.C., McConney, M.E., Lin, Y.-H., Singamaneni, S., Jiang, H., Bunning, T.J. and Tsukruk, V.V. Nano Letters 6, 730 (2006).
56. Dareing, D.W. and Thundat, T.J. App. Phys. 97, 043526 (2005).

57. Chen, J. and De Wolf, I. Semicond. Sci. Technol. 18, 261 (2003).
58. Morinaka, A. and Asano, Y.J. Appl. Polym. Sci. 27, 2139 (1982).
59. Yu, Q.S. et al. J. Poly. Sci. A. 37, 1577 (1999).
60. Yasuda, H. et al. J. Appl Polym Sci. 21, 3167 (1977).
61. Sader, J.E., Chon, J.W.M. and Mulvaney, P. Rev. Sci. Instrum. 70, 3967 (1990).
62. Bruno, P. et al. Sens. Act. 100, 126 (2004).
63. Radeva E.I. et al. Mater. Sci. Eng. C 12, 71 (2000).
64. Yasuda, H. and Hirotsu, T. J. App Poly Sci. 21, 3152 (1977).
65. Yasuda, H. J. Macromol. Sci.-Chem. A10, 383 (1976).
66. Oran, U. et al. Plasma Proc. Polym. 1, 141 (2004).
67. Adhikari, B. and Majumdar, A. Prog. Poly. Sci. 2004, 29, 699.
68. Scholz, G. Technisches Messen 59, 88 (1992).
69. Salonen, J., Tuura, Bjorkqvist, M. and Lehto, V.P. Sens. and Actuators B. 114, 423 (2006).
70. Chakraborthy, S., Hara, K., and Lai, P.T. Rev. Sci. Instr. 70, 1565 (1999).
71. Decres, H., and Narayanaswamy, R. Talanta 69, 631 (2006).
72. Haaland, P. and Targove, J. Appl. Phys. Lett. 61, 34 (1992).
73. Tsukruk, V.V. Rubber Chem. Technol. 70, 430 (1997).
74. Jiang, H. et al. Chem. Mater. 16, 1292 (2004).
75. Structural Mechanics Module Model User's Guide for Femlab3, COMSOL AB (2004).

Chapter 10

Reversible Negative Thermal Expansion in Ultrathin Plasma Polymer Films

A paper submitted to *Chemistry Materials*

Srikanth Singamaneni[1,2], *Melburne C. LeMieux*[*1], *Hao Jiang*[3], *Timothy J. Bunning*[3], *and Vladimir V. Tsukruk*[1,2*]

[1]Department of Materials Science and Engineering, Iowa State University, Ames, Iowa 50011

[2]School of Materials Science and Engineering, Georgia Institute of Technology, Atlanta, Georgia 30332

[3]Materials and Manufacturing Directorate, Air Force Research Laboratory, Wright-Patterson Air Force Base, Ohio 45433

10.1 Introduction

Plasma polymers are very unconventional and should be viewed as an entirely new class of materials. With the complex chemistry and volatile nature of plasma polymerization, it is reasonable to expect very remarkable physical properties Owing to the increasing applications of ultra thin polymer films with nanoscale thickness, it is imperative to characterize the physical properties in these films, which would be significantly different from the bulk properties due to the surface and interfacial effects. Several factors such as interactions with the substrate, significant volume at the interface (film/ air and

[*] M.C.L.: Primary researcher, all sample preparation, setup experiment, assisted with analysis and writing of all drafts

film/substrate) can cause the deviation of the properties of the ultrathin polymer films from those of the bulk films.[1,2] In a recent study the glass transition of a free standing PS film was found to be very different compared to the substrate supported film.[3] Other studies have unveiled several interesting phenomena such as the depth dependent glass transition temperature and thickness dependent thermal expansion coefficient.[4,5] It has been reported that substrate interactions alter the thermal properties (transition temperature and thermal expansivities) of ultrathin poly-(2)-vinylpyridine films with a reduction in the thermal expansion.[6] A non monotonic thermal expansion was observed in ultrathin polycarbonate films with a negative and positive thermal expansion below and above glass transition temperature respectively.[7]

Plasma Enhanced Chemical Vapor Deposition (PECVD) one of the popular nanoscale film fabrication techniques involves the creation of plasma at low temperatures and pressure. Plasma polymerization is a solvent less (dry) process that results in organic films with high solvent resistance, pinhole free surfaces, scratch resistance, corrosion resistance, and excellent thermal and chemical stability.[8] Plasma polymerization allows the deposition of ultra thin polymers films compatible with lithographic fabrication methods, finding applications in sensing devices, MEMS, and optical devices.[9,10,11] In fact, the growth of plasma polymers exploded during the early development of the microelectronics industry in the late 60s inspired by the goal of incorporating organic materials and dielectric films into these devices.[12] The chemical reactions involved during the plasma polymerization are significantly different from those observed in conventional polymerization reactions.[8] Excited organic species, free radicals and ions react with each other to produce high molecular weight and highly crosslinked chains resembling polymers. The technique offers a unique advantage of the ability to polymerize almost any organic molecule, some of which are difficult or impossible otherwise. This has led to plasma polymers being increasingly used as an alternative material in applications such as nanoscale photonics[11, 13] to biocompatible interfaces.[14]

The high energy induced fragmentation of the monomer might result in a polymer whose physical and chemical properties are significantly different compared to the conventional polymers.[15] Due to the missing groups and lack of repeat units, physical organization of the polymer chains which can completely dictate the properties, and with high degrees of branching and cross-linking, plasma polymers are essentially a novel (and largely unexplored) class of materials.[16] Along with these unique characteristics in an organic film, an additional aspect of plasma polymers is that when deposited as thin films, they have some intrinsic level of residual stresses due to their fundamental growth mechanisms.[17] Overall, the relatively little research of plasma polymers has been on understanding their chemical structure as a function of deposition conditions, with almost no work regarding the actual determination of physical properties.[18]

In this communication, we report on the thermal expansion properties of ultrathin plasma polymerized polymer films. An intriguing hysteresis behavior was observed between the heating and cooling cycles in these films. Remarkably, a large, reversible negative thermal expansion of ultrathin plasma polymerized Polyacrylonitrile (ppPAN) and plasma polymerized Polytrimethyl silyl acetonitrile (ppPTSA) in the film normal direction was observed. The polymer films were deposited by PECVD technique with styrene, acrylonitrile, trimethylsilyl acetonitrile as precursors in custom built PECVD reactor and throughouly characterized with FTIR, AFM, and XPS according to the procedures described in detail elsewhere (see Supporting Information for some technical details).[11, 19,20,21,22] (Table 10-1).

10.2 Results and Discussion

The chemical structures of the monomers used as precursors for the plasma polymerization are shown Figure 10-1(a). FTIR analysis was used to identify the chemical composition of the polymer films under investigation. The FTIR spectra of the plasma polymer films of PAN, PTSA and PS are shown in Fig. 10-1. The FTIR of the PS (Fig. 10-1(b)) was characterized with aromatic ring stretching mode (1600 cm^{-1} and 1450 cm^{-1}),

aliphatic C-H stretch mode (2930 cm^{-1}), C-H out of plane vibration (760 cm^{-1}) and ring out-of-plane deformation (690 cm^{-1}).[23] However, it is interesting to note the absence of =C-H aromatic ring vibrations between 3000-3100 cm^{-1} which indicates that the double bonds of the phenyl ring underwent dissociation leading to a high cross-linking in the polymer. The PAN spectrum (Fig 10-1(c)) shows the characteristic C≡N stretch at 2240 cm^{-1} corresponding to the cyano group. The spectrum also displays a strong C=N stretching mode at 1650 cm^{-1} and N-H stretching at 3300 cm^{-1} suggesting a high degree of cross linking in the polymer film. The spectrum displays other characteristic bands such as -CH_2- stretch (2920 cm^{-1}), C-C stretch and C-H bending (1450 cm^{-1}). The FTIR spectrum obtained from PTSA (Fig 10-2(d)) shows the representative -Si-$(CH_3)_3$- band (770- 860cm^{-1}), -Si-CH_2R- group (1250 cm^{-1}), cyano group (2220 cm^{-1}) and CH_3 stretch (2960 cm^{-1}). The interesting aspect is the presence of a strong band at 1050 cm^{-1} which corresponds to C-N indicating the cyano group dissociation causing a highly crosslinked network. A relatively weak band corresponding to C=N stretch (1650 cm^{-1}) also indicates cross linking of the polymer. Several other weak bands correspond to the small amount of oxygen impurity the presence of which is confirmed with XPS (not shown here).

Table 10-1. Thermal characteristics of nanoscale polymer films

Polymer	Ultrathin films from present study							Bulk Material	
	Plasma polymerized				Wet deposited				
	α (K^{-1})	t (nm)	R (nm)	C (deg)	α (K^{-1})	t (nm)	R (nm)	α (K^{-1})	T_g(°C)
PS	1.9×10^{-4}	148	1.5	69	1.7×10^{-4}	169	0.25	$(0.8\text{-}2.8)\times10^{-4}$ * [Ref. 4,24]	65-100 * [Ref. 4,25]
PAN	-3.1×10^{-4}	95	1.7	55	1.6×10^{-4}	20	0.20	1.0×10^{-4} [Ref. 26]	85-104 [Ref. 26]
PTSA	-2.5×10^{-4}	97	0.5	75	NA **	-	-	-	-

α: Linear thermal expansion coefficient below T_g
t: Thickness
R: RMS roughness over 1×1 μm^2 area
C: Contact angle
* Thickness dependent
** Cannot be polymerized by conventional techniques

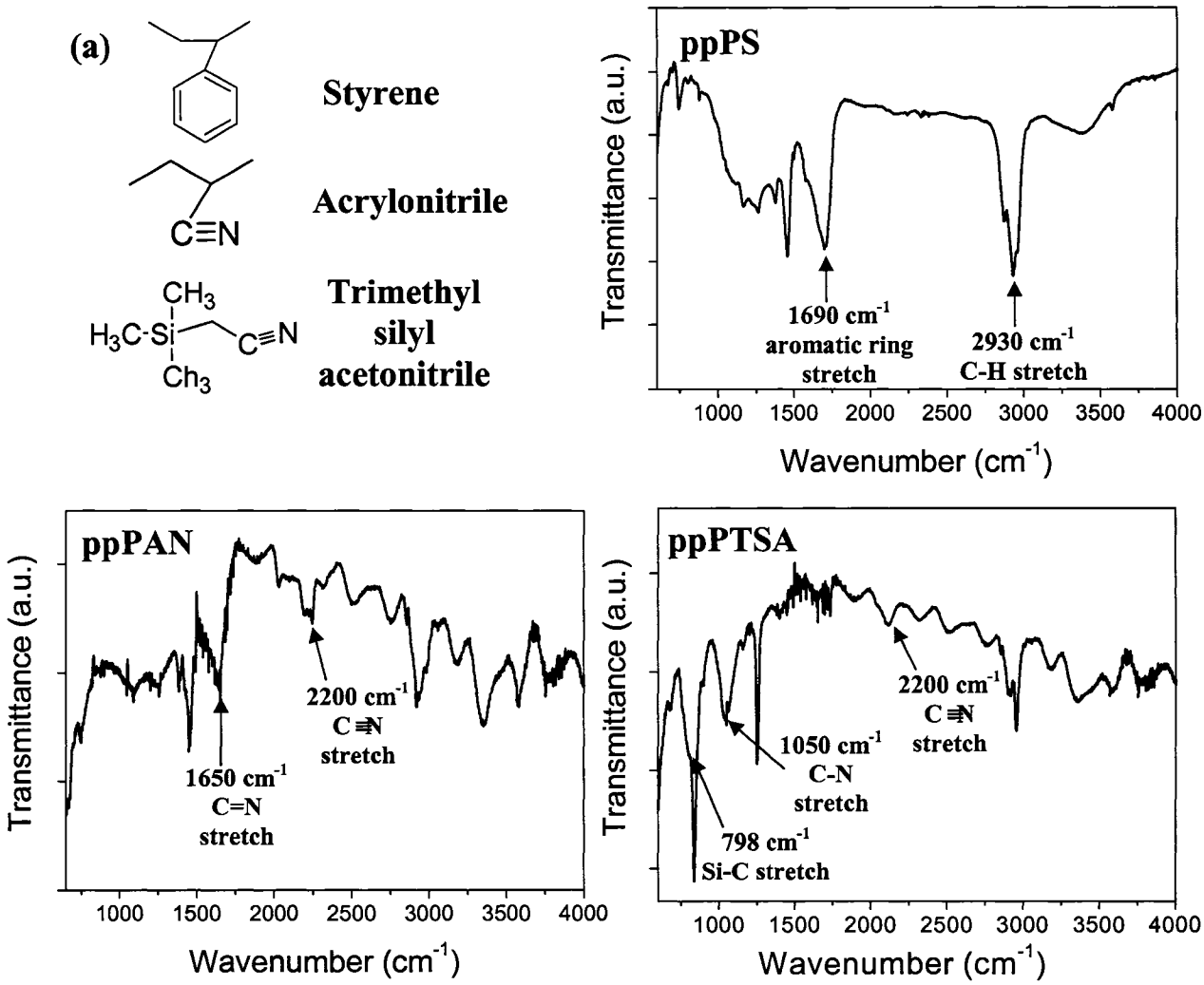

Figure 10-1. (a) Chemical structures of various monomers under study. FTIR spectra of pp PAN, pp PS and pp PTSA showing the characteristic bands.

AFM images of the polymer films under investigation are shown in Fig 10-2. The plasma polymerized (ppX) polymer films exhibited a significantly different surface morphology compared to the spin deposited counterparts. While the wet deposited films exhibited a uniform surface (micro roughness shown in Table 10-1) with no specific features (not shown here), all the pp films had a granular morphology a characteristic pinhole free surface. Figure 10-2(a) depicts the AFM image of the ppPS and Figure 10-2(b) shows the high magnification image of the same. It can be observed from the AFM image that the

sample had uniform granular features of size ranging from 40-50 nm. The surface morphology of the ppPAN closely resembled that of pp PS except for slight difference in the grain size (Fig. 10-2(c) and (d)). The RMS surface microroughness was found to be 1.5 and 1.7 nm for pp PS and ppPAN respectively. ppPTSA had an extremely smooth morphology with almost no obvious features except for occasional small bumps and the surface roughness was found to be 0.5 nm, significantly smaller compared to pp PS and ppPAN (Figure 10-2(c) and (d).

Thermal expansion of spin coated PS films (M_w = 2.5 × 10^5 g/mol) used as a reference sample was measured and the thickness vs. temperature is plotted in Fig 10-3(a). The thermal expansion coefficient was found to be $1.7 \pm 0.3\times10^{-4}$ K^{-1}. Figure 10-3(b) shows the thickness Vs Temperature plot of two consecutive heating and cooling cycles for ppPS and the linear thermal expansion coefficient was found to be $1.9 \pm 0.3\times10^{-4}$ K^{-1}. In all the experiments the first heating and cooling cycle were disregarded and not used for the computation of the thermal expansion coefficient. It can be noted that the expansion coefficient of ppPS is very close to that of the spin coated sample. The linear thermal expansion coefficient observed here in spin coated and plasma polymerized film is slightly higher than that of bulk polystyrene (1.0×10^{-4} K^{-1}). It has been previously reported that linear thermal expansion of PS films is thickness dependent exhibiting increase of α with decrease in thickness below T_g and a decrease of α with decrease in thickness above T_g.[4] They have proposed a three layer model in which they assume that the thin polymer film on a substrate can be divided in to three regimes: layer very close to the substrate (dead layer), layer at the air interface with higher mobility compared to the bulk (liquid like layer) and the layer between these two layers (bulk layer). They have proposed simple analytical relation to estimate the thermal expansion coefficient in substrate normal direction which can be significantly different (~100 %) from the bulk films due to the non trivial contributions from dead and liquid like layers as opposed to the bulk films where these effects become insignificant. The other interesting aspect one can observe from Figure 10-3(b) is the contraction during the reduction of the temperature in ppPS films followed a significantly different path compared to that during expansion.

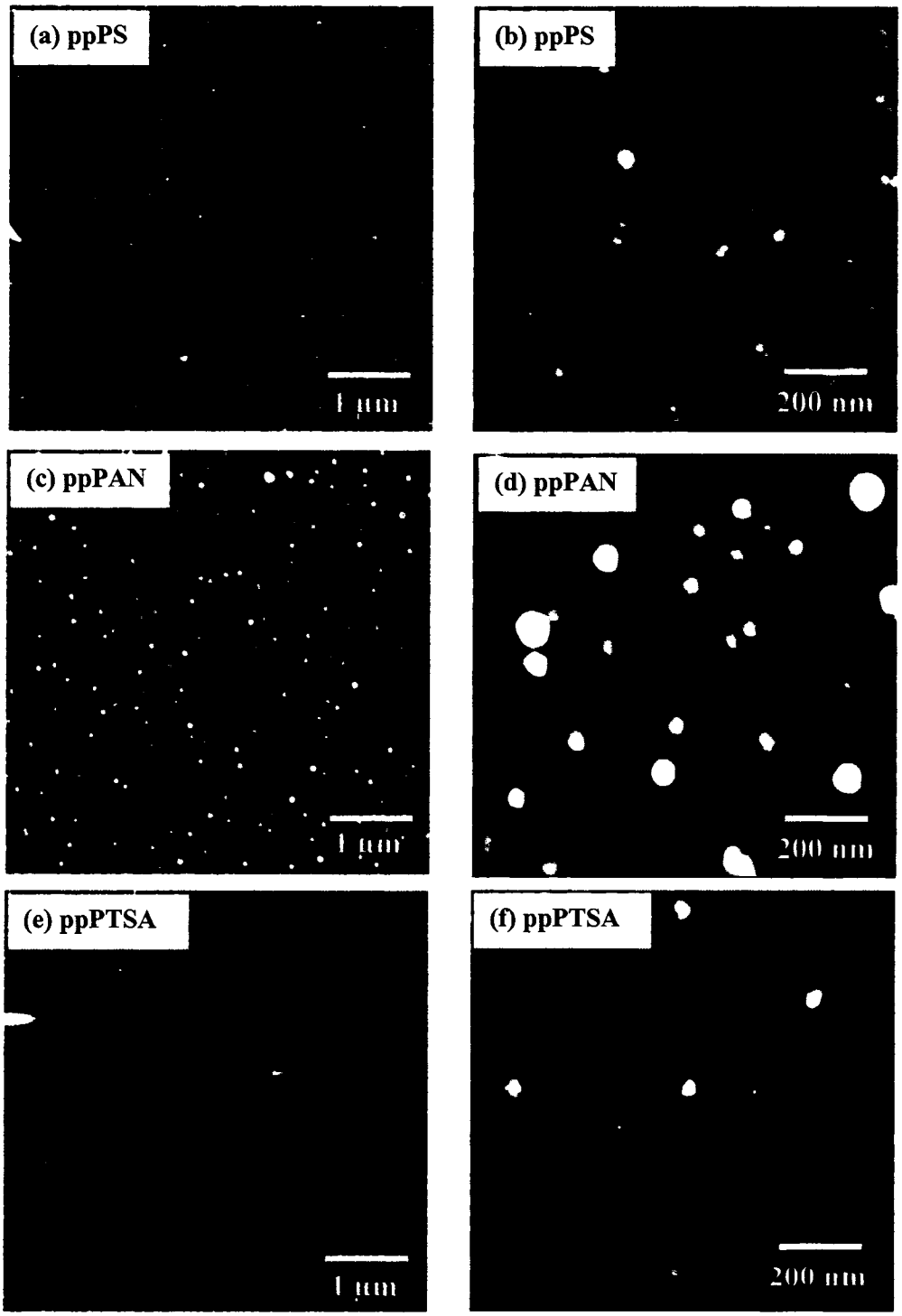

Figure 10-2. AFM images showing the surface morphology of pp PS (a) and (b), pp PAN (c) and (d) and pp PTSA (e) and (f). The z range is 20nm for images (a) (b) and (c), 10nm for image (d), and 5 nm for images (e) and (f).

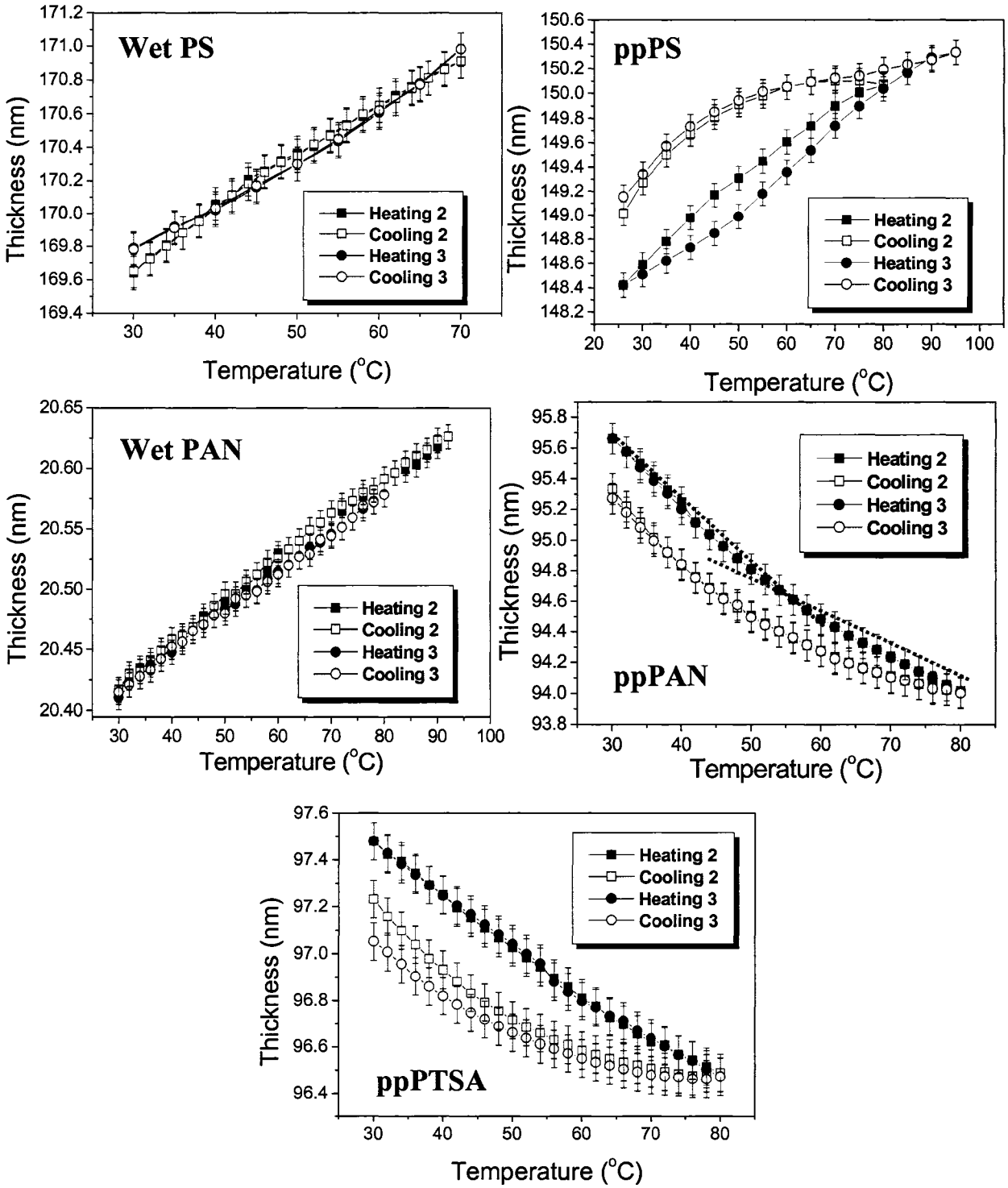

Figure 10-3. Plots of temperature Vs thickness of ppPAN, Spin coated PAN, PECVD PS, Spin coated PS, and PECVD PTSA.

In the cooling cycle all the plasma polymerized polymers exhibited a significantly non-linear variation of thickness with temperature and final thickness at the completion of the cooling cycle was 0.3-0.5 nm smaller than the initial. Since cycle 2 and cycle 3 were performed consecutively the initial thickness of cycle 3 was smaller by 0.3-0.5 nm. For clarity purposes the thickness values of cycle 3 were offset to make the initial thickness equal to that of the cycle 2. However, the film restored to original thickness after long relaxation time (~ 8 hours). This behavior was observed for all the plasma polymerized films (including ppPAN and ppPTSA) while the wet deposited films exhibited no such hysteresis. Variation in thickness between heating and cooling cycles has been reported in ultra thin (52.8 nm and 29 nm) PS films with the thickness during heating always more than that during cooling followed by slow recovery.[27] We suggest that the observed hysteresis in thermal expansion might be due to the stresses developed in the polymer during the deposition process. A hysteresis behavior of residual stresses in plasma deposited amorphous thin films during thermal cycling was previously reported and accounted to different rates of relaxation and stress release.[28,29]

Spin coated films of PAN (3500 g/mol) had a smooth surface morphology with RMS microroughness of 0.2 nm (Table 10-1). Thermal expansion of the spin coated PAN during (3500 g/mol) of thickness 20.5 nm is shown in Fig 10-3(c). Thermal expansion coefficient was calculated to be $1.6\times10^{-4}\,K^{-1}$ which is slightly higher than that for the bulk film ($1.0\times10^{-4}\,K^{-1}$) for the same reasons discussed earlier. Fig. 10-3(d) shows the temperature Vs thickness during cycle 2 and 3 for PAN film with a thickness of 96 nm. We have observed thermal contraction of the film in substrate normal direction. Furthermore, the negative thermal expansion was found to reversible with an increase in the thickness for decreasing temperature. One can observe that the thickness Vs temperature during heating and cooling cycles exhibited significant nonlinearity and the thermal expansion was computed over the initial linear region from 30°C to 50°C of the heating cycle. The thermal expansion coefficient was calculated to be $-3.1 \pm 0.2\times10^{-4}\,K^{-1}$. Similar thermal contraction of ppPTSA (with a thickness of 97.5 nm) is shown in Fig. 10-3(e) and the linear thermal expansion coefficient was found to be $-2.5 \pm 0.2\times10^{-4}\,K^{-1}$. As mentioned earlier, ppPAN and ppPTSA

films also exhibited a hysteresis behavior in thermal expansion followed by a slow relaxation process with complete reversibility. This non linearity in thermal expansion can be associated with glass transition which introduce change in slope indicating a higher thermal expansion coefficient. The transition temperature observed for ppPAN was ~55° C within is lower than for bulk PAN (85°C, Table 10-1) and can be caused by significant amount of unreacted monomers and oligomers present in the film.

To explain negative thermal expansion here we suggest that the unusual thermal expansion behavior is due to the presence high residual stress in the polymer film common for PECVD materials. The presence of residual stress in the polymer films was also confirmed by the bent state of the microcantilevers which were coated with plasma polymer films along with the samples (silicon wafers) investigated here. From the radii of curvature of the cantilevers the residual stress in the polymer films was estimated using Finite element Analysis (FEA) and theoretical calculations (stoney's equation) to be as high as 50 MPa.[9] Negative thermal expansion (NTE) has been previously observed along the chain direction for fully aligned linear chain polymers. [30] For example, polyethylene exhibiting orthorhombic crystal structure showed a small negative thermal expansion in the axial direction of the chains and variable positive thermal expansion is observed in the transverse direction. A different effect exhibited by thermal stresses and elasticity in the negative axial thermal expansion of crystalline polyethylene has been discussed by Lacks and coworkers.[31] Several other models have been proposed to explain the NTE and zero thermal expansion (ZTE) observed in ultrathin polymers films. Recently, it has been proposed that a decrease in the entropy associated with expansion in some systems makes thermal contraction thermodynamically favorable.[27]

Although the residual stresses occur for all the plasma polymerized polymers the magnitude depends on other factors such as the chemical nature of the monomer and conditions of deposition. Both the NTE polymers (ppPAN and ppPTSA) have a C≡N group which leads to a high degree of crosslinking. As discussed earlier, FTIR analysis of the polymer films also confirms the high level of cross linking in these films. The highly cross

linked polymer film is frozen in a metastable state with high residual stresses. The residual stresses arise due to the wedging effect during the deposition process where the high energy fragments wedge in the existing film. The polymer globules (as seen in the AFM images) can be considered as the wedges in the polymer film. Figure 10-4 shows a schematic

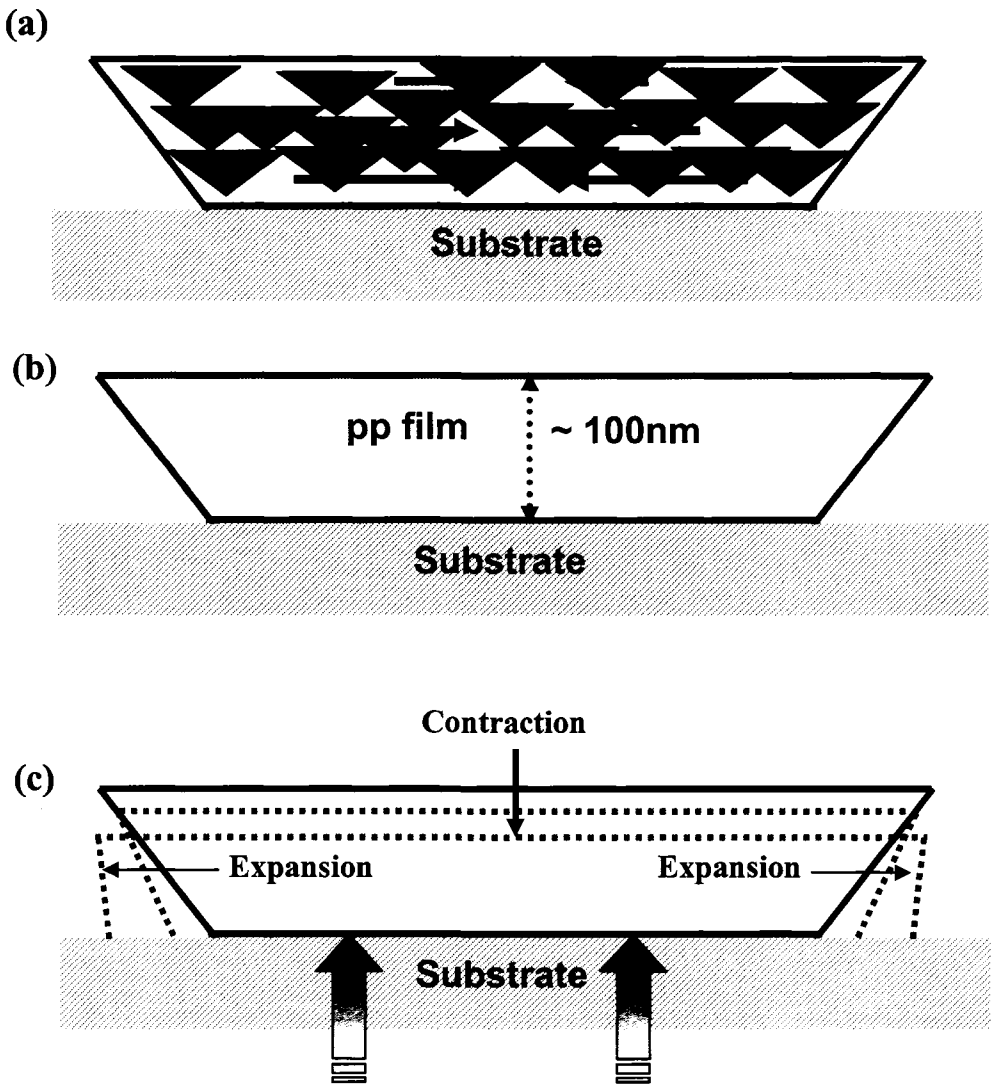

Figure 10-4. Schematic representation of (a) Plasma polymerized film with high intrinsic residual stress (red arrows indicate intrinsic compressive stresses from deposition) due to wedge effect into the nascent film (b) Final structure of the pp film with high residual stress and asymmetrical structure (c) Thermal expansion in plane of the film and contraction in substrate normal direction on heating.

representation of the plasma polymer films with individual grain in highly compressive state. Increase in the temperature causes these polymer grains to expand laterally and a simultaneous contraction of the entire film in substrate normal direction. It has been previously reported that high tensile or compressive stresses comparable to the yield stress of the polymer can significantly alter the thermal expansion behavior of the polymer films.[32] The residual stress in the polymer films can cause rupture in thin polymer films weakly adsorbed on the surface and thereby playing an important role in the dewetting process.[33] We believe that due to the small thickness and highly crosslinked state of the films investigated in the present study, high stress developed in the polymer films during the deposition process control the thermal expansion behavior in polymers films.

The physical phenomenon of NTE in nanoscale polymer films may find important applications in technologies requiring strong organic/dielectric coatings with zero thermal expansion. Apparently, while high residual stresses are typically unfavorable aspects in a thin film, this represents an example where this quality can be advantageous by leading to unexpected properties[32,33], especially if they can be tuned and controlled, such as in a process of plasma polymerization where the deposition conditions are easily changed. Harnessing these residual stresses will be key issue for hard organic coatings either by refining the deposition procedures, or by 'freezing' in non-equilibrium conformations in the plasma polymer by excessive crosslinking. By designing composite materials with positive and negative thermal expansion the effective structural variations in the composite material for temperature changes could be minimized or eliminated. Due to the simple and efficient deposition method to fabricate them, these materials have excellent potential for applications in MEMS, IC, and optical devices as means to control and compensate the conventional materials which expand on heating.

10.3 Experimental

The polymer films were deposited in a custom built PECVD chamber described in detail elsewhere.[34] All of the PECVD polymer films were deposited on freshly cleaned (100)

three inch silicon wafers. Argon (20 cm^3/min, 99.999%), used as the noble gas for generating a plasma, flows into the 10-cm diameter reactor at 0.02-0.5 Torr vacuum through a capacitively coupled radio frequency (RF, 13.56 MHz) discharge of 45 W power. The plasma density is controlled to approximately 10^8 cm^{-3} in the afterglow region. The precursor gas/vapor is added 10 cm downstream from the plasma generation zone. The substrate is located about 2 cm further downstream from the precursor inlet. The precursor flow rate of 1.125 cm^3/min was employed during all the depositions.

Wet deposited ultrathin films of polystyrene (PS) (M_w = 250,000 g/mol) were spin coated (3000 rpm) on freshly cleaned[35] (piranha solution) silicon substrates from 3% solution in toluene while poly acrylonitrile (PAN) films (M_w = 3,500 g/mol) were spin coated from 2% solution in DMF. The spin-casting was carried out in a class 100 clean room condition. PAN was polymerized according to established procedure, reported by Matyjaszewski et al.[36], but using S-1-dodecyl-S'-(α,α'-dimethyl-α''-acetic acid) trithiocarbonate[37] as the RAFT agent. Acrylonitrile monomer, PS, DMF, and toluene were purchased from Aldrich and used as received, except that toluene was distilled prior to use.

Chemical compositions of the plasma-polymerized films were identified through Fourier transform infrared (FTIR) analysis. FTIR was performed on a Perkin-Elmer Spectrum 2000 FT-IR spectrometer in the transmission mode. A range of 400 to 4000 cm^{-1} was scanned 128 times with 1 cm^{-1} resolution and averaged.

The surface morphology of polymer films was studied in the light tapping mode in the range of magnifications (from 1x1 to 30x30 □m) with a Dimension 3000 (Veeco) Atomic Force Microscope (AFM) according to the procedure adapted in our lab. [38] AFM scratch test was used as an independent technique to confirm the thickness of the polymer films obtained from the ellipsometry with the refractive indices from independent measurements.[22] The thickness of the polymers films at various temperatures was measured using COMPEL automatic Ellipsometer (InOmTech, Inc.) equipped with a He-Ne laser with collimated beam of 1 mm diameter. The thickness at different temperatures was computed using a two-layer

model (polymer film on 1.4 nm SiO_2 layer). The refractive indices of the plasma polymer films used for computing thickness were obtained using Woollam variable-angle spectroscopic Ellipsometer system including a VB-200 ellipsometer control module and a CVI Instruments DigiKrom 242 monochromator with a 75-W xenon light source. The reflected polarization states were acquired over the range of 300-900 nm at 1-nm intervals and at angles of incidence equal to 53°, 55°, and 57°.

To study thermal expansion the samples were heated using a Nanoscope heater (Veeco) and the sample temperature was controlled with a precision of ± 0.1 K. The sample located directly on the ellipsometry stage was held for 10 min at each temperature and the thickness recorded. The heating-cooling cycles (each about 6 hrs long) were repeated 3-4 times. Prior to the thermal expansion measurements the polymer films (both plasma polymerized and wet-deposited) were annealed at 50° C under vacuum for 15 hours to remove any residual solvent and allow stress relaxation.

10.4 Acknowledgements

The authors thank S. Peleshanko for the synthesis of PAN used in spin coated films. The authors acknowledge the financial support from AFOSR through grants FA9550-04-C-0099, F49620-03-C-0069 and NSF-CTS-0506832 Grants.

10.5 References

[1] LeMieux, M.C.; Minko, S.; Usov, D.; Stamm, M.; Tsukruk, V. V. *Langmuir* **2003**, *19*, 6126.

[2] Julthongpiput, D.; LeMieux, A.; Tsukruk, V. V. *Polymer* **2003**, *44*, 4557.

[3] Forrest, J. A.; Dalnoki-Veress, K.; Dutcher, J. R. Phys. Rev. E **1997**, *56*, 5705.

[4] Fakao, K.; Miyamoto, Y. Phys. Rev. E **2000**, *61*, 1743.

[5] Forrest, J.A.; Mattsson, J. Phys. Rev. E **2000**, 61, R53.

[6] Zanten, J.J.; Wallace, W.E; Wu, W. Phys. Rev. B **1996,** 53, R2053.

[7] Soles, C.L.; Douglas, J.F.; Jones, R.L.; Wu, W. Macromolecules **2004**, *37*, 2901.

[8] Yasuda, H. *Plasma Polymerization;* Academic Press,Inc: NewYork, 1985.

[9] LeMieux, M.; McConney, M. E.; Lin, Y-H.; Singamaneni, S.; Jiang, H.; Bunning, T.J.; and Tsukruk, V.V.; Nanoletters, **2006**, *6*, 730.

[10] Bruno, P.; Cicala, G.; Corsi, F.; Dragone, A.; Losacco, A.M. Sensors and Actuators B **2004**, *100*, 126.

[11] Jiang, H.; Johnson, W.E.; Grant, J.T.; Eyink, K.; Johnson, E.M.; Tomlin, D.W.; Bunning, T.J. Chem. Mater. **2003**, *15*, 340.

[12] Goodman, J. J. Polym. Sci. 1960, *44*, 551.

[13] Jiang, H.; O'Neill, K.; Grant, J.T.; Tullis, S.; Eyink, K.; Johnson, W.E.; Fleitz, P.; Bunning T.J. Chem. Mater. **2004**, *16*, 1292.

[14] Shen, M.; Pan, Y.V.; Wagner, M.S.; Hauch, K.D.; Castner, D.G.; Ratner, B.D.; Horbett. T.A. J. Biomater. Sci.-Polym Ed. **2001**, *12*, 961.

[15] Grill, A. *Cold Plasma in Materials Fabrication* (IEEE Press, New York, 1994).

[16] Biederman, H. *Plasma Polymer Films* (Imperial College Press, London, 2004).

[17] Yasuda, H.; Hirotsu, T. J. Appl. Polym. Sci. **1977**, *21*, 3179.

[18] Yasuda, H. Plasma Proc. Poly. **2005,** *2*, 293.

[19] Haaland, P.; Targove, J. Appl. Phys. Lett., 1992, *61*, 34.

[20] Tsukruk, V.V.; Bliznyuk, V.N. Langmuir 1998, *14*, 446.

[21] Tsukruk, V.V. Rubber Chem. Technol. **1997**, *70*, 430.

[22] Lemieux, M.C.; Usov, D.; Minko, S.; Stamm, M.; Shulha, H.; and Tsukruk, V. V. Macromolecules **2003**, *36*, 7244.

[23] Socrates, G. *Infrared and Raman characteristic group frequencies Tables and Charts* 3rd Ed. Wiley, NY, 2001.

[24] Boundy, R.H.; Boyer R.F. (Eds.), *Styrene, Its Polymers, Copolymers and Derivatives*, Reinhold, NY, 1952.

[25] Fox, T.G.; Flory, P.J. J. Appl. Phys., **1950**, *21*, 581.

[26] Brandrup, J.; Immergut, E.H.; Grulke, E.A. (Eds.) *Polymer hand book*, 4th Ed., Wiley, NY, 1999.

[27] Mukherjee, M.; Bhattacharya, M.; Sanyal, M.K.; Geue, Th.; Grenzer, J.; Pietsch, U. Phys. Rev. E **2002**, *66*, 061801.

[28] Thurn, J.; Cook, R.F.; J. Appl. Phys. **2002**, *91*, 1988,.

[29] Cao, Z.; Zhang, X. Sensor. Actuator. A-Phys. **2006**, *127*, 221.

[30] White G.K.; Choy, C.L. J. Polym. Sci. Polym. Phys. Ed. **1984**, *22*, 835.

[31] Lacks D.J.; Rutledge, G.C. Macromolecules **1995**, *28*, 1115.

[32] Reiter, G.; de Gennes, P.G.; Eur. Phys. J. E, **2001**, *6*, 25.

[33] Reiter, G.; Hamieth, M.; Damman, P.; Sclavons, S.; Gabriele S.; Vilmin, T.; Raphael, E. Nat. Mater. **2005**, *4*, 754.

[34] Jiang, H.; Grant, J.T.; Tullis, S.; Eyink, K.; Fleitz, P.; Bunning, T.J. *Polymer* **2004**, *45*, 84, 8475.

[35] Tsukruk, V.V.; Bliznyuk, V.N. *Langmuir* **1998**, *14*, 446.

[36] Tang, C.; Kowalewski, T.; Matyjaszewski, K. *Macromolecules* **2003**, *36,* 8587.

[37] Lai, J.T.; Filla, D.; Shea, R. *Macromolecules* **2002**, *35*, 6754.

[38] Tsukruk, V.V. *Rubber Chem. Technol.* **1997**, *70*, 430.

Chapter 11

General Conclusions

The significance and impact of this research is wide-ranging because it offers design considerations and presents results and very potential technology to advance key components of nanotechnology, a frontier that is increasingly changing society. Specifically, surface responsive organic materials designed and implemented here as nanoscale modifying layers of inorganic surfaces and silicon based microdevices in the form of multifunctional coatings and active layers in sensors.

Scientists researching nanoscale systems are control freaks. Prime goals include being able to *control* the surface properties, or *controlling* an interface, or *controlling* specific interactions, or *controllable* physical properties. Polymeric surfaces, because of their dynamic nature, more often than not, are exploited for these applications as ultrathin nanoscale layers on typically inorganic substrates. However, this development is not simple, and there are three general stages to tackle: 1) the layer needs to be successfully fabricated, which is not a trivial task to get ultra-clean, uniform nanolayers with molecular roughness (i.e. close to the cross sectional area of the polymer chain). 2) Their properties fully characterized, and 3) finally it should be proven that they can possess controllable properties. Very little research gets to stage 2 because stage 1 cannot be accomplished. As shown in this work, significant results are presented that characterize the nanomechanical properties of these layers. Very few research groups have been able to develop techniques and procedures that allow for AFM to obtain nanomechanical properties of these layers. Through the work in this research devoted to characterizing polymer brushes at the nanoscale, *quantitative* values of elastic modulus, as well as mechanical behavior are verified. Theoretical papers are published constantly inquiring how nanoscale polymers will react in different environments, and what the corresponding mechanical properties will be, because to develop

working NEMS devices, the physical properties at this scale need to be known. Not only are complex techniques developed here to *directly* probe and interpret mechanical behavior at this scale and get quantitative results, but intricate experiments are done also in fluidic environments and different temperatures because these will be the real working conditions of next generation NEMS.

Throughout the course of this work, several important innovations and significant contributions were made for the development of surface responsive materials applied to inorganic surfaces, which can be divided into three categories: fabrication, understanding of nanoscale/molecular properties and, most importantly, integration into working hybrid sensors.

Fabrication: For reversibly switchable surfaces, the absolute easiest way to design such surfaces is through binary brush surfaces in which two different monomers are attached to the same surface randomly. Many researchers believe that when you graft a single polymer to a surface and expose it to different environments resulting in different morphologies, this is a switchable surface. Technically, this is correct, and many claim this because they are easy to fabricate. However, the diversity of morphologies and properties is *vastly* enhanced if two polymers are grafted to a surface and can each occupy the topmost layer in different conditions, and that this topmost chemical composition can be switched (binary brush). This is a *true* reversibly switchable surface, and these are immensely difficult to fabricate with factors such as dewetting and kinetics (which are affected by factors like the molecular weights, glass transition temperature of each component, van der Waals radius, affinities to substrate, etc.) that must be accounted in order to have *active* complete switching. To date, this issue has not been addressed in sequentially grafted mixed (binary) brushes with total thickness less than 10 nm. In this work, we go far beyond this, and achieve a record of designing and conclusively showing the reversible switching of binary brushes grafted to a silicon surface with total layer thickness *only* 1 – 3 nm (Chapter 4). This in of itself is significant for the fact that these coatings offering powerful interfacial control can be implemented in the tightest spatial constraints of NEMS devices. Moreover, these layers

were comprised of polystyrene and poly (butyl acrylate) for strong mechanical disparities, as well as PS and poly (acrylic acid). The PS and PAA layer was designed for two reasons: 1) to produce an switchable amphiphilic surface less than 3 nm thick, as well as for 2) to amplify this switching in surface wettability which serves a purpose to verify the switching directly.

The brush system in Chapter 5 represents the only research in assembling complex molecules into *true* brush structures with the idea to act as responsive and load bearing surface nanolayers in engineered devices. The logic behind this work is as follows: it is unfortunate that many polymer chemists are synthesizing extravagant complex molecules just for aesthetics. Why not do some engineering with these complex molecules and integrate them into true brush layers where their unique structure-properties relationship can be taken advantage of? This is the first work to characterize the nanomechanical behavior of these complex branched-brushes. Importantly, these "complex" structures were fabricated by facile UV-polymerization by literally flipping a switch on and off. UV-grown branched brushes with unique nanomechanical response represents a major breakthrough in SRMs, this work will stimulates further development of this field, and it is just a matter of time before SRMs in the form of brush layers comprised of these complex molecules are the mainstream, and the next step beyond linear binary brushes.

The fabrication of plasma polymers here resulted in polymeric materials with significantly new properties. For example, not only did these materials result in high thermal expansion combined with high elastic modulus, a combination impossible to achieve with conventional polymers, but some of the plasma polymers exhibited large *negative* thermal expansion (Chapter 10). While such a phenomenon has been observed in ultrathin polymers due to confinement and entropic effects, such negative expansion has never been recorded in polymer coatings thicker than the radius of gyration, and here, this is observed in layers 100+ nm thick. Furthermore, plasma polymerization is advantageous because any monomer can be deposited in a dry process. There is very little research on the properties of plasma polymers, and while beyond the scope of this work, several significant properties were

discovered such as negative refractive index, that will be explored in the future in our lab. The significance of plasma polymers is that by adjusting deposition conditions, intrinsic aspects such as residual stresses, cross-linking density, and charge concentration can be tuned and 'freeze' in metastable states (because it is a room temperature deposition) that lead to amazing values of modulus, thermal expansion, etc.

In Chapters 6 and 7, a significant deviation of fabrication is embarked upon here in which 2D and 3D structures are *carved* out of polymer layers using interference lithography. While such structures have been fabricated previously, the novelty here is to use these structures in load-bearing applications with extremely high specific strength (modulus of 3GPa for a coating with 80% of the material removed). Owing to the fact that lithography variances can lead to gradients in cross-linking density, this leads to gradients in modulus, and thus the ability to control and *direct* crack propagation and failure mechanism.

Probing nanoscale/molecular properties. The most direct and powerful approach to this is by directly measuring interactions forces between single molecular groups/entities with AFM. In Chapter 3, significant work is done in this regard. Here, the interaction force of a *single* functional group with a single wall carbon nanotube was measured (SWCNT). This is the first time the interaction force of single molecules with a SWCNT was measured, and this is very critical breakthrough in nanotechnology because SWCNT are viewed as the most important material in this frontier. Understanding how molecules interact with them will lead to their application in everything from nanoscale sensors to composite materials. This study conclusively showed that functional groups will bind through either a H atom, or through a lone electron pair, depending upon nanotube charge. The fact that this could be done with clean AFM measurements is absolutely remarkable, and will motivate researchers to use the relatively easy AFM technique for fundamental studies such as this.

The context of Chapter 5 deals with complex brushes with unique nanomechanical response. In this chapter, the nanomechanical properties of these SRMs where characterized in fluidic environments with variable temperature. These results are significant for a couple

of reason: 1) this is the first study to give *quantitative* results of modulus of complex brushes under these varying experimental conditions. 2) Such experiments in varying fluidic/temperature environment with nanoscale resolution is only attainable with AFM, and it is imperative for more of these types of studies to appear in the literature because the properties of these materials need to be *absolutely* understood in these types of environments that will likely mimic application conditions. Only until now, however, these experimental variables have yet to be adapted for AFM nanoprobing experiments for complex cases of layered surface coatings, compliant binary layers with vertical and lateral phase separation, and switchable nanostructured layers.

Hybrid sensors. The significant contribution of this research is the actual integration of carefully designed nanoscale SRM into inorganic microscale structures (Chapters 8 and 9) to produce hybrid microsensors with unprecedented sensitivities. Inorganic (silicon) microfabricated devices are readily available and cheap to make. When 'crossed' with polymeric surface responsive materials, the result here are hybrid sensors that are economically produced and provides a platform for the ultimate sensor. The results produced in this research show thermal sensors with more than two orders of magnitude better sensitivity then what is attainable currently, as well as a humidity response on the order of parts per trillion, which is vastly more sensitive than current designs. Therefore, this work represents a *complete* and successful effort to develop working sensors with nanoscale dimensions: Specific SRM are designed and fabricated, carefully integrated into sensors as active nanolayers, and the response to various environments is fully proven, and thus the working sensor is conceptualized. The fact that these sensors have unprecedented sensitivities with microfabrication compatible active sensing layers will prove to be instrumental to the sensor community.

Clearly, nanotechnology is changing our lives, and the impact is just being felt. Nothing emphasizes this more then when in 2000, the United States government developed the National Nanotechnology Initiative (NNI) by devoting extensive funding to understanding and developing working structures in the nanometer range (actually, NEMS

are an official part of this program). The result of the research in this thesis forwards the foundation in perhaps two of the most critical broad areas of nanotechnology: ultrathin multifunctional polymer coatings and miniaturized sensors.

This work represents a broad effort, covering all scales. To complete this research, nature has put nine orders of magnitude between me, and the nanoscale SRM developed here that must be linked, interestingly enough, at intervals of three orders of magnitude. Molecular interactions and forces are characterized at the picoscale to optimize nanoscale layer design that in turn optimize and lead to microscale sensors with unprecedented sensitivities.

Appendix 1

A Champion Material

Throughout this research, several different monomers were initially screened for their performance in responding to thermal flux. The initial screening began by looking at close to 1000 monomers. The initial goal of this project was to produce IR sensors that absorbed very strongly in atmospheric windows (Figure A1-1). The main windows of interest are

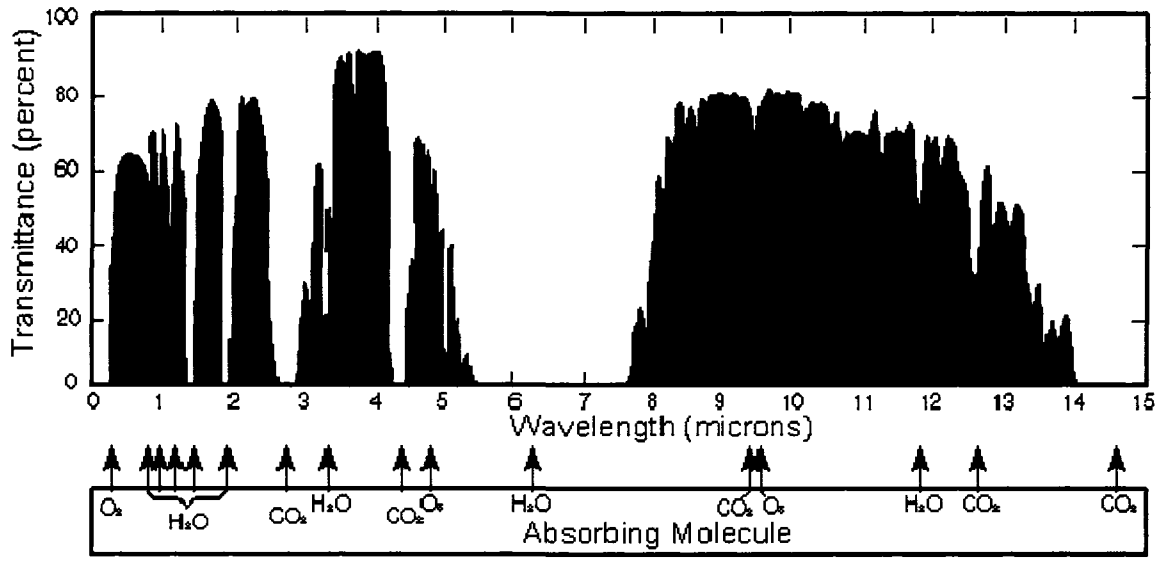

Figure A1-1. Atmospheric windows for IR radiation.

black body radiation (3-5μm, near IR) and hot body radiation (8-12μm, mid IR), mainly for defense related applications. Many functional groups partially absorb within these windows, but there are two that are nearly specific to these windows. Cyano groups are known for their strong absorption with 3-5μm, while fluoro groups are known for strong absorption at 8-12μm. Thus, FTIR traces of nearly 1000 monomers were analyzed for potential PECVD

onto microsensors to fabricate hybrid IR sensors. While nearly all monomers can be vapor deposited, some are more practical and others, and so the prospective monomers were narrowed further based on molecular weight, vapor pressure (higher is better), pricing, and toxicity. Finally, for the first two rounds of deposition, roughly 20 'final' prospective monomers were deposited on microsensors, and their thermal response was tested.

The following monomers displayed the best response in combination with best properties:

Styrene (Aldrich) W323306	100-42-5	Liquid	104.15	12.4	BP=145°C MP=-31°C ρ=0.909	1L = $19.30
Acrylonitrile (Aldrich) 110213	107-13-1	Liquid	53.06	86	BP = 77°C MP=-83°C ρ=0.806	500ml = $12.70 1L = $20.60
Pentafluoro styrene (Aldrich) 196916	653-34-9	Liquid	194.1	1	BP = 139°C MP=na ρ=1.406	5g= $42.20 25g = 140.50
MMA (Aldrich) M55909	80-62-6	Liquid	100.12	29	BP = 100°C MP=-48°C ρ=0.936	500ml=$20.10 1L= $36.20
Methacrylonitrile (Aldrich) 195413	126-98-7	Liquid	67.09	48.3	BP=90°C MP=-35°C ρ=0.8	100mL=$26.00
Benzonitrile (Aldrich) 294098	100-47-0	Liquid	103.1	1.00	BP=191°C MP=-13°C ρ=1.01	100mL=$66.40
Trimethylsilyl acetylene (Aldrich) 218170	1066-54-2	Liquid	98.22	216	BP=53°C MP=na ρ=0.709	1g=$14.60
(Trimethylsilyl) acetonitrile (Aldrich) 295965	18293-53-3	Liquid	113	5	BP=65°C MP=na ρ=0.83	1g=$20.60

The chemical structure for each of these monomers is given in Figure A1-2.

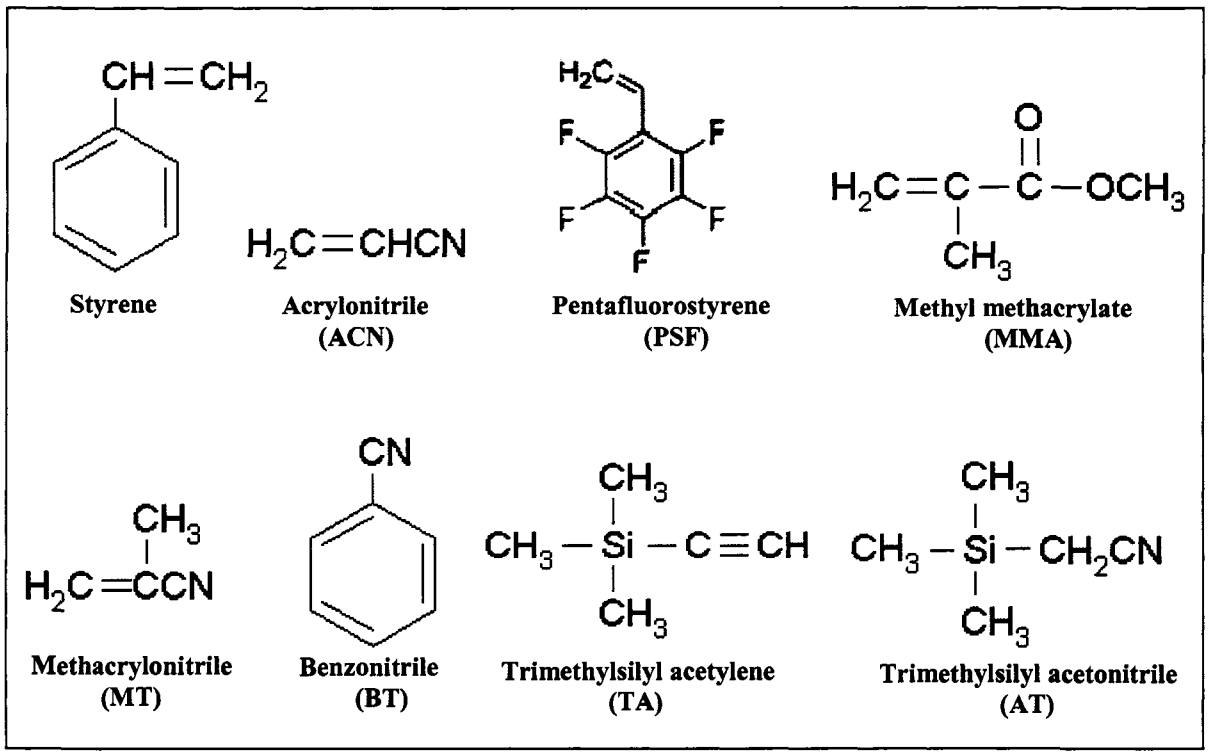

Figure A1-2. Chemical structures of best monomers for PECVD onto hybrid sensors.

All of these monomers were then subjected to thermal sensitivity tests, as well as characterized by AFM, and thermal expansion measurements by ellipsometry. The results of most of these monomers deposited onto microsensors, i.e. the properties of the overall hybrid sensor are listed in the table below.

PFS (#1) (Wafer1)	200 nm	3.8	Huge (180°)	Large (+30μm)	Up (relaxation)	133
PFS (#2) (Wafer1)	200 nm	3.8	Huge (180°)	Large (+30μm)	Up (relaxation)	133
PFS (#3) (Wafer2)	150 nm	3.8	N/A	N/A	N/A	133
PFS (#4) (Wafer2)	150 nm	3.8	N/A	N/A	N/A	133
PFS (#5) (Wafer3)	50 nm	1.5	Large (50°)	Large (+50μm)	Up (relaxation)	133
PFS (#6) (Wafer3)	50 nm	1.5	Large (50°)	Large (+50μm)	Up (relaxation)	133
ACN (#7) (Wafer4)	50 nm	0.9	Minimal (5° at most)	Small (10 μm)	Up (relaxation)	-18
ACN (#8) (Wafer4)	50 nm	0.9	Minimal (5° at most)	Small (10 μm)	Up (relaxation)	-18
[redacted]	[redacted]	[redacted]	[redacted]	[redacted]	[redacted]	[redacted]
[redacted]	[redacted]	[redacted]	[redacted]	[redacted]	[redacted]	[redacted]
ACN (#11) (Wafer6)	101 nm (AFM)	1.7	Minimal	Large (40μm)	Up (relaxation)	-18
ACN (#12) (Wafer6)	101 nm (AFM)	1.7	Minimal	Large (40μm)	Up (relaxation)	-18
MT (#13) (Wafer7)	50 nm	0.9	Minimal	Small (10μm)	Up (relaxation)	19
MT (#14) (Wafer7)	50 nm	0.9	Minimal	Small (10μm)	Up (relaxation)	19
[redacted]	[redacted]	[redacted]	[redacted]	[redacted]	[redacted]	[redacted]
[redacted]	[redacted]	[redacted]	[redacted]	[redacted]	[redacted]	[redacted]
BT (#17) (Wafer9)	340 – 390 nm (AFM)	2.5	Large (50°)	HUGE (100μm)	Up (relaxation)	31
BT (#18) (Wafer9)	340 – 390 nm (AFM)	2.5	Large (50°)	HUGE (100μm)	Up (relaxation)	31
[redacted]	[redacted]	[redacted]	[redacted]	[redacted]	[redacted]	[redacted]
[redacted]	[redacted]	[redacted]	[redacted]	[redacted]	[redacted]	[redacted]
TA (#21) (Wafer11)	100 nm (AFM)	0.6	Minimal	Large (30μm)	DOWN	4.7
TA (#22) (Wafer11)	100 nm (AFM)	0.6	Minimal	Large (30μm)	DOWN	4.7
AT (#23) (Wafer12)	95 nm (AFM)	0.5	Minimal	Large (40μm)	Up (relaxation)	-52
AT (#24) (Wafer12)	95 nm (AFM)	0.5	Minimal	Large (40μm)	Up (relaxation)	-52
AT (#25) (Wafer13)	Very thin (~20nm)	0.4	Minimal	Small (10μm)	DOWN	-52
AT (#26) (Wafer13)	Very thin(~20nm)	0.4	Minimal	Small (10μm)	DOWN	-52
MMA (#27) (Wafer14)	101 nm (AFM)	0.4	Minimal	Fluctuation	N/A	? (NEGATIVE n!)
MMA (#28) (Wafer14)	101 nm (AFM)	0.4	Minimal	Fluctuation	N/A	? (NEGATIVE n!)
MMA (#29) (Wafer15)	300 nm	0.4	Minimal	Small (20μm)	DOWN	? (NEGATIVE n!)

As seen form the chart, several monomers had extraordinary response to thermal flux, with the best candidates highlighted in green. In general, the nitriles performed very well. However, late in the last deposition, it was realized that the best response was with Methacrylonitrile (MT). It was found that the PSF generally had far too much residual stresses to be useful, and would only damage MEMS devices. Furthermore, PSF is unstable (see below). Although styrene would be a good material for hybrid sensor, it was eliminated from further studies because of its absorption window (does not contain a cyano or a fluoro group). The huge response of MT to thermal flux is shown in Figure A1-3.

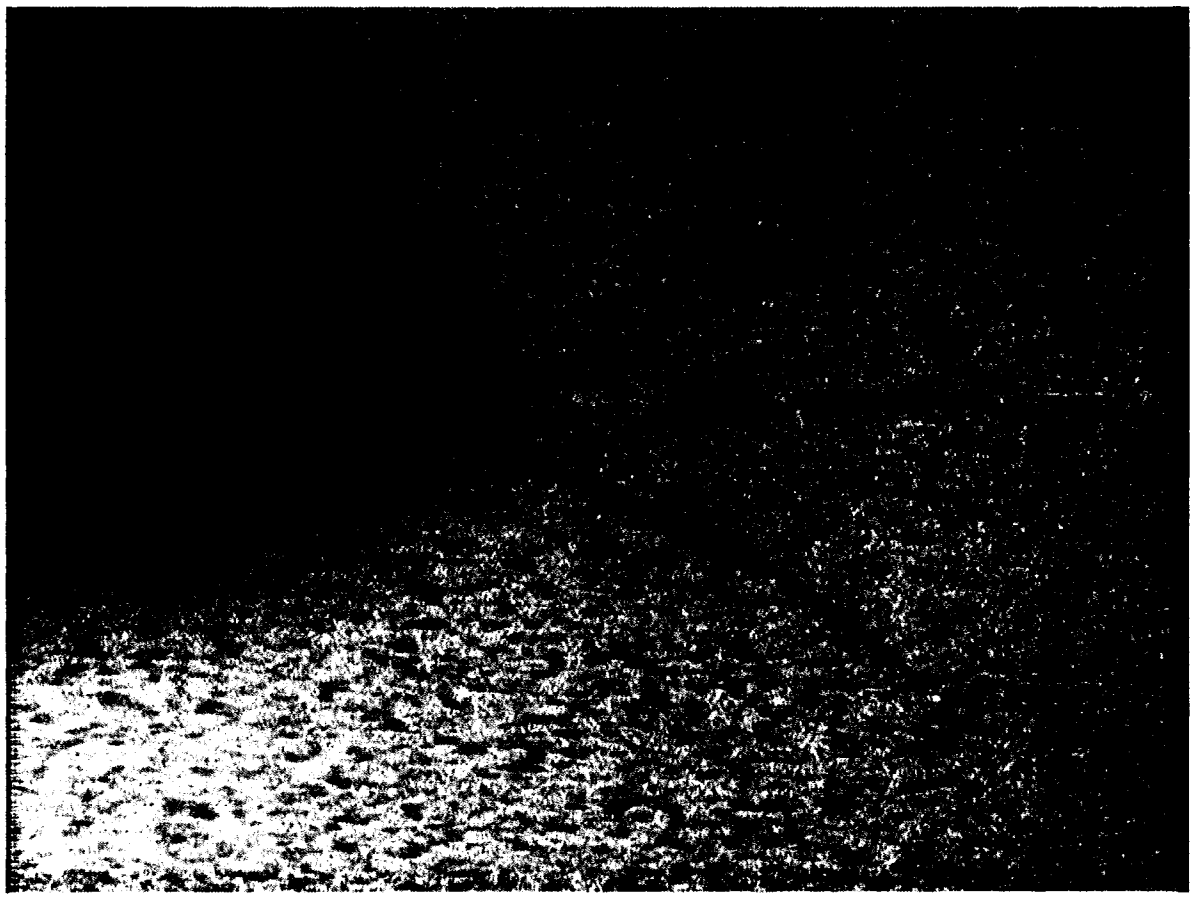

Figure A1-3. The response of the MT modified hybrid sensor to temperature. The overlayed images are taken at 0°C, room temperature (25°C), and 60°C. The overall length of the cantilever is about 350 μm.

This material (MT) is clearly a 'champion' monomer for thermal response. However, what makes this a true champion is that this monomer also exhibited the best, by far, response to humidity, as shown in Figure A1-4.

Figure A1-4. The response of the MT modified hybrid microsensor to humidity at room temperature (numbers indicate % relative humidity). Clearly, the huge response over the wide range indicated makes this an excellent choice for a humidity sensor.

Upon varying the humidity inside the testing chamber, the polymer on the surface of the cantilever absorbs or desorbs water vapor from the ambient. This *reversible* mechanism causes the polymer to undergo swelling and thus cause a bending of the polymer coated Si cantilever due to the bimaterial effect.

The deflection of the cantilever showed a small non-linearity (R^2 = 0.97730) and almost no hysteresis (<2%) as can be noticed from Figure A1-5, and which is actually typically common for organic materials as humidity sensors, but is advantageously avoided here. Any hysteresis is a result of absorbed water molecules failing to completely free themselves of the polymer network upon drying, and this can be improved upon by adding hydrophobic components in the layer. And herein lies one of the unique aspects of plasma polymer films that make them excellent humidity sensing materials: while its well-known that they have a high concentration of trapped radicals and ionic charges that act to strongly absorb large quantities of water that makes them hydrophilic in nature, they also have a high degree of cross-linking leading to large areas of CH_2 and CH_3 hydrophobic moieties randomly spread out in the network.

From the optical images the deflection of the cantilever for a variation of humidity from 6% to 66% (ΔRH= 60%) at room temperature (25 °C) was found to be 214 μm. Assuming a linear variation over the entire range, the sensitivity was calculated to be 3.5 μm/%. For comparison, the response of uncoated silicon cantilevers, with the same exact geometry and specifications, to humidity was recorded. Within the resolution of the optical detection scheme, we observed no change (zero deflection) in the cantilever position between 7% and 66% humidity.

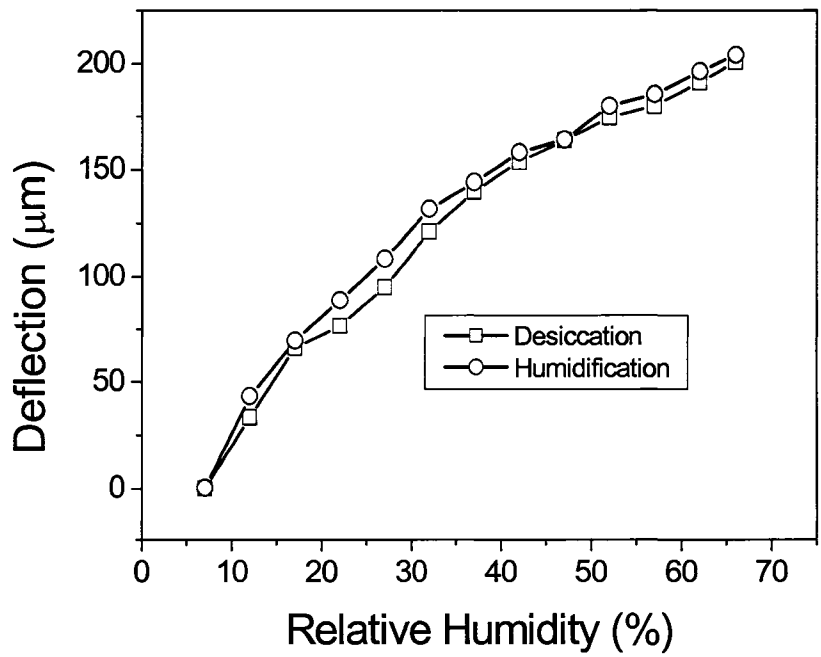

Figure A1-5: Sensor response to humidification and drying.

The thermal vibrations of the cantilevers used here were determined to be to roughly 1 nm. Therefore, the smallest detectable deflection was assumed to be 3nm, which is safely higher than the thermal noise (essentially, we are calculating lowest possible sensitivity). With these assumptions, the smallest detectable change in the humidity was calculated to be 8.9×10-4 % RH. Since the experiment was performed at room temperature (25°C), from the saturation vapor pressure, the 1% RH corresponds to 0.23 g/m3 of absolute humidity. Remarkable, the detection resolution of the cantilever was estimated to be 200 Parts per Trillion. To our knowledge there is no technique with such high sensitivity, either available commercially, or reported in the literature earlier. Apart from the unprecedented sensitivity of the sensor, there are several other attributes which makes the technology viable for numerous applications.

In addition to this, there is strong push to develop sensors to detect toxic chemicals and vapors. The response of the MT hybrid sensor was monitored in response to various organic solvents, and while this will be the subject of future work, depicted below (Figure A1-5) is the response to acetone vapor. The response here is nearly 50 μm, but the concentration of the vapor was not calibrated, and in the future, these tests will be systematically done to obtain 'toxicity plots', which are response of one microsensor to an array of vapors.

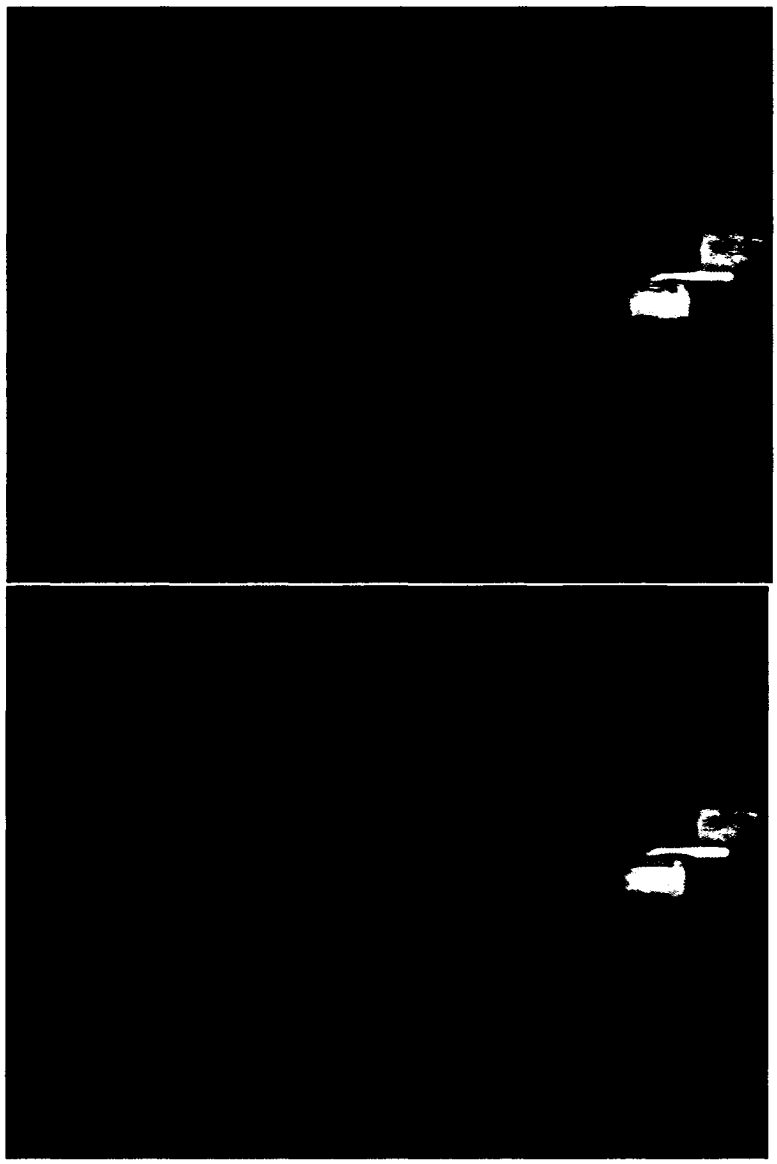

Figure A1-5. Response of the MT microsensor to acetone (top and ethanol (bottom) vapors.

These results are summarized in the chart below. As can be seen, the MT hybrid sensors exhibit the best overall response to temperature, humidity, and organic solvent vapor, making this material a true champion

ACN	40 μm	50 μm	3-5 μm	Forms cracks	55 °
PSF	50 μm	50 μm	5-8 μm	Swells and removed from the substrate	84 °
MT				Stable	58 °
TA	30 μm	5-10 μm	None	Stable	86 °
AT	30 μm	35 μm	None	Dissolves locally	75 °
BT	100 μm	30 μm	None	Swells and removed from the substrate	68 °
MMA	<5 μm	3-5 μm	None	Stable	71 °

Appendix 2

Supplemental Experiments

While the physics of plasma polymer are beyond the scope of this research (and certainly could easily be an additional thesis project all by itself), some supplemental experiments were attempted to give some insight to these properties to further explain the very strong response to certain stimuli observed, as well as peculiar properties such as high thermal expansion/high modulus combination. One theory for the response to humidity is the concentration of trapped radicals and charges within the network. Furthermore, the fact that most of the cantilevers bend down upon heating could be due to a couple affects: 1) Radicals that obtain mobility upon heating and interact stronger with each other, forming a stronger plasma polymer layer (similar to temperature responsive ionic gels with reversible charge density in a polyectrolytic polymer network[1]). 2) High intrinsic residual stresses as a result of metastable states being frozen into the layer during deposition. Two experiments to potentially elucidate these two items, respectively, are electric field testing and μ-Raman analysis that can directly quantify stresses in these structures.

Electric field tests. Using the electric field experimental setup described in Chapter 2, the sensors were brought into the field, and their deflection was monitored versus applied voltage. From Figure A2-1 below, clearly the electric field has a huge effect presumably on the plasma polymers, as their deflection is well beyond electrostatic force effects (see Fig. A2-1 control). From the data (Fig. A2-1), clearly ACN has the strongest shift, which seems to agree with the previous finding that the polymer with higher cross-linking, as directly evidenced by elastic modulus data (Chapter 9) will have a higher concentration of free radicals.[2] Another interesting point is that some of the monomers seem to exhibit a small degree of cycling or fluctuations. Indeed, some of the microsensors tested could have the

deflection measured by AFM because of huge oscillations in the electric field (see movies in presentation). This may be attributed to electrostriction[3], but this needs further analysis.

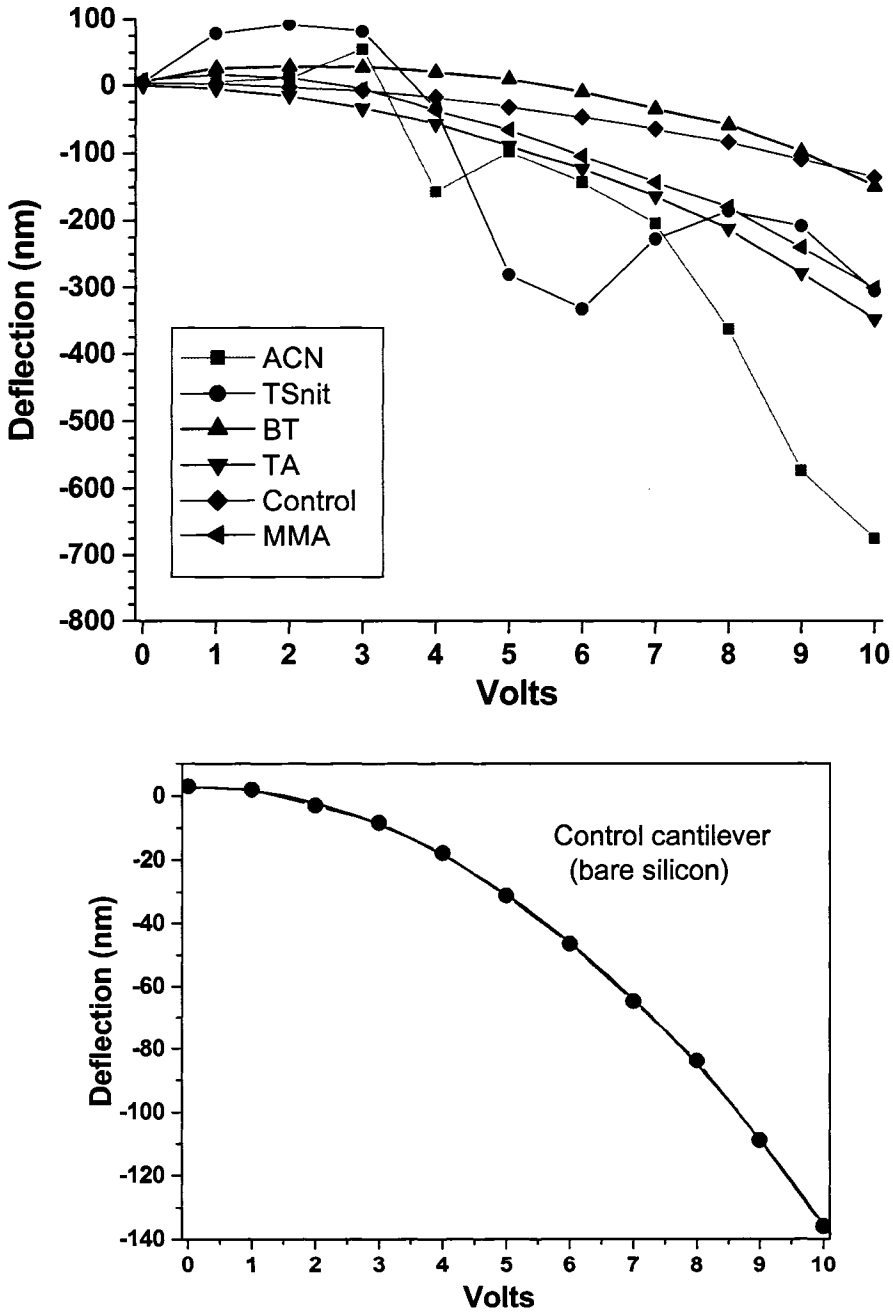

Figure A2-1. At top is the response of the indicated hybrid microsensor to electric field with the deflection monitored by AFM. At bottom is the control cantilever magnified to show the perfect square relationship expected.

Clearly, the microsensors are sensitive to electric field, with monomer-specific variations. The reasons for this at this time are not completely known, although certainly, the high concentration of free radicals and charges within the plasma network is a factor. Electrostriction may be occurring as well: upon feeling the electric field, the high concentration of ionized moieties and free radicals will try to align through the cross-linked network, and this alignment can cause a change in the mechanical properties, inducing stress and strain response to the electric field. If this is indeed electrostriction of these plasma polymers, this would make them ideal materials for nanoscale actuation applications.

Raman stress measurements. μ-Raman was employed to map the stress in silicon based microsensors coated with plasma polymer. The Raman spectrum is a plot of the scattered (stokes-shifted) intensity as a function of the Raman shift and contains information about the physical and chemical characteristics of the analyte. The Raman scattering frequency of Silicon is at 521 cm^{-1}, which is very sensitive to mechanical strain, thus making this technique one of the few that can directly measure residual stresses with sub-micron resolution. A shift of only 0.02 cm^{-1} corresponds to a stress of 10 MPa.[4] By monitoring this frequency at different positions on the sample, a "stress map" can be obtained with micrometer spatial resolution. In the present study, Raman peak position along the length of the cantilever was obtained to attempt to discern the exact residual stresses within the polymer layer, as well as to compare this with modeling results.

Initially, the stresses were mapped in the uncoated cantilevers as control for further measurements. Surprisingly, a huge stress in uncoated cantilevers was recorded. The peak position varied along the length of the cantilever as shown in Figure A2-2. A representative spectrum of Si obtained from the cantilever is shown in Figure A2-3. As one can observe, the peak is split into two components indicating the stress in the silicon as reported earlier.[5]

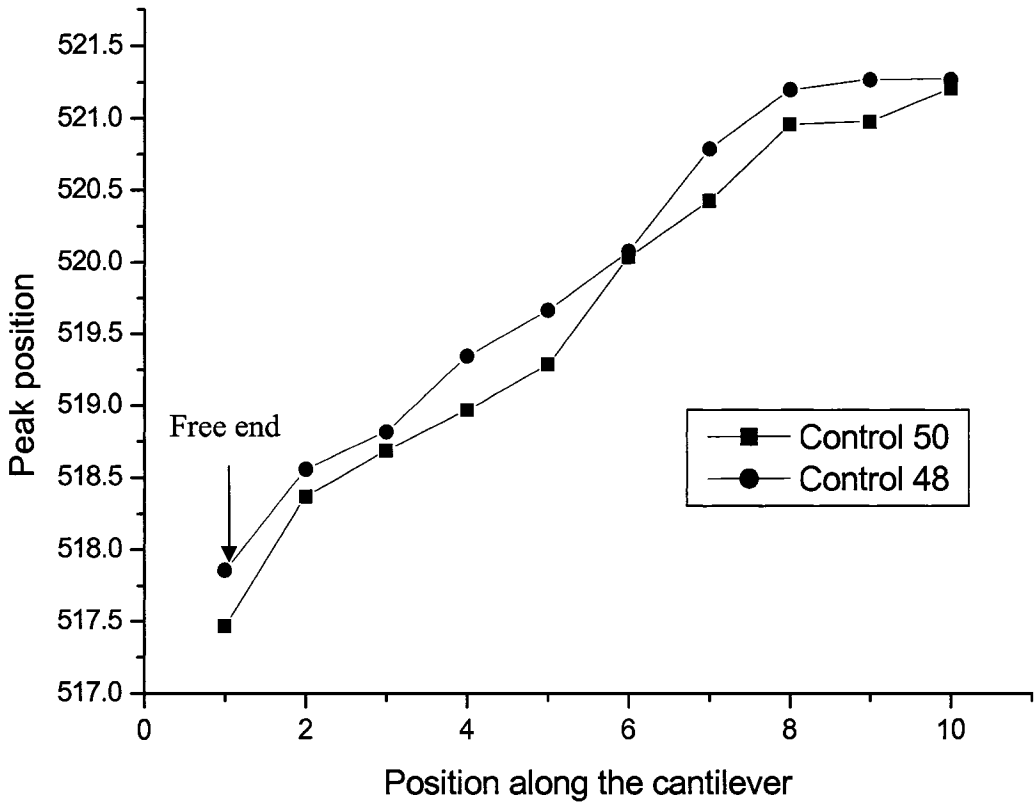

Figure A2-2: Si peak position along the length of the cantilever. The 'position' is a relative value as these 10 locations are divided equally over 350 μm.

The stress at the free end of the cantilever was found to be 1.75 GPa. Several uncoated cantilevers were tested to obtain similar results and this stress was considered as the baseline. Stress in two different cantilevers coated with ppPMAN and ppPMMA with pre-bending of 200μm and 10μm was mapped.

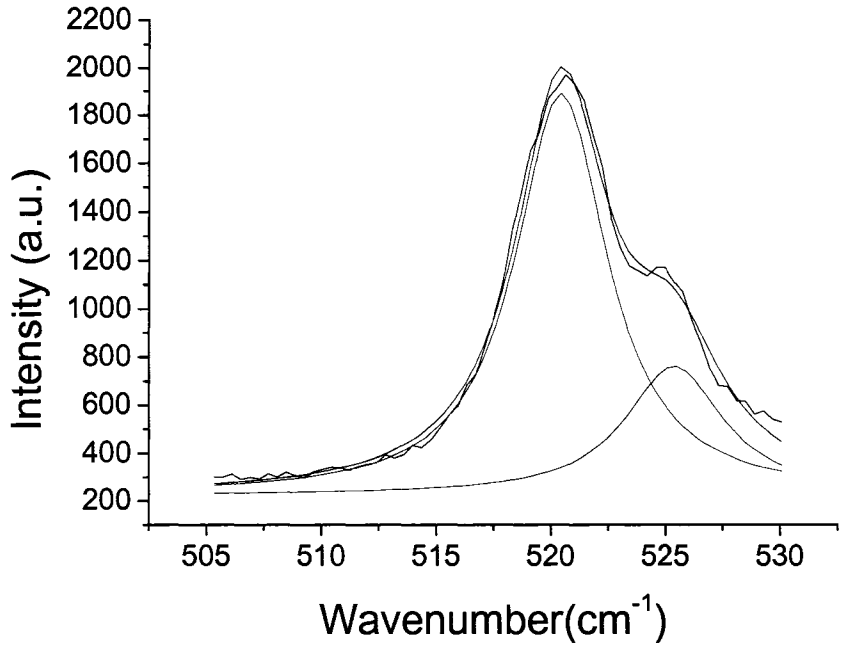

Figure A2-3: High resolution Raman spectrum of uncoated Si cantilever.

Figure A2-4 shows the Raman peak positions along the length of the cantilever for cantilevers coated with ppPMAN, ppPMMA compared with an uncoated control cantilever. It can be observed that the cantilever coated with ppPMAN with 200μm pre-bending exhibited a shift of 1.7 cm^{-1} with respect to the control cantilever which corresponds to a stress of 850 MPa, while the PMMA cantilever with a pre-bending of 10μm showed a shift of 0.75 cm^{-1} (375 MPa).

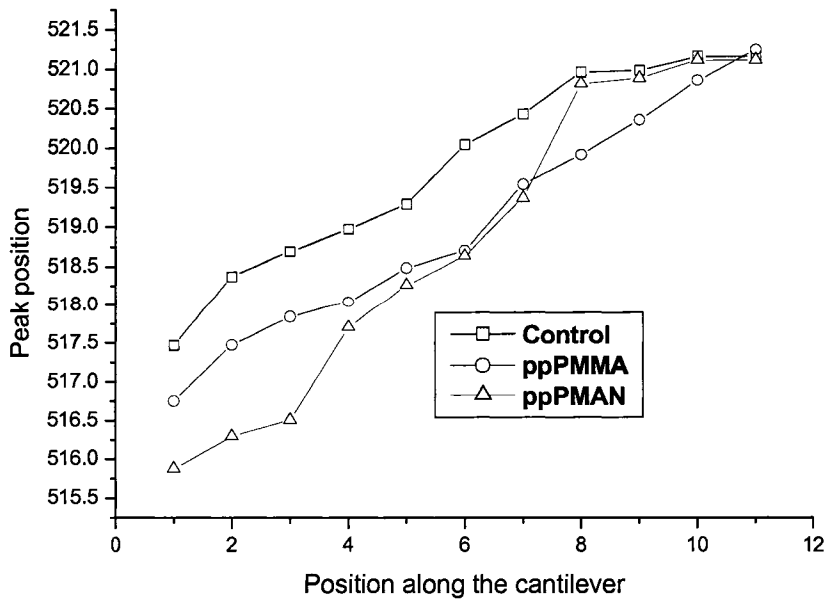

Figure A2-4: Raman peak position along the length of the cantilevers.

Finite Element analysis was used to theoretically estimate the stress in the pre-bent cantilevers. Figure A2-5 shows the stress along the length of the cantilever at the silicon surface. It can be noted that stress along the length of the cantilever is uniform except for the edge effects at the constrained edge and is equal to 160 MPa.

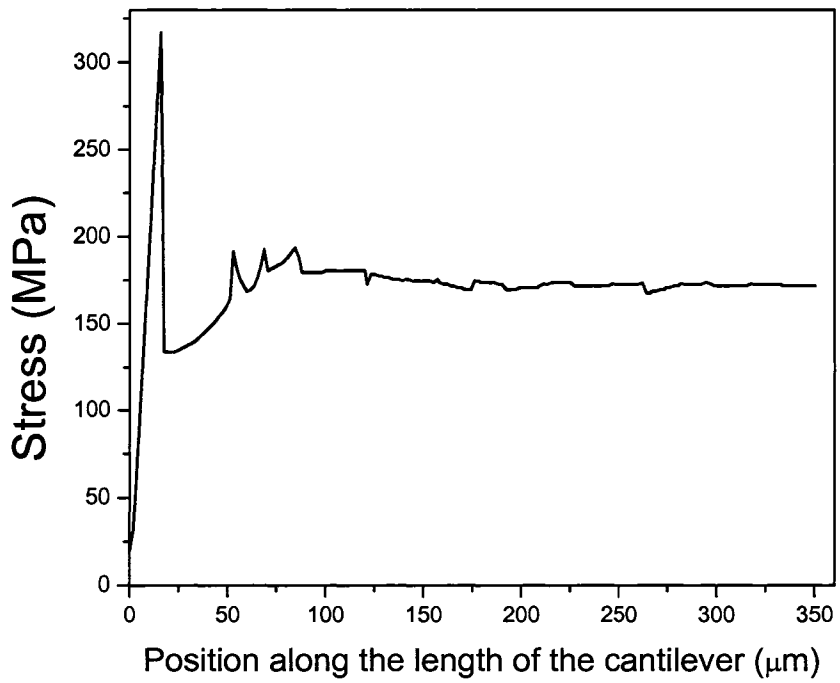

Figure A2-5: Stress along the length of the cantilever with a pre-bending of 200μm .

While the Raman stress mapping shows a gradient stress distribution along the length of the cantilever no such gradient was observed in the FEA results. Here, the speculation is that the gradient stress is inherent in the cantilevers from the microfabrication and the plasma polymer coating causes the bending resulting in a uniform stress along the cantilever. One can also note that the magnitude of stress obtained from the Raman measurements (850 MPa) is significantly higher compared to that obtained from FEA (160 MPa). This can be due to the fact that the plasma deposition process additionally introduced stress in the silicon which is not captured in the FEA.

References

1 Higa, M.; Yamakawa, T. J. Phys. Chem. B. **108**, 16703, 2004.

2 Yasuda, H.; Hirotsu, T. J. App. Poly. Sci. **21**, 3167, 1977.

3 Pelrine, R.E.; Kornbluh, R.D.; Joseph, J.P. Sens. Act. A. **64**, 77, 1998.

4 Godin, M.; Tabard-Cossa, V.; Grutter, P.; Williams, P. App. Phys. Lett. **79**, 4, 2001.

5 Sugii, N. J. Appl. Phys. **89**, 6459, 2001

Biographical Sketch

Melburne Charles LeMieux was born September 1, 1978 in Alpena, Michigan. He attended Western Michigan University for four years, enrolled in the Department of Construction and Materials Design, before transferring to Iowa State University for his final year of undergraduate work in 2001. He received the Master of Science in Materials Science and Engineering from Iowa State University in 2003, and his Doctor of Philosophy in Materials Science and Engineering from Iowa State University in 2006. Throughout his graduate work, he had three prestigious internships at Sandia National Labs (2001), Lawrence Livermore National Laboratory (2004), and the Institute for Soldier Nanotechnology at MIT (2005). During his PhD work (2003-2006), he has given several presentations at national conferences and generated several refereed publications (see below). He has accepted a position in the Chemical Engineering Department at Stanford University.

Presentations

Invited Talks:

- "AFM beyond imaging". Invited talk at The Institute for Soldier Nanotechnology, MIT, Cambridge, MA, April 14, 2005.

- "Polymer nano-assemblies". Invited talk at Agiltron, Corp., Wilmington, MA, Nov. 12, 2004.

- "AFM based thermal analysis of organic and inorganic surfaces." Invited talk at Thermomicroscopes, Inc., Sunnyvale, CA, Feb. 28, 2003.

- "Thermal analysis of decagonal phase quasicrystal by scanning thermal microscopy." Invited talk at University of Wisconsin, Madison, Nov. 11, 2001.

Oral Presentations at National Conferences:

- "Nanomechanical response of palm-tree architecture polymer brush surfaces". 230th American Chemical Society (ACS) National Meeting, Washington, DC, Aug. 30, 2005.

- "Manipulating polymer interfaces: adaptive morphology of mixed brushes in a selective and non-selective surrounding". 227th ACS National Meeting, Anaheim, CA, March 30, 2004.

- "Nanoscale forces in complex systems of multi-layered polymer brushes and compliant individual molecules." 227th ACS National Meeting, Anaheim, CA, March 30, 2004.

- "Switching between sticky and slippery surfaces in adaptive polymer surfaces". 227th ACS National Meeting, Anaheim, CA, April 1, 2004.

- "Thermo-elastic properties in confined ultrathin films". 32nd Annual conference of the North American Thermal Analysis Society (NATAS), Williamsburg, VA, Oct. 4, 2004.

- "AFM based thermal analysis of organic and inorganic surfaces". 32nd Annual NATAS National Meeting, Williamsburg, VA, Oct. 5, 2004.

- "Tunable microstructure and nanomechanical properties in a binary polymer brush." 226th ACS National Meeting, New York, NY, Sept. 9, 2003.

- "Nanomechanical properties of switchable binary polymer brush films." 225th ACS National Meeting, New Orleans, LA, March 25, 2003.

- Presentation of results at the Sandia National Laboratory Summer Symposium in Albuquerque, NM on August 9, 2001.

Poster Presentations at National Conferences:

- 216th American Chemical Society National Meeting in Boston, MA on August 23-27, 1998.

- 1998 Gordon Research Conference on Tribology: Wear and Contact Damage. Held at Holderness School in Plymouth, NH on June 28 – July 3, 1998.

- Tribology Issues and Opportunities in MEMS Workshop held at The Ohio State University in Columbus Ohio on November 9-11, 1997.

Refereed publications

- **LeMieux, M.C.**; Friddle, R.W.; Artyukhin, A.B.; Tsukruk, V.V.; Noy, A. "Functional group interactions with sidewalls of individual carbon nanotubes". *In review, Nature Materials* **2006**.

- **LeMieux, M.C.**; Peleshanko, S.; Anderson, K; Tsukruk, V.V. "Adaptive nanomechanical response of stratified polymer brush structures." *In review, Langmuir* **2006**.

- Jang, J.H.; Ullal, C.K.; Choi, T.; **LeMieux, M.C.**; Tsukruk, V.V.; Thomas, E.L. "3D polymer microtrusses". *Advanced Materials, published online* **July 2006**.

- Choi, T.; Jang, J.H.; Ullal, C.K.; **LeMieux, M.C.**; Tsukruk, V.V.; Thomas, E.L. "The elastic properties and plastic behavior of two-dimensional polymer structures fabricated with laser interference lithography". *Advanced Functional Materials* **2006**, 16, 1324-1330.

- **LeMieux, M.C.**; McConney, M.E.; Lin, Y.-H.; Singamaneni, S.; Jiang, H.; Bunning, T.J.; Tsukruk, V.V. "Polymeric nanolayers as actuators for ultra-sensitive thermal bimorphs". *Nano Letters* **2006**, 6, 730-734.
- Lin, Y.-H.; McConney, M.; **LeMieux, M.C.**; Peleshanko, S.; Jiang, C.; Singamaneni, S.; Tsukruk, V.V. "Tri-layered ceramic-metal-polymer microcantilevers with dramatically enhanced thermal sensitivity". *Advanced Materials* **2006**, 18, 1157-1161.

- **LeMieux, M.C.**; Lin, Y.-H.; Coung, P.D.; Ahn, H.-S.; Zubarev, E.R.; Tsukruk, V.V. "Microtribological and nanomechanical properties of switchable Y-shaped amphiphilic polymer brushes". *Advanced Functional Materials* **2005**, 15, 1529-1540.

- **LeMieux, M.C.**; Usov, D.; Minko, S.; Stamm, M.; V.V. Tsukruk. "Local chain organization of switchable binary polymer brushes in selective solvents" in *Polymer Brushes*, Advincula, R.; Brittain, W.J.; Caster, K.C.; Ruhe, J. Eds. Wiley-VCH: Weinheim, **2004**, 427-439.

- **LeMieux, M.C.**; Julthongpiput, D.; Bergman, K.; Cuong, P.D.; Ahn, H-S.; Lin, Y.-S.; Tsukruk, V.V. "Ultrathin binary grafted polymer layers with switchable morphology". *Langmuir* **2004**, *20*, 10046-10054.

- Kovalev, A.; Shulha, H.; **LeMieux, M.C.**; Myshkin, M.; Tsukruk, V.V. "Nanomechanical probing of layered nanoscale polymer films with atomic force microscopy". *Journal of Materials Research* **2004**, *19*, 716-728.

- Bonhomme, G.; **LeMieux, M.C.**; Weisbecker, P.; Tsukruk, V.V.; Dubois, J.M. "Oxidation kinetics of an AlCuFeCr approximant compound: an ellipsometry study". *Journal of Non-Crystalline Solids* **2004**, *334&335*, 532-539.

- Barrow, J.A.; **LeMieux, M.C.**; Cook, B.A.; Ross, A.R.; Tsukruk, V.V.; Canfield, P.C.; Sordelet, D.J. "Micro-surface and bulk thermal behavior of a single-grain decagonal Al-Ni-Co quasicrystal". *Journal of Non-Crystalline Solids* **2004**, *334&335*, 312-316.

- **LeMieux, M.C.**; Usov, D.; Minko, S.; Stamm, M.; Shulha, H.; Tsukruk, V.V. "Reorganization of binary polymer brushes: Reversible switching of surface microstructures and nanomechanical properties". *Macromolecules* **2003**, *19*, 7244-7255.

- Julthongpiput, D.; **LeMieux, M.C.**; Tsukruk, V.V. "Micromechanical properties of glassy and rubbery polymer brush layers as probed by atomic force microscopy". *Polymer* **2003**, *16*, 4557-4562.

- **LeMieux, M.C.**; Minko, S.; Usov, D.; Stamm, M.; Tsukruk, V.V. "Thermo-elastic properties of glassy and rubbery polymer brushes grown by "grafting from" approach". *Langmuir* **2003**, *15*, 6126-6134.